

**Numerical Simulations of Convection and  
Convection-Driven Dynamos in Spherical Shells**

by

**Ryan J. Orvedahl**

B.S., Stony Brook University, 2013

M.S., University of Colorado at Boulder, 2016

A thesis submitted to the

Faculty of the Graduate School of the

University of Colorado in partial fulfillment

of the requirements for the degree of

Doctor of Philosophy

Department of Astrophysical & Planetary Sciences

2020

Committee Members:

Michael Calkins, Chair

Dr. David Brain

Dr. Benjamin Brown

Dr. Bradley Hindman

Dr. Keith Julien

Orvedahl, Ryan J. (Ph.D., Astrophysical & Planetary Sciences)

Numerical Simulations of Convection and Convection-Driven Dynamos in Spherical Shells

Thesis directed by Dr. Michael Calkins

The majority of Solar System planets, in addition to the Sun and other stars, possess global, or large-scale, magnetic fields. These magnetic fields are all thought to be generated by the dynamo mechanism, whereby the kinetic energy associated with convectively stirred motions of an electrically conducting fluid is converted into electromagnetic energy. The large-scale magnetic fields of most of these bodies are aligned with their respective rotation axis, and often are characterized by a relatively strong dipolar component. In this work, large-scale magnetic field properties are investigated using two separate cases: a simplified model similar to the Sun, and a more comprehensive model that shares similarities with the Earth. For the Sun-similar cases, the beginning of the dynamo process is studied more closely to see how the kinetic energy of the system behaves as the fluid properties are varied. The simplified model has no magnetic fields and no rotation. Scaling relations for the kinetic energy are established enabling description of how the boundary layer influences the dynamics. The Earth-like cases include rotation and magnetic fields in an effort to study the saturation of the large-scale magnetic field as the thermal forcing is increased. This saturation is explored over a wide range of system parameters and is found to be a robust feature of rapidly rotating dynamo simulations. These results are described using a semi-magnetostrophic force balance, where the Lorentz force enters the leading-order mean force balance in only a single component direction. Techniques from asymptotic theory are applied in order to determine the scaling behavior of the fields as well as the scaling behavior of the individual forces present in the mean momentum equation.

## **Dedication**

It is both an honor and a privilege and a pleasure to dedicate this work to my parents, Donna and Jeff. I would not be the person I am today without their constant love, support, and encouragement.

## Acknowledgements

I would like to express my deepest appreciation to my advisor, Dr. Michael Calkins, for providing guidance and feedback throughout each stage of this dissertation.

I will be forever thankful to all of my friends and colleagues at CU who helped me grow as a person/scientist and helped make graduate school that much more fun.

A very special thank you to both of my parents for enduring long conversations as I tried to hash out various research roadblocks and new techniques, and then always ending with their unwavering confidence that I would eventually figure it out and finish.

## Contents

### Chapter

<b>1</b>	<b>Background</b>	<b>1</b>
1.1	Magnetic Fields of Astrophysical Bodies . . . . .	1
1.1.1	The Planets . . . . .	1
1.1.2	The Sun . . . . .	3
1.1.3	The Earth . . . . .	6
1.2	Dynamo Theory . . . . .	12
1.2.1	Fluid Equations . . . . .	14
1.3	Numerical Methods . . . . .	21
1.3.1	Spectral Decomposition . . . . .	21
1.3.2	Boundary Conditions . . . . .	23
1.4	Nondimensional Control Parameters . . . . .	24
1.5	Force Balances in Rapidly Rotating Systems . . . . .	28
<b>2</b>	<b>Prandtl-number Effects in High-Rayleigh-number Spherical Convection</b>	<b>31</b>
2.1	Preamble . . . . .	31
2.2	Published Work . . . . .	32
2.2.1	Introduction . . . . .	32
2.2.2	Numerical Model . . . . .	36
2.2.3	Numerical Experiment . . . . .	37

2.2.4	Survey of Results . . . . .	40
2.2.5	Perspectives and Conclusions . . . . .	48
<b>3</b>	<b>Force Balances and Asymptotic Scaling Behavior of the Large-Scale Dynamics</b>	<b>51</b>
3.1	Introduction . . . . .	51
3.2	Methods . . . . .	55
3.3	Asymptotic Scaling Behavior . . . . .	60
3.4	Comparison with Numerical Simulations . . . . .	66
3.4.1	Mean Heat Equation . . . . .	66
3.4.2	Mean Momentum Equation . . . . .	70
3.5	Force Balances . . . . .	73
3.6	Flow Morphology . . . . .	79
3.7	Comments on Taylor's Constraint and Torsional Oscillations . . . . .	82
3.8	Loss of Balance in Multipolar Dynamos . . . . .	83
3.9	Additional Computational Details . . . . .	86
3.9.1	Changing Scalings: $\text{Ra}/\text{Ra}_{\text{crit}}$ versus $\text{Ra}\text{Ek}^{4/3}$ . . . . .	86
3.9.2	Ekman Layer: Including versus Excluding . . . . .	89
3.10	Conclusions . . . . .	90
<b>4</b>	<b>Large-Scale Magnetic Field Generation: Saturation and Scaling Behavior</b>	<b>93</b>
4.1	Introduction . . . . .	93
4.1.1	Methods . . . . .	97
4.2	Energetics . . . . .	97
4.3	Flow Morphology . . . . .	103
4.4	Influence of $\text{Rm}$ . . . . .	105
4.5	Dipolarity . . . . .	106
4.6	Scaling of the Mean Lorentz Force . . . . .	108
4.7	Energy Source Terms . . . . .	111

4.8 Heat Transfer Induced by the Mean Field . . . . .	114
4.9 Induction Equation Balances . . . . .	116
4.10 Conclusions . . . . .	121
<b>5 Final Thoughts</b>	<b>124</b>
5.1 Simplified Stellar Models . . . . .	124
5.2 Force Balances in Rapidly Rotating Planetary Systems . . . . .	125
5.3 Saturation of the Large-scale Magnetic Field in Planetary Systems . . . . .	126
5.4 Concluding Remarks . . . . .	128
<b>Bibliography</b>	<b>129</b>
<b>Appendix</b>	
<b>A Selected Output Parameters</b>	<b>144</b>
<b>B Semi-Magnetostrophic Energetics</b>	<b>146</b>
<b>C Additional Scaling Relations</b>	<b>147</b>

**Tables****Table**

1.1	Nondimensional parameters of the Earth and Sun . . . . .	25
2.1	Input and output parameters for all solar-like simulations . . . . .	38
3.1	Saturated mean magnetic energy input/output parameters . . . . .	57
3.2	Critical Rayleigh numbers . . . . .	61
3.3	Scaling relations . . . . .	74

## Figures

### Figure

1.1	Schematic of Uranus and Neptune magnetic field . . . . .	3
1.2	Composite image of the Sun . . . . .	4
1.3	Upper bound of longitudinal KE . . . . .	6
1.4	Partial reversal history of Earth . . . . .	11
1.5	Obtainable regimes using current simulations . . . . .	27
2.1	Dimensional kinetic energy and Reynolds . . . . .	40
2.2	Velocity power spectra and shell slices . . . . .	43
2.3	Energy transport and thermal boundary layer . . . . .	46
2.4	Entropy profiles and boundary layer location . . . . .	47
3.1	Mean temperature equation scaling . . . . .	66
3.2	Diffusion-based length scale for the mean temperature . . . . .	68
3.3	Mean meridional circulation scaling . . . . .	69
3.4	Fluctuating temperature scaling and radial profiles . . . . .	69
3.5	Fluctuating velocity and mean zonal flow scaling . . . . .	71
3.6	Mean and fluctuating magnetic field scaling . . . . .	72
3.7	Diffusion-based length scales for mean magnetic field . . . . .	73
3.8	Mean force versus time for the $E_k = 10^{-5}$ , $Ra = 10 R_{a_{\text{crit}}}$ case . . . . .	75
3.9	Mean force versus latitude for the $E_k = 10^{-5}$ , $Ra = 10 R_{a_{\text{crit}}}$ case . . . . .	77

3.10 Mean force versus Ekman number . . . . .	78
3.11 Mean Lorentz force and advection versus Ekman number . . . . .	80
3.12 Meridional views of the velocity for different Ekman . . . . .	81
3.13 Butterfly comparison between dipolar and multipolar case . . . . .	84
3.14 Force balance in the multipolar case . . . . .	85
3.15 Changing scalings based on criticality and reduced Rayleigh . . . . .	88
3.16 Comparison of including the Ekman layer . . . . .	89
4.1 Mean and fluctuating KE and ME . . . . .	99
4.2 Mean ME for specific spherical harmonics . . . . .	100
4.3 Velocity power spectra for $\text{Ek} = 10^{-5}$ cases . . . . .	101
4.4 Magnetic field power spectra for $\text{Ek} = 10^{-5}$ cases . . . . .	101
4.5 Mean magnetic field versos Rossby . . . . .	102
4.6 Meridional views of the velocity for two different Ra . . . . .	104
4.7 Ratio of mean ME to total ME . . . . .	105
4.8 Dipolarity as a function of Ra . . . . .	107
4.9 Mean Lorentz force versus Ra . . . . .	109
4.10 Meridional views of the mean Lorentz force for a specific case . . . . .	110
4.11 Magnetic energy source terms . . . . .	112
4.12 Zonal component of mean Lorentz work compared to buoyancy work . . . . .	115
4.13 Heat transport vs Ra . . . . .	117
4.14 Mean induction source terms . . . . .	118
4.15 Mean induction terms versus Ekman number . . . . .	119
C.1 Mean temperature scaling . . . . .	148
C.2 Extra mean field scalings . . . . .	149
C.3 Taylor microscale for fluctuating magnetic field . . . . .	150

# **Chapter 1**

## **Background**

Convection is a fundamental physical process that controls the heat transport and therefore thermal evolution of many planets and stars. Cumulus clouds are the result of convective motions and can be observed nearly every day in Earth's atmosphere (see Yano (2014) for a review of atmospheric convection). The surface of the Sun is covered in large convective granules ( $\sim 1$  Mm) that overturn with a roughly five minute time scale (Leighton et al., 1962). The Earth's interior also is believed to be convecting; convection in the mantle (Schubert et al., 2001) drives plate tectonics (Bercovici, 2003). More exotic systems also show evidence of convection, such as the planes of accretion disks (Held and Latter, 2018) and the magnetospheres of giant planets (Thomsen et al., 2012). These systems all involve electrically conducting regions, and convection in such a region is believed to build magnetic fields through the dynamo process (Jones, 2011).

### **1.1 Magnetic Fields of Astrophysical Bodies**

#### **1.1.1 The Planets**

Magnetic fields are ubiquitous throughout the solar system. Self-generated magnetic fields (dynamo action) have been detected on nearly every large body in the solar system including the Sun, Mercury, Earth, the giant planets, and one of the Jovian satellites (Connerney, 2015). The magnetic field of Mercury was first detected in 1975 by the Mariner 10 spacecraft. It is largely dipolar with a very weak magnitude and its origin can be explained by dynamo theory (Ness et al., 1975a,b; Stevenson, 1975). Venus was found to have a magnetic field in 1967 by

the Venera 4 spacecraft, but its origin is more exotic. The strong solar wind produced by the Sun interacts with the upper ionosphere of Venus causing an induced magnetic field, compared to the internally generated field produced from a dynamo process (Dolginov et al., 1969; Elphic and Russell, 1983; Luhmann et al., 1983; Stevenson, 2003). Mars does not show any evidence of a global magnetic field, but observations show that portions of the crust are magnetized, suggesting a global magnetic field existed at one point in the martian past (Hood and Hartdegen, 1997; Acuna et al., 1998). Jupiter, the largest planet in the solar system, has the largest magnetic field, excluding the Sun. The magnetic field of Jupiter was observed directly first by the Pioneer 10 spacecraft in 1973 (Smith et al., 1976), although indirect radio observations suggested a magnetic field as early as the mid 1950s (Burke and Franklin, 1955). The dipole component of Jupiter's magnetic field is significantly larger in magnitude than any other component and is moderately aligned with the rotation axis possessing a dipole tilt of  $\sim 10^\circ$ . Saturn has the second largest magnetic field among the planets. After the indirect detection of Jupiter's field in the 1950s, many studies attempted to find evidence for Saturn's magnetic field, but the results were inconclusive. Saturn's magnetic field was detected definitively in 1979 when Pioneer 11 flew directly through it and measured an exceptionally axisymmetric dipolar magnetic field (Smith et al., 1980a,b; Todoechuck et al., 1981), that is well-aligned with its rotation axis. Uranus has a rather peculiar magnetic field, first detected by Voyager 2 in 1986 (Ness et al., 1986). A schematic for the magnetic field of Uranus is shown on the left side of Figure 1.1. The field does not originate from the geometric center of the planet and is tilted by  $\sim 60^\circ$  from the rotation axis. The dipole field is significantly shifted from the center by as much as a third of the planetary radius, leading to vastly different magnitudes of the field in both hemispheres. As a result, the magnetic field does not have a strong dipolar component, it is multipolar. Neptune is quite similar to Uranus in that both have peculiar magnetic fields. The magnetic field of Neptune was measured first by Voyager 2 in 1989 and shows a significant tilt of  $\sim 50^\circ$  between the dipolar component and the rotation axis (Warwick et al., 1989). Neptune's magnetic field is shown schematically on the right side of Figure 1.1. Like Uranus, Neptune's field does not originate from the geometric center; it is offset by roughly half a planetary radius. As

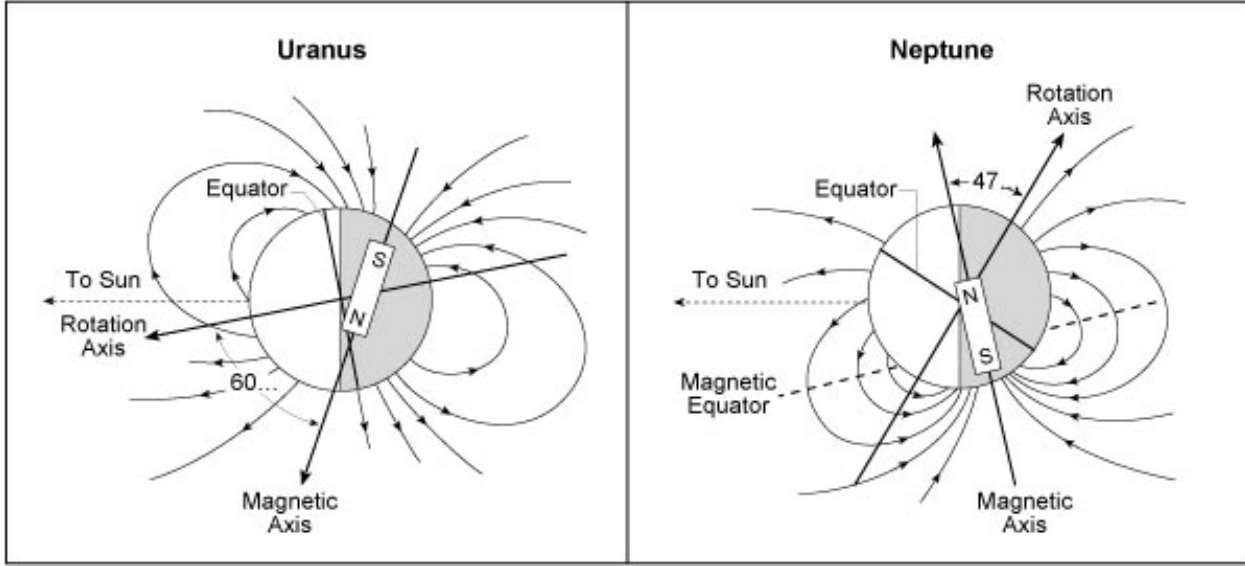


Figure 1.1: Schematic drawing of the magnetic fields that appear at Uranus (Ness et al., 1986) and Neptune (Ness, 1994).

nearly every planet in our solar system has a magnetic field, extrasolar planets also are expected to have magnetic fields (e.g., Gaidos et al., 2010).

The inner planets have relatively hot inner cores allowing ions and free electrons to move around in a fluid interior. The outer planets have a core composition that is highly conducting. If these objects rotate fast enough, the freely moving charges can generate an electrical current that in turn can generate a large-scale magnetic field. There is a large variety of observed magnetic fields within the planets in the solar system. This raises the question of what controls this variety? If the dynamo process is believed to explain many of these fields, then what parameters are responsible for the different magnitudes in field strength and what parameters control the different field topologies?

### 1.1.2 The Sun

Galileo was the first person to point a telescope at the Sun over 400 years ago, where he would observe dark spots on the surface, known as sunspots. It would be another 300 years before Hale (1908) showed that these sunspots contained strong, coherent magnetic fields. Nearly continuous space-based observations provide a full-disk picture of how the solar magnetic field

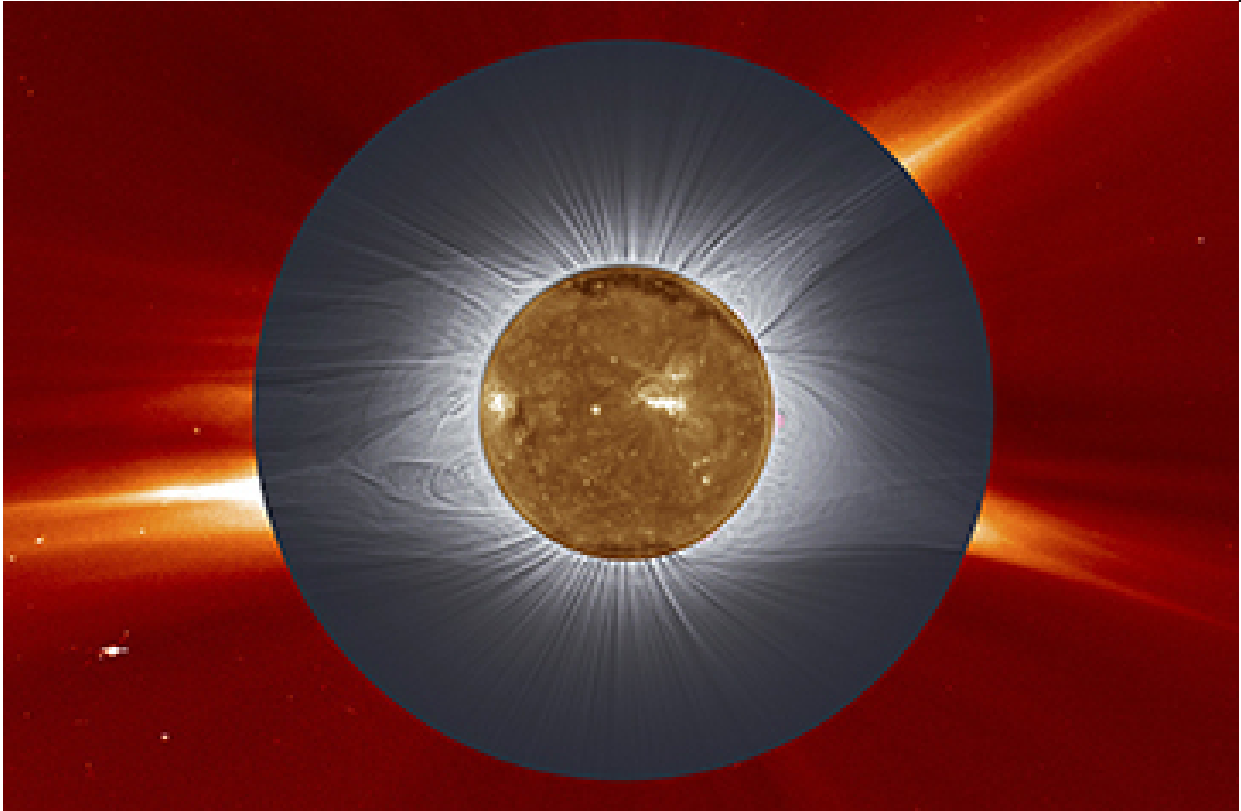


Figure 1.2: A composite image of the Sun from Pasachoff et al. (2018). The inner image is from GOES-16 at 19.5 nm, corresponding to Fe XI/XII emission at about 1.5 MK. The middle-gray and outer-red portions are from the LASCO C2 coronagraph on SOHO, occulting up to 2.5 solar radii.

behaves. The Solar and Heliospheric Observatory (SOHO) was launched in 1995 (Scherrer et al., 1995) and continues to operate today. The Solar Dynamics Observatory (SDO) was launched in 2010 (Scherrer et al., 2012) and continues to collect data at unprecedented temporal and spatial resolutions. Before space-based observatories, photographic plates were used to map the magnetic field, but were produced only occasionally (Howard et al., 1984, 1990). Figure 1.2 shows an image of the Sun that was generated using multiple spacecraft taken during the total solar eclipse in August 2017. The center of the image shows the disk of the Sun with many active regions taken by the Solar Ultraviolet Imager (SUVI, Seaton and Darnel, 2018) on NOAA's Geostationary Operational Environmental Satellite-16 (GOES-16) spacecraft. The middle-gray and outer-red portions of the image are different resolution photos from the Large Angle Spectrometric Coronograph (LASCO, Brueckner et al., 1995) on board SOHO. There is fine-scale structure of the magnetic field as well

as larger scale field.

The Sun exhibits a cycle of activity with maxima every 10-12 years, first noted in 1849 (Schwabe, 1849). The roughly 11 year cycle corresponds to half of a 22 year magnetic cycle where the polarity in each hemisphere reverses each cycle (Hale et al., 1919). The magnetic field is easily observed at the surface, yet the field permeates both the atmosphere above and the interior below. Directly measuring the field in the interior is extremely difficult and there have been considerable efforts made to map the flows and thermal fields surrounding sunspots using helioseismology (Hindman et al., 2009; Borrero and Ichimoto, 2011). The prevailing theory concerning the generation of the solar magnetic field relies heavily on the turbulent fluid motions of the electrically conducting interior (Ossendrijver, 2003; Cameron et al., 2017). As such, great effort has been focused on understanding the flows beneath the solar surface. Perhaps the most intriguing result is that the Sun exhibits a differential rotation profile that is a well-known function of both latitude and radius (Schou et al., 1998). The convective motions in the outer 30% of the Sun are responsible for transporting heat from the core to the surface. The dominant scale of this convection near the surface (granulation) is well understood (Stein and Nordlund, 1989).

Recent observations have revealed that there is a fundamental misunderstanding concerning the deep convective dynamics in the Sun. Surface observations and helioseismic observations of the deeper interior suggest that numerical simulations may be overestimating the amplitude of the solar convection on large spatial scales (Hanasoge et al., 2012; Lord et al., 2014). However, the results of Greer et al. (2015) suggest that helioseismic measurements of the subsurface flows in the near-surface shear layer exhibit good agreement with convection models. The results of Hanasoge et al. (2012) suggest an upper limit of only  $5\text{-}6 \text{ m s}^{-1}$  on spatial scales larger than 70 Mm, whereas theoretical estimates based on gyroscopic pumping suggest convective flows of at least  $30 \text{ m s}^{-1}$  on similar spatial scales Miesch et al. (2012). Weaker flows may not be strong enough to maintain the solar differential rotation. Figure 1.3 shows the horizontal velocity power from each method as a function of spherical harmonic degree. There is a significant discrepancy between the earlier helioseismic results of Hanasoge et al. (2012) and the results of Greer et al. (2015), with the global

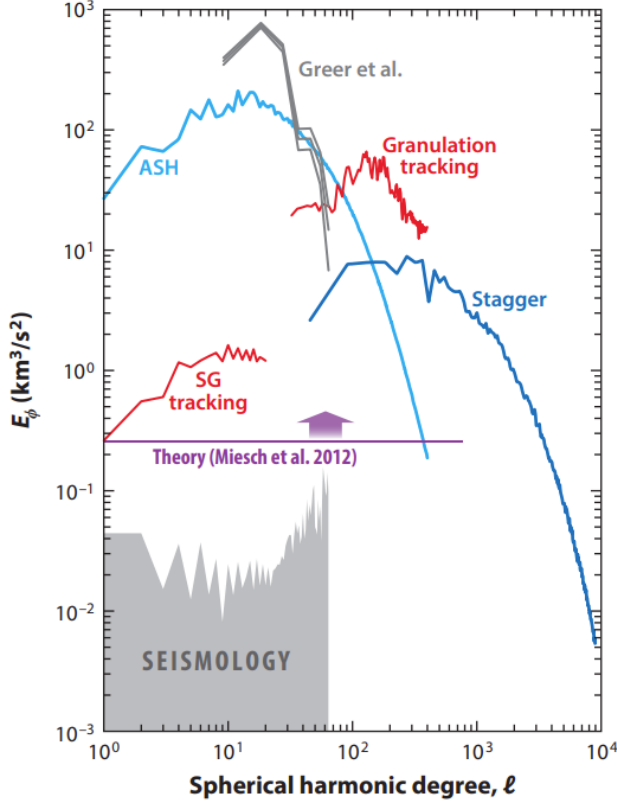


Figure 1.3: Comparison of horizontal velocity power spectra adapted from Hanasoge et al. (2016). The different colors indicate different sources: blue are global simulations, red are surface measurements, and grey are helioseismic measurements. The helioseismic measurements from Greer et al. (2015) are shown in the upper left: these broadly agree with the global simulation results. The upper limits from Hanasoge et al. (2012) are shown in the lower left.

simulation data showing a similar amplitude as the results of Greer et al. (2015). These theoretical and observational disagreements suggest something fundamental, related to the transport of heat and angular momentum by magnetized convection, may be missing in stellar convection models. A resolution to this problem requires a better theoretical understanding of convective dynamics under stellar conditions.

### 1.1.3 The Earth

The magnetic field of the Earth is believed to be at least 3.5 billion years old (Tarduno et al., 2010) with newer estimates extending the age to 4.2 billion years old (Tarduno et al., 2015). The

first observations of the Earth's magnetic field date back to the third century AD, where Chinese geomancers knew a spoon made of magnetic lodestone would spin on a horizontal surface and come to rest pointing in a unique direction (du Trémolet de Lacheisserie et al., 2005). Lodestone was known for its uses in making a magnetic compass. Repeatedly rubbing a piece of iron with the lodestone would magnetize the iron pieces allowing them to be used as the compass needle. This process was first mentioned by Shen Kua in 1088, well before the first European reference by Alexander Neckham of St Albans England in 1190 (Roberts and King, 2013). By the fourteenth century, the magnetic compass was in common use by the British navy. Christopher Columbus carried one on his famous voyage in 1492.

William Gilbert, court physician of Queen Elizabeth 1st of England, is attributed with first suggesting that the magnetic field of the Earth originates from its interior. He constructed a small spherical block of lodestone and placed iron pins on the surface. The pins became oriented at different points on the surface in ways similar to how magnetic compass needles behaved at different points on the Earth's surface. In this way, he mapped the magnetic field lines and named the two antipodal points of convergence the poles (Roberts and King, 2013). Gilbert believed the Earth's magnetic field was static in time, but Henry Gellibrand produced evidence to the contrary in 1635. He measured small deviations between magnetic north and geographic north (this deviation is called declination) that were  $7^\circ$  smaller than similar measurements made by William Borough some 50 years earlier. This was the first indication that the Earth's magnetic field was dynamic and evolved in time. In 1683, Edmund Halley theorized the existence of four magnetic poles, two attached to the crust and two drifting in the core below the crust (Halley, 1683). Halley conducted two voyages to the Atlantic Ocean between 1698 and 1700 where he discovered the westward drift of some geomagnetic features, but his idea of four magnetic poles did not explain the observations.

The next breakthrough did not occur until the early 1800s, when electromagnetic theory started to take shape. In 1800, Allessandro Volta built the first electrical battery that could provide a continuous electric current through a conducting wire (Volta, 1800). This led to Hans Christian Oersted's experiment that showed deflection of a compass needle placed near a wire

carrying electric current (Oersted, 1820). After Oersted’s discovery, research into electromagnetic theory developed rapidly. Within a few months of Oersted’s findings, Jean-Baptise Biot and Félix Savart published their results explaining the magnetic field that is generated by a constant electric current through a conducting wire (Biot and Savart, 1820). Shortly thereafter, André-Marié Ampère performed several fundamental experiments to deduce the force between current-carrying wires (Ampère, 1823). Throughout the early 1830s, Michael Faraday published his experimental results that showed an electrical current could be produced by a magnet in motion (Faraday, 1832). Most of the results to date had been purely observations of experiments, e.g., Faraday did not offer any mathematical formulas to explain his results. The commonly referred to “Maxwell” equations that govern electromagnetic theory did not come along until the 1860s. James Clerk Maxwell compiled all of the previous findings and developed mathematical laws to describe the observations. His work resulted in a daunting system of 20 differential equations (Maxwell, 1861). It would take another 20 years before the original Maxwell equations would be recast into their well-known form. Oliver Heaviside applied elements of vector calculus to reformulate the 20 equations down to only four (Heaviside, 1892). The first relevant equation is commonly called Faraday’s law written as

$$\nabla \times \mathbf{E} = -\frac{\partial \mathbf{B}}{\partial t}, \quad (1.1)$$

where  $\mathbf{B}$  is the magnetic field and  $\mathbf{E}$  is the electric field. For this thesis work, we will only consider the “pre-Maxwell” version of Ampère’s law, written as

$$\nabla \times \mathbf{B} = \mu_0 \mathbf{J}, \quad (1.2)$$

where  $\mathbf{J}$  is the current density, and  $\mu_0$  is a constant of nature called the vacuum permeability. The pre-Maxwell version is only valid for time scales longer than those in which individual electrons and ions might evolve, large spatial scales compared to individual particles, and nonrelativistic speeds. The standard Maxwell equations do allow for these conditions to be violated; Maxwell “fixed” the original equations by including a displacement current that maintained charge conservation (Maxwell, 1865).

With the development of electromagnetic theory, an alternate origin of the Earth's magnetic field begins to emerge: the flow of electric currents inside the Earth. Joseph Larmor is commonly attributed as the first one to postulate that the electric currents of the Earth and Sun are created in much the same way as an electric generator in a power station (Larmor, 1919). Larmor originally developed his ideas to answer questions related to the Sun, but also noted that if his theory were to operate within the Earth, it would require a fluid region in the interior. A more complete discussion of dynamo theory as it relates to this work will be postponed until Section 1.2.

The start of the 20th century brought with it new ideas concerning the interior structure of the Earth, in particular the core. For a more complete history, the reader is directed to Brush (1980). The idea that the Earth's interior was composed of different materials with different densities was used throughout the 1800s. However, one assumption was a continuously varying density. The first mention of a discontinuous interior was made by Emil Wiechert (Wiechert, 1897), while Richard Dixon Oldham is widely credited with the first model (Oldham, 1900). The model assumed a constant density inner core, predominantly made of iron, surrounded by a different constant density rocky shell. Seismic observations later would identify this discontinuity as the boundary between the upper mantle and the outer core, or core-mantle boundary (CMB). The next twenty years would see a great debate as to whether the core was solid or not. At the time, seismologists enjoyed the idea of a fluid interior to help explain volcanoes, but the data did not always support such a hypothesis. In 1926, measurements of the Earth's interior showed that the core was indeed liquid (Jeffreys, 1926). Only ten years later, Inge Lehmann discovered another discontinuity that separated the liquid outer core from a solid iron inner core (Lehmann, 1936). This boundary is often called the inner core boundary (ICB).

As electromagnetic theory was being uncovered, new ways to measure the Earth's magnetic field also were being explored. In the early 1850s, two groups discovered that rocks could become magnetized in the direction of the Earth's magnetic field (Delesse, 1849; Melloni, 1853). Some time later, Folgheraiter (1899) discovered remanent magnetic fields in archaeological sites that could record the history of the geomagnetic field. These results paved the way for paleomagnetism,

whose goal is to study the record of Earth's magnetic field by looking at its effect on rocks, sediment, and archaeological materials. The permanent magnetism of an object such as a rock or a kiln-fired pot is determined by the intrinsic magnetic moments of the component electrons and atoms. If the magnetic moments are aligned in an organized way, the material will exhibit some magnetic properties. If they are randomly aligned, they can become aligned in the presence of an external magnetic field, a process called induced magnetism. The Curie temperature is the critical point at which a material's intrinsic magnetic moments change direction (Griffiths, 1999). As new rocks are formed or pottery is heated in a kiln, they can reach temperatures above their Curie temperature, thus becoming susceptible to external magnetic influences such as the global magnetic field of the Earth. The Earth's magnetic field can align the magnetic moments in the rocks and pots, then as they cool down below their Curie temperatures, the induced magnetism is locked in place storing a record of the direction and magnitude of the geomagnetic field.

The next large discovery occurred as Bernard Brunhes and Pierre David made observations of "natural bricks" that are the result of baking clay-rich soil from an overlying lava flow. Brunhes collected a few samples of the bricks and found that the magnetization was homogeneous, yet different from the present-day field orientation at the site (Brunhes and David, 1901). A few years later, Brunhes and David were studying lavas, as baked clays were rare, when they found a layer of clay sandwiched between two lava flows. The direction of the magnetic field inferred from one flow was different from the clay and flow above. Another key discovery was of a baked clay layer that showed a magnetization that was identical to samples from 100 m away, excluding the possibility that these samples are the result of lightning strikes (Brunhes, 1906). These results indicated that the Earth's magnetic field was periodically reversing directions. Then in the late 1920s into the early 1930s, samples from all over the world showed evidence that the magnetic field not only reversed directions locally, but reversed directions globally (Mercanton, 1926). These were the first results that indicated the Earth's magnetic field underwent polarity reversals. Figure 1.4 shows the history of the Earth's polarity reversals over the past 5 million years. Periods that appear black indicate similar polarity orientation to today's field. There are periods when the field stays in one

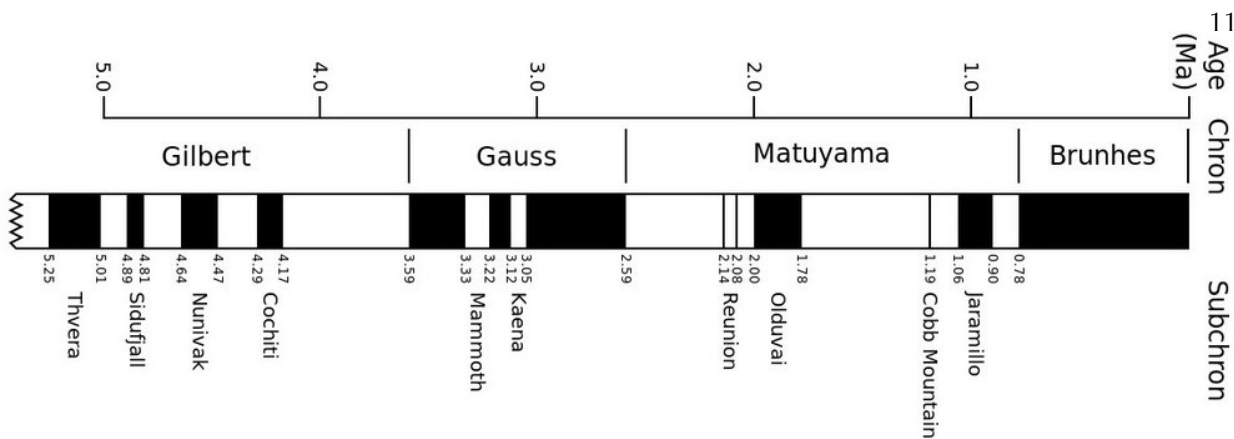


Figure 1.4: Reversal history of the Earth going back 5 million years adapted from Cande and Kent (1995). Periods of black (white) indicate the magnetic field has the same (opposite) polarity as it does today.

configuration for a significant time and other instances where the reversal was short-lived. The length of time the field spends in any given orientation is random.

With the advancement of technology and more sensitive magnetometers, researchers have been able to map the magnetic field on the ocean floor. The observations showed a particular pattern of magnetic stripe “anomalies” where one stripe would be magnetized in a particular direction and the next stripe would be magnetized in the opposite direction. These anomalies tend to appear at a mid-ocean ridge, where new seafloor is being dredged up from the hotter layers just beneath the ocean (Vine and Matthews, 1963; Vine, 1966). As the new seafloor cools down below its Curie temperature, it records the global magnetic field characteristics. Today, the Earth is constantly surrounded by a team of satellites. The first such experiment was Magnetic Field Satellite, MAGSAT, launched in late 1979 (Langel, 1982). It used two magnetometers to measure the surface field to a precision of 20 nT.

In summary, the Earth has undergone polarity reversals throughout its history as shown by paleomagnetic data (Layer et al., 1996; Strik et al., 2003; Pavlov and Gallet, 2010), with the length of time between reversals having varied by nearly three orders of magnitude, from 40 million year long superchrons to short subchrons lasting under 40 thousand years (Cande and Kent, 1995; Merrill et al., 1998). It remains an open question as to what controls these chaotic reversals.

The objects in the solar system possess quite different magnetic fields that are all believed to be generated through the dynamo process. This process must be able to explain the different magnetic field magnitudes among the planets as well as the vastly different magnetic field morphologies. There are many different controlling parameters in these systems, e.g., composition and rotation rate. A key question is what controls the variability of the observed magnetic field systems. To help answer this question, the work in this thesis will systematically vary the controlling parameters to determine the scaling behavior of the resulting magnetic fields.

## 1.2 Dynamo Theory

The Earth's magnetic field has been known for quite some time. In the absence of any generation mechanism, the Earth's field would just diffuse away in a characteristic time estimated as  $\tau = L^2/\eta$ , where  $L$  is some length scale and  $\eta$  is the magnetic diffusivity. An order of magnitude estimate can be made using the thickness of the liquid outer core,  $L \approx 2000$  km, and  $\eta \approx 1 \text{ m}^2 \text{ s}^{-1}$ , that gives a time scale on the order of  $\tau \approx 100,000$  yrs (Davies et al., 2015). The Earth is known to be about 4.2 billion years old (Tarduno et al., 2015), indicating that some mechanism is actively regenerating the geomagnetic field.

The dynamo process, whereby the geomagnetic field is produced by the flow of electric currents in the core, is the only surviving theory that can explain the observations. Rival theories cannot handle the fact that reversed and normal states of the geomagnetic field are largely indistinguishable, apart from the sign difference (Roberts and King, 2013). Theories that hope to explain the magnetic field,  $\mathbf{B}$ , must also be able to explain how  $-\mathbf{B}$  is equally possible.

Larmor's 1919 paper suggested a self-excited dynamo process where internal motions could induce an electric field that would act on the moving matter (Larmor, 1919). This would lead to an electric current, that in turn would increase the inducing magnetic field. After Larmor's insights, there were rapid developments in dynamo theory. Thomas Cowling and Walter Elsasser provided many of the insights throughout the 1930s and 1940s. Cowling showed that the magnetic induction equation does not permit a 2D dynamo solution (Cowling, 1933), i.e., an axisymmetric

magnetic field cannot be maintained through self-sustaining dynamo action by an axisymmetric current. Elsasser later would write a review article detailing the importance of the Coriolis force in inducing correlations between the velocity and the temperature at all turbulent scales in the Earth’s interior, that in turn would drive an electromotive force (emf) (Elsasser, 1939). After his service in the second world war, Elsasser went on to show that purely toroidal flows alone cannot sustain a field; there need to be poloidal flows as well (Elsasser, 1946). That paper marks the first use of the terms “toroidal” and “poloidal”. A collaborative effort between Cowling and Elsasser continued with their work of a more rigorous and general proof that showed axisymmetric flows cannot sustain axisymmetric magnetic fields (Elsasser, 1947).

Most of the work in dynamo theory up to this point had shown how dynamos could not exist invoking various symmetry arguments. In the 1947 article, Elsasser built upon previous ideas and described a process to build mean toroidal magnetic fields using the inductive coupling of bulk fluid motions to the mean poloidal field. The bulk toroidal fluid motions act to stretch the poloidal magnetic field repeatedly over many rotation periods. The now toroidal field begins to accumulate in regions with a gradient in the bulk fluid motions. In the same article, Elsasser also states that a coupling of turbulent convection with rotation can provide a means by which the poloidal field can be regenerated from the mean toroidal field.

The mechanism laid out by Elsasser was confirmed later in the calculations of Bullard and Gellman (1954), where a kinematic dynamo in a 3D sphere was computed on an early supercomputer called ACE at the National Physics Laboratory in the UK. The simulation included 10 radial grid points and four spherical harmonics. Their results indicated that flows aligned along the rotation axis can maintain and build both toroidal and poloidal magnetic fields. Eugene Parker took this work a little further, describing how the poloidal field can be regenerated from a toroidal field in the presence of cyclonic flows (Parker, 1955). The cyclonic flows interact with the toroidal magnetic fields causing small loops of magnetic field. These small loops twist under the Coriolis force generating a contribution in both the poloidal and toroidal directions. With enough small loops, the toroidal contributions largely cancel out, leaving only the poloidal contributions.

Rigorous proofs of self-consistent dynamo solutions remained elusive for the full system of equations; solutions for very idealized systems began to emerge. Backus (1958) showcased a spherical dynamo that explicitly constructed a set of continuously differentiable velocity fields that were able to maintain indefinitely and amplify the dipole component of the magnetic field, even with the inclusion of resistive dissipation. Other authors produced solutions that were built in a similar manner, but were often rather prolonged (e.g., Herzenberg, 1958). Herzenberg described a system including a solid, uniformly conducting medium with two or more conducting rotors that were in electrical contact with the other rotors. Under such a setup, dynamo action could be proven possible when the rotors spin faster than a critical value (Gailitis, 1973; Moffatt, 1978; Brandenburg et al., 1998).

The existence of such provably self-sustaining dynamos was essential to the development of dynamo theory, but a problem of greater interest and active research became how best to model the dynamo processes of the Earth, the Sun, as well as other astrophysical bodies. At this stage it is prudent to introduce the mathematical framework within which the more recent work has been completed.

### 1.2.1 Fluid Equations

Fluid dynamics are described by the fully compressible Navier-Stokes equations,

$$\frac{\partial \rho}{\partial t} + \nabla \cdot (\rho \mathbf{u}) = 0, \quad (1.3)$$

$$\rho \left( \frac{\partial \mathbf{u}}{\partial t} + \mathbf{u} \cdot \nabla \mathbf{u} \right) = -\nabla P + \rho \mathbf{g} + \nabla \cdot \boldsymbol{\Pi} + \mathbf{f}. \quad (1.4)$$

Here  $\mathbf{u}$  is the velocity,  $\rho$  is the density,  $P$  is the nonhydrostatic pressure,  $\mathbf{g}$  is the gravitational acceleration,  $\boldsymbol{\Pi}$  is the viscous stress tensor, and  $\mathbf{f}$  includes any additional forces that could be important for a particular physical system. Other forces could include effects due to rotation or magnetic fields and will be explicitly discussed where appropriate. These equations are solved in a spherical coordinate system using basis vectors  $(\hat{\mathbf{r}}, \hat{\theta}, \hat{\phi})$  and a position vector defined as  $\mathbf{r} \equiv r \hat{\mathbf{r}}$ .

Throughout this work the fluid is assumed to be ideal with an equation of state given by

$$P = \mathcal{R}\rho T, \quad (1.5)$$

where  $T$  is the temperature and  $\mathcal{R}$  is the gas constant. This introduces another unknown quantity and therefore the full system of equations is closed with the inclusion of an evolution equation for the thermal energy. This could be written in terms of the internal energy, the entropy, or the temperature, and the choice will depend on the physical system of interest. The fully compressible equations are used when the velocity is comparable to the sound speed or the effects due to compressibility are important.

### 1.2.1.1 Anelastic Equations

A common approximation to the fully compressible equations is the anelastic approximation. Under this approximation, any density fluctuations about a background state are assumed to be small,

$$\rho' \equiv \rho - \bar{\rho} \ll \bar{\rho}, \quad (1.6)$$

where the background density stratification is given by  $\bar{\rho}$  and the prime indicates the fluctuations. This simplifies the continuity equation to be

$$\nabla \cdot (\bar{\rho} \mathbf{u}) = 0. \quad (1.7)$$

One benefit of this approximation is that it “filters out” acoustic waves from the linear equations. This is particularly useful if the fluid flow is quite slow compared to the sound speed. There are many different formulations of the anelastic equations, here we describe the Lantz-Braginsky-Roberts formulation (Lantz, 1992; Braginsky and Roberts, 1995). This formulation conserves energy (Brown et al., 2012) and can be derived using Lagrangian constraints (Vasil et al., 2013). The equation of state is linearized by assuming that the thermodynamic fluctuations are small compared to the background state and is given by

$$\frac{\rho'}{\bar{\rho}} = \frac{P'}{\bar{P}} - \frac{T'}{\bar{T}} = \frac{P'}{\gamma \bar{P}} - \frac{S}{c_p}, \quad (1.8)$$

where  $S$  is the entropy,  $c_p$  is the specific heat at constant pressure, and  $\gamma = 5/3$  is the adiabatic index. The momentum equation is written in terms of the entropy and is given by

$$\bar{\rho} \left( \frac{\partial \mathbf{u}}{\partial t} + \mathbf{u} \cdot \nabla \mathbf{u} \right) = -\bar{\rho} \nabla \left( \frac{P'}{\bar{\rho}} \right) - \bar{\rho} \frac{S}{c_p} \mathbf{g} + \nabla \cdot \boldsymbol{\Pi} + \mathbf{f}. \quad (1.9)$$

The viscous stress tensor is given by

$$\boldsymbol{\Pi}_{ij} = 2\bar{\rho}\nu \left[ E_{ij} - \frac{1}{3} \delta_{ij} \partial_k u_k \right], \quad (1.10)$$

where  $\nu$  is the kinematic viscosity,  $E_{ij}$  is the strain rate tensor, and  $\delta_{ij}$  is the Kronecker delta.

Lastly, the thermal energy equation is written in terms of the entropy and is given by

$$\bar{\rho} \bar{T} \frac{DS}{Dt} = \nabla \cdot (\bar{\rho} \bar{T} \kappa \nabla S) + 2\bar{\rho}\nu \left[ E_{ij} E_{ij} - \frac{1}{3} (\nabla \cdot \mathbf{u})^2 \right] + \mathcal{Q}. \quad (1.11)$$

Here  $\kappa$  is the thermal diffusivity, and  $\mathcal{Q}$  represents any sources or sinks of energy associated with the other forces  $\mathbf{f}$ , e.g., ohmic dissipation. The first term on the right hand side represents entropy diffusion and the second term is viscous dissipation.

### 1.2.1.2 Boussinesq Equations

The simplest approximation in which buoyancy driven flows are studied is the Boussinesq approximation (Oberbeck, 1879; Boussinesq, 1903). As with the anelastic equations, the Boussinesq approximation applies when the thermodynamic and density fluctuations are small compared to the background state. The Boussinesq approximation assumes further that the length scales in the direction aligned with gravity are significantly smaller than the atmospheric scale height. The fluid is nearly incompressible, but buoyant forces are still important. Under these conditions the continuity equation becomes

$$\nabla \cdot \mathbf{u} = 0. \quad (1.12)$$

The background density,  $\bar{\rho}$ , is assumed to be constant everywhere, except where it enters the gravitational term in the momentum equation. The background state is an ideal gas in hydrostatic equilibrium and the gravitational acceleration is given by

$$\mathbf{g} = -g_o \frac{\mathbf{r}}{r_o}, \quad (1.13)$$

where  $g_o$  is the gravitational acceleration at the outer boundary and  $r_o$  is the radius of the outer boundary. The fluctuations in the density are assumed to be linearly related to the temperature fluctuations as

$$\frac{\rho'}{\bar{\rho}} = -\alpha T', \quad (1.14)$$

where  $\alpha$  is the thermal expansion coefficient, assumed to be constant. The viscosity and thermal diffusivity are assumed to be homogeneous throughout the domain as well. This of course simplifies the equations, but for the interior structure of the Earth, it is a well-founded approximation (e.g., Davies et al., 2015; Dziewonski and Anderson, 1981). The assumption of incompressibility introduces errors on the order of 20%, but these are smaller than other geophysical uncertainties (e.g., Roberts and King, 2013). The momentum equation appears as

$$\frac{\partial \mathbf{u}}{\partial t} + \mathbf{u} \cdot \nabla \mathbf{u} = -\frac{1}{\bar{\rho}} \nabla P - \alpha T' \mathbf{g} + \nu \nabla^2 \mathbf{u} + \mathbf{f}. \quad (1.15)$$

The thermal energy equation is written in terms of the temperature and appears as

$$\frac{\partial T'}{\partial t} + \mathbf{u} \cdot \nabla (\bar{T} + T') = \kappa \nabla^2 T'. \quad (1.16)$$

Only the thermal diffusion term remains, all other heating sources and sinks are significantly smaller and therefore neglected.

### 1.2.1.3 Adding Rotation and Magnetic Fields

Adding effects due to rotation only affects the momentum equation and is achieved by considering a rotating frame of reference. Newton's second law (i.e., the momentum equation) is only valid for inertial frames of reference. In order to use the momentum equation, the velocities and accelerations in the rotating frame must be related to the inertial frame. The velocity in the inertial frame can be written as

$$\mathbf{u}_i = \mathbf{u} + \boldsymbol{\Omega} \times \mathbf{r} \quad (1.17)$$

where  $\boldsymbol{\Omega}$  is the rotation rate of the reference frame and the subscript indicates it refers to the inertial frame, no subscript refers to the rotating frame. The acceleration has a few more terms,

$$\mathbf{a}_i = \mathbf{a} + 2\boldsymbol{\Omega} \times \mathbf{u} + \boldsymbol{\Omega} \times (\boldsymbol{\Omega} \times \mathbf{r}) + \frac{d\boldsymbol{\Omega}}{dt} \times \mathbf{r}. \quad (1.18)$$

The terms on the right hand side correspond to 1) the acceleration in the rotating frame, 2) the Coriolis effect, 3) the centrifugal effect, and 4) the Euler acceleration due to changes in the rotation rate. If the inertial acceleration that appears in the momentum equation is rewritten using the above frame transformation, then the momentum equation can be used without further modification. The three new “forces” (Coriolis, centrifugal, and Euler) are just an artifact of the frame transformation, but do cause a real observable effect from within the rotating reference frame.

If the rotation rate is constant in time, then the Euler term can be neglected. The centrifugal term acts always perpendicular to the rotation axis and can therefore be written in terms of a potential and treated as a perturbation to the gravitational potential. This term can be neglected if the perturbation to the gravitational potential is considered small. For astrophysical systems, this means the object must be rotating well-below the breakup rotation rate in order to neglect the centrifugal effects.

Throughout this thesis work, only constant rotation rates that would be considered small perturbations to the gravitational potential are considered. This means the only difference to the momentum equation would be the addition of the Coriolis force. The Boussinesq momentum equation in the rotating frame would appear as

$$\frac{\partial \mathbf{u}}{\partial t} + \mathbf{u} \cdot \nabla \mathbf{u} = -\frac{1}{\rho} \nabla P - \alpha T' \mathbf{g} + \nu \nabla^2 \mathbf{u} + 2\mathbf{u} \times \boldsymbol{\Omega} \hat{\mathbf{z}}, \quad (1.19)$$

where the rotation vector is assumed to be aligned along the z-axis,  $\boldsymbol{\Omega} = \Omega \hat{\mathbf{z}}$ .

To include the effects due to magnetic fields, the pre-Maxwell equations that govern electricity and magnetism must be used. They appear as

$$\nabla \times \mathbf{E} = -\frac{\partial \mathbf{B}}{\partial t}, \quad (1.20)$$

$$\nabla \times \mathbf{B} = \mu_0 \mathbf{J}, \quad (1.21)$$

$$\nabla \cdot \mathbf{E} = \frac{\rho_c}{\epsilon_0}, \quad (1.22)$$

$$\nabla \cdot \mathbf{B} = 0, \quad (1.23)$$

where  $\mathbf{E}$  is the electric field,  $\mathbf{B}$  is the magnetic field,  $\mathbf{J}$  is the current density,  $\mu_0$  is the vacuum permeability,  $\epsilon_0$  is the vacuum permittivity, and  $\rho_c$  is the charge density which is assumed to be approximately zero. These equations are only valid for time scales longer than those on which the individual electrons and ions might evolve, large spatial scales compared to individual particles, and nonrelativistic speeds. The electric field and the current are also related through Ohm's law. In a conducting fluid that moves with velocity  $\mathbf{u}$ , Ohm's law reads

$$\mathbf{J} = \sigma (\mathbf{E} + \mathbf{u} \times \mathbf{B}), \quad (1.24)$$

where  $\sigma$  is the conductivity of the fluid. There are other terms that enter into the generalized Ohm's law, but they typically become important on very small length scales. The work in this thesis is focused on larger scales such that the other terms can be neglected. To add magnetic effects into the fluid equations, the Lorentz force must be added to the momentum equation. The Lorentz force describes how charged particles move in the presence of a magnetic field and is given by

$$\mathbf{f}_{\text{Lor}} = \mathbf{J} \times \mathbf{B} = \frac{1}{\mu_0} (\nabla \times \mathbf{B}) \times \mathbf{B}. \quad (1.25)$$

The Boussinesq momentum equation for a rotating fluid that includes effects due to magnetism would appear as

$$\frac{\partial \mathbf{u}}{\partial t} + \mathbf{u} \cdot \nabla \mathbf{u} = -\frac{1}{\rho} \nabla P - \alpha T' \mathbf{g} + \nu \nabla^2 \mathbf{u} + 2\mathbf{u} \times \Omega \hat{\mathbf{z}} + \frac{1}{\rho} \mathbf{J} \times \mathbf{B}. \quad (1.26)$$

This introduces another unknown quantity into the fluid equations. As a result, another equation must be added that describes the evolution of the magnetic field. Faraday's law already includes

the time derivative of the magnetic field. Ohm's law can be combined with Faraday's law to completely remove the need for the electric field. This leads to the induction equation that governs the evolution of the magnetic field and appears as

$$\frac{\partial \mathbf{B}}{\partial t} = \nabla \times (\mathbf{u} \times \mathbf{B}) - \nabla \times (\eta \nabla \times \mathbf{B}), \quad (1.27)$$

where  $\eta$  is the magnetic diffusivity. The magnetic field has a further constraint that it is solenoidal,

$$\nabla \cdot \mathbf{B} = 0. \quad (1.28)$$

To fully include the magnetic effects into the fluid equations, the Lorentz force must be added to the momentum equation and two more equations for the magnetic field must be included in the system: the solenoidal constraint and the induction equation.

When including the effects due to magnetic fields, it is useful to decompose the dependent variables (velocity, magnetic field, etc.) into mean and fluctuating components, as typically is used in mean field electrodynamics (e.g., Steenbeck et al., 1966). In particular, the magnetic field is written as

$$\mathbf{B} = \bar{\mathbf{B}} + \mathbf{B}', \quad (1.29)$$

where the mean operation is an azimuthal average, i.e.,

$$\bar{\mathbf{B}} = \frac{1}{2\pi} \int_0^{2\pi} \mathbf{B} \, d\phi, \quad (1.30)$$

and the fluctuating contribution is defined as

$$\mathbf{B}' \equiv \mathbf{B} - \bar{\mathbf{B}}, \quad (1.31)$$

which implies

$$\bar{\mathbf{B}'} = 0. \quad (1.32)$$

Applying the mean operation to the induction equation leads to an evolution equation for the mean magnetic field, given by

$$\frac{\partial \bar{\mathbf{B}}}{\partial t} = \nabla \times (\bar{\mathbf{u}} \times \bar{\mathbf{B}}) + \nabla \times \bar{\mathcal{E}} - \nabla \times (\eta \nabla \times \bar{\mathbf{B}}), \quad (1.33)$$

where the electromotive force (emf) is defined as

$$\bar{\mathcal{E}} \equiv \overline{\mathbf{u}' \times \mathbf{B}'}. \quad (1.34)$$

Solving these equations is a difficult prospect, but with the continuous advancements in computing power, numerical solutions are becoming progressively easier. Early global-scale simulations began in the mid 1970s with the work of Gilman (1975, 1977), but were focused more toward solar and stellar convection zones. The first simulations tailored to the Earth began in the mid 1990s with the work of Glatzmaier and Roberts (1995a); Kageyama et al. (1995). The results of Glatzmaier and Roberts (1995b) even show a solution with spontaneous reversals of polarity.

### 1.3 Numerical Methods

#### 1.3.1 Spectral Decomposition

The model equations are evolved using the pseudospectral code Rayleigh (Featherstone and Hindman, 2016a; Matsui et al., 2016). The solenoidal constraints on the mass flux and the magnetic field are incorporated by performing a toroidal-poloidal decomposition and rewriting the velocity and magnetic field as

$$\bar{\rho}\mathbf{u} \equiv \nabla \times (Z\hat{\mathbf{r}}) + \nabla \times [\nabla \times (W\hat{\mathbf{r}})] \quad (1.35)$$

$$\mathbf{B} \equiv \nabla \times (A\hat{\mathbf{r}}) + \nabla \times [\nabla \times (C\hat{\mathbf{r}})], \quad (1.36)$$

where  $Z$  and  $A$  are the toroidal streamfunctions and  $W$  and  $C$  represent the poloidal streamfunctions. The evolution variables used in Rayleigh are the mass flux streamfunctions  $W$  and  $Z$ , the buoyancy variable, the pressure  $P$ , and the magnetic streamfunctions  $A$  and  $C$ . The buoyancy variable will be either the specific entropy if the anelastic approximation is used or it will be the temperature under the Boussinesq approximation. The resulting equation for  $P$  is not an evolution equation, but is elliptic and must be satisfied at each instant over the entire domain. Physically, this indicates that information about pressure perturbations is propagated instantly everywhere.

**Rayleigh** uses spherical harmonic transforms to compute derivatives in the latitudinal and longitudinal directions. Formally, spherical harmonics are solutions to the Laplace equation on the surface of a sphere, and as a result form a natural set of basis functions when working in spherical coordinates. Spherical harmonics can be written in terms of Fourier modes and associated Legendre functions as

$$Y_\ell^m(\theta, \phi) = (-1)^m \sqrt{\frac{2\ell+1}{4\pi} \frac{(\ell-m)!}{(\ell+m)!}} P_\ell^m(\cos \theta) e^{im\phi}, \quad (1.37)$$

where  $\ell$  is the spherical harmonic degree,  $m$  is the azimuthal wavenumber, and the  $P_\ell^m$  are the associated Legendre functions without the Condon-Shortley phase. Each variable is then expanded as a finite sum of spherical harmonics, e.g., the generic variable  $Q$  is expanded as

$$Q(r, \theta, \phi, t) = \sum_{\ell=0}^{\ell_{\max}} \sum_{m=-\ell}^{\ell} Q_\ell^m(r, t) Y_\ell^m(\theta, \phi), \quad (1.38)$$

where  $\ell_{\max}$  is the largest spherical harmonic kept in the truncation. The spherical harmonic transforms are computed with a combination of a Fast Fourier Transform (FFT) and a Legendre transform. There does not yet exist a robust fast Legendre transform, so **Rayleigh** uses a matrix transform that scales as  $\ell_{\max}^2$ , whereas the FFT scales as  $\ell_{\max} \log(\ell_{\max})$ . Using spherical harmonics provides uniform resolution over the surface of the sphere, spectral convergence when computing derivatives, and the coordinate singularities at the poles are removed.

The radial direction makes use of a Chebyshev collocation method where all variables are expanded as a finite sum of Chebyshev polynomials, e.g.,

$$Q_\ell^m(r, t) = \sum_{n=0}^{N_r} \tilde{Q}_{\ell,n}^m(t) T_n(r), \quad (1.39)$$

where  $T_n$  is the Chebyshev polynomial of degree  $n$  and  $N_r$  is the maximum degree included in the truncation. Chebyshev polynomials have a nonuniform distribution of grid points that cluster near the boundaries, which can help resolve boundary layers. Derivatives can be computed with spectral accuracy and the Chebyshev transform can be reduced to a discrete cosine transform (DCT). The DCT is related closely to the FFT and scales as  $N_r \log(N_r)$ .

### 1.3.2 Boundary Conditions

Mechanical boundary conditions can play an important role in the dynamo mechanism. Simulations of planetary dynamos aimed at understanding rocky planets usually employ no-slip boundary conditions to model the surrounding rigid mantle (e.g., Kageyama et al., 1995; Glatzmaier and Roberts, 1995a,b; Soderlund et al., 2012; Wicht and Meduri, 2016; Schaeffer et al., 2017). For simulations that attempt to model gas-giant planets or stellar convection zones, stress-free boundaries typically are used to approximate the free-surface boundaries. It has been argued that a stress-free boundary may be a better choice than no-slip, because the Ekman layers in the no-slip models are much thicker than the extremely thin layers in the Earth's core (Kuang and Bloxham, 1997, 1999). Although this reduces the effect of the Ekman layer, it will not remove it entirely. However, laboratory experiments, direct numerical simulations, and theory indicate that Ekman pumping remains important even in the asymptotic limit of small Ekman number (Stellmach et al., 2014; Cheng et al., 2015; Julien et al., 2016; Plumley et al., 2016).

Rayleigh employs impenetrable boundary conditions for both the inner and outer boundary such that the radial velocity vanishes

$$u_r = 0. \quad (1.40)$$

The transverse velocity components can be either no-slip or stress-free. Under the no-slip condition, all velocity components must vanish, giving

$$u_\theta = u_\phi = 0. \quad (1.41)$$

Using the stress-free condition, the boundary conditions may be written as

$$\frac{\partial}{\partial r} \left( \frac{u_\theta}{r} \right) = \frac{\partial}{\partial r} \left( \frac{u_\phi}{r} \right) = 0. \quad (1.42)$$

The magnetic boundary conditions are assumed to be perfectly insulating at both boundaries. This means that the magnetic field must match onto an external potential field at the boundaries as

$$\mathbf{B} = -\nabla\Phi \quad \text{and} \quad \nabla^2\Phi = 0 \quad (1.43)$$

for both the inner and outer boundaries. This condition has the benefit of being quite straightforward to implement in spectral space. A potential field boundary condition is most appropriate when the region outside the boundary is a vacuum or some other extremely good insulator. For the Earth, the mantle has an exceptionally low conductivity compared to the fluid outer core (Pozzo et al., 2012; Civet et al., 2015; Jault, 2015) so a potential field boundary condition would be perfectly adequate. On the other hand, the inner core of the Earth is mostly solid iron and nickel with a very large conductivity (Davies et al., 2015). However, Wicht (2002) did a direct comparison of a conducting inner core to an insulating inner core; they did not find a significant difference in the two resulting dynamos. The “correct” boundary condition might be perfectly conducting, but it would require the added complexity of adding a few more nonlinear equations to the system, and would negatively influence the performance of the code. As a result, we decided to take advantage of the simplifications and numerical savings associated with an insulating inner core.

Once the various source terms, derivatives, and nonlinearities have been calculated and the boundary conditions have been applied, the system is ready to be advanced forward in time. An implicit-explicit, 2nd order accurate time-stepping algorithm is used, with a Crank-Nicolson scheme applied to the linear terms, and an Adams-Bashforth scheme applied to the nonlinear terms.

#### 1.4 Nondimensional Control Parameters

Exploring convection-driven dynamos under planetary core conditions remains challenging since it occurs in parameter regimes that are considered to be extreme by modern computational and laboratory standards. These regimes can be characterized by several nondimensional parameters. In particular, the Rayleigh number expresses the relative strength of buoyancy driving and diffusive effects, defined as

$$\text{Ra} = \frac{\alpha g_o \Delta \tilde{T} D^3}{\nu \kappa}, \quad (1.44)$$

where  $\Delta \tilde{T}$  is the dimensional temperature contrast between the inner and outer radii,  $\Delta \tilde{T} = \tilde{T}(r_i) - \tilde{T}(r_o)$ . The shell depth is given by  $D = r_o - r_i$ . The Ekman number measures the relative

Table 1.1: Nondimensional control parameters for the Earth (King et al., 2010), the Sun (Ossendrijver, 2003), and what is attainable in current numerical simulations at moderate computational expense. The Earth and Sun are rapidly rotating and highly turbulent. <sup>†</sup>The most demanding calculations have reached  $\text{Ek} = 10^{-8}$  and  $\text{Ra} = 10^{11}$ , such extreme simulations require substantially more computational resources (see e.g., Aubert et al., 2017; Schaeffer et al., 2017; Guervilly et al., 2019).

Parameter	Symbol	Sun	Earth	Simulations
Ekman	$\text{Ek}$	$10^{-15}$	$10^{-15}$	$10^{-3} - 10^{-6}$ <sup>†</sup>
Rayleigh	$\text{Ra}$	$10^{20}$	$10^{24}$	$10^6 - 10^9$ <sup>†</sup>
Thermal Prandtl	$\text{Pr}$	$10^{-7}$	$10^{-1}$	0.1-10
Magnetic Prandtl	$\text{Pm}$	$10^{-3}$	$10^{-6}$	0.1-10

importance of viscous forces to the Coriolis force and is expressed as

$$\text{Ek} = \frac{\nu}{\Omega D^2}. \quad (1.45)$$

The thermal Prandtl number specifies the relative importance of viscosity to thermal diffusion, and the magnetic Prandtl number gives the relative strength of viscosity to magnetic diffusion. The thermal Prandtl number ( $\text{Pr}$ ) and the magnetic Prandtl number ( $\text{Pm}$ ) are defined as

$$\text{Pr} = \frac{\nu}{\kappa}, \quad \text{and} \quad \text{Pm} = \frac{\nu}{\eta}, \quad (1.46)$$

respectively. The background state of the simulation can be described in part by these parameters. Therefore, the above parameters can be described as input parameters to the simulation. Table 1.1 provides some estimates for these values in the Earth and the Sun. The extreme parameters indicate that these systems are rapidly rotating and highly turbulent.

The most important implication from Table 1.1 is that current direct numerical simulations (DNS) cannot reach realistic values of the Ekman number and the Rayleigh number for systems like the Earth and Sun. Since DNS cannot reach small Ekman and large Rayleigh number regimes, we are interested in the scaling behavior of the simulations as these parameters are varied. Understanding the asymptotic scaling behavior and the achieved force balances is crucial for developing better models of spherical convection and spherical dynamos.

There are several nondimensional parameters that can be used to characterize the results of a simulation and are described as output quantities. The first is the Reynolds number which measures the relative importance of inertial effects to viscous effects and is defined as

$$\text{Re} = \frac{\mathcal{U}D}{\nu}, \quad (1.47)$$

where  $\mathcal{U}$  is a characteristic velocity of the system. The characteristic velocity is computed as

$$\mathcal{U} = \sqrt{\langle |\mathbf{u}|^2 \rangle}, \quad (1.48)$$

where the angled brackets indicate a volume average over the entire computational domain. A closely related nondimensional parameter is the magnetic Reynolds number given by

$$\text{Rm} = \text{RePm}, \quad (1.49)$$

representing the relative importance of magnetic induction compared to magnetic diffusion. The last output parameter is the Rossby number which provides the ratio of inertial forces to the Coriolis force and is defined as

$$\text{Ro} = \frac{\mathcal{U}}{\Omega D} = \text{ReEk}. \quad (1.50)$$

Figure 1.5 shows the Reynolds number as a function of the Ekman number for what is achievable using current laboratory experiments and simulations. The colored regions in the bottom right of the figure indicate what values of Re and Ek are obtainable. The Earth is in the upper left several orders of magnitude removed from the shaded regions. The simulations in this work are firmly in the middle of the shaded regions far removed from the parameters that characterize the systems of interest. The projects in this thesis use parameter sweeps: run many simulations that systematically vary the input parameters. The purpose of a parameter sweep is to identify scaling relationships that describe how a particular quantity of interest behaves as the input parameters are varied. Once a scaling relation has been obtained, it can be applied to more extreme parameter regimes that did not fall within the original parameter sweep. If the simulations are dynamically similar (in a qualitative sense) to the system of interest, then extrapolating the scaling relations to further extremes can be carried out with more confidence in the final result.

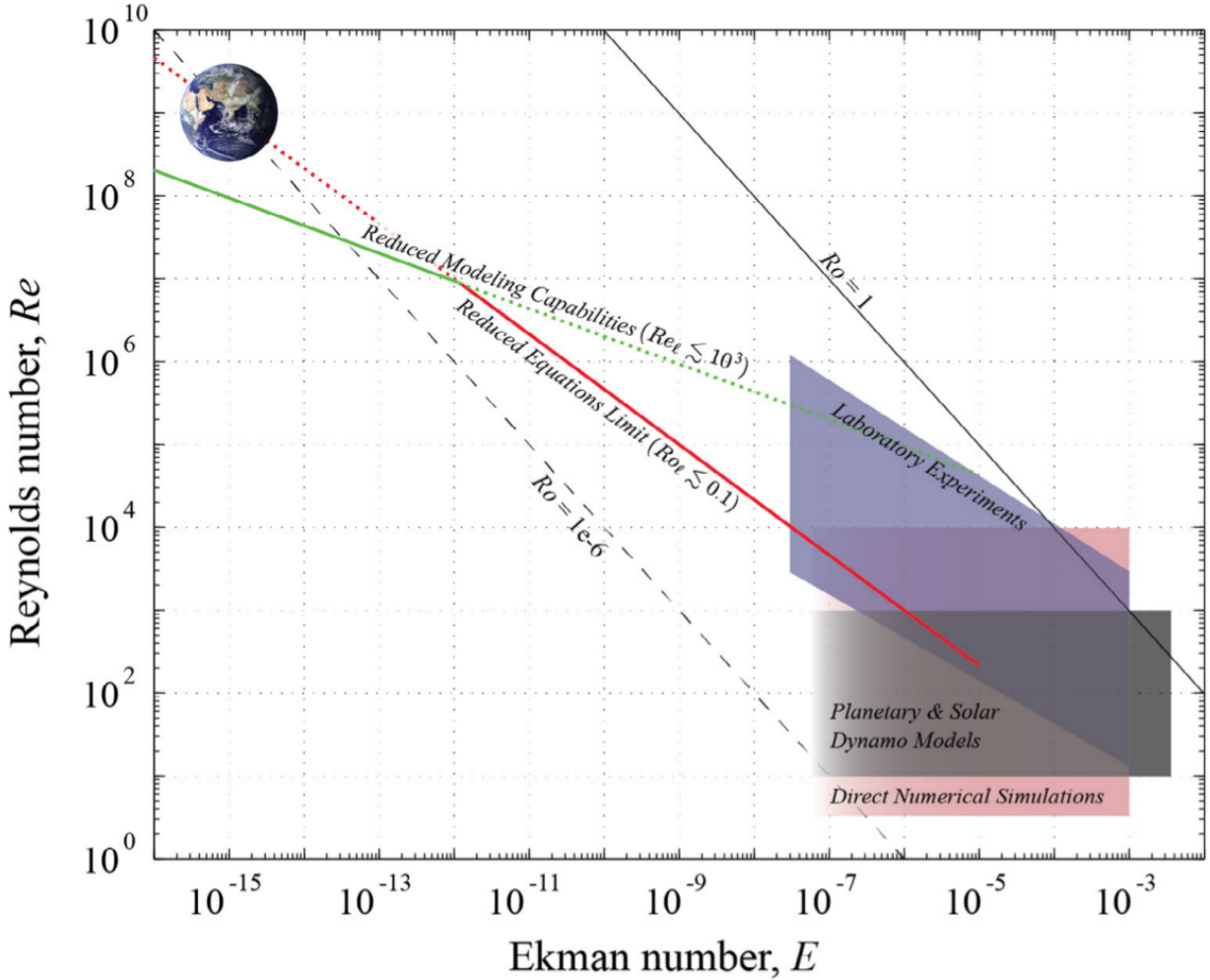


Figure 1.5: Schematic of what parameter regimes can currently be achieved in simulations and laboratory experiments adapted from Aurnou et al. (2015). The Earth is several orders of magnitude removed from what is currently achievable.

Scaling laws are an essential part of a comprehensive dynamo theory. Such relations also provide predictions for the magnetic field of an object at times when the control parameters were different from their current values. This could be applied to now extinct dynamos, such as Mars. Most scaling laws make an assumption that a particular force balance is present, usually between the Coriolis and Lorentz forces. The main differences are the assumptions on the characteristic velocity and length scales. Christensen (2010) provides a nice review of the various scaling laws. Numerical simulations allow a large suite of models to be computed in order to obtain the necessary scaling relations.

## 1.5 Force Balances in Rapidly Rotating Systems

Rotation is known to play a fundamental role in the generation of large-scale magnetic fields, and so the Coriolis force is thought to be one of the most important forces in natural dynamos (Elsasser, 1939). Determining which forces balance the Coriolis force and which forces perturb such a balance is important for constraining the resulting dynamics. Two balances have been discussed before, geostrophic and magnetostrophic. Geostrophic refers to an approximate balance between Coriolis and pressure gradient forces; other forces, such as the Lorentz force, enter in as secondary balances with magnitudes much smaller than the Coriolis force. Quasi-geostrophic dynamics are characterized by a dominant geostrophic balance, but other forces still can play important roles. The magnetostrophic balance involves a four way balance including the Coriolis, pressure gradient, buoyancy, and Lorentz forces. Another related balance is called thermal wind and involves a three way balance between the Coriolis, pressure gradient, and buoyancy force.

No direct observations of the Earth's core currently are possible. Instead, insight into core dynamics is obtained from temporal variations of the geomagnetic field. These observations can be used to provide estimates of a typical flow speed that are of order  $\mathcal{U} \sim 10^{-4}$  m s<sup>-1</sup> (Roberts and King, 2013). Coupled with physical properties of the core obtained from laboratory experiments and simulations (Roberts and King, 2013), this value provides vital clues to the inner workings of the core by enabling estimates of important nondimensional parameters describing the dynamics of the core. However, the sizes of the individual forces are debated still (e.g., Aurnou et al., 2015). The particular forces that develop have a direct impact on the observed dynamics, therefore characterizing the force balances can provide useful insight into understanding the observed properties of the magnetic field.

The rapid rotation that leads to geostrophic balances also leads to anisotropic flow structures. These structures can have small scales perpendicular to the rotation axis and long scales aligned along the rotation axis. This can be seen immediately from the Taylor-Proudman theorem. For an

incompressible fluid in geostrophic balance, the momentum equation can be written as

$$0 = 2\mathbf{u} \times \Omega \hat{\mathbf{z}} - \frac{1}{\rho} \nabla P. \quad (1.51)$$

After applying the curl to this equation and using a vector identity to expand  $\nabla \times (\mathbf{u} \times \hat{\mathbf{z}})$ , the momentum equation becomes

$$\hat{\mathbf{z}} \cdot \nabla \mathbf{u} = 0. \quad (1.52)$$

This means the flow is approximately invariant along lines parallel to the rotation axis, indicating a vastly different length scale compared to directions perpendicular to the rotation axis. This result was derived first in 1897, then Proudman published another derivation in 1916, followed by Taylor in 1917 (Hough and Darwin, 1897; Proudman and Lamb, 1916; Taylor and Lamb, 1917). Then Taylor demonstrated the effect experimentally in 1923 (Taylor, 1923).

Spatial scale separation is an intrinsic property of rapidly rotating flows. Rotating convection is characterized by at least two disparate length scales: the small-scale  $L$  measured in one or more directions perpendicular to the rotation axis, and the large-scale  $D$  characterizing motions on the extent of the domain. In rotating spherical geometries,  $L$  can be distinct in both the radial and azimuthal directions (Soward, 1977). Multiscale asymptotics can exploit this scale separation in order to understand convection and convection-driven dynamos in both planar and spherical geometries. The planar asymptotic model developed by Julien et al. (1998) was shown to match results from simulations (Stellmach et al., 2014; Plumley et al., 2016), provided the flow remained geostrophically balanced. Only linear asymptotic models have been developed for spherical geometries (Roberts, 1968; Busse, 1970; Jones et al., 2000; Dormy et al., 2004). The primary difficulty in extending nonlinear models to spherical geometries is the presence of multiple radial length scales and three dimensional anisotropy in the flows. The main length scales that appear in the linear spherical models scale with the Ekman number in different ways and are the system scale  $D$ , the convective onset scale  $L/D \sim \text{Ek}^{1/3}$ , a radial convective envelope scale  $L/D \sim \text{Ek}^{1/6}$ , and a length scale that relates to radial waves  $L/D \sim \text{Ek}^{2/9}$ . Childress and Soward (1972) developed and later studied (Soward, 1974) a weakly nonlinear asymptotic model for convection-

driven dynamos in the planar geometry that later was extended to the fully nonlinear regime by Calkins et al. (2015).

Consequences of magnetostrophic balances were explored first by Taylor (1963). Under the assumption of a magnetostrophic force balance, Taylor showed that the component of the Lorentz torque pointing in the direction of the rotation axis must vanish. This condition is now referred to as ‘Taylor’s constraint’. Implicit in Taylor’s original analysis is that the magnetostrophic balance occurs on the large, longitudinally-averaged scale.

Several authors directly quantify the force balance in their simulations (Wicht and Christensen, 2010; Soderlund et al., 2015; Dormy, 2016; Yadav et al., 2016; Aubert et al., 2017; Schaeffer et al., 2017; Dormy et al., 2018) by computing the vorticity equation (curl of the momentum equation). This procedure will remove the pressure gradient, but also removes all the conservative contributions from the Coriolis and Lorentz forces. This could emphasize the small-scale contributions and thus completely miss the large-scale balances (Yadav et al., 2016). From all of these studies, there is consensus that the small-scale force balance is characterized as a leading order geostrophic balance, and a secondary magnetostrophic balance. In contrast, Aubert (2005) found a thermal wind balance on the large scale dynamics in the meridional plane, whereas the azimuthal balance was between the Coriolis and Lorentz forces.

## Chapter 2

### Prandtl-number Effects in High-Rayleigh-number Spherical Convection

#### 2.1 Preamble

The work described in this chapter was published in the *Astrophysical Journal* (Orvedahl et al., 2018). The text from Section 2.2 is the text of the paper as it was accepted for publication ©AAS, reproduced with permission.

This project was motivated by the results of Featherstone and Hindman (2016a). The fluid motions in the Sun’s convective region are believed to be important in the generation of its global magnetic field. Despite the relative ease in observing the Sun due to its proximity, helioseismic measurements of the underlying flows do not agree with one another. Such a disagreement suggests that something fundamental may be missing in stellar convection models. Featherstone and Hindman (2016a) started with a simplified model of the Sun that did not include rotation or magnetism. They proceeded with a parameter sweep over different values of the thermal diffusivity (the Prandtl number was assumed to be unity) as well as different values of the stratification. One of the main results from their study was that models could capture correctly the integrated kinetic energy, but naturally may overestimate the low-wavenumber power because the Rayleigh number is still far too small compared to the actual star.

As an extension, this work investigated the influence of different values of the viscosity and performed a parameter sweep over different Prandtl numbers. An important result of this study involved the boundary-layer thickness scaling. Achieving the correct driving scale, where the boundary layer has a physically realistic thickness, may be possible with a modest Rayleigh number and

a Prandtl number of unity. The scaling also suggests that in order to maintain a boundary layer whose physical extent is confined to a small region of the convective domain in a global simulation without radiation transfer, the Prandtl number should be decreased as the Rayleigh number is increased.

## 2.2 Published Work

### 2.2.1 Introduction

Convective motions within the outer one third of the Sun transport energy from the radiative interior to the photosphere. In the process, these overturning motions that are thought to drive the solar differential rotation play a pivotal role in generating solar magnetic field. Any model of the solar dynamo necessarily requires a description of the Sun's underlying convective motions, and yet those motions remain poorly characterized in spite of the observational coverage enabled by the Sun's proximity to Earth.

On the largest spatial scales, photospheric convection manifests in cellular patterns known as supergranules that were first noted by Hart (1954) and better characterized by Leighton et al. (1962). The horizontal extent of these cells is approximately 35 Mm, and they possess a spectral peak in photospheric Dopplergram power around spherical harmonic degree  $\ell \approx 120$  (e.g., Hathaway et al., 2000, 2015). In addition, smaller-scale motions known as granulation are clearly visible in the photosphere, possessing a characteristic size of about 1 Mm and a clear peak in photospheric Dopplergram power around  $\ell \approx 10^3$  (Bray et al., 1984).

Presently, only the granular component of photospheric convection is reliably captured in direct numerical simulations. Radiative hydrodynamic simulations of solar surface convection that can simulate granulation fail to yield clear evidence for supergranulation (e.g., Stein et al., 2009; Ustyugov, 2010). Inconsistencies between numerical models and the Sun also have been observed in the velocity power distribution associated with larger scales of convection (e.g., Miesch et al., 2008). Measurements of deep convective flow speeds, made using time-distance helioseismology,

suggest that convection models may overestimate the amplitude of the convection on spatial scales larger than 30 Mm (Hanasoge et al., 2012). The results of Hanasoge et al. (2012) estimate that the convective velocities on spatial scales larger than 70 Mm are at most  $5\text{-}6 \text{ m s}^{-1}$ , about an order of magnitude weaker than that expected from simulations or theoretical arguments (e.g., Miesch et al., 2012). Ring-analysis measurements of the subsurface flows in the near-surface shear layer, however, exhibit good agreement with models and theory (Greer et al., 2015).

Resolving these discrepancies requires careful comparison of these two different helioseismic techniques, and perhaps improvements to both. A resolution to this problem also requires a better theoretical understanding of convective dynamics under stellar conditions. Exploring stellar convection numerically remains challenging owing to the fact that it occurs within parameter regimes that are considered extreme by modern computational and laboratory standards alike. These regimes can be characterized by several nondimensional parameters. In particular, the Reynolds number measures the relative importance of inertial forces to viscous forces, the Rayleigh number expresses the relative strength of buoyancy driving and diffusive effects, and the Prandtl number specifies the relative importance of viscosity to thermal diffusion. Estimates for the Sun lead to values of the Reynolds, Rayleigh, and Prandtl numbers on the order of  $10^{13}$ ,  $10^{20}$ , and  $10^{-7}$ , respectively, indicating the solar convection zone is highly turbulent (e.g., Ossendrijver, 2003).

Such extreme values of nondimensional parameters are largely an expression of the fact that while diffusion in stellar interiors may be active on very small scales, it tends to be negligible at the system scale. Achieving such a situation, wherein diffusion plays no appreciable role in the leading-order force balance, is possible in those parameter regimes already accessible through computational models. Featherstone and Hindman (2016a,b) identified two such regimes by exploring the response of convection to changes in Rayleigh number and Ekman number (expresses the relative importance of the Coriolis force and viscous diffusion), while using a fixed Prandtl number of unity. In so doing, they identified asymptotic scaling laws for spectral properties of the convection that could in principle be extrapolated to the stellar parameter regime. The purpose of this paper is to extend those studies by exploring the response of the convective spectrum to changes in the Prandtl

number.

This paper is organized as follows. In Section 2.2.1.1, we summarize earlier investigations into the role of the Prandtl number. In Sections 2.2.2 and 2.2.3, we discuss our numerical model and the parameter space that was explored. Results are discussed in Section 2.2.4, followed by a discussion of their implications in Section 2.2.5.

### 2.2.1.1 Prandtl Number in Convection

The Prandtl number  $\text{Pr} = \nu/\kappa$ , where  $\nu$  is the kinematic viscosity and  $\kappa$  is the thermal diffusivity, is known to be small in the dynamo regions of planets and stars (Ossendrijver, 2003; Roberts, 2007). It is well known from linear theory that the value of the Prandtl number both influences the structure and amplitude of convective motions and controls the critical Rayleigh number required for the onset of rotating convection (e.g., Chandrasekhar, 1961). Asymptotic approximations to the governing fluid equations can be carried out based on the size of the Prandtl number. Such approximations yield some insight into the convective dynamics arising under different Prandtl number regimes. In the large Prandtl number limit, the influence of inertia is weak and can be neglected; this limit is routinely exploited in studying the convection of planetary mantles where the Prandtl number can be of order  $10^{20}$  (Schubert et al., 2001). Spiegel (1962) developed an approximate set of equations valid in the limit  $\text{Pr} \rightarrow 0$  that showed that inertia plays a leading-order role in the convective dynamics (see also Thual, 1992). The low- $\text{Pr}$  approximate model has been applied only to nonrotating and incompressible Boussinesq systems to date.

Much less is known about the role of the Prandtl number in compressible convection. Earlier studies of compressible convection have primarily used Prandtl number of order unity (e.g., Gilman, 1977; Gilman and Glatzmaier, 1981; Goudard and Dormy, 2008; Christensen, 2011; Soderlund et al., 2012; Schrinner et al., 2012; Gastine et al., 2015, 2016; Wicht and Meduri, 2016). While there are also many studies that make use of nonunity Prandtl numbers (e.g., Brown et al., 2011; Käpylä et al., 2013; Nelson et al., 2014; Jones, 2014; Augustson et al., 2015, 2016; Duarte et al., 2016; Brun et al., 2017), no parameter studies that vary the Prandtl number systematically have been carried out.

One exception to this trend is the work of O’Mara et al. (2016), who explored the characteristics of high Prandtl compressible convection. These authors found that high Prandtl convection tended to possess lower characteristic flow-speeds with respect to unity Prandtl number convection, owing to the enhanced entropy content of its downflow plumes. Finally, we note that recent work using a small Prandtl number with rapid rotation has found that the anelastic approximation can yield spurious behavior (Calkins et al., 2015c) that does not appear in nonrotating anelastic convection (Calkins et al., 2015b). These results raise serious questions regarding the applicability of the anelastic approximation within rotating stellar interiors where it remains to be seen if the convective flows are well-approximated by a Prandtl number of unity.

Systematic parameter space studies of convective dynamics in stellar interiors have, so far, focused largely on the role of buoyancy driving and rotation. Featherstone and Hindman (2016a) investigated the response of the convection to varying Rayleigh number and varying degrees of density stratification. Those simulations were nonrotating, hydrodynamic,  $\text{Pr} = 1$  and demonstrated a clear scaling relationship between kinetic energy and Rayleigh number. Those results also suggest that a naive interpretation of model results (by ascribing solar values to all problem parameters but the diffusion coefficients) will naturally overestimate the low-wavenumber power in the convective power spectrum. The influence of rotation was investigated using a similar methodology by Featherstone and Hindman (2016b) who identified a complementary scaling law relating convective-cell-size and rotational influence. When rotation is present and diffusive effects are negligible, the typical spatial-size of convective cells is determined primarily through the Rossby number that expresses the ratio of the rotation period to a characteristic convective time scale. Their work was also restricted to  $\text{Pr} = 1$ .

Through this paper, we extend these studies and examine the effects of Prandtl number variation on the convective dynamics. We present a series of numerical simulations designed to examine how the structure and amplitude of the convective flow within a stellar interior depends on the Prandtl number and the convective forcing. We vary the Prandtl number and the convective forcing in a systematic way, covering both low and high Prandtl numbers. Effects due to rotation

and magnetism are not included. We will show that the convection develops smaller-scale structures as the convective forcing is increased and the Prandtl number is decreased, corresponding to an increase in high-wavenumber power. As the high-wavenumber power increases, the low-wavenumber power decreases and this trend occurs for all Prandtl numbers studied. We also show that the Prandtl number has an important influence on the boundary-layer thickness.

### 2.2.2 Numerical Model

This study is based on a series of 3D, nonlinear convection simulations that use the pseudo-spectral convection code `Rayleigh` (e.g., Featherstone and Hindman, 2016a). We employ a spherical geometry and represent the horizontal variation of all variables along spherical surfaces using spherical harmonics  $Y_\ell^m(\theta, \phi)$ . Here  $\ell$  is the spherical harmonic degree, and  $m$  is the azimuthal mode order. In the radial direction, we employ a Chebyshev collocation method, expanding all variables in Chebyshev polynomials  $T_n(r)$ , where  $n$  is the degree of the polynomial.

We are particularly interested in understanding convection in the deep stellar interior, far removed from the photosphere. In this region, plasma motions are subsonic and perturbations to thermodynamic variables are small compared to their mean, horizontally averaged values (represented using overbars). Under these conditions, the anelastic approximation provides a convenient description of the system's thermodynamics (Gough, 1969; Gilman and Glatzmaier, 1981). The governing evolution equations include the continuity equation

$$\nabla \cdot (\bar{\rho} \mathbf{u}) = 0, \quad (2.1)$$

where  $\bar{\rho}$  is the background density and  $\mathbf{u}$  is the fluid velocity. The momentum equation is given by

$$\frac{D\mathbf{u}}{Dt} = -\nabla \frac{P}{\bar{\rho}} - \frac{S}{c_p} \mathbf{g} + \frac{1}{\bar{\rho}} \nabla \cdot \mathcal{D}, \quad (2.2)$$

where  $P$  is the pressure,  $S$  is the entropy,  $c_p$  is specific heat at constant pressure,  $\mathbf{g}$  is the gravitational acceleration, and the viscous stress tensor  $\mathcal{D}$  is given by

$$\mathcal{D}_{ij} = 2\bar{\rho}\nu \left[ e_{ij} - \frac{1}{3} \partial_k u_k \delta_{ij} \right]. \quad (2.3)$$

Here,  $e_{ij}$  is the strain rate tensor and  $\delta_{ij}$  is the Kronecker delta. Written in terms of the entropy, the thermal energy equation is given by

$$\bar{\rho}\bar{T}\frac{DS}{Dt} = \nabla \cdot (\bar{\rho}\bar{T}\kappa\nabla S) + Q(r, \theta, \phi) + 2\bar{\rho}\nu \left[ e_{ij}e_{ij} - \frac{1}{3}(\nabla \cdot \mathbf{u})^2 \right], \quad (2.4)$$

where  $\bar{T}$  is the background temperature. Sources of internal heating and cooling are encapsulated in the functional form of  $Q$ . A linearized equation of state closes the system and is given by

$$\frac{\rho}{\bar{\rho}} = \frac{P}{\bar{P}} - \frac{T}{\bar{T}} = \frac{P}{\gamma\bar{P}} - \frac{S}{c_p}, \quad (2.5)$$

assuming the ideal gas law

$$\bar{P} = \mathcal{R}\bar{\rho}\bar{T}, \quad (2.6)$$

where  $\mathcal{R}$  is the gas constant and  $\gamma = 5/3$  is the adiabatic index.

### 2.2.3 Numerical Experiment

We have constructed a set of 34 model stellar convection zones designed to explore how the convective kinetic energy depends on both the thermal diffusion and the viscous diffusion as characterized by the Prandtl number. The diffusion coefficients are taken to be constant values within each simulation. In particular, they have no variation with radius. Table 2.1 has a detailed list of all model parameters for each run.

Each model is constructed using a polytropic background state following Jones et al. (2011). The background states were constructed in a similar fashion to the models presented in Featherstone and Hindman (2016a). We use a polytropic index of  $n = 1.5$ , that corresponds to the adiabatic value, and model the innermost 3 density scale heights of the convection zone. The spherical shell has an aspect ratio of  $\chi = r_i/r_o = 0.759$  corresponding to a dimensional shell depth of 159 Mm, where  $r_i$  and  $r_o$  are the inner and outer radii of the domain, respectively.

Our models are fully characterized by two parameters: a Rayleigh number and a Prandtl number. As discussed in Featherstone and Hindman (2016a), a flux Rayleigh number  $\text{Ra}_F$  appro-

Table 2.1: List of all the simulation parameters for each run. Each simulation used a polytropic background state with an adiabatic index  $\gamma = 5/3$ , three density scale heights across the domain  $N_\rho = 3$ , and a polytropic index of  $n = 1.5$ . The inner and outer radii of each simulation were  $r_i = 5 \times 10^{10}$  cm and  $r_o = 6.586 \times 10^{10}$  cm. The variable input parameters are the thermal diffusivity  $\kappa$ , the kinematic viscosity  $\nu$ , the Rayleigh number, the Prandtl number, the radial resolution, and the azimuthal resolution. The output parameters are the dimensional kinetic energy KE, nondimensional kinetic energy  $\widehat{\text{KE}}$ , the fractional convective flux  $f_{\text{conv}}$ , the dimensional thermal boundary layer thickness  $\delta_{\text{BL}}$ , the Reynolds number and the peak Reynolds number.

Input Parameters				Output Parameters							
$\kappa$ ( $10^{12}$ cm $^2$ s $^{-1}$ )	$\nu$	Ra $_F$	Pr	$n_{\text{max}}$	$\ell_{\text{max}}$	KE ( $10^{38}$ erg)	$\widehat{\text{KE}}$	$f_{\text{conv}}$	$\delta_{\text{BL}}$ (Mm)	Re	Re <sub>peak</sub>
10	1	$6.88 \times 10^4$	0.1	85	1023	34.43	19064.7	0.6620	15.57	248.3	342.1
4	1	$4.30 \times 10^5$	0.25	85	1023	42.59	23582.9	0.8301	10.36	261.2	376.9
8	2	$5.37 \times 10^4$	0.25	85	511	46.56	6446.4	0.7026	13.76	132.8	192.8
12	3	$1.59 \times 10^4$	0.25	85	511	42.08	2588.8	0.5876	16.18	85.1	123.4
16	4	$6.72 \times 10^3$	0.25	85	263	35.80	1238.4	0.5087	17.68	58.7	83.6
24	6	$1.99 \times 10^3$	0.25	85	127	21.07	324.8	0.3251	20.78	30.8	44.9
32	8	$8.40 \times 10^2$	0.25	85	127	9.36	81.6	0.1569	23.26	15.7	23.0
4	2	$2.15 \times 10^5$	0.5	85	511	42.24	5847.2	0.8403	9.87	129.0	186.0
6	3	$6.37 \times 10^4$	0.5	85	511	40.46	2489.6	0.7750	11.98	83.7	121.9
8	4	$2.68 \times 10^4$	0.5	85	263	39.62	1371.2	0.7167	13.71	62.7	91.9
12	6	$7.96 \times 10^3$	0.5	85	127	34.51	530.8	0.6031	16.18	38.5	56.5
16	8	$3.36 \times 10^3$	0.5	85	127	24.84	214.8	0.4860	18.18	25.6	38.4
24	12	$9.96 \times 10^2$	0.5	85	127	79.94	30.4	0.2314	22.21	10.4	16.5
1	1	$6.81 \times 10^6$	1	85	1023	36.22	20057.7	0.9480	4.96	229.8	320.4
2	2	$8.53 \times 10^5$	1	85	511	34.73	4807.6	0.9120	6.93	114.1	166.5
4	4	$1.06 \times 10^5$	1	85	263	33.42	1156.7	0.8470	9.83	56.3	85.6
6	6	$3.16 \times 10^4$	1	85	127	32.92	506.4	0.7910	12.18	37.5	58.2
8	8	$1.33 \times 10^4$	1	85	127	31.62	273.5	0.7360	14.09	27.5	42.4
12	12	$3.94 \times 10^3$	1	85	127	22.08	84.9	0.6230	16.03	15.4	24.0
16	16	$1.66 \times 10^3$	1	42	127	12.02	26.0	0.4420	19.06	9.0	15.6
24	24	$4.93 \times 10^2$	1	42	63	2.05	2.0	0.1220	23.77	2.5	4.5
2	4	$4.30 \times 10^5$	2	85	511	27.22	941.9	0.9145	6.92	53.5	78.0
4	8	$5.37 \times 10^4$	2	85	263	25.60	221.4	0.8539	10.18	26.6	40.0
6	12	$1.59 \times 10^4$	2	85	127	24.37	93.7	0.8038	13.43	17.3	26.2
8	16	$6.72 \times 10^3$	2	85	127	20.11	43.5	0.7398	15.22	12.1	18.7
12	24	$1.99 \times 10^3$	2	85	127	10.04	9.6	0.5277	18.35	6.1	9.9
16	32	$8.40 \times 10^2$	2	42	127	4.33	2.3	0.3393	20.65	3.1	5.2
1	4	$1.72 \times 10^6$	4	85	1023	17.10	591.8	0.9490	5.02	45.3	67.1
2	8	$2.15 \times 10^5$	4	85	511	20.26	175.2	0.9150	7.11	24.6	37.9
4	16	$2.68 \times 10^4$	4	85	263	17.12	37.0	0.8641	11.62	11.7	18.5
6	24	$7.96 \times 10^3$	4	85	127	11.88	11.4	0.7953	14.10	6.9	11.5
8	32	$3.36 \times 10^3$	4	85	127	8.10	4.3	0.6808	15.86	4.2	7.1
12	48	$9.96 \times 10^2$	4	85	127	3.66	0.8	0.4438	19.16	1.9	3.2
16	64	$4.29 \times 10^2$	4	42	127	0.63	0.1	0.0969	24.08	0.6	1.0

priate for this system may be defined as

$$\text{Ra}_F = \frac{\tilde{g}\tilde{F}H^4}{c_p\tilde{\rho}\tilde{T}\nu\kappa^2}, \quad (2.7)$$

where tildes indicate volume averages over the full shell, making  $\text{Ra}_F$  a bulk Rayleigh number. In this definition,  $F$  is the thermal energy imposed by the radiative heating and  $H$  is chosen to be the shell depth,  $r_o - r_i$ . The nondimensionalization was carried out using the shell depth and the viscous diffusion time scale  $H^2/\nu$ .

Heat enters the system through the internal deposition by  $Q$ , which drops to zero at the upper boundary. In all simulations we adopt a functional form of  $Q$  that depends only on the background pressure profile such that

$$Q(r, \theta, \phi) = \alpha (\bar{P}(r) - \bar{P}(r_o)). \quad (2.8)$$

The normalization is defined so that

$$L_\star = 4\pi \int_{r_i}^{r_o} Q(r) r^2 \, dr, \quad (2.9)$$

where  $L_\star$  is the stellar luminosity. The thermal energy flux  $F(r)$  that convection and conduction must transport across a spherical surface at radius  $r$  is then given by

$$F(r) = \frac{1}{r^2} \int_{r_i}^r Q(x) x^2 \, dx. \quad (2.10)$$

For all simulations, we have adopted impenetrable and stress-free boundary conditions on the velocity. The radial entropy gradient is forced to vanish at the lower boundary of the convection zone, and the entropy perturbations are forced to vanish at the upper boundary.

Our numerical experiments span the range of  $4 \times 10^2 \lesssim \text{Ra}_F \lesssim 7 \times 10^6$  and  $0.1 \leq \text{Pr} \leq 4$ . Each simulation was initialized using a small random thermal perturbation, evolved until the kinetic energy reached a statistically steady state, and further evolved for at least one diffusion time. Since there are two diffusion time scales, the larger of the two was used for this purpose. The larger of the two diffusion times is also the time interval over which a time average is computed when necessary. This averaging interval includes several tens of convective overturning times.

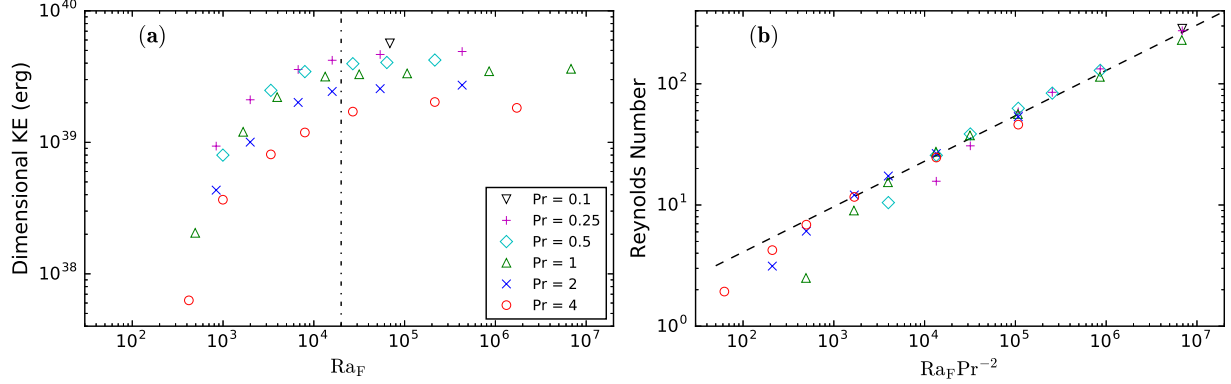


Figure 2.1: (a) Dimensional kinetic energy vs. flux Rayleigh number  $\text{Ra}_F$  for all cases. Colored symbols indicate different Prandtl numbers. Low Prandtl number runs have higher kinetic energies for a given  $\text{Ra}_F$ . Beyond the high- $\text{Ra}_F$  cutoff, denoted by the vertical dotted-dashed line, the kinetic energy tends toward an asymptotic value. (b) Reynolds number vs.  $\text{Ra}_F \text{Pr}^{-2}$ . The high- $\text{Ra}_F$  region reaches an asymptotic regime with a power law scaling exponent that is very close to 1/3. The dashed line is  $(\text{Ra}_F \text{Pr}^{-2})^{0.373}$ . Colored symbols are the same as in panel (a).

## 2.2.4 Survey of Results

### 2.2.4.1 Kinetic Energy Scaling

We begin our examination of the convective energetics by looking at the integrated kinetic energy KE, defined as

$$\text{KE} = \frac{1}{2} \int \bar{\rho}(r) |\mathbf{u}(r, \theta, \phi)|^2 d^3x, \quad (2.11)$$

where the integration is computed over the entire domain and then time averaged.

Figure 2.1(a) shows the dimensional kinetic energy vs.  $\text{Ra}_F$ . Different symbols indicate different values of Pr. As the Prandtl number is lowered, the kinetic energy increases for any given  $\text{Ra}_F$ . The kinetic energy for those runs with  $\text{Ra}_F \gtrsim 2 \times 10^4$  appears to have reached a steady value that is independent of  $\text{Ra}_F$ . The level at which the kinetic energy saturates is dependent on the Prandtl number. The saturation of the kinetic energy as the Rayleigh number is changed was also found in Featherstone and Hindman (2016a), although their study was restricted to a Prandtl number of unity.

As Pr is increased,  $\nu$  becomes larger leading to enhanced viscous dissipation and a smaller

Reynolds number. The Reynolds number measures the relative ratio of inertial forces to viscous forces and is given by

$$\text{Re} = \frac{\sqrt{|\tilde{\mathbf{u}}|^2 H}}{\nu}, \quad (2.12)$$

where  $H$  and the tilde retain the same meaning as before, representing the shell depth and a volume average, respectively. Larger Prandtl numbers will produce smaller Reynolds numbers for a given  $\text{Ra}_F$ .

Figure 2.1(a) indicates that below some  $\text{Ra}_F$  cutoff, diffusion plays a leading-order role in the force balance. Beyond  $\text{Ra}_F \sim 2 \times 10^4$ , which we denote the high- $\text{Ra}_F$  regime<sup>1</sup>, this is no longer the case; diffusion no longer plays a leading-order role in the global force balance and the kinetic energy remains constant as  $\text{Ra}_F$  is increased. We note that the cutoff for the high- $\text{Ra}_F$  region is based on the  $\text{Pr} = 1$  results of Featherstone and Hindman (2016a). Importantly, the cutoff is a decreasing function of the Prandtl number; lower Prandtl numbers will have a lower high- $\text{Ra}_F$  cutoff. To simplify the analysis, only a single cutoff is used.

The kinetic energy can also be discussed from a nondimensional point of view. To do this, we choose a nondimensional measure of the kinetic energy  $\widehat{\text{KE}}$  as

$$\widehat{\text{KE}} \equiv \frac{H^2}{\nu^2 M} \text{KE}. \quad (2.13)$$

The nondimensionalization has been carried out using the mass  $M$  contained within the spherical shell, the shell depth, and the viscous diffusion time scale. Under such a nondimensionalization, the kinetic energy can be related to the Reynolds number as

$$\widehat{\text{KE}} \sim \text{Re}^2. \quad (2.14)$$

Therefore we do not plot the nondimensional kinetic energy separately, but do list it for each run in Table 2.1.

If  $\text{Ra}_F$  is large enough to be in the high- $\text{Ra}_F$  regime, then the kinetic energy is largely insensitive to the level of diffusion. This implies that the velocity is not strongly dependent on the

---

<sup>1</sup> This is the same cutoff used in Featherstone and Hindman (2016a). Their reported  $\text{Ra}_F$  are too high by a factor of  $\pi$ ; we correct for that here.

level of diffusion and that the Reynolds number should scale with the viscosity as  $\text{Re} \sim \nu^{-1}$ . Given our definition of  $\text{Ra}_F$  and  $\text{Pr}$ , namely that  $\text{Ra}_F \sim \nu^{-1}\kappa^{-2}$  and  $\text{Pr} \sim \nu\kappa^{-1}$ , the Reynolds number scaling becomes  $\text{Re} \sim \text{Ra}_F^{1/3}\text{Pr}^{-2/3}$ . In Figure 2.1(b), we plot the Reynolds number vs.  $\text{Ra}_F\text{Pr}^{-2}$ , where the different symbols are the same as in panel (a). Each data point is time averaged. A least-squares fit to the data in the high- $\text{Ra}_F$  region yields a scaling law of

$$\text{Re} \propto (\text{Ra}_F\text{Pr}^{-2})^{0.373 \pm 0.008}. \quad (2.15)$$

These results indicate that there are two distinct parameter regions; one in which diffusion is an important factor in the global force balance (the low- $\text{Ra}_F$  region), and one where diffusion no longer plays an appreciable role in the interior, bulk global force balance (the high- $\text{Ra}_F$  region).

#### 2.2.4.2 Spectral Distribution

We find the kinetic energy may reach a  $\text{Ra}_F$ -independent regime, but the flow's morphology is still affected by the level of diffusion. This can be seen in the relative spectral distribution of velocity between the high- and low- $\text{Ra}_F$  systems. Figure 2.2 shows the velocity power spectra for all runs with Prandtl numbers of  $\text{Pr} = 0.25$ ,  $\text{Pr} = 1.0$ , and  $\text{Pr} = 4.0$ . Each spectrum has been normalized such that it has unit integrated power. The rows correspond to the different Prandtl numbers. The first column shows the spectra taken at the lower convection zone or  $r/r_o \approx 0.775$ . The second column shows the spectra near the upper boundary, or  $r/r_o \approx 0.985$ , in the thermal boundary layer. In each panel, all spectra with the given Prandtl number are plotted. Each spectrum is colored by  $\text{Ra}_F\text{Pr}$ , with high values taking on red tones and low values displaying blue tones. Each spectrum is a time average over several tens of overturnings.

Across all cases, as  $\text{Ra}_F$  increases from low values, the point-wise velocity power increases at nearly all spherical harmonic degrees. The  $\ell$  value associated with the peak for each spectra increases with increasing  $\text{Ra}_F$ . This indicates smaller-scale structures become more apparent with increasing  $\text{Ra}_F$ . At sufficiently high Rayleigh number, power in the high- $\ell$  portion continues to increase, but the low- $\ell$  portion starts to decrease. This suggests a break down of large-scale coherent

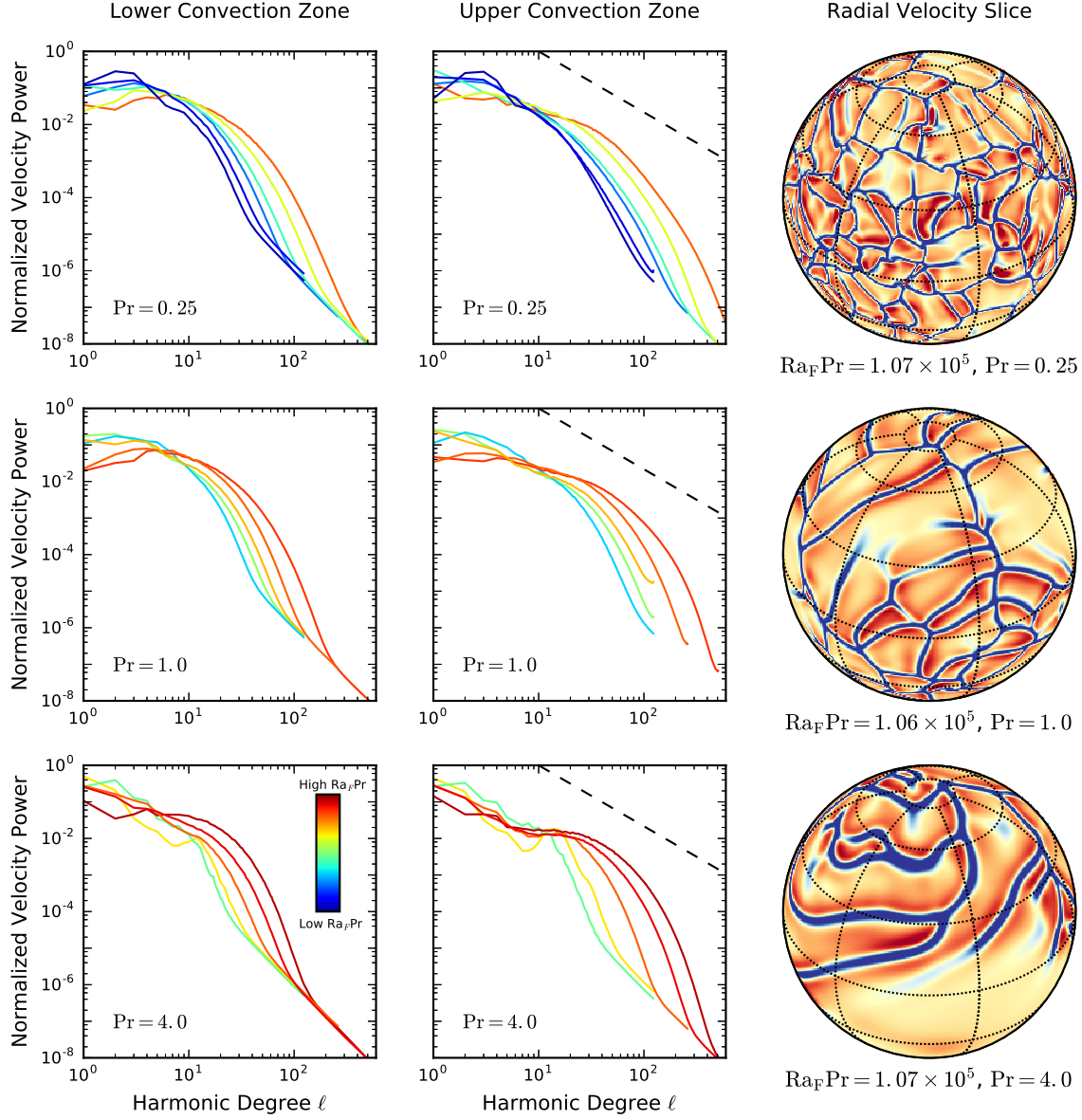


Figure 2.2: Time-averaged velocity power spectra and shell slices for cases with  $\text{Pr} = 0.25$ ,  $\text{Pr} = 1.0$ , and  $\text{Pr} = 4.0$ . The power spectra have been normalized such that each curve has unit integrated power. Each row represents a different value of  $\text{Pr}$ . The first two columns correspond to power spectra at a single depth within the convective shell. The dashed black line in the center column has a slope of  $-5/3$  for reference. Within each panel, spectra for all cases at that depth and  $\text{Pr}$  are displayed. Each curve is colored by  $\text{Ra}_F \text{Pr}$  with low  $\text{Ra}_F \text{Pr}$  in blue tones and high  $\text{Ra}_F$  cases are in red tones. As  $\text{Ra}_F$  is increased, the power at low  $\ell$ -values increases initially. At high  $\text{Ra}_F$ , it decreases as high-wavenumber power is generated at the expense of low-wavenumber power. This trend occurs at all Prandtl numbers studied. The last column shows shell slices of the radial velocity taken near the outer boundary at  $r/r_o \approx 0.985$ . The larger  $\text{Pr}$  run shows wider down flow lanes compared to the small  $\text{Pr}$  run.

structures. The highest Rayleigh number runs have lower power in the large scales compared to the low- $\text{Ra}_F$  counterparts. The low-wavenumber region occurs in the approximate range of  $\ell \lesssim 10$  for most simulations in this study. This trend occurs for all values of  $\text{Pr}$  that were studied. If viscosity played a significant role in the asymptotic regime, one might expect there to be some variation in the spectra when the Prandtl number is varied. We do not observe large variations between the spectra for the Prandtl numbers within our range indicating that viscosity only plays a minor role in the asymptotic regime.

The third column in Figure 2.2 plots shell slices of the radial velocity taken near the upper boundary, the same location in radius as the second column. Each slice is a single snapshot in time. The color scale is the same for all three shell slices with red tones indicating positive, outward flows and blue tones indicating negative, inward flows. The lower Prandtl number run (the top panel) displays larger velocities and more small-scale structures compared to the larger Prandtl cases. The Reynolds numbers of all three slices cover a large range. The top row  $\text{Pr} = 0.25$  run has  $\text{Re} = 261.2$ , the middle slice with  $\text{Pr} = 1.0$  has  $\text{Re} = 56.3$ , and the bottom slice with  $\text{Pr} = 4.0$  has  $\text{Re} = 11.7$ . The large range in Reynolds numbers indicates that the inertial subrange for each simulation is different.

At sufficiently high Rayleigh number, the integrated KE becomes independent of the level of diffusion (both thermal and momentum diffusion). As  $\nu$  is decreased and  $\text{Ra}_F$  is increased, the flow becomes more turbulent with smaller-scale structures. To leading-order, once the high- $\text{Ra}_F$  regime is reached, the total integrated dimensional KE is constant as the diffusion is further reduced. This fact is largely independent of  $\text{Pr}$  for the Prandtl numbers that were within our range, however, a weak  $\text{Pr}$  dependence remains because the inertial subrange is extended as the viscosity is reduced individually. These trends are similar to those found in the simulations of Featherstone and Hindman (2016a), which used a Prandtl number of unity.

#### 2.2.4.3 Energy Transport

The energy transport across the layer can be characterized by four radial energy fluxes: the enthalpy flux  $F_e$ , the kinetic energy flux  $F_{\text{KE}}$ , the conductive flux  $F_c$ , and the viscous flux  $F_\nu$ , which we define as

$$F_e = \bar{\rho} c_p u_r T, \quad (2.16)$$

$$F_{\text{KE}} = \frac{1}{2} \bar{\rho} u_r |\mathbf{u}|^2, \quad (2.17)$$

$$F_c = \kappa \bar{\rho} T \frac{\partial S}{\partial r}, \quad (2.18)$$

$$F_\nu = -(\mathbf{u} \cdot \mathcal{D}) \cdot \hat{\mathbf{r}}, \quad (2.19)$$

respectively. Note that the conductive flux  $F_c$  is associated with the diffusion of entropy perturbations, and it should not be confused with radiative diffusion arising from the reference state temperature gradient; that effect is represented by  $Q$  in our models. Averages are taken of these fluxes over several diffusion times, indicated using brackets. We consider the contribution of conduction by looking at the fractional convective flux  $f_{\text{conv}}$ , defined as

$$f_{\text{conv}} \equiv \frac{\int \langle F_e + F_\nu + F_{\text{KE}} \rangle \, d^3x}{\int \langle F_c + F_e + F_\nu + F_{\text{KE}} \rangle \, d^3x} \quad (2.20)$$

Upon rearranging this quantity, we can write

$$\frac{1}{1 - f_{\text{conv}}} = \frac{\int \langle F_c + F_e + F_\nu + F_{\text{KE}} \rangle \, d^3x}{\int \langle F_c \rangle \, d^3x} \quad (2.21)$$

$$= 1 + \frac{\int \langle F_e + F_\nu + F_{\text{KE}} \rangle \, d^3x}{\int \langle F_c \rangle \, d^3x} \quad (2.22)$$

This resembles the traditional Nusselt number, but differs in two important ways. Firstly, the traditional Nusselt number does not include the viscous flux or the kinetic energy flux, both of which we include. Secondly, the conductive flux that appears in our definition is the established conductive flux, not the conductive flux in the absence of convection. Values of  $1 / (1 - f_{\text{conv}})$  that

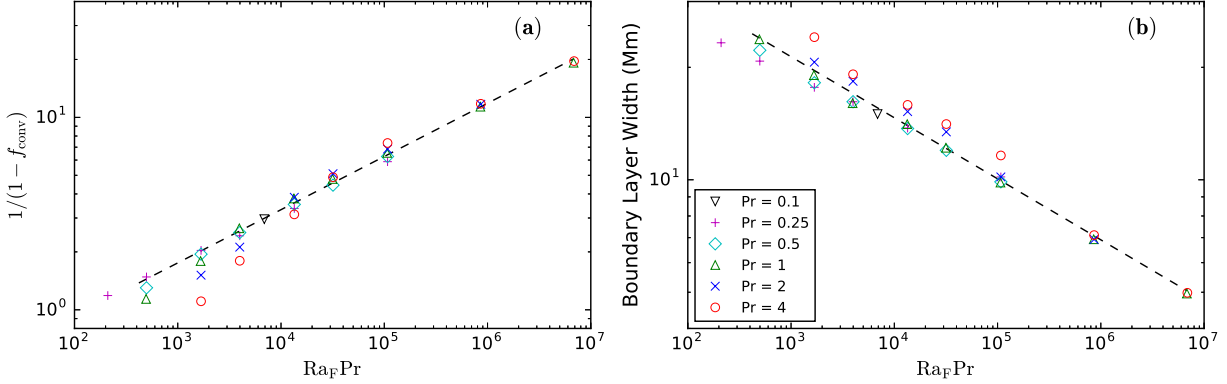


Figure 2.3: Energy transport and thermal boundary layer scaling with  $\text{Ra}_F \text{Pr}$ . (a) Fractional convective flux  $1/(1 - f_{\text{conv}})$  vs.  $\text{Ra}_F \text{Pr}$ . The dashed line is  $(\text{Ra}_F \text{Pr})^{0.275}$ , very close to a  $2/7$  scaling. (b) Thermal boundary layer width plotted vs.  $\text{Ra}_F \text{Pr}$ . The dashed line is  $(\text{Ra}_F \text{Pr})^{-0.164}$ , very close to  $-1/6$ .

are of order unity translate to a lack of convective heat transport. Large values indicate convection plays a dominant role over thermal conduction in transporting energy through the shell. Figure 2.3(a) plots  $1/(1 - f_{\text{conv}})$  as a function of  $\text{Ra}_F \text{Pr}$ . Viscosity is not expected to play a large role in the heat transport across the shell, which is why we plot against  $\text{Ra}_F \text{Pr}$  and not simply  $\text{Ra}_F$ . The plot shows a clear trend that can be fit using least-squares to obtain

$$\frac{1}{1 - f_{\text{conv}}} \propto (\text{Ra}_F \text{Pr})^{0.275 \pm 0.002} \quad (2.23)$$

with a scaling exponent that is approximately  $2/7$  ( $\sim 0.286$ ). Other studies have found that the Nusselt number scales with the Rayleigh number to the  $2/9$  power ( $\sim 0.222$ ) (e.g., Gastine et al., 2015), when a flux based Rayleigh number is used. Our results have a steeper exponent because we include the viscous flux and the kinetic energy flux, which act to increase  $1/(1 - f_{\text{conv}})$  at any given Rayleigh number.

#### 2.2.4.4 Boundary Layer Thickness

We can further characterize the role of conduction by determining how  $\text{Ra}_F$  and  $\text{Pr}$  control the thermal boundary layer thickness. We define the thermal boundary layer thickness in terms of

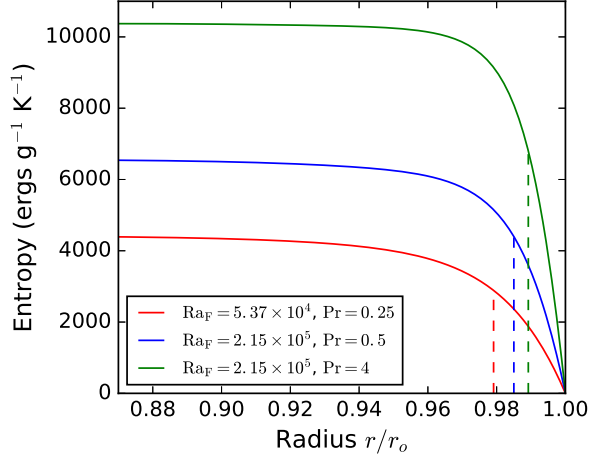


Figure 2.4: Time-averaged mean entropy profiles for three cases in the high- $\text{Ra}_F$  regime. The vertical dashed lines indicate the location of the boundary layer as calculated using Equation 2.24.

the time-averaged mean entropy, such that

$$\delta_{\text{BL}} = \int \frac{\sup \langle S(r) \rangle - \langle S(r) \rangle}{\sup \langle S(r) \rangle} dr, \quad (2.24)$$

where the brackets indicate a time-average as before and sup indicates the supremum. Figure 2.4 shows three examples of the time-averaged mean entropy profiles and the associated boundary layer location as calculated using Equation 2.24. We plot the variation of  $\delta_{\text{BL}}$  with  $\text{Ra}_F \text{Pr}$  for different Prandtl numbers in Figure 2.3(b). We plot against  $\text{Ra}_F \text{Pr}$  because we do not expect the thermal boundary to depend on the viscosity and the quantity  $\text{Ra}_F \text{Pr}$  is independent of the viscosity and scales as  $\text{Ra}_F \text{Pr} \sim \kappa^{-3}$ . A least-squares fit gives the scaling law

$$\delta_{\text{BL}} \propto (\text{Ra}_F \text{Pr})^{-0.164 \pm 0.003}. \quad (2.25)$$

The scaling exponent is very close to  $-1/6$  ( $\sim -0.166$ ), indicating that the boundary layer width scales purely as the thermal diffusivity, i.e.,  $\delta_{\text{BL}} \propto \sqrt{\kappa}$ . There is no strong dependence on viscosity within the range of  $\text{Pr}$  studied here.

We note that the highest Rayleigh number run had a boundary layer width of about 3% of the shell depth ( $\sim 5$  Mm). Our thermal boundary layer lacks the radiative processes at work in a star like the Sun, but its physical extent is confined to a similarly small region of the convective

domain.

Figure 2.1 showed that a free-fall regime that is independent of both viscosity and thermal diffusion could be obtained for different Prandtl numbers. We find that in order to have a bulk kinetic energy that is independent of both viscosity and thermal diffusion, the thermal boundary layer thickness must depend on both the Rayleigh number and the Prandtl number with the scaling law given in Equation 2.25.

For a fixed Prandtl number, this scaling relation suggests that the boundary layer thickness will continually decrease as the Rayleigh number is increased. In global simulations that employ explicit diffusivities, the Prandtl number is therefore critical in maintaining a boundary layer that is confined to a small region of the convective domain without becoming vanishingly small as the Rayleigh number is increased.

Certainly, simulations with a conductive boundary layer cannot match every feature of the Sun's thermal boundary layer, for the simple reason that the Sun's boundary layer is regulated by radiative transfer instead of thermal conduction. In a global simulation without radiative transfer, one hopes that the microphysics of the cooling layer can be ignored and only the gross properties of the boundary layer (thickness and entropy contrast) are important. When the boundary layer is conductive, the entropy contrast and thickness are inherently linked. Thus, the best one could hope to do is achieve a physically realistic thickness; this requires that the product  $H(\text{Ra}_F \text{Pr})^{-1/6}$  take on the desired thickness, i.e., as the Rayleigh number is increased, the Prandtl number must be decreased. This realistic thickness will probably not, however, coincide with a convective power spectrum that possesses a realistic inertial range.

### 2.2.5 Perspectives and Conclusions

The results presented here have interesting consequences for several aspects of stellar/solar convection zone dynamics. Many of these results will depend on rotation and magnetism, both of which were omitted in this study.

We find that simulations with a lower Pr number have faster flows and a broader range of

scales compared to high Pr models with the same  $\text{Ra}_F$ . The higher Pr models have more viscous dissipation, resulting in slower flows (equivalent to a lower Reynolds number). This is consistent with the results found in O’Mara et al. (2016).

The higher  $\text{Ra}_F$  simulations obtain a free-fall state where diffusion no longer plays an important role in the interior bulk global force balance. In this state the kinetic energy becomes independent of both viscosity and thermal diffusion. Similar results were found in Featherstone and Hindman (2016a), although their study was restricted to  $\text{Pr} = 1$ .

The boundary layer thickness scaling suggests that most simulations may be achieving the correct driving scale with a modest Rayleigh number of about  $10^6$  and a Prandtl number of unity. The obtained scaling also suggests that in order to maintain a boundary layer whose physical extent is confined to a small region of the convective domain in a global simulation without radiative transfer, the Prandtl number should be decreased as the Rayleigh number is increased.

We did not find that the Prandtl number substantially alters the earlier observed behavior in the spectral distribution of the velocity for  $\text{Pr}$  unity simulations (e.g., Featherstone and Hindman, 2016a). As the  $\text{Ra}_F$  is increased, the convection develops smaller scale structures and a corresponding increase in the high-wavenumber power. The high-wavenumber power increases, but the low-wavenumber power decreases indicating the break down of coherent large-scale structures. The spectral range  $\ell \leq 10$  appears to be the most sensitive region of the power spectrum. This occurs for all Prandtl numbers studied here.

Our results indicate that care needs to be taken when interpreting convection simulations and comparing the results to observations of real solar/stellar systems. Simulations that do not access a high enough  $\text{Ra}_F$ , may overestimate the low-wavenumber power that is accessible to helioseismology. Stellar convection simulations must run with parameters that place it in the high-Rayleigh-number regime in order to correctly capture the integrated kinetic energy and the large scale motions of the flow. We used rather modest levels of diffusion ( $\kappa \leq 4 \times 10^{12} \text{ cm}^2 \text{ s}^{-1}$ ) to put our simulations in the high-Rayleigh-number regimes.

Most importantly, our simulations did not include rotation or magnetism. Featherstone and

Hindman (2016b) looked at the effects of rotation, but restricted their study to hydrodynamical,  $\text{Pr} = 1$  simulations. It will be important to examine how our Prandtl number findings are modified by rotation and magnetism before we can fully trust comparisons of power spectra between observations and simulations.

## Chapter 3

### Force Balances and Asymptotic Scaling Behavior of the Large-Scale Dynamics

#### 3.1 Introduction

The geomagnetic field has existed for at least 3.5 billion years, and possibly as long as 4.2 billion years (Tarduno et al., 2015). Both recent observations and historical measurements show that the geomagnetic field is characterized by a broad range of spatiotemporal scales. Along with the 100 thousand year time scale associated with magnetic polarity reversals, several distinct time scales are present in observations of the secular variation of the geomagnetic field, ranging from years to hundreds of years (Courtillot and Le Mouel, 1988). During times of stable polarity the field is dominated by its dipole contribution, yet small-scale features and inferred flow patterns also are prevalent (Hulot et al., 2002; Amit and Olson, 2004; Gillet et al., 2015; Livermore et al., 2017). Fluid motion within the electrically-conducting liquid outer core of the Earth is the primary source of the geomagnetic field (see e.g., Jones, 2011). Understanding the origin of these different spatiotemporal scales and our ability to understand their subsequent evolution requires knowledge of the predominant forces within the core. It is generally accepted that the Coriolis force is a key ingredient for the generation of the geomagnetic field in the core. The relative sizes of the other forces in the core still is debated (see e.g., Christensen, 2010). One view is that the core dynamics are dominated by a four-way, magnetostrophic balance in which the Coriolis, pressure gradient, buoyancy, and Lorentz forces are all of comparable magnitude (e.g., Roberts and King, 2013). An alternative view is that the core is more accurately characterized by a geostrophic balance in which only the Coriolis and pressure gradient forces balance, and the Lorentz force would contribute only

as a perturbation to the primary geostrophic balance (Calkins, 2018). Yet another possibility is that distinct force balances are present on different scales of motion (e.g., Calkins et al., 2015). Here we use data from numerical dynamo models, along with a multiscale analysis of the governing equations to interrogate the force balance in more detail. Recent numerical simulations indicate that a leading order geostrophic force balance is present on the small-scale motions (Yadav et al., 2016; Aubert et al., 2017; Schaeffer et al., 2017), so here we focus on the dynamics of the large-scale motions.

No direct observations of the core currently are possible. Instead, insight into core dynamics is obtained from temporal variations of the geomagnetic field. These observations can be used to provide estimates of a typical flow speed that are of order  $\mathcal{U} \sim 10^{-4}$  m s<sup>-1</sup> (Roberts and King, 2013). Coupled with physical properties of the core obtained from laboratory experiments and simulations (Roberts and King, 2013), this value provides vital clues to the inner workings of the core by enabling estimates of important nondimensional parameters describing the dynamics of the core. In particular, the relative size of inertia compared to the Coriolis force is quantified by the Rossby number  $\text{Ro} \approx 10^{-6}$ , and the relative size of the viscous force to the Coriolis force is measured by the Ekman number  $\text{Ek} \approx 10^{-15}$  (King et al., 2010). The Elsasser number  $\Lambda$  characterizes the relative size of the Lorentz and Coriolis forces; studies suggest  $\Lambda \approx 1$  in the core (see e.g., Stevenson, 2003; King et al., 2010). The small magnitudes of the Rossby and Ekman numbers suggest that inertia and viscosity are small on the global scale of the core, whereas  $\Lambda \approx 1$  suggests that the Lorentz force and Coriolis force are comparable in magnitude. However, these estimates must be interpreted carefully as it is unclear what scales of motion are observed in secular variation studies. Numerical dynamo simulations cannot reach the Ekman number of the core due to computational restrictions. Nevertheless, simulations can reproduce some key features of the geomagnetic field while also obtaining an Elsasser number of order unity.

The small values of the Rossby and Ekman numbers indicate further that the Earth is rapidly rotating. Spatial scale separation is an intrinsic property of rapidly rotating flows, where perturbation theory has been used successfully to describe the linear dynamics of spherical convection

(Roberts, 1968; Busse, 1970; Soward, 1977; Jones et al., 2000; Dormy et al., 2004). These tools have been applied to both the linear (Chandrasekhar, 1961) and nonlinear dynamics (Julien et al., 1998) of the plane layer geometry in the asymptotic limit of small Ekman number. The plane layer theory is significantly simpler in comparison to the spherical theory primarily due to the fact that only two scales (the depth  $D$ , and the small  $DEk^{1/3}$  convective length scale) are present in the system. In contrast, the sphere contains a multitude of different length scales, including the system scale  $D$ , the convective radial envelope scale  $DEk^{1/6}$ , a length scale of radial waves  $DEk^{2/9}$ , and the convective length scale  $DEk^{1/3}$ . Linear and nonlinear asymptotic theories for the sphere must account for all of these scales. Here we attempt to use elements of asymptotic theory to explain the large-scale dynamics of rotating spherical dynamos. Understanding the asymptotic behavior of this system is important for comparing modeling results to natural systems such as the Earth's core.

When effects due to inertia and viscosity are small, such as small Rossby and Ekman number regimes, Taylor (1963) showed that the component of the Lorentz torque aligned along the rotation axis must vanish. This condition is now referred to as ‘Taylor’s constraint’ and is expressed mathematically as

$$\int \hat{\phi} \cdot (\overline{\mathbf{J} \times \mathbf{B}}) dz = 0. \quad (3.1)$$

where  $\hat{\phi} \cdot (\overline{\mathbf{J} \times \mathbf{B}})$  is the zonal component of the Lorentz force and  $z$  is the cylindrical coordinate aligned along the rotation axis. Flows that obey this constraint are said to be in a ‘Taylor state’. Since real fluids experience both viscous and ohmic dissipation, and undergo acceleration, Taylor’s constraint is expected to be satisfied only in an approximate sense. Deviations from a Taylor state lead to a form of axisymmetric Alfvén waves known as torsional oscillations (Braginsky, 1976). The original analysis of Braginsky (1976) neglected the influence of buoyancy. Here we show that its inclusion is crucial to the torsional dynamics and indicates that axially-invariant torsional oscillations are but a single component of richer dynamics. We note that whereas Roberts and Wu (2014) develop what they consider a ‘modified Taylor constraint’ that includes inertia, here we

argue from the viewpoint of perturbation theory that Taylor's (original) constraint is satisfied at leading asymptotic order; and inertia, along with all other terms, enters the dynamics at higher order.

Recent studies have been devoted to finding exact Taylor states (see e.g., Livermore et al., 2016; Hardy et al., 2018; Li et al., 2018). Recent investigations have used a mean-field electrodynamics approach to produce kinematic dynamos that satisfy leading-order magnetostrophic balance (Wu and Roberts, 2015; Li et al., 2018). However, numerical dynamo simulations do not observe a leading-order magnetostrophic balance (Yadav et al., 2016; Aubert et al., 2017). One argument is that such simulations are dominated by viscosity, and the simulated dynamics therefore are in a parameter regime that is not representative of the geodynamo (Hardy et al., 2018). However, the available data does not support this view in the sense that simulations do not show any sudden changes in dynamical behavior as the Ekman number is reduced. This asymptotically ‘smooth’ behavior is confirmed in the present work and argued from an asymptotics standpoint.

There is strong evidence that axially-invariant torsional oscillations appear to be present in geomagnetic field observations, and have been observed in numerical simulations (e.g., Gillet et al., 2010; Roberts and Aurnou, 2012; Schaeffer et al., 2017). Not surprisingly, their amplitude is larger when viscous effects are weaker, and more recent simulations using smaller values of the Ekman number therefore observe clearer torsional oscillation signals (Schaeffer et al., 2017). The work of Wicht and Christensen (2010) examined how the relative sizes of the forces in numerical dynamo simulations affect torsional oscillations. In particular, by decomposing the velocity field into toroidal and poloidal components, (Wicht and Christensen, 2010) find that the toroidal balance is dominated by the Lorentz and Coriolis forces, but this component is much weaker than the forces present in the poloidal balance. Here, we provide an argument for why this ordering occurs and, crucially, tie it to Taylor's constraint.

Although several recent numerical studies have analyzed the force balances observed in numerical dynamo simulations (e.g., Soderlund et al., 2012; Yadav et al., 2016; Aubert et al., 2017; Schaeffer et al., 2017), the majority of these investigations have focused on the small-scale force

balances. There is consensus among these studies that the small-scale force balance is characterized by a leading order geostrophic force balance, and a secondary (i.e., higher order) magnetostrophic balance. In contrast, Aubert (2005) showed that the large-scale dynamics observed in dynamo simulations are well-described by a thermal wind balance in meridional planes, whereas the azimuthal force balance is dominated by a balance between the mean Coriolis force and the mean Lorentz force. Recent work has confirmed that this azimuthal force balance persists at lower Ekman numbers and is nearly scale independent (Yadav et al., 2016; Schaeffer et al., 2017).

Our primary goal with the present work is to investigate further these observations by applying ideas from asymptotic theory and showing that the force balances are directionally distinct. The results suggest that rapidly rotating spherical dynamos satisfy Taylor's constraint up to order  $\mathcal{O}(\text{Ek}^{1/6})$ , despite not being characterized by a magnetostrophic balance. We also highlight that this balance is consistent with the so-called Malkus-Proctor scenario (Malkus and Proctor, 1975) in which a large-scale magnetic field is saturated by the generation of a large-scale flow. However, we emphasize that this large-scale flow consists of the mean meridional overturning motions, or meridional circulation. Thus, we believe that the present work offers additional physical insight into large-scale magnetic field generation in systems driven by rapidly rotating convection.

### 3.2 Methods

The work discussed in this chapter solves the equations previously described in Section 1.2.1, specifically the Boussinesq approximation from Section 1.2.1.2 including effects due to rotation and magnetic fields. The equations are nondimensionalized with the large-scale viscous diffusion time  $D^2/\nu$  (where  $D = r_o - r_i$  is the shell thickness), the dimensional temperature contrast between the inner and outer radii,  $\Delta\tilde{T} = \tilde{T}(r_i) - \tilde{T}(r_o)$ , the pressure scale  $\rho\nu\Omega$ , and the magnetic field is scaled with  $\sqrt{\mu_0\rho\eta\Omega}$ . The aspect ratio is defined to be  $\chi = r_i/r_o$ . The nondimensional equations appear as

$$\frac{\partial \mathbf{u}}{\partial t} + \mathbf{u} \cdot \nabla \mathbf{u} = -\frac{1}{\text{Ek}} \nabla P + \frac{\text{Ra}}{\text{Pr}} T \frac{\mathbf{r}}{r_o} + \nabla^2 \mathbf{u} + \frac{1}{\text{PmEk}} \mathbf{J} \times \mathbf{B} + \frac{2}{\text{Ek}} \mathbf{u} \times \hat{\mathbf{z}}, \quad (3.2)$$

$$\frac{\partial T}{\partial t} + \mathbf{u} \cdot \nabla T = \frac{1}{\text{Pr}} \nabla^2 T, \quad (3.3)$$

$$\frac{\partial \mathbf{B}}{\partial t} = \nabla \times (\mathbf{u} \times \mathbf{B}) + \frac{1}{\text{Pm}} \nabla^2 \mathbf{B}, \quad (3.4)$$

$$\nabla \cdot \mathbf{u} = 0, \quad (3.5)$$

$$\nabla \cdot \mathbf{B} = 0, \quad (3.6)$$

and are numerically solved using the ideas of Section 1.3.

We fix the aspect ratio at  $\chi = 0.35$  and use a Prandtl number of unity. The magnetic Prandtl number, the Ekman number, and the Rayleigh number are all varied. The total nondimensional simulation time used in any given simulation generally decreases with the Ekman number due to computational constraints. For the highest Ekman number cases with  $\text{Ek} = 10^{-4}$ , up to 100 magnetic diffusion times were simulated, whereas up to 0.4 magnetic diffusion times were simulated for cases that used  $\text{Ek} = 3 \times 10^{-6}$ . Table 3.1 shows a summary of the input parameters and selected measured output quantities (defined in Appendix A).

The majority of the simulations are initialized with random noise perturbations to the temperature and random noise to the magnetic field; the most extreme cases were initialized from previous dynamo simulations. Simulations with the highest Ekman  $\text{Ek} = 10^{-4}$  and a Rayleigh number of  $\text{Ra} \leq 30 \text{ Ra}_{\text{crit}}$  were started with random noise. Higher supercriticality runs were initialized from lower Rayleigh number cases with the same magnetic Prandtl number. Similarly, the  $\text{Ek} = 3 \times 10^{-5}$  runs were initialized from noise if  $\text{Ra} \lesssim 25 \text{ Ra}_{\text{crit}}$ . Only the first two  $\text{Ek} = 10^{-5}$  cases were initialized with random perturbations. All simulations with  $\text{Ek} = 3 \times 10^{-6}$  were restarted from cases that originally used  $\text{Ek} = 10^{-5}$ .

Table 3.1: Various input and output quantities for each numerical simulation. The first 5 columns give the input quantities; the Ekman number  $\text{Ek}$ , the magnetic Prandtl number  $\text{Pm}$ , the Rayleigh number  $\text{Ra}$ , the radial resolution  $n_r$ , the angular resolution given as the maximum spherical harmonic order  $\ell_{\max}$ . The remaining columns give the output quantities; the magnetic Reynolds number  $\text{Rm}$ , the bulk Rossby number  $\text{Ro}$ , the mean harmonic degree  $\bar{\ell}_p$ , the local Rossby number  $\text{Ro}_\ell$ , the dipolarity  $f_{\text{dip}}$  (using the full magnetic field restricted to  $\ell \leq 13$ ), the Nusselt number  $\text{Nu}$ , the Taylor microscale of the velocity, and the Taylor microscale of the magnetic field (see Appendix A for definitions of the various output quantities).

$\text{Ek}$	$\text{Pm}$	$\text{Ra}$	$n_r$	$\ell_{\max}$	$\text{Rm}$	$\text{Ro}$	$\bar{\ell}_p$	$\text{Ro}_\ell$	$f_{\text{dip}}$	$\text{Nu}$	$\ell'_u$	$\ell'_B$
$10^{-4}$	2	$4.20 \times 10^6$	64	127	106.068	$5.303 \times 10^{-3}$	13.280	$2.242 \times 10^{-2}$	0.675	2.102	0.072	0.065
$10^{-4}$	2	$7.00 \times 10^6$	64	127	152.699	$7.635 \times 10^{-3}$	16.860	$4.097 \times 10^{-2}$	0.632	3.039	0.056	0.057
$10^{-4}$	2	$1.05 \times 10^7$	64	127	228.753	$1.144 \times 10^{-2}$	19.311	$7.031 \times 10^{-2}$	0.585	4.332	0.049	0.045
$10^{-4}$	2	$1.40 \times 10^7$	72	159	302.902	$1.515 \times 10^{-2}$	19.748	$9.520 \times 10^{-2}$	0.576	5.185	0.048	0.039
$10^{-4}$	2	$2.10 \times 10^7$	92	199	536.589	$2.683 \times 10^{-2}$	20.060	$1.713 \times 10^{-1}$	0.133	7.159	0.045	0.025
$10^{-4}$	2	$2.80 \times 10^7$	96	215	630.677	$3.153 \times 10^{-2}$	20.308	$2.038 \times 10^{-1}$	0.181	8.456	0.043	0.024
$10^{-4}$	2	$3.50 \times 10^7$	128	255	676.616	$3.383 \times 10^{-2}$	21.679	$2.334 \times 10^{-1}$	0.139	9.783	0.041	0.022
$10^{-4}$	3	$3.50 \times 10^6$	64	127	124.309	$4.144 \times 10^{-3}$	12.674	$1.672 \times 10^{-2}$	0.616	1.894	0.073	0.063
$10^{-4}$	3	$7.00 \times 10^6$	64	127	229.975	$7.666 \times 10^{-3}$	16.924	$4.130 \times 10^{-2}$	0.504	3.382	0.054	0.049

*Continued on next page*

Table 3.1 – *Continued from previous page*

$E_k$	$P_m$	$R_a$	$n_r$	$\ell_{\max}$	$R_m$	$Ro$	$\bar{\ell}_p$	$Ro_\ell$	$f_{\text{dip}}$	$Nu$	$\ell'_u$	$\ell'_B$
$10^{-4}$	3	$1.05 \times 10^7$	64	127	344.312	$1.148 \times 10^{-2}$	18.715	$6.837 \times 10^{-2}$	0.470	4.593	0.049	0.040
$10^{-4}$	3	$1.40 \times 10^7$	72	159	450.617	$1.502 \times 10^{-2}$	19.795	$9.464 \times 10^{-2}$	0.517	5.064	0.046	0.033
$10^{-4}$	3	$2.10 \times 10^7$	84	179	625.060	$2.084 \times 10^{-2}$	20.571	$1.364 \times 10^{-1}$	0.416	6.822	0.043	0.028
$10^{-4}$	5	$3.50 \times 10^6$	64	143	190.295	$3.806 \times 10^{-3}$	13.258	$1.606 \times 10^{-2}$	0.647	2.146	0.065	0.056
$10^{-4}$	5	$7.00 \times 10^6$	64	143	387.446	$7.749 \times 10^{-3}$	16.564	$4.086 \times 10^{-2}$	0.448	3.260	0.053	0.043
$10^{-4}$	5	$1.05 \times 10^7$	64	143	529.593	$1.059 \times 10^{-2}$	18.210	$6.139 \times 10^{-2}$	0.480	4.369	0.046	0.036
$10^{-4}$	5	$1.40 \times 10^7$	84	179	727.794	$1.456 \times 10^{-2}$	20.221	$9.369 \times 10^{-2}$	0.440	5.586	0.044	0.029
$10^{-4}$	5	$2.10 \times 10^7$	92	199	1031.816	$2.064 \times 10^{-2}$	19.777	$1.299 \times 10^{-1}$	0.386	6.891	0.042	0.023
$10^{-4}$	10	$1.40 \times 10^7$	96	215	1314.482	$1.314 \times 10^{-2}$	18.845	$7.885 \times 10^{-2}$	0.355	5.152	0.041	0.025
$10^{-4}$	10	$2.10 \times 10^7$	128	239	1881.839	$1.882 \times 10^{-2}$	19.206	$1.150 \times 10^{-1}$	0.337	6.374	0.039	0.021
$3 \times 10^{-5}$	2	$1.42 \times 10^7$	84	239	113.681	$1.705 \times 10^{-3}$	17.825	$9.675 \times 10^{-3}$	0.689	1.544	0.055	0.048
$3 \times 10^{-5}$	2	$2.83 \times 10^7$	92	239	191.783	$2.877 \times 10^{-3}$	21.117	$1.934 \times 10^{-2}$	0.693	3.500	0.043	0.048
$3 \times 10^{-5}$	2	$4.25 \times 10^7$	92	239	313.915	$4.709 \times 10^{-3}$	23.927	$3.586 \times 10^{-2}$	0.620	4.928	0.038	0.039
$3 \times 10^{-5}$	2	$5.67 \times 10^7$	92	239	422.756	$6.341 \times 10^{-3}$	25.751	$5.198 \times 10^{-2}$	0.599	6.352	0.035	0.032
$3 \times 10^{-5}$	2	$7.08 \times 10^7$	128	255	474.392	$7.116 \times 10^{-3}$	26.665	$6.040 \times 10^{-2}$	0.601	6.688	0.033	0.032
$3 \times 10^{-5}$	2	$9.92 \times 10^7$	128	323	672.669	$1.009 \times 10^{-2}$	29.832	$9.581 \times 10^{-2}$	0.567	9.350	0.030	0.025

*Continued on next page*

Table 3.1 – *Continued from previous page*

$E_k$	Pm	Ra	$n_r$	$\ell_{\max}$	Rm	Ro	$\bar{\ell}_p$	$\text{Ro}_\ell$	$f_{\text{dip}}$	Nu	$\ell'_u$	$\ell'_B$
$3 \times 10^{-5}$	2	$1.27 \times 10^8$	128	323	832.567	$1.249 \times 10^{-2}$	30.539	$1.214 \times 10^{-1}$	0.534	10.911	0.028	0.021
$3 \times 10^{-5}$	2	$1.56 \times 10^8$	128	359	997.755	$1.497 \times 10^{-2}$	30.202	$1.439 \times 10^{-1}$	0.546	12.591	0.027	0.019
$10^{-5}$	2	$7.00 \times 10^7$	96	255	187.228	$9.361 \times 10^{-4}$	24.261	$7.229 \times 10^{-3}$	0.715	2.281	0.040	0.042
$10^{-5}$	2	$8.00 \times 10^7$	96	255	204.217	$1.021 \times 10^{-3}$	25.046	$8.141 \times 10^{-3}$	0.700	2.513	0.038	0.040
$10^{-5}$	2	$1.00 \times 10^8$	96	287	240.137	$1.201 \times 10^{-3}$	24.822	$9.487 \times 10^{-3}$	0.659	3.892	0.033	0.044
$10^{-5}$	2	$1.20 \times 10^8$	96	287	257.756	$1.289 \times 10^{-3}$	23.650	$9.702 \times 10^{-3}$	0.622	4.208	0.033	0.047
$10^{-5}$	2	$1.50 \times 10^8$	96	287	349.233	$1.746 \times 10^{-3}$	28.677	$1.594 \times 10^{-2}$	0.641	5.346	0.030	0.036
$10^{-5}$	2	$2.00 \times 10^8$	128	359	460.731	$2.304 \times 10^{-3}$	32.800	$2.405 \times 10^{-2}$	0.640	6.833	0.027	0.031
$3 \times 10^{-6}$	2	$1.84 \times 10^8$	128	323	189.189	$2.838 \times 10^{-4}$	31.186	$2.817 \times 10^{-3}$	0.338	1.949	0.032	0.042
$3 \times 10^{-6}$	2	$2.30 \times 10^8$	140	359	210.503	$3.158 \times 10^{-4}$	32.082	$3.224 \times 10^{-3}$	0.650	2.017	0.030	0.034
$3 \times 10^{-6}$	2	$3.21 \times 10^8$	140	359	288.910	$4.334 \times 10^{-4}$	33.737	$4.654 \times 10^{-3}$	0.651	3.100	0.028	0.031
$3 \times 10^{-6}$	2	$4.59 \times 10^8$	140	383	314.152	$4.712 \times 10^{-4}$	30.756	$4.613 \times 10^{-3}$	0.575	4.404	0.026	0.039
$3 \times 10^{-6}$	2	$6.89 \times 10^8$	144	399	498.131	$7.472 \times 10^{-4}$	36.728	$8.735 \times 10^{-3}$	0.599	6.462	0.022	0.031
$3 \times 10^{-6}$	2	$9.18 \times 10^8$	144	431	726.041	$1.089 \times 10^{-3}$	40.828	$1.415 \times 10^{-2}$	0.493	9.434	0.019	0.025

### 3.3 Asymptotic Scaling Behavior

Previous numerical studies have shown that the large-scale force balance in rapidly rotating spherical dynamos consists of a thermal-wind balance in the meridional plane described by the  $\hat{\mathbf{r}}$  and  $\hat{\theta}$  components of the thermal wind equation

$$\frac{2}{\text{Ek}} \hat{\mathbf{z}} \times \bar{\mathbf{u}} \approx -\frac{1}{\text{Ek}} \nabla \bar{P} + \frac{\text{Ra}}{\text{Pr}} \bar{T} \frac{\mathbf{r}}{r_o}, \quad (3.7)$$

and a mean Coriolis-Lorentz force balance in the zonal (longitudinal,  $\phi$ ) direction (e.g., Aubert, 2005),

$$\frac{2}{\text{Ek}} \bar{u}_s \approx \frac{1}{\text{EkPm}} (\bar{\mathbf{J}} \times \bar{\mathbf{B}}) \cdot \hat{\phi}, \quad (3.8)$$

where the cylindrical radial component of the mean velocity is  $\bar{u}_s \equiv \bar{u}_r \sin \theta + \bar{u}_\theta \cos \theta$ . As the Lorentz force only enters a single component of the leading-order force balance, we refer to this force balance as semi-magnetostrophic (MS). Under the semi-MS force balance we wish to know the asymptotic size of each term. This process constitutes one of the main differences between this work and that of Taylor (1963) where the asymptotic scaling was not discussed. The small magnitude of the Ekman number suggests that the Coriolis force controls the dynamics of rapidly rotating systems. Therefore we choose our small parameter as

$$\varepsilon \equiv \text{Ek}^{1/3}. \quad (3.9)$$

Convection only takes place when the Rayleigh number exceeds a critical value,  $\text{Ra}_{\text{crit}}$ , which scales as  $\text{Ra}_{\text{crit}} = \mathcal{O}(\varepsilon^{-4})$  (Chandrasekhar, 1961; Roberts, 1968; Busse, 1970). The critical values that were used throughout this work are shown in Table 3.2. We use a reduced Rayleigh number (see e.g., Jones et al., 2000) defined as

$$\widetilde{\text{Ra}} \equiv \varepsilon^4 \text{Ra} = \mathcal{O}(1). \quad (3.10)$$

The assumption on the scaling of the Rayleigh number is valid so long as the dynamo is driven by rapidly rotating convection. This assumption is automatically satisfied in any small-Ekman number dynamo simulation that has a supercritical Rayleigh number. All other nondimensional parameters

Table 3.2: Critical Rayleigh numbers,  $\text{Ra}_{\text{crit}}$ , and the critical azimuthal wavenumber,  $m_{\text{crit}}$ , used throughout this work. These apply for simulations with  $\text{Pr} = 1$  and no-slip boundary conditions (Christensen and Aubert, 2006).

Ek	Ra <sub>crit</sub>	m <sub>crit</sub>
$10^{-4}$	$6.965 \times 10^5$	8
$3 \times 10^{-5}$	$2.833 \times 10^6$	11
$10^{-5}$	$1.057 \times 10^7$	15
$3 \times 10^{-6}$	$4.591 \times 10^5$	22

are assumed to be order one in the sense that they do not scale with the Ekman number. The influence of small values of  $\text{Pm}$  is beyond the scope of the present work since the present work is focused on regimes of  $\text{Pm}$  that are currently accessible to numerical simulations.

With the above definitions, the mean buoyancy force can be written as

$$\bar{\mathbf{F}}_b = \varepsilon^{-4} \frac{\widetilde{\text{Ra}}}{\text{Pr}} \frac{\mathbf{r}}{r_o} \bar{T}. \quad (3.11)$$

The geometric factor  $r/r_o = \mathcal{O}(1)$ , and given that the mean temperature should not depend on Ekman, we have

$$\bar{T} = \mathcal{O}(1) \quad \Rightarrow \quad |\bar{\mathbf{F}}_b| = \mathcal{O}(\varepsilon^{-4}). \quad (3.12)$$

The mean Coriolis force is given by

$$\bar{\mathbf{F}}_c = \begin{pmatrix} \bar{F}_{c,r} \\ \bar{F}_{c,\theta} \\ \bar{F}_{c,\phi} \end{pmatrix} = \frac{2}{\varepsilon^3} \begin{pmatrix} \bar{u}_\phi \sin \theta \\ \bar{u}_\phi \cos \theta \\ -\bar{u}_s \end{pmatrix}, \quad (3.13)$$

thus the meridional components scale as  $\mathcal{O}(\varepsilon^{-3} \bar{u}_\phi)$  and the zonal component scales as  $\mathcal{O}(\varepsilon^{-3} \bar{u}_s)$ .

For the thermal wind balance to occur, the radial components must balance such that

$$\bar{F}_{b,r} \sim \bar{F}_{c,r} \quad \Rightarrow \quad \bar{u}_\phi = \mathcal{O}(\varepsilon^{-1}). \quad (3.14)$$

This suggests that the zonal flow becomes increasingly strong as the Ekman number is decreased. The scaling for the mean zonal flow is identical to the scaling of the small-scale velocity field in

rapidly rotating convection in both spherical and Cartesian geometries (Julien et al., 1998; Jones et al., 2000). The pressure gradient must also balance with the buoyancy force so that

$$\overline{F}_{p,r} \sim \overline{F}_{b,r} = \mathcal{O}(\varepsilon^{-4}). \quad (3.15)$$

The  $\theta$  component gives

$$\overline{F}_{p,\theta} \sim \overline{F}_{c,\theta} = \mathcal{O}(\varepsilon^{-4}). \quad (3.16)$$

The zonal force balance between the Coriolis and Lorentz forces requires

$$(\overline{\mathbf{J}} \times \overline{\mathbf{B}})_\phi = \mathcal{O}(\bar{u}_s), \quad (3.17)$$

where we assume that  $Pm = \mathcal{O}(1)$ . The induction equation is linear in the magnetic field indicating that the above zonal force balance provides a constraint on the size of the mean magnetic field, provided a constraint on the size of  $\bar{u}_s$  can be obtained. This is the first appearance of the mean Lorentz force (in terms of asymptotic size) in the governing equations, which suggests that these dynamos are saturated by the so-called Malkus-Proctor scenario (Malkus and Proctor, 1975): the mean magnetic field becomes saturated through the formation of a mean flow, in this case the meridional circulation.

From a dynamical perspective, we expect that the zonal flow is much stronger than the meridional circulation such that  $\mathcal{O}(\bar{u}_s) \ll \mathcal{O}(\bar{u}_\phi)$ . In the simulations discussed here the meridional circulation is roughly an order of magnitude smaller than the mean zonal flow. Therefore, we expect the meridional dynamics will be asymptotically decoupled from the mean zonal dynamics in the sense that the leading-order components of the forces will be of different asymptotic order. We note that the continuity equation provides no constraint on the size of  $\bar{u}_s$  since both components of the meridional circulation are assumed to scale with  $\varepsilon$  in the same manner and are assumed to vary on similar length scales.

A constraint on the scaling of the meridional circulation can be found by comparing the Lorentz force to the buoyancy force. First, we assume that the individual components of the

Lorentz force are of comparable size,

$$\overline{(\mathbf{J} \times \mathbf{B})}_r \approx \overline{(\mathbf{J} \times \mathbf{B})}_\theta \approx \overline{(\mathbf{J} \times \mathbf{B})}_\phi. \quad (3.18)$$

The numerical data discussed later supports the above relations. For the semi-MS force balance to occur, the Lorentz force must be weaker than the buoyancy force,

$$\frac{1}{PmEk} \overline{(\mathbf{J} \times \mathbf{B})}_r \ll \overline{F}_{b,r}, \quad \Rightarrow \quad \overline{(\mathbf{J} \times \mathbf{B})}_r = o(\varepsilon^{-1}), \quad (3.19)$$

where  $o(\cdot)$  indicates little-o notation. Little-o notation describes an upper bound, i.e.,  $f = o(g)$  indicates that  $f$  is asymptotically smaller than  $g$ . Since the Lorentz force components are all of comparable magnitude, the above constraint also can be written as

$$\overline{(\mathbf{J} \times \mathbf{B})}_\phi = o(\varepsilon^{-1}). \quad (3.20)$$

Then, using the Coriolis-Lorentz force balance in the zonal component of the mean momentum equation, we can place a constraint on the asymptotic size of the meridional circulation as

$$\overline{u}_s = o(\varepsilon^{-1}). \quad (3.21)$$

The numerical data supports a scaling of

$$\overline{u}_s = \mathcal{O}(\varepsilon^\gamma) \quad \gamma > -1. \quad (3.22)$$

We can attempt further to constrain the asymptotic size of the meridional circulation by examining the dominant balances in the mean temperature equation, rewritten here as

$$\partial_t \overline{T} + \overline{\mathbf{u}} \cdot \nabla \overline{T} + \nabla \cdot (\overline{\mathbf{u}' T'}) = \frac{1}{Pr} \nabla^2 \overline{T}. \quad (3.23)$$

In what follows we denote all mean length scales as  $\bar{l}$  and all fluctuating length scales as  $\ell'$ . A subscript is used to specify the quantity that a given length scale characterizes. We will assume that the del operator scales as  $\nabla = \mathcal{O}(\bar{l}_T^{-1})$  when applied to the convective heat flux and the mean temperature.

Balancing the convective heat flux and the large-scale thermal diffusion leads to

$$\nabla \cdot (\bar{\mathbf{u}}' \bar{T}') \sim \frac{1}{\text{Pr}} \nabla^2 \bar{T} \quad \Rightarrow \quad \bar{\ell}_T = \mathcal{O} \left( \frac{1}{u' T'} \right), \quad (3.24)$$

where we have assumed  $\text{Pr} = \mathcal{O}(1)$  and  $\bar{T} = \mathcal{O}(1)$ . An estimate for the scale of the fluctuating velocity can be found by assuming

$$u' = \mathcal{O}(\text{Re}), \quad (3.25)$$

since the velocity is scaled in the nondimensional large-scale Reynolds number units. The large-scale Reynolds number has an implicit dependence on  $\varepsilon$ , i.e.,

$$\text{Re} \equiv \frac{\mathcal{U}D}{\nu} = \frac{\mathcal{U}L}{\nu} \frac{D}{L} = \varepsilon^{-1} \text{Re}_L, \quad (3.26)$$

where  $\mathcal{U}$  is a characteristic velocity,  $L$  is a small-scale length, and the small-scale Reynolds number is  $\text{Re}_L = \mathcal{O}(1)$ . We also have assumed that the small-scale length is associated with the onset of convection and therefore scales as  $L/D \sim \text{Ek}^{1/3}$ . Equivalently, the above scaling for the fluctuating velocity can be found by enforcing geostrophic balance on the small scale motions. These relationships indicate that the fluctuating velocity is expected to scale as

$$u' = \mathcal{O}(\varepsilon^{-1}). \quad (3.27)$$

The above scaling is well supported by the numerical data presented later. Using this scaling for the fluctuating velocity then leads to

$$\bar{\ell}_T = \mathcal{O} \left( \frac{\varepsilon}{T'} \right). \quad (3.28)$$

Similarly, if we balance the advection by the mean flow with mean diffusion we obtain

$$\bar{\mathbf{u}} \cdot \nabla \bar{T} \sim \frac{1}{\text{Pr}} \nabla^2 \bar{T} \quad \Rightarrow \quad \bar{u}_s = \mathcal{O} \left( \frac{1}{\bar{\ell}_T} \right). \quad (3.29)$$

Finally, we note that combining the scalings for  $\bar{u}_s$  and  $\bar{\ell}_T$  relates the fluctuating temperature to the meridional circulation

$$T' = \mathcal{O}(\varepsilon \bar{u}_s). \quad (3.30)$$

There is some evidence in the numerical data to support the above scaling. Plane layer theory produces  $T' = \mathcal{O}(\varepsilon)$  (Julien et al., 1998). The numerical data does not support such a strong scaling of the fluctuating temperature with  $\varepsilon$  in the sphere; this point is discussed more later.

One possible scaling for  $\bar{\ell}_T$  is the ‘convective envelope’ scale that varies like  $\text{Ek}^{1/6} = \varepsilon^{1/2}$  (Jones et al., 2000). We find a posteriori that this scale is roughly consistent with the numerical data. Thus, the following asymptotic estimates are obtained

$$\nabla^2 \bar{T} = \mathcal{O}(\varepsilon^{-1}), \quad (3.31)$$

$$\bar{\mathbf{u}} \cdot \nabla \bar{T} = \mathcal{O}(\bar{u}_s \varepsilon^{-1/2}). \quad (3.32)$$

We therefore have the estimates

$$\bar{u}_s = \mathcal{O}(\varepsilon^{-1/2}), \quad (3.33)$$

and

$$T' = \mathcal{O}(\varepsilon^{1/2}). \quad (3.34)$$

With an estimate for the scaling of  $\bar{u}_s$ , the Lorentz-Coriolis balance in the zonal momentum equation now suggests

$$(\overline{\mathbf{J} \times \mathbf{B}})_\phi = \mathcal{O}\left(\frac{1}{\bar{\ell}_T}\right). \quad (3.35)$$

The zonal component of the mean Lorentz force contains only magnetic tension since the averaging removes the magnetic pressure gradient. The magnetic tension term can be split further into two terms, the mean-mean and eddy-eddy contributions. Since the derivatives appearing in those terms act on mean magnetic quantities, we scale them as  $\nabla = \mathcal{O}(\bar{\ell}_B^{-1})$ . The Lorentz force terms then can be written as

$$(\overline{\mathbf{B} \cdot \nabla \mathbf{B}})_\phi = \mathcal{O}\left(\frac{\bar{B}^2}{\bar{\ell}_B}\right), \quad (3.36)$$

$$(\overline{\mathbf{B}' \cdot \nabla \mathbf{B}'})_\phi = \mathcal{O}\left(\frac{B'^2}{\bar{\ell}_B}\right). \quad (3.37)$$

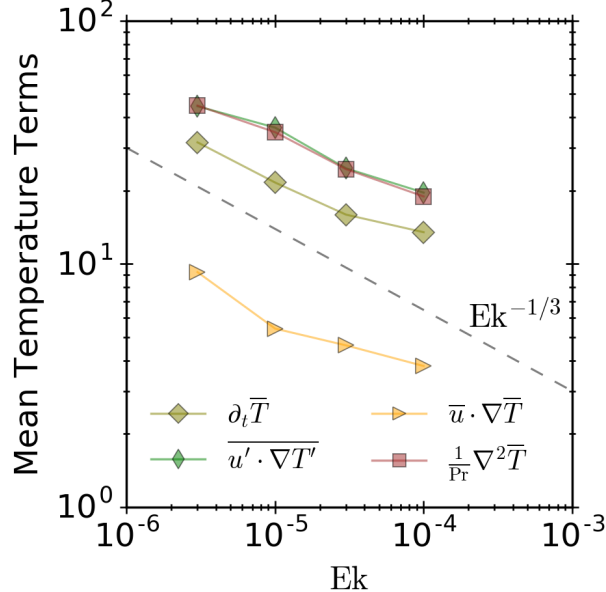


Figure 3.1: Scaling behavior of all terms in the mean heat equation. The rms value of each term is shown as a function of Ekman number with a fixed supercriticality  $\text{Ra} = 15 \text{ Ra}_{\text{crit}}$ .

Combining these with the scaling relation for the full mean zonal Lorentz force provides

$$\bar{B} = B' = \mathcal{O} \left( \frac{\bar{\ell}_B^{1/2}}{\bar{\ell}_T^{1/2}} \right). \quad (3.38)$$

In the next section we attempt to constrain the possible scalings with  $\varepsilon$  using data from numerical simulations.

### 3.4 Comparison with Numerical Simulations

In this section we make a direct comparison between the arguments presented in the previous section with data from numerical dynamo models. We begin with a discussion of the mean heat equation since it is a scalar equation and therefore characterized by the simplest behavior. We then discuss the terms appearing in the mean momentum equation.

#### 3.4.1 Mean Heat Equation

Figure 3.1 shows all terms in the mean heat equation as a function of Ekman number. For clarity, only the cases with  $\text{Ra} = 15 \text{ Ra}_{\text{crit}}$  are shown. One obvious trend is that all terms in the

equation increase in magnitude as the Ekman number is reduced for a fixed supercriticality. We also see that the convective heat flux is balanced with large-scale thermal diffusion. The time derivative is smaller than both the convective heat flux and thermal diffusion by a factor of  $\approx 2/3$ . Finally, advection of heat by the mean flow is noticeably weaker than all of the other terms, and is a factor of  $\approx 1/5$  smaller than either the convective flux or thermal diffusion across all of the Ekman numbers investigated.

It is tempting to conclude that advection of heat by the mean flow is negligible in comparison to the convective flux and thermal diffusion. However, the advection due to the mean flow increases in magnitude with decreasing Ekman number. This suggests that it does have an Ekman number dependence. Thus, this dependence may still be used to constrain the size of the meridional circulation.

The time derivative of the mean temperature is smaller than both the convective heat flux and thermal diffusion, but appears to scale with the Ekman number in a similar way. Balancing the time derivative with either of these two terms provides an estimate for the mean thermal evolution time scale.

$$\partial_t \bar{T} = \mathcal{O}(\tau^{-1}) \sim \nabla^2 \bar{T} = \mathcal{O}(\varepsilon^{-1}). \quad (3.39)$$

This indicates that the mean thermal evolution time scale is  $\tau = \mathcal{O}(\varepsilon)$ .

Figure 3.2(a) shows the mean thermal diffusion length scale defined as

$$\bar{\ell}_T = \left( \frac{\langle \bar{T}^2 \rangle}{\langle |\nabla^2 \bar{T}|^2 \rangle} \right)^{1/4}, \quad (3.40)$$

where the angled brackets indicate a volume average. The Laplacian is used to calculate the length scale since it will naturally magnify small length scales. There is evidence that  $\bar{\ell}_T$  depends on Ek. We note that the computed values are not strongly influenced by the inclusion or exclusion of the Ekman layers in the volume average and that the presented results do not include the Ekman layer. The Ekman layer thickness was estimated to be  $\alpha \text{Ek}^{1/2}$ , where  $\alpha$  is a small parameter usually taken to be in the range of 1 to 5. With this assumption, the Ekman layer encompasses less than 3% of

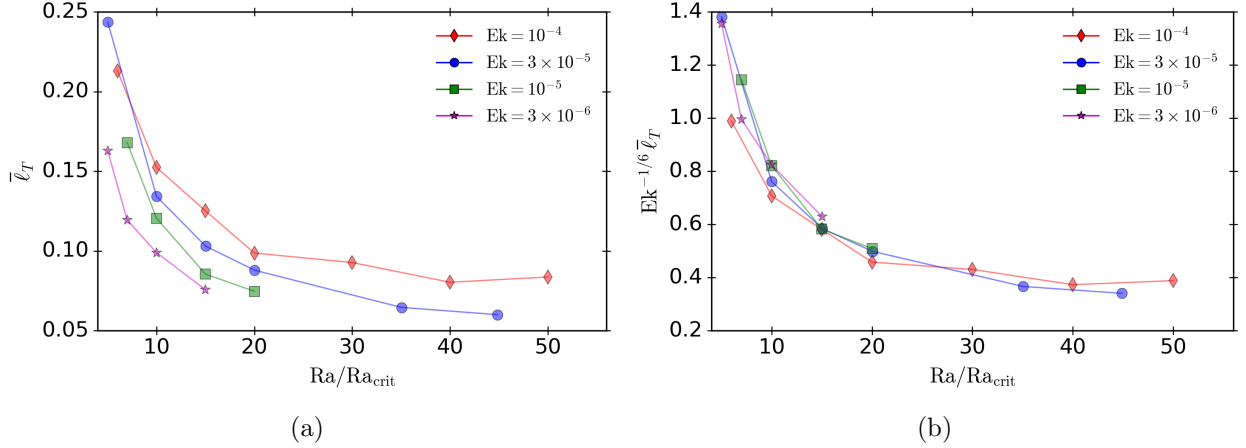


Figure 3.2: Diffusion-based length scale as a function of Rayleigh number for (a) the mean temperature, (b) rescaled by  $\text{Ek}^{-1/6}$ .

the domain shell depth. If the data are rescaled by  $\text{Ek}^{-1/6} = \varepsilon^{-1/2}$ , shown in Figure 3.2(b), there is a collapse of the data, indicating the following scaling

$$\bar{\ell}_T = \mathcal{O}\left(\varepsilon^{1/2}\right). \quad (3.41)$$

In addition to collapsing the data, the rescaling shown in Figure 3.2(b) shows that the rescaled mean thermal diffusion length scale is order unity, i.e.,  $\varepsilon^{-1/2} \bar{\ell}_T = \mathcal{O}(1)$ .

The meridional circulation was estimated by balancing the advection of heat due to the mean flow with the mean thermal diffusion. Figure 3.3(a) shows the meridional circulation as a function of supercriticality. There is a weak dependence on  $\text{Ek}$ . Figure 3.3(b) shows the meridional circulation rescaled by  $\text{Ek}^{1/6} = \varepsilon^{1/2}$ . The data shows a reasonable collapse indicating a scaling for the meridional circulation of

$$\bar{u}_s = \mathcal{O}\left(\varepsilon^{-1/2}\right), \quad (3.42)$$

in good agreement with the estimate from the previous section.

The fluctuating temperature scaling was estimated through a balance of the convective heat flux with the mean thermal diffusion. That estimate suggested a scaling of  $T' = \mathcal{O}(\varepsilon^{1/2})$ . Figure 3.4(a) shows the rms of the fluctuating temperature as a function of supercriticality. Figure 3.4(b) shows the rms fluctuating temperature as a function of radius computed as

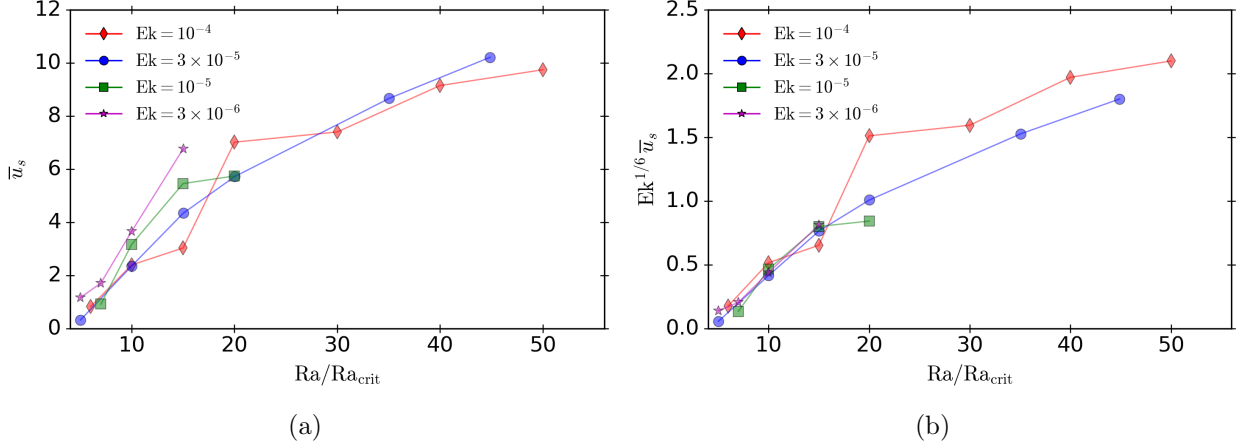


Figure 3.3: Scaling behavior of the cylindrical radial component of the mean velocity (i.e., the meridional circulation): (a) rms meridional circulation; (b) rescaled meridional circulation.

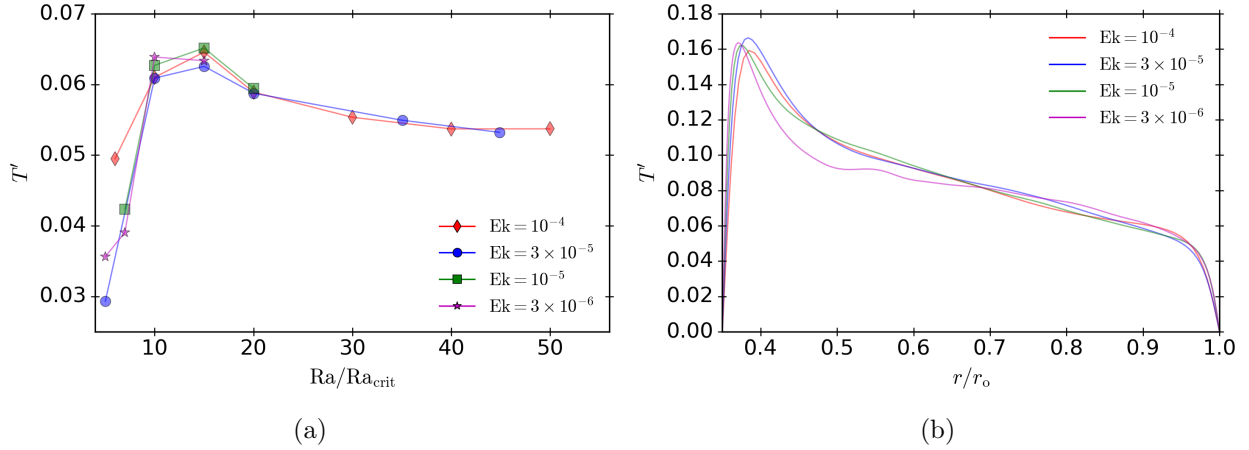


Figure 3.4: Scaling behavior of the fluctuating temperature: (a) rms of the fluctuating temperature as a function of Rayleigh number for all Ekman numbers; (b) radial profiles of the rms fluctuating temperature for all Ekman numbers with  $Ra = 15 Ra_{\text{crit}}$ . The fluctuating temperature appears to be  $\mathcal{O}(1)$ , showing no dependence on the Ekman number.

$$T'^{\text{rms}} = \left\{ \left( \frac{1}{4\pi} \int T'^2 \sin \theta d\theta d\phi \right)^{1/2} \right\}, \quad (3.43)$$

where the curly braces indicate an average in time. The radial profiles show no dependence on the Ekman number. The observed scaling behavior for the fluctuating temperature does not seem to match the expected scaling prediction. The reason for this is not known. One possible explanation is that the argument to determine the scaling for the meridional circulation invoked a balance between

the mean advection of heat and the mean thermal diffusion term. Figure 3.1 indicates that such a balance might be true in an asymptotic sense because both terms share a similar slope with  $\text{Ek}$ , but the dynamics are clearly a balance between the fluctuating heat flux and the diffusive term. Perhaps another balance should be invoked to determine the scaling of the meridional circulation. Another possible explanation could be that the previous analysis makes no use of the evolution equation for the fluctuating temperature. Perhaps more insight can be gained by including it during a future study.

### 3.4.2 Mean Momentum Equation

One of the first scalings that was predicted in the previous section was that the mean zonal velocity and the fluctuating velocity strongly scaled with Ekman number. The mean zonal velocity scaling came from assuming a thermal wind balance in the radial direction. The fluctuating velocity was assumed to scale with the large-scale Reynolds number, which contains an implicit dependence on Ekman number. These assumptions are verified in Figure 3.5, where we plot the fluctuating velocity as well as the mean zonal velocity. Figure 3.5(a) shows the fluctuating velocity and it is rescaled by  $\text{Ek}^{1/3}$  in Figure 3.5(c). The mean zonal velocity is shown in Figure 3.5(b) and rescaled in Figure 3.5(d). Both velocities increase as the Ekman number is lowered for any particular criticality. When the velocities are rescaled by  $\text{Ek}^{1/3}$ , the curves for separate cases with different  $\text{Ek}$  collapse onto a single curve, indicating the appropriate scaling has been applied.

We now turn our attention to estimating the scaling of the magnetic field. The previously obtained scaling relations for the magnetic field are

$$\bar{B} = B' = \mathcal{O} \left( \frac{\bar{\ell}_B^{1/2}}{\bar{\ell}_T^{1/2}} \right). \quad (3.44)$$

The data suggests that a good estimate for the scaling of the mean temperature length scale is  $\bar{\ell}_T = \mathcal{O}(\varepsilon^{1/2})$ . If we assume that  $\bar{\ell}_B = \mathcal{O}(\bar{\ell}_T)$  then

$$\bar{B} = B' = \mathcal{O}(1). \quad (3.45)$$

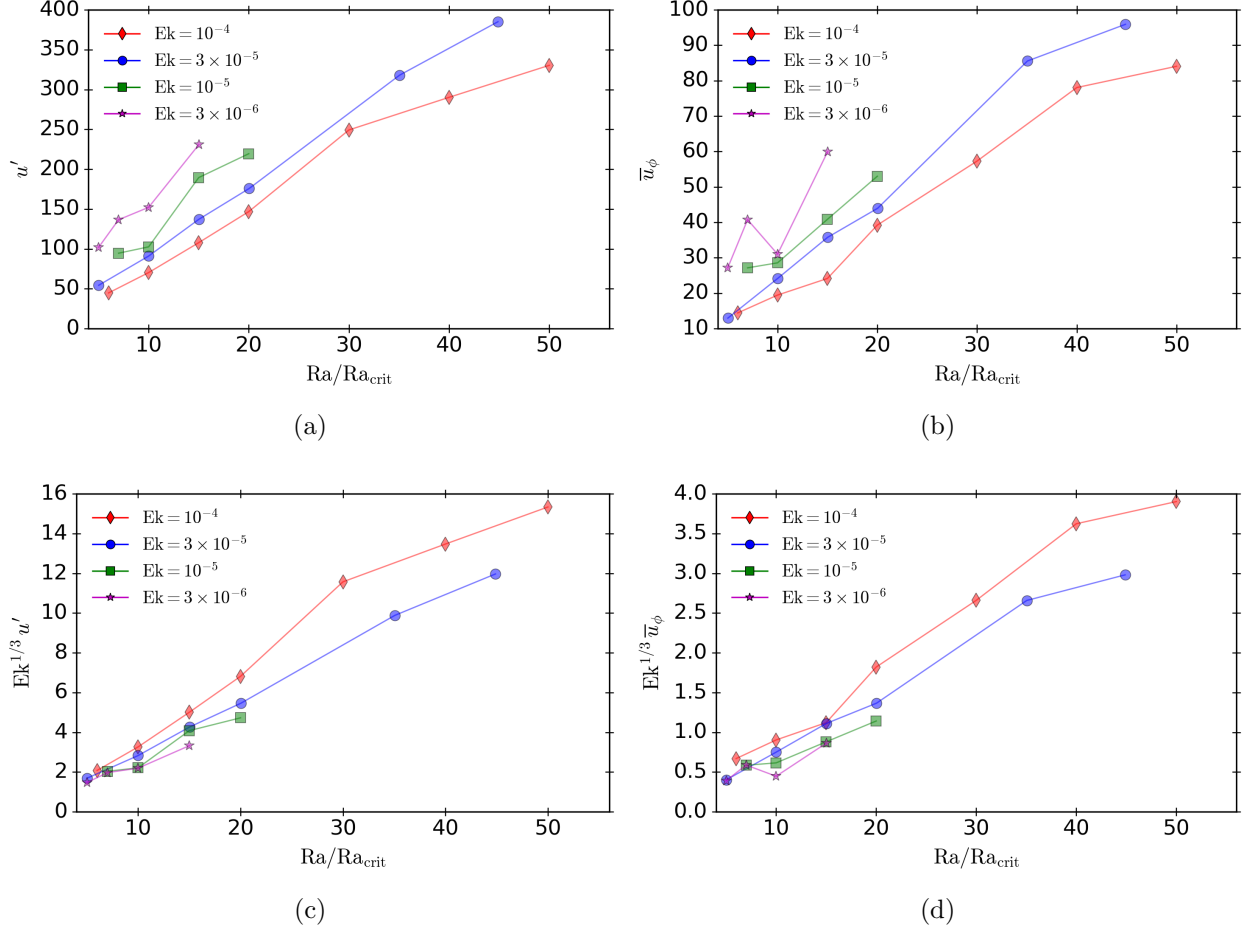


Figure 3.5: Scaling behavior of various flow speeds: (a) rms of the fluctuating velocity as a function of Rayleigh number; (b) rms of the mean zonal velocity as a function of Rayleigh number. Both speeds are rescaled by  $\text{Ek}^{1/3}$  in (c) and (d).

Figure 3.6 shows the scaling of both the mean and fluctuating magnetic fields as a function of the Rayleigh number. The mean magnetic field is plotted in Figure 3.6(a) and shows what appears to be  $\mathcal{O}(1)$  behavior, but there is still a weak variation with Ekman. Figure 3.6(c) shows the data after being rescaled by  $\text{Ek}^{1/9}$ . This scaling provides a slightly better collapse of the data indicating that the mean magnetic field scales as

$$\overline{B} = \mathcal{O}\left(\varepsilon^{-1/3}\right). \quad (3.46)$$

The fluctuating magnetic field is plotted in Figure 3.6(b) and shows a very clear trend with Ekman number. Figure 3.6(d) shows the data after being rescaled by  $\text{Ek}^{1/6}$ . This scaling provides a slightly

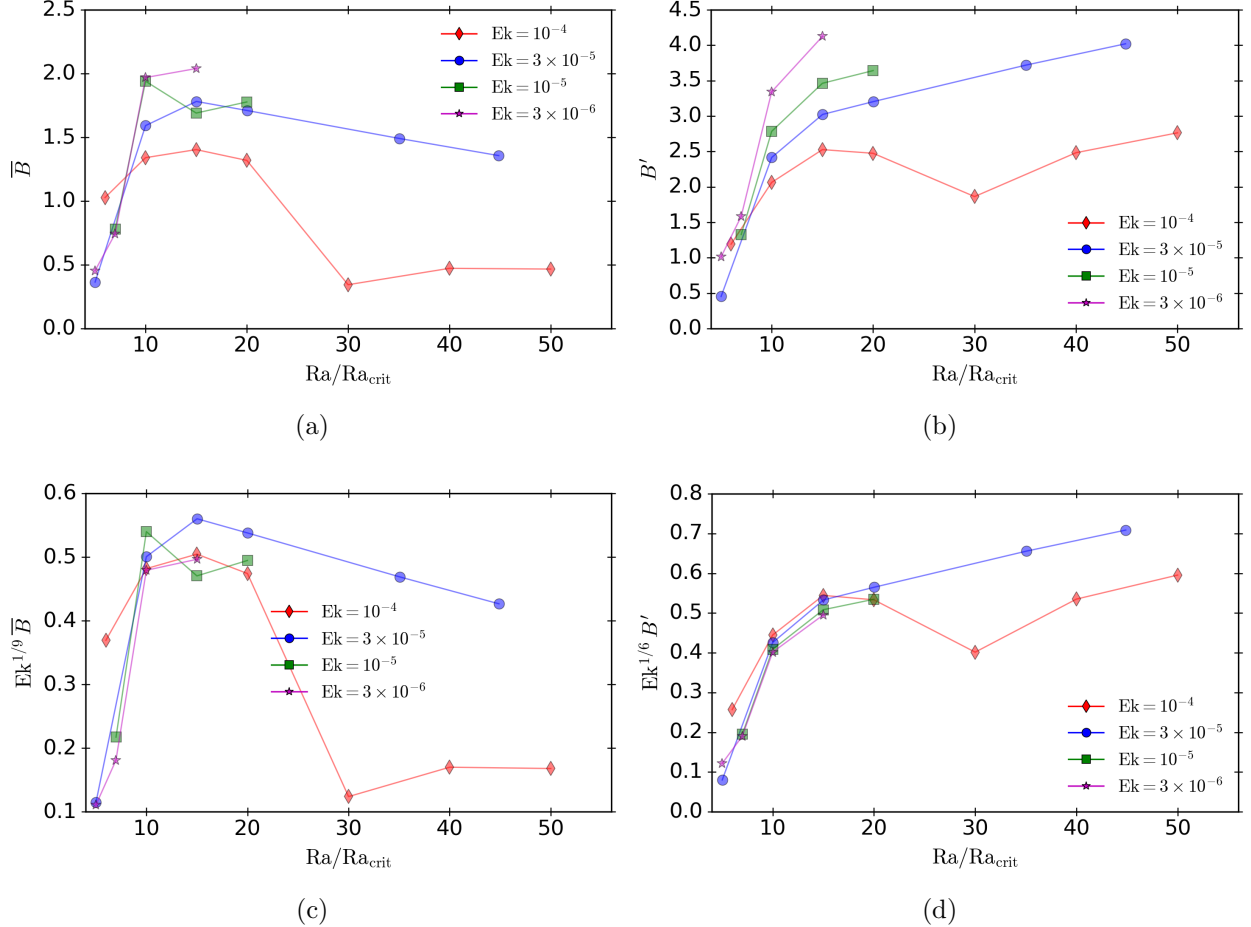


Figure 3.6: Scaling behavior of the mean and fluctuating magnetic field as a function of the Rayleigh number: (a) rms of the mean magnetic field; (b) rms of the fluctuating magnetic field; (c) rescaled mean magnetic field; (d) rescaled fluctuating magnetic field. The mean field shows a weak scaling with the Ekman number and appears to be  $\mathcal{O}(\text{Ek}^{-1/9})$ . The fluctuating magnetic field shows a more distinct dependence on the Ekman number, with a scaling of  $\mathcal{O}(\text{Ek}^{-1/6})$ .

better collapse of the data indicating that the fluctuating magnetic field scales as

$$B' = \mathcal{O}(\varepsilon^{-1/2}), \quad (3.47)$$

slightly stronger than the mean field. This scaling is different than that of the mean magnetic field, but the difference is very small over our investigated range of Ekman numbers. If the scalings are written in the form  $\text{Ek}^\gamma$ , the fluctuating magnetic field scaling is  $\gamma \approx -0.167$  and the mean magnetic field scaling is  $\gamma \approx -0.111$ .

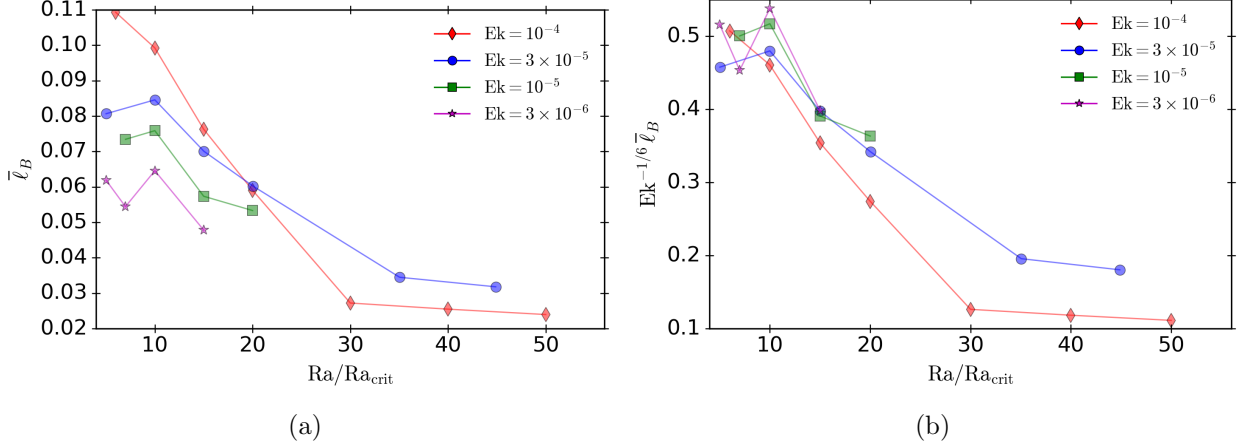


Figure 3.7: Diffusion-based length scales as a function of Rayleigh number for (a) the mean magnetic field (b) rescaled by  $Ek^{-1/6}$ .

The scaling behavior of the magnetic field depends on the scaling of the mean temperature length scale and an estimate for the length over which the mean magnetic field varies. Figure 3.7(a) shows the data for the mean magnetic field diffusive length scale as a function of Rayleigh number. Figure 3.7(b) shows the data rescaled by  $Ek^{-1/6}$ . There is good collapse indicating the scaling is indeed  $\bar{\ell}_B = \mathcal{O}(\varepsilon^{1/2})$ .

A summary of all the scaling relations that were determined from the data can be found in Table 3.3. The scaling model discussed in Section 3.3 accurately describes many of the quantities of interest. It is able to capture the correct scaling relations for the mean meridional circulation, the mean zonal velocity, and the fluctuating velocity. There are small discrepancies for the mean magnetic field. Larger differences occur for fluctuating magnetic field and fluctuating temperature. All of these discrepancies suggest that a more comprehensive model might be warranted in future work, e.g., one that includes the evolution equation for the fluctuating quantities.

### 3.5 Force Balances

Force balances, if present, are satisfied point-wise and instantaneously. Distinct balances can be present in different regions of the flow domain; for instance, within the Ekman layers near the

Table 3.3: Scaling relations for various quantities discussed in this section with a reference to the figure where it first appeared. Some results are discussed in Appendix C. Scalings that do not mention a figure location were not explicitly discussed, but are included just for reference.

Quantity (symbol)	Scaling	Figure	Description
$\bar{T}$	$\mathcal{O}(1)$	Figure C.1(a)	Mean temperature
$T'$	$\mathcal{O}(1)$	Figure 3.4(a)	Fluctuating temperature
$ \bar{\mathbf{B}} $	$\mathcal{O}(\varepsilon^{-1/3})$	Figure 3.6(a)	Mean magnetic field
$ \mathbf{B}' $	$\mathcal{O}(\varepsilon^{-1/2})$	Figure 3.6(b)	Fluctuating magnetic field
$ \mathbf{u}' $	$\mathcal{O}(\varepsilon^{-1})$	Figure 3.5(a)	Fluctuating velocity
$\bar{u}_\phi$	$\mathcal{O}(\varepsilon^{-1})$	Figure 3.5(b)	Mean zonal velocity
$\bar{u}_s$	$\mathcal{O}(\varepsilon^{-1/2})$	Figure 3.3	Mean meridional circulation
$\bar{\ell}_T$	$\mathcal{O}(\varepsilon^{1/2})$	Figure 3.2	Length scale for mean temperature
$\bar{\ell}_B$	$\mathcal{O}(\varepsilon^{1/2})$	Figure 3.7	Length scale for mean magnetic field
$\bar{\ell}_B$	$\mathcal{O}(1)$	-	Taylor microscale for $\bar{\mathbf{B}}$
$\ell'_B$	$\mathcal{O}(\varepsilon^{1/3})$	Figure C.3	Taylor microscale for $\mathbf{B}'$
$\bar{\ell}_u$	$\mathcal{O}(\varepsilon^{1/2})$	-	Taylor microscale for $\bar{\mathbf{u}}$
$\ell'_u$	$\mathcal{O}(\varepsilon^{2/3})$	Figure 3.15	Taylor microscale for $\mathbf{u}'$
$\bar{\ell}_u$	$\mathcal{O}(\varepsilon)$	-	Diffusion-based length scale for $\bar{\mathbf{u}}$
$\bar{\ell}_T$	$\mathcal{O}(1)$	Figure C.1(b)	Gradient length scale $\sim \bar{T}/ \nabla \bar{T} $
$\ell'_T$	$\mathcal{O}(1)$	-	Gradient length scale $\sim T'/ \nabla T' $
$\ell'_T$	$\mathcal{O}(\varepsilon^{1/3})$	-	Heat flux length scale $\sim \bar{u}'_r T' /  \mathbf{u}' \cdot \nabla T' $

inner and outer boundaries we expect different balances in comparison to the bulk. Schaeffer et al. (2017) have examined balances in the vorticity equation in five distinct regions. Other work has used global rms values of the forces that both include (Soderlund et al., 2012) and exclude the Ekman layers (Yadav et al., 2016), and Aubert et al. (2017) used a spectral decomposition of the forces. All results presented here do not include the Ekman layer when computing the global rms value. Here we extend these previous analyses to show how the large-scale balances are directionally distinct, and that such balances are perturbative. The numerical data is used to help constrain the ordering of the perturbative dynamics.

We introduce the following shorthand notation

$$\frac{\partial \bar{\mathbf{u}}}{\partial t} = \bar{\mathbf{F}}_a + \bar{\mathbf{F}}_c + \bar{\mathbf{F}}_p + \bar{\mathbf{F}}_b + \bar{\mathbf{F}}_l + \bar{\mathbf{F}}_v, \quad (3.48)$$

where the mean forces on the right-hand side are advection, Coriolis, pressure gradient, buoyancy,

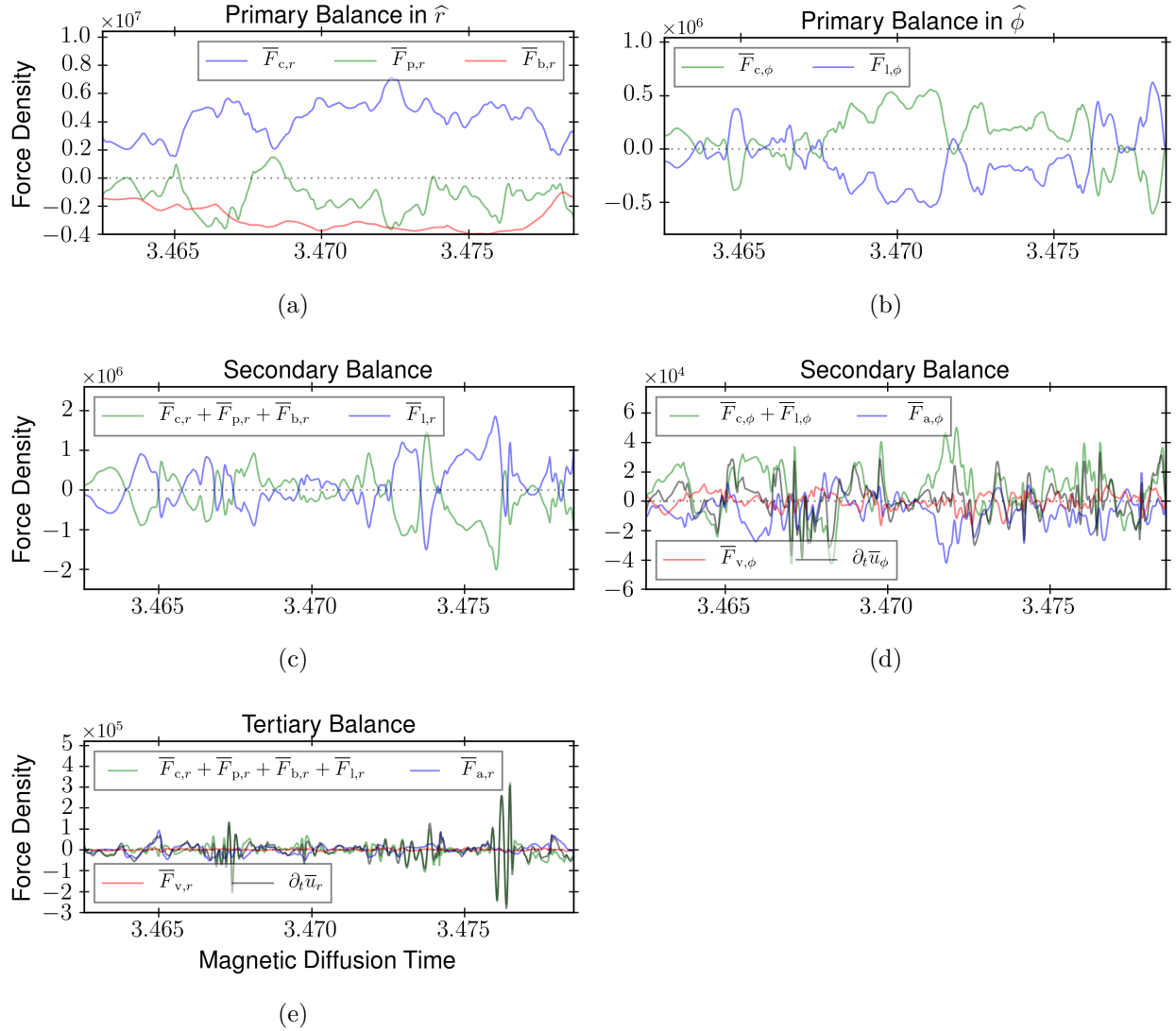


Figure 3.8: Point-wise measurements of forces (as a function of time) in the mean momentum equation at the point  $(r, \theta) = (0.74 r_o, 40^\circ)$ . The parameters are  $\text{Ek} = 10^{-5}$ ,  $\text{Ra} = 10 \text{Ra}_{\text{crit}}$ . The left column shows the radial direction and the right column shows the zonal direction. The top row shows the primary force balance and higher order balances are shown in the subsequent rows. The dotted black line indicates zero.

Lorentz, and viscous, respectively.

Figure 3.8 shows the numerically computed forces for the particular case with  $\text{Ek} = 10^{-5}$ ,  $\text{Ra} = 10 \text{Ra}_{\text{crit}}$ . All other small Rossby number cases show qualitatively similar behavior. The figure shows the mean forces extracted at a particular point in space and plotted as a function of time. The spatial location is chosen to be  $r = 0.74 r_o$  and a latitude of  $40^\circ$ , far-removed from the

Ekman layer and the tangent cylinder region. Analyses at other locations show similar behavior. The left column shows the radial component and the right column is the zonal component. The rows indicate the various orders of observed balances, with the primary force balance shown in the top row. Each subsequent higher order balance is shown with the sum of the terms appearing in the preceding lower order balance. The radial direction shows a sequence of force balances: (1) leading order balance between the (mean) Coriolis, pressure gradient, and buoyancy forces; (2) a secondary balance between the sum of the thermal wind terms and the mean Lorentz force; and (3) a tertiary ‘balance’ where all forces become relevant. This latter balance is not a true balance since at this order inertia becomes important and the momentum equation is therefore prognostic. We observe that the approximate magnitude of the forces appearing in a given balance decreases by approximately one order of magnitude in each higher order balance.

The point-wise computed forces show that the leading order balance in the zonal direction is between the mean Coriolis force and the mean Lorentz force, indicating a semi-MS balance. All other forces (inertia, advection, viscous diffusion) appear at the next order. We note that the forces appearing in the primary force balance in the zonal direction are approximately one order of magnitude weaker than those appearing in the primary force balance of the radial component. Our previous analysis suggests that the leading order forces in the radial direction are larger than the leading order forces in the zonal direction by approximately  $\varepsilon^{1/2} = \text{Ek}^{1/6}$ . Thus, for  $\text{Ek} = 10^{-5}$ , this difference should be approximately one order of magnitude, which is in agreement with the computed forces shown in Figure 3.8(a) and Figure 3.8(b).

The instantaneous mean force balance as a function of latitude is shown in Figure 3.9. The forces from the case with  $\text{Ek} = 10^{-5}$  and  $\text{Ra} = 10\text{Ra}_{\text{crit}}$  are plotted at a particular time and at a radius of  $r = 0.68r_o$ . Consistent with previous results, the primary balance is semi-MS with the Lorentz force entering at the secondary level in the meridional directions. The vertical lines indicate the location of the tangent cylinder at a latitude of  $\pm 58.9^\circ$ . None of the forces show any changes in behavior near the tangent cylinder. This suggests that there are no shear layers near the tangent cylinder that drastically affect the large-scale force balance.

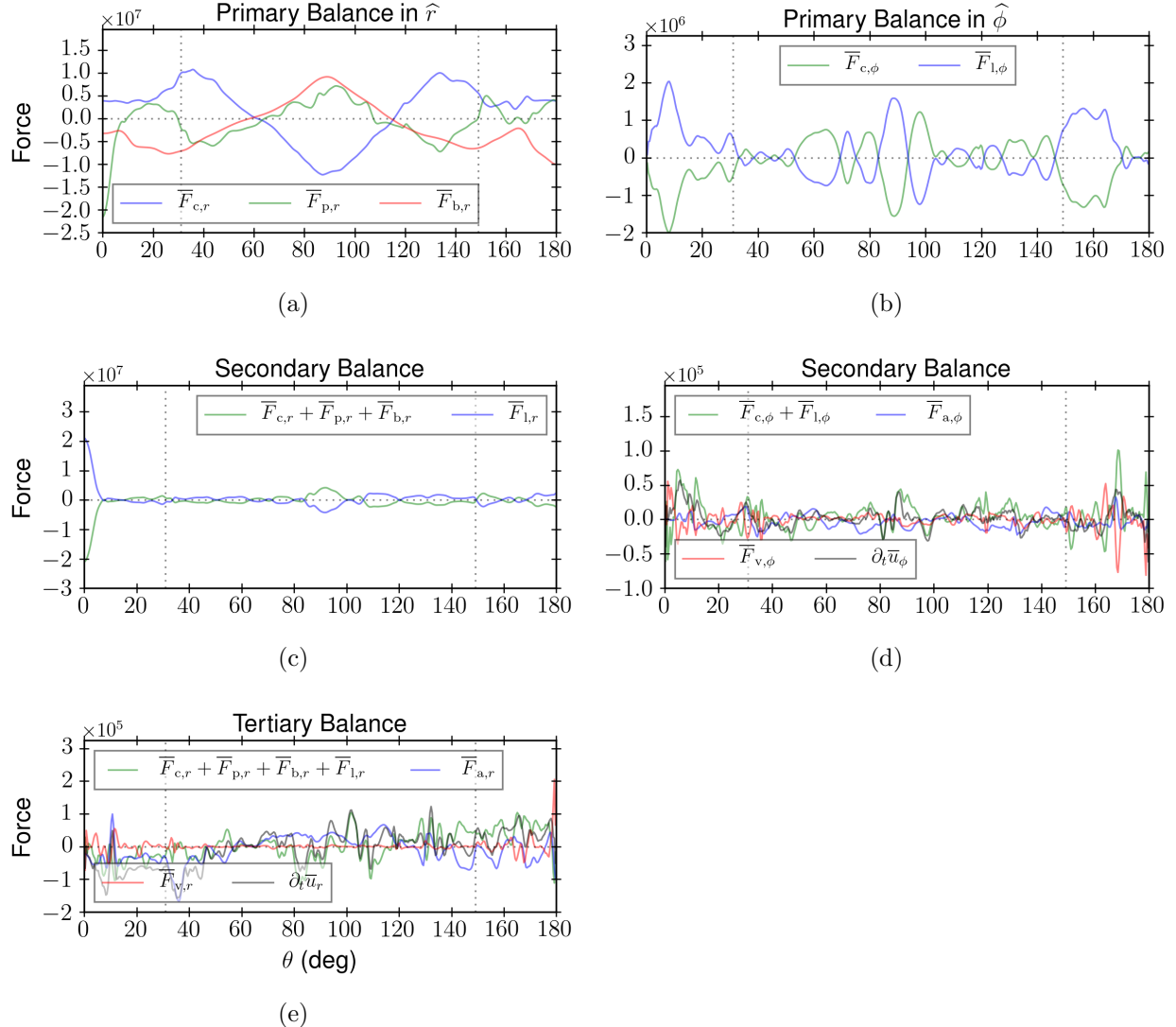


Figure 3.9: Instantaneous point-wise measurements of forces (as a function of latitude) in the mean momentum equation at the radius  $r = 0.68 r_o$ . The parameters are  $Ek = 10^{-5}$ ,  $Ra = 10 Ra_{crit}$ . The left column shows the radial direction and the right column shows the zonal direction. The top row shows the primary force balance, which is thermal wind in the meridional plane and Coriolis-Lorentz in the zonal direction. The second and third rows show the secondary and tertiary force balances. The horizontal dotted black line indicates zero. The vertical dotted black lines indicate the location of the tangent cylinder at the chosen radius, which occurs at a latitude of  $\pm 58.9^\circ$ .

The point-wise analysis is useful for clearly showing which forces balance, their time dependence, and at what asymptotic order they balance. However, to show how each force scales with  $\epsilon$ , it is helpful to consider global rms values of the forces, as has been done previously for determining

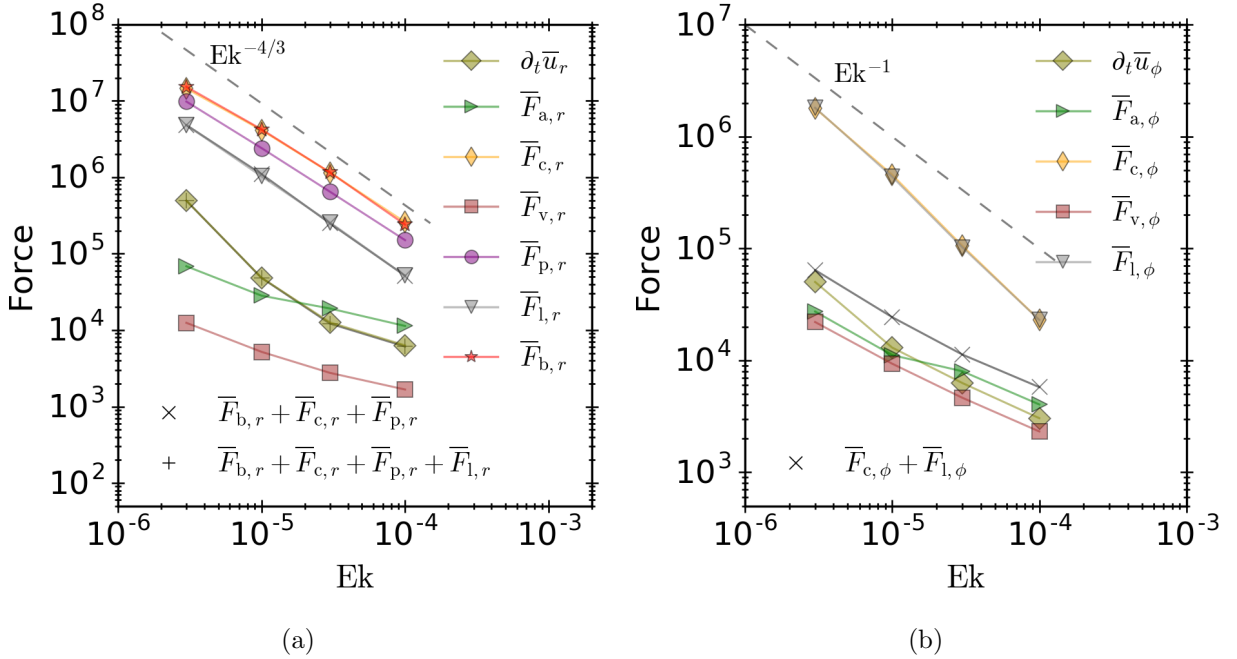


Figure 3.10: Global rms values of the mean forces as a function of the Ekman number: (a) radial components; (b) zonal components. In all cases the supercriticality is fixed at  $Ra = 10 Ra_{crit}$  and  $Pm = 2$ . The rms of the sum of the primary force balance is marked with the “x” symbols and the rms of the sum of the secondary force balance is shown by the “+” symbols.

the Rayleigh number dependence of the forces (Soderlund et al., 2012; Yadav et al., 2016). In what follows, the Ekman layers have been excluded from the calculation, since our current focus is on the interior dynamics.

Figure 3.10 shows the rms of the mean forces as a function of Ekman number for all cases with  $Ra = 10 Ra_{crit}$  and  $Pm = 2$ . All of the cases shown have reached the regime where the mean magnetic energy has saturated, but still are characterized by relatively small Rossby numbers. The cross symbols indicate the sum of the terms appearing in the primary semi-MS balance, and the plus symbols indicate the secondary force balance (for the radial direction). The asymptotic scaling slopes are shown for reference. The radial forces are shown in Figure 3.10(a); the primary thermal wind balance between the Coriolis, pressure gradient and buoyancy forces is evident, and the Lorentz force is consistently smaller than this primary balance by approximately an order of magnitude for all Ekman numbers. Again, this difference in magnitude is roughly in agreement

with the predicted  $\text{Ek}^{1/6}$  scaling. The sum of the thermal wind balance terms is approximately equal to the Lorentz force, suggesting that distinct perturbative balances are present in the large scale dynamics. Inertia, advection, and the viscous force are all small relative to the leading order thermal wind balance. Furthermore, these same three forces show a significantly weaker scaling behavior with Ekman number, which is also evidence for perturbative dynamics. The plus symbols, showing the sum of the Coriolis, pressure gradient, buoyancy, and Lorentz forces, are approximately the same magnitude as these three smallest forces.

Figure 3.10(b) shows the zonal components of the mean forces. The primary Lorentz-Coriolis balance is evident, as is the steeper scaling with Ekman number in comparison to inertia, advection, and the viscous force. The sum of the Lorentz and Coriolis forces is approximately equal in magnitude to these three smaller forces. We note that the prognostic dynamics (e.g., torsional oscillations) enter at this higher order. We also see that all three of these higher order forces scale similarly with the Ekman number, indicating that they are all important in the dynamics at this order. While the viscous force is the weakest in magnitude, it nevertheless still scales approximately in the same way as inertia.

Figure 3.11 shows the rms values of the Lorentz force and the advection terms, separated into mean-mean and eddy-eddy components. For the Lorentz force, we find that both of these terms show similar scaling behavior with the Ekman number, though the mean-mean term is slightly smaller than the eddy-eddy term over our investigated range of Ekman numbers. As expected, the advection terms are significantly weaker than the Lorentz force terms, and show different scaling behavior with the Ekman number. Based on the relative sizes of the mean and fluctuating components of the velocity, we expect that the mean-mean terms are weaker asymptotically than the eddy-eddy (Reynolds stress) terms; this expectation is evident in the data.

### 3.6 Flow Morphology

Figure 3.12 shows meridional views of the velocity field for several different Ekman numbers. The rows correspond to the different Ekman numbers:  $\text{Ek} = 10^{-4}$ ,  $\text{Ek} = 10^{-5}$ , and  $\text{Ek} = 3 \times 10^{-6}$ .

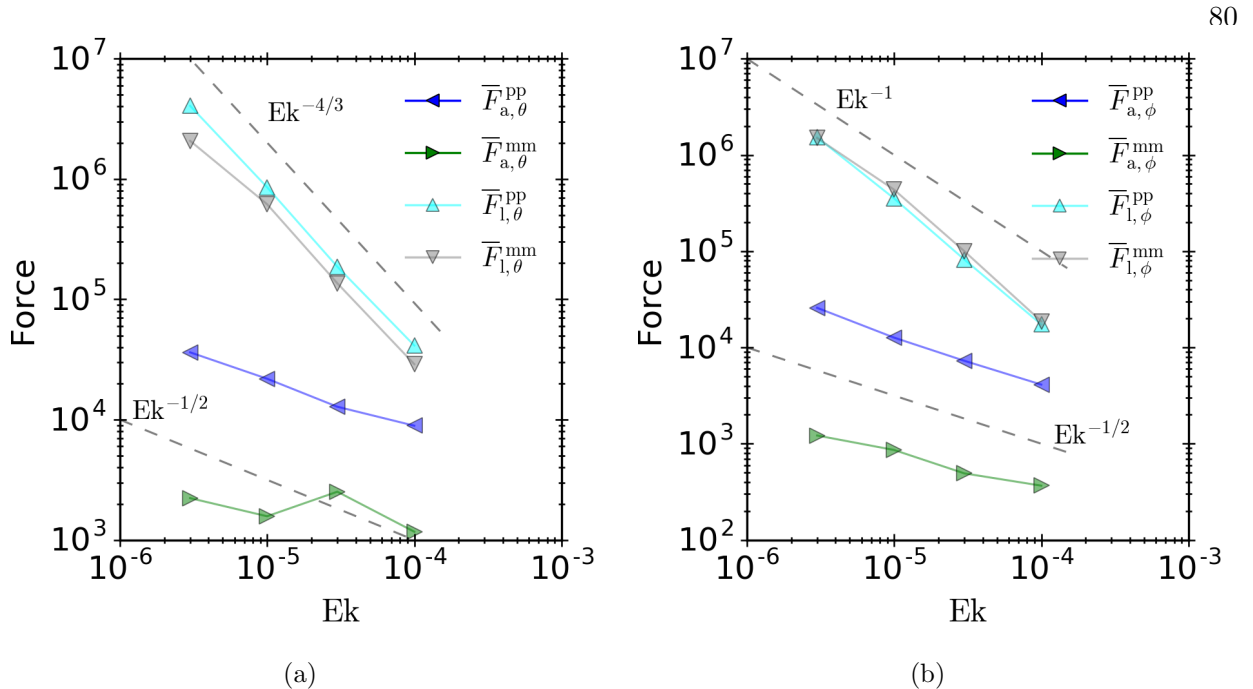


Figure 3.11: Global rms values of the different terms in the Lorentz force and advection force as a function of the Ekman number: (a) Theta components; (b) zonal components. The terms are separated into mean-mean (denoted by the superscript ‘mm’) and eddy-eddy (or prime-prime, denoted by the superscript ‘pp’). In all cases the supercriticality is fixed at  $\text{Ra} = 10 \text{Ra}_{\text{crit}}$  and  $\text{Pm} = 2$ .

The columns show the different components of the flow: radial, co-latitudinal, and zonal. All cases shown used  $\text{Ra} = 10 \text{ Ra}_{\text{crit}}$  and  $\text{Pm} = 2$ . The zonal velocity shows very little variation across the three different Ekman numbers. The low latitudes and equatorial regions are dominated by a retrograde flow and higher latitudes near the tangent cylinder become prograde. The co-latitudinal component of the mean velocity shows small variations across the Ekman numbers. The lower Ekman case exhibits features that are slightly more narrow compared to the highest Ekman number flow. The largest magnitude flows predominantly are confined to the tangent cylinder boundary in the high-Ek case. The large-magnitude co-latitudinal flows for the lowest Ek case do not show a preference for the tangent cylinder; they are more broadly spread out throughout the domain. The radial flows generally are aligned along the axial direction, with the exception of the equatorial regions. The lower Ek case shows slightly smaller scale features compared to the highest

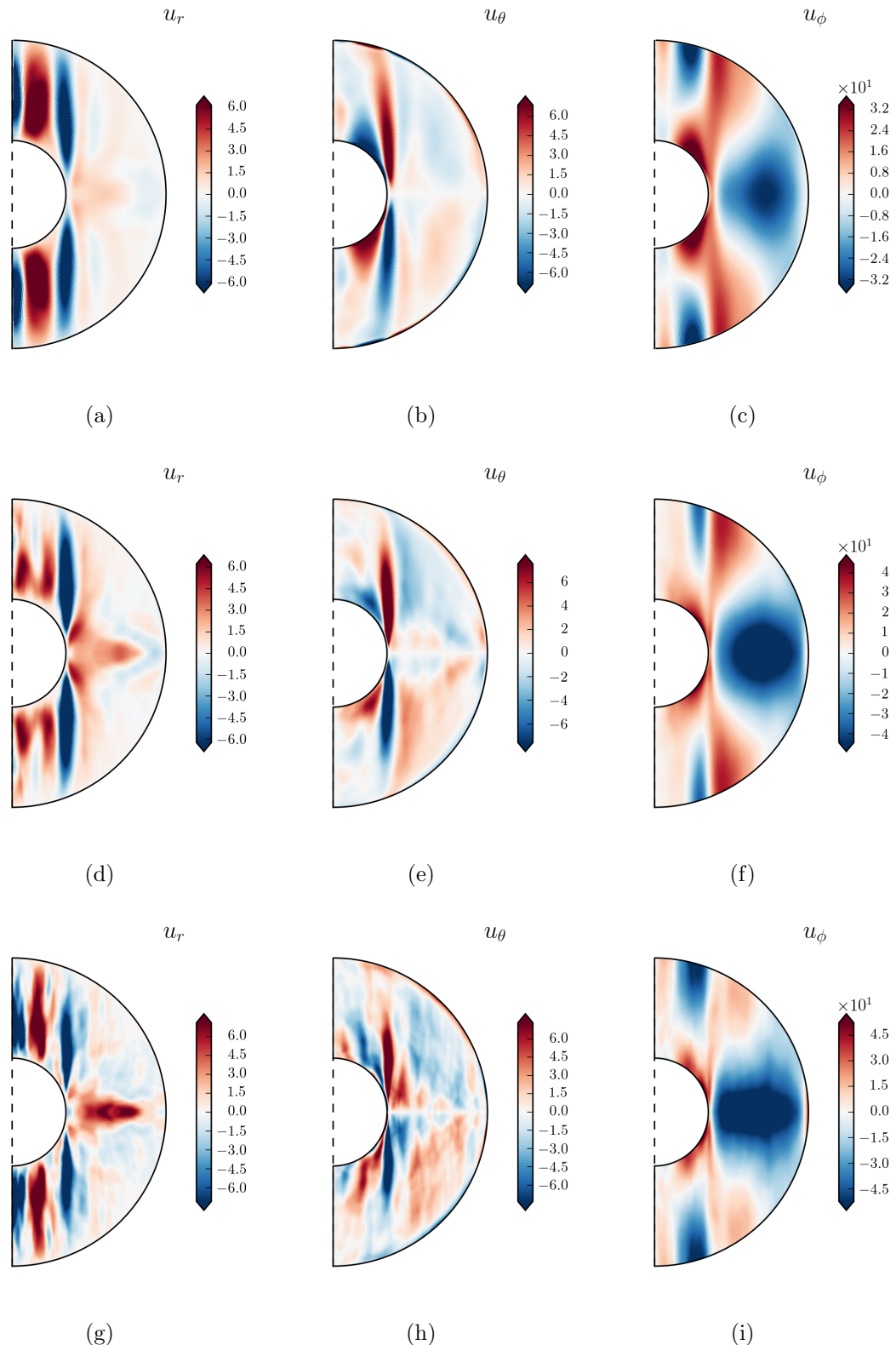


Figure 3.12: Time-averaged meridional views of the mean velocity for different Ekman numbers. The columns indicate the flow component: radial, co-latitudinal, and zonal. The rows indicate the Ekman number:  $\text{Ek} = 10^{-4}$ ,  $\text{Ek} = 10^{-5}$ ,  $\text{Ek} = 3 \times 10^{-6}$ . All cases use  $\text{Ra} = 10 \text{ Ra}_{\text{crit}}$  and  $\text{Pm} = 2$ .

Ek case.

### 3.7 Comments on Taylor's Constraint and Torsional Oscillations

If we integrate the zonal component of the large-scale force balance in the direction along the rotation axis we obtain Taylor's constraint

$$\int_{-h}^h \hat{\phi} \cdot (\overline{\mathbf{J} \times \mathbf{B}}) dz \approx 0. \quad (3.49)$$

Through conservation of mass, the Coriolis term vanishes when integrated over the height of the outer boundary  $h \equiv \sqrt{r_o^2 - s^2}$  (measured from the equatorial plane) for some cylindrical radius  $s \equiv r \sin \theta$ .

We note that satisfaction of Taylor's constraint does not require a leading order magnetostrophic balance since the constraint is only imposed on the zonal component of the mean momentum equation. In the present work we provide arguments and numerical data that suggests the large-scale force balance in rapidly rotating convection-driven dynamos is more accurately termed semi-magnetostrophic since the Lorentz force is asymptotically smaller than the mean buoyancy force. Our analysis suggests, however, that this asymptotic difference is modest, the leading order terms in the meridional and zonal components appear to be separated asymptotically only by  $\mathcal{O}(Ek^{1/6})$ . This small difference may be one of the reasons that dynamo simulations do not show a strong satisfaction of Taylor's constraint (e.g. Schaeffer et al., 2017).

Taylor's constraint often is interpreted as implying that the large-scale dynamics of spherical dynamos are characterized by axially-invariant motions consisting of 'rigid' cylindrical annuli. There are two problems with this interpretation within the context of the present work. First, we recall that the large-scale meridional force balance is thermal wind, i.e., the mean buoyancy force enters at leading order. Because of this leading order thermal wind balance, the Taylor-Proudman theorem does not apply and we therefore expect zonal motions to exhibit order one variations along the rotation axis. The analysis in Braginsky (1976) of torsional oscillations relied on the absence of the buoyancy force; only if the buoyancy force is absent would we expect to see axial invariance in

the dynamics at leading order (see e.g., Jault, 2008). While many previous studies find evidence for axially-invariant torsional oscillations in numerical simulations driven by convection, this is likely due to a preference for equatorially-symmetric motions, rather than a preference for axially-invariant motions. The operation of axially-averaging would preferentially select this component of the flow. Second, the leading order Coriolis-Lorentz force balance in the zonal component of the mean momentum equation is satisfied in a point-wise fashion. This point-wise balance indicates that there is no net torque on any ‘ring’ of fluid (with the axis of the ring parallel to the rotation axis), suggesting that torsional oscillations are point-wise in the meridional plane. Taken together, these arguments suggest that the semi-MS force balance will yield large-scale wave motion that is inherently more complex than previously thought.

### 3.8 Loss of Balance in Multipolar Dynamos

Of all the simulations discussed in this work, only the three highest Rayleigh number cases for  $Ek = 10^{-4}$  and  $Pm = 2$  showed evidence of magnetic polarity reversals. Figure 3.13 shows two example butterfly diagrams, where the mean radial magnetic field is plotted on the outer boundary as a function of latitude and time. A characteristic dipolar case is shown on the top from the case with  $Ra = 10 Ra_{crit}$ . The bottom panel shows a distinctly multipolar simulation from the case with  $Ra = 30 Ra_{crit}$ . The magnitude of the radial magnetic field at the outer boundary for the multipolar case is reduced by almost a factor of ten compared to the dipolar case. The dipolar case shows predominantly two regions: a northern hemisphere with inward magnetic field and a mostly outward magnetic field in the southern hemisphere. This corresponds to the largest scales of the magnetic field. The multipolar case shows far more small-scale variability. These multipolar cases are characterized by low dipolarity, defined as

$$f_{dip} = \left( \frac{\int \mathbf{B}_{\ell=1}(r=r_o) \cdot \mathbf{B}_{\ell=1}(r=r_o) dS}{\int \mathbf{B}(r=r_o) \cdot \mathbf{B}(r=r_o) dS} \right)^{1/2}, \quad (3.50)$$

where  $\mathbf{B}(r=r_o)$  is the total magnetic field evaluated at the outer boundary (see e.g., Christensen and Aubert, 2006; Soderlund et al., 2012). The integration is taken over the entire spherical shell,

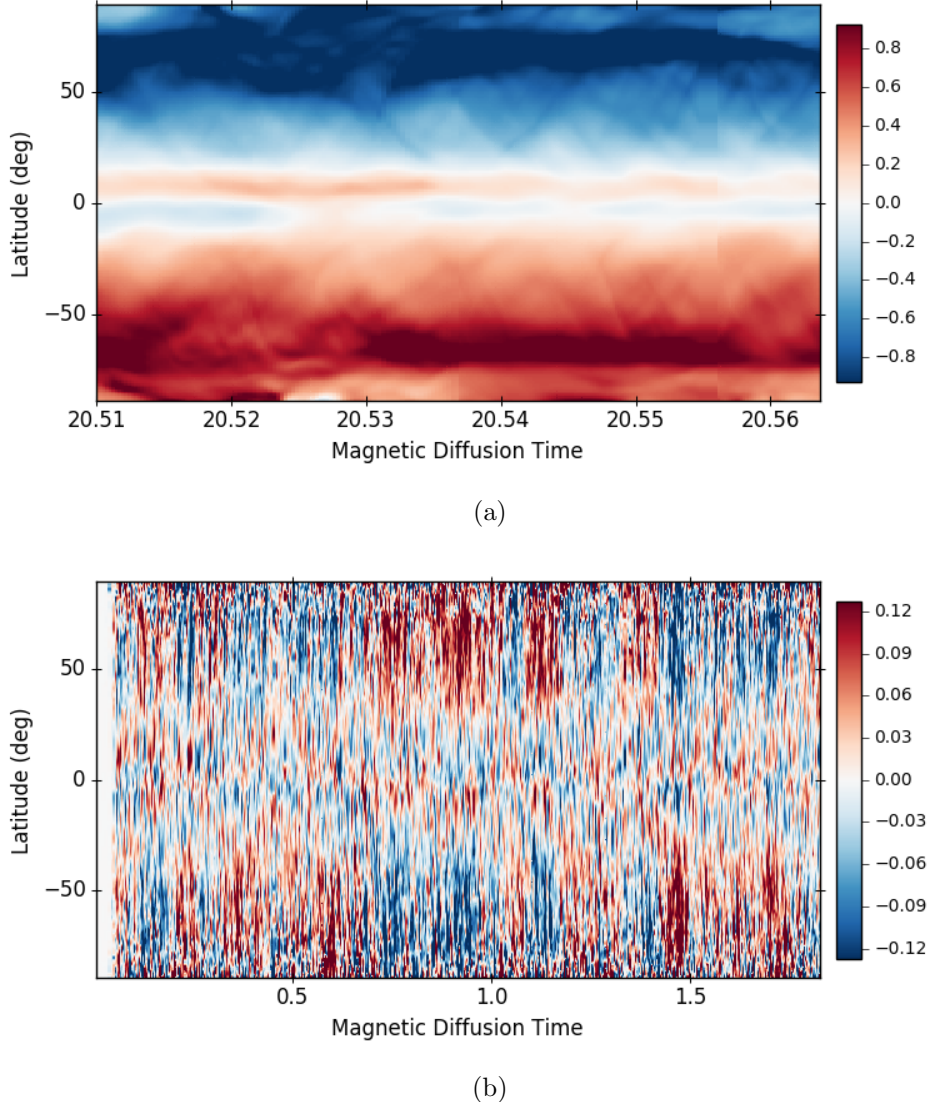


Figure 3.13: Mean radial magnetic field at the outer boundary for the (a) dipolar case with  $\text{Ra} = 10 \text{ Ra}_{\text{crit}}$  and (b) multipolar case with  $\text{Ra} = 30 \text{ Ra}_{\text{crit}}$ . Both cases used  $\text{Ek} = 10^{-4}$  and  $\text{Pm} = 2$ .

but only values of  $\ell \leq 13$  are used to provide comparison with previous work. The reversing cases in this work exhibit low dipolarity values with  $f_{\text{dip}} \lesssim 0.2$ , suggesting that the  $\ell = 1$  component plays only a minor role in the resulting dynamics.

The existence of the multipolar cases for  $\text{Ek} = 10^{-4}$  can be understood by looking at the force balances that develop. Figure 3.14 shows the forces in the  $\theta$  direction as a function of time taken at  $r = 0.74 r_o$  and a latitude of  $40^\circ$ . The left column shows the dipolar case with  $\text{Ra} = 15 \text{ Ra}_{\text{crit}}$

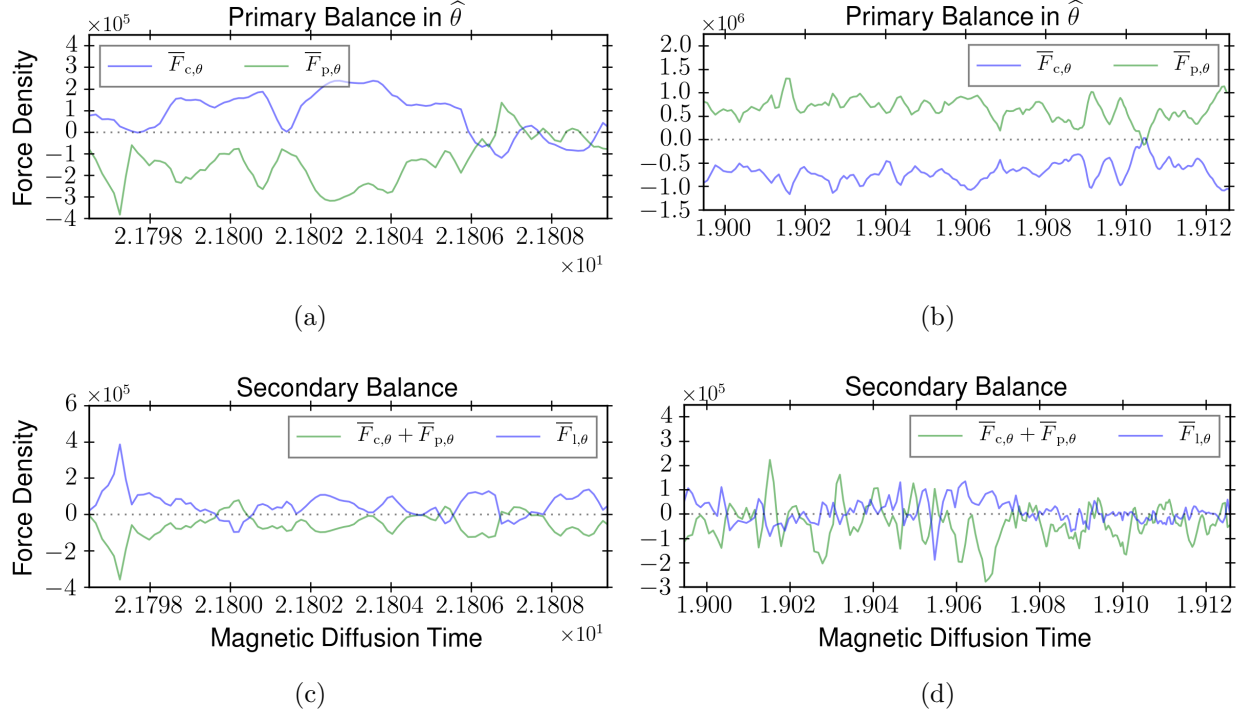


Figure 3.14: Force balances in the  $\theta$  direction at a particular point in space as a function of time for two  $\text{Ek} = 10^{-4}$  cases. The left column shows the dipolar case with  $\text{Ra} = 15 \text{Ra}_{\text{crit}}$  and the right column shows  $\text{Ra} = 30 \text{Ra}_{\text{crit}}$ , which is a multipolar solution. The dipolar case is in thermal wind balance with the Lorentz force entering at the next order. The multipolar case shows a thermal wind balance at first order, but the secondary balance is lost.

from the saturated mean magnetic energy regime and the right column is the multipolar case with  $\text{Ra} = 30 \text{Ra}_{\text{crit}}$ . The force balances indicate the dipolar case is acting as expected: the primary balance of thermal wind is present with a relatively strong Lorentz force entering at the next order. Increasing the supercriticality from 15 times to 30 times results in a similar primary balance of thermal wind, but unbalanced motions at the next (higher, secondary) order. The multipolar case shows no match between Coriolis, pressure, and Lorentz, indicating that the Lorentz force has become smaller, thus entering the force balance at a higher order.

The multipolar case is also characterized by a larger Rossby number. The force balance arguments and scaling relations discussed in previous sections all assume that the system is rapidly rotating. This allowed a choice of a small parameter. The larger Rossby number cases may have

crossed into a regime where our choice of small parameter is no longer ‘small enough’. This violation will lead to a breakdown in the perturbative force balance argument.

### 3.9 Additional Computational Details

This section describes some of the more nuanced details that were discovered during analysis of the results discussed in previous sections. Some of the results discussed below are of a computational nature, such as when to perform a time average. Other results have their roots in physical considerations, such as how to treat the boundary layer.

#### 3.9.1 Changing Scalings: $\text{Ra}/\text{Ra}_{\text{crit}}$ versus $\text{Ra}\text{Ek}^{4/3}$

In rapidly rotating systems, the critical Rayleigh number for hydrodynamic convection depends on the Ekman number as (Chandrasekhar, 1961; Roberts, 1968; Busse, 1970).

$$\text{Ra}_{\text{crit}} \sim \text{Ek}^{-4/3}. \quad (3.51)$$

This allows the criticality of any case to be rewritten in terms of the Rayleigh number and the Ekman number as

$$\frac{\text{Ra}}{\text{Ra}_{\text{crit}}} \sim \text{Ra}\text{Ek}^{4/3} \equiv \widetilde{\text{Ra}}. \quad (3.52)$$

This new quantity is the reduced Rayleigh number and asymptotically will approach a finite value rather quickly as the Ekman number is reduced (Roberts, 1968).

To determine the asymptotic scaling of a given quantity,  $Q$ , we first plot the quantity as a function of criticality or reduced Rayleigh number. If the quantity does in fact scale with the Ekman number, the plot will include multiple curves (one for every  $\text{Ek}$ ) that all exhibit similar behavior, but may be offset from one another. Mathematically,

$$Q(x) = \text{Ek}^\gamma \mathcal{F}(x) = \mathcal{O}(\text{Ek}^\gamma) \quad (3.53)$$

where  $x$  is either the criticality  $\text{Ra}/\text{Ra}_{\text{crit}}$  or the reduced Rayleigh number, the scaling exponent  $\gamma$  determines the offset, and the shape of each curve is described by some unknown function  $\mathcal{F}$ . If the

correct value of  $\gamma$  is chosen, then the quantity  $\text{Ek}^{-\gamma}Q$  should not depend strongly on the Ekman number and all of the data will collapse onto a single curve. Multiple examples of this were shown in Section 3.4, e.g., the mean thermal diffusion length scale in Figure 3.2.

When plotting the quantity of interest, there are two possible choices for the independent variable: criticality or reduced Rayleigh number. This choice can affect the observed scaling exponent  $\gamma$ . To illustrate this observation we will use the Taylor microscale for the fluctuating velocity defined as

$$\ell'_u = \left( \frac{\langle |\mathbf{u}'|^2 \rangle}{\langle |\nabla \times \mathbf{u}'|^2 \rangle} \right)^{1/2}, \quad (3.54)$$

where the angled brackets indicate a time average. The Taylor microscale is plotted against the criticality in Figure 3.15(a) and against the reduced Rayleigh number in Figure 3.15(b). Both figures show a distinct dependence on the Ekman number. The only difference between the two plots is an Ekman dependent horizontal shift in the data. This is to be expected since the relation  $R_{\text{crit}} \sim \text{Ek}^{-4/3}$  is not an equality. The rescaled length scale is shown in Figure 3.15(c) as a function of criticality. There is a considerable amount of collapse between the various curves indicating the scaling relation should be  $\ell'_u = \mathcal{O}(\text{Ek}^{2/9})$ . Had we chosen a scaling exponent of  $1/3$ , the spread in different Ekman numbers still would occur indicating an incorrect scaling relation. Figure 3.15(d) shows the same Taylor microscale data plotted as a function of reduced Rayleigh number. Once again, there is a considerable amount of collapse indicating a different asymptotic scaling of  $\ell'_u = \mathcal{O}(\text{Ek}^{1/3})$ .

The difference between the obtained scalings is quite small, but it is clear in our data. We also note that similar differences were observed in the Taylor microscales of the mean and fluctuating magnetic field as well as the gradient length scale of the mean temperature. All differences in scaling exponents were  $1/9$  or smaller. It is possible that with the addition of more Ekman numbers, both scalings would converge.

Throughout this work we chose to use criticality as opposed to the reduced Rayleigh number. As discussed in Chapter 4, the mean magnetic energy was observed to saturate as the Rayleigh

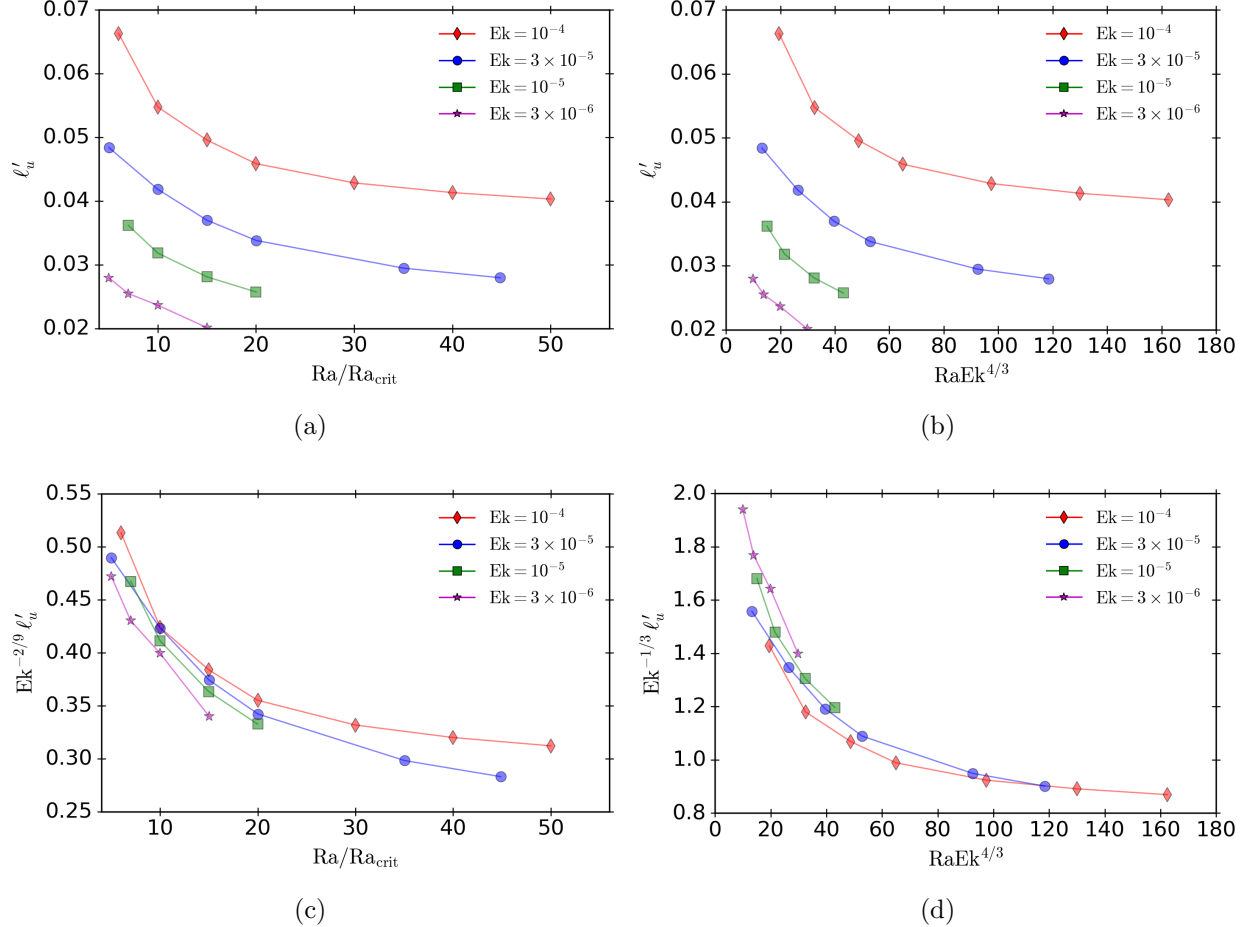


Figure 3.15: Taylor microscales for the fluctuating velocity field as a function of (a) criticality and (b) reduced Rayleigh number. Rescaled length scales are shown as a function of (c) criticality and (d) reduced Rayleigh number. The scaling derived from the criticality is  $\mathcal{O}(\text{Ek}^{2/9})$  and the scaling derived from the reduced Rayleigh number is  $\mathcal{O}(\text{Ek}^{1/3})$ .

number was increased. The critical Rayleigh number at which the saturation first occurs is  $\text{Ra} \approx 10 \text{Ra}_{\text{crit}}$  for all Ekman numbers. The critical reduced Rayleigh number at which the saturation first occurs is a range of  $\widetilde{\text{Ra}} \approx 20 - 35$ . For this reason we chose to use criticality instead of reduced Rayleigh number.

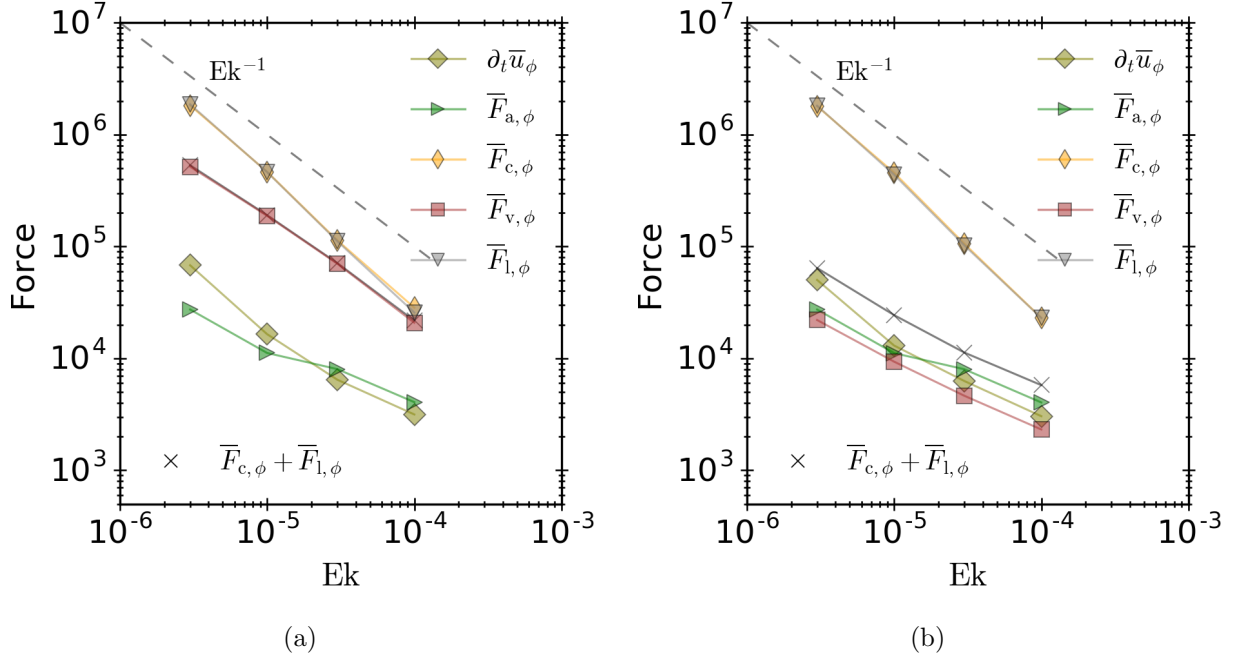


Figure 3.16: Comparison of including the Ekman layer when computing rms force densities in the zonal direction as a function of Ekman. Only cases with  $\text{Ra} = 10 \text{Ra}_{\text{crit}}$  and  $\text{Pm} = 2$  are shown for clarity. The rms force is computed either (a) including the full domain of the spherical shell or (b) excluding both of the Ekman layers (this is a reproduction of Figure 3.10(b) to make a side-by-side comparison easier).

### 3.9.2 Ekman Layer: Including versus Excluding

Different regions of the domain can exhibit distinct force balances. Within the Ekman layer near the inner and outer boundaries, viscous forces are expected to be important. Far removed from the boundaries and under sufficient thermal forcing, viscosity is not expected to play a major role in the dynamics. When analyzing the forces present in the system, mixing these regions can have a significant impact on the results. Global rms values of the forces have been computed using the whole domain (Soderlund et al., 2012), excluding the Ekman layer (Yadav et al., 2016), and spectral decompositions have been employed (Aubert et al., 2017).

In this work, we are focused on the large scales that are far removed from the boundary layers. Under these conditions we do not expect viscosity to play a major role and therefore most of the results discussed in this work have excluded the Ekman layer before any average or rms

operation is applied. Figure 3.16 shows the affect that excluding the Ekman layer can have on the force balances. The rms of the zonal force balances from the mean momentum equation are shown. Figure 3.16(a) included the Ekman layer in the rms, whereas Figure 3.16(b) excluded the Ekman layer. Both the mean advection as well as the inertial term remain small compared to all other forces regardless of whether the Ekman layer is included or not. This indicates that inertia plays a minor role in the large-scale dynamics. The viscous force shows just over an order of magnitude difference. If the tiny extent of the Ekman layer is included in the global rms then the viscous force is only a factor of two to three smaller than the Coriolis force and Lorentz force. This indicates it would have a leading-order impact on the zonal dynamics. It further suggests that the simulation would be well-described by an order unity Ekman number, but the Ekman number is  $\text{Ek} = 10^{-5}$ . If the Ekman layer is excluded before computing the rms, the viscous force becomes the weakest force in the zonal direction. This is more consistent with what is expected in small Ekman and small Rossby number simulations: both inertia and viscous forces are small compared to the Coriolis force.

### 3.10 Conclusions

We have presented an analysis of the large-scale balances in convection-driven dynamos in a rotating spherical shell. With respect to the leading order balances, the findings are in agreement with previous studies that show a thermal wind balance in the meridional directions and a Coriolis-Lorentz balance in the zonal direction (Aubert, 2005; Wicht and Christensen, 2010; Sheyko et al., 2018). The present work is the first study that uses ideas from asymptotic theory to explain the scaling behavior of the large-scale force balances. We have focused on understanding the asymptotic scaling behavior of these forces and the various quantities appearing within them. Our analysis suggests that the leading order terms in the meridional components of the mean momentum equation are larger than the leading order terms in the corresponding zonal component by a factor of  $\mathcal{O}\left(\text{Ek}^{1/6}\right)$ . Thus, we suggest that such a force balance should be more accurately termed semi-magnetostrophic. A leading order large-scale magnetostrophic dynamo requires that the three

components of the mean Coriolis force would be of comparable magnitude, which is a scenario that is not supported by the simulation data. The thermal wind balance requires that the mean zonal velocity scales as  $\mathcal{O}(\text{Ek}^{-1/3})$ .

The asymptotic analysis allows us to place an upper bound on the level to which Taylor's constraint is satisfied in both simulations and natural systems. This upper bound was not previously known and is  $\mathcal{O}(\text{Ek}^{1/6})$  for our simulations, which is a relatively weak asymptotic dependence that is consistent with the findings of previous simulations in which Taylor's constraint is only satisfied to an accuracy of about one part in ten (Schaeffer et al., 2017). Even for the Earth's core, where  $\text{Ek} = \mathcal{O}(10^{-15})$ , this scaling suggests a deviation from Taylor's constraint that is  $\mathcal{O}(10^{-3})$ . We note that a similar value for the deviation in the core was estimated by Aubert et al. (2017) that was based on very different considerations. It should be emphasized that, based on the asymptotic ordering of the forces, Taylor's constraint can be satisfied (in an approximate sense) even in the absence of a leading order magnetostrophic balance. This conclusion is not in conflict with the results of Taylor (1963) since the ordering of the forces was not investigated there.

The numerical data shows that all terms appearing in the mean heat equation exhibit an Ekman number dependence. The two largest terms in the mean heat equation are the convective heat flux and large-scale thermal diffusion and both are balanced. The time dependence of the mean temperature and advection of the mean temperature by the mean meridional velocity both are weaker than the convective flux and diffusion. The data suggests a mean temperature evolution timescale of  $\mathcal{O}(\text{Ek}^{1/3})$ . The fluctuating temperature appearing in the convective heat flux shows no obvious dependence on the Ekman number, in contrast to theory for the plane layer geometry where it scales as  $\mathcal{O}(\text{Ek}^{1/3})$ . Radial profiles of the fluctuating temperature show that the primary distinction between different Ekman numbers, for a fixed supercriticality, is a thinner thermal boundary layer as the Ekman number is reduced.

The magnitudes of the mean and fluctuating magnetic fields do not show a strong dependence on the Ekman number. The rms of the fluctuating magnetic field shows evidence of a  $\mathcal{O}(\text{Ek}^{-1/6})$  scaling, whereas the mean magnetic field shows some improved collapse when rescaled

by  $\mathcal{O}(\text{Ek}^{-1/9})$ . The data shows some evidence of a  $\mathcal{O}(\text{Ek}^{1/6})$  length scale for the mean magnetic field. If this scaling is valid for all Ekman numbers (smaller than those accessible in the current study), it implies that both the mean and fluctuating magnetic fields should be independent of the Ekman number. Under these circumstances, it may be possible that the fluctuating magnetic field asymptotically approaches a finite value as the Ekman number is reduced (assuming the scaling of the mean magnetic field is order one).

Although we have attempted to shed light on the multiscale dynamics of planetary interiors with the use of an asymptotic interpretation of numerical simulation results, our approach comes with many limitations. Because of the relatively weak asymptotic dependence of the scalings, e.g., powers of  $\mathcal{O}(\text{Ek}^{1/6})$ , the limited range in Ekman numbers available implies these scalings cannot be rigorously tested at present. Extending the present results to lower Ekman numbers would allow for better constraints on the scalings, though such an effort is computationally demanding. Our definition of the mean (large-scale) dynamics focuses only on the azimuthally averaged flows. It seems likely that non-axisymmetric ‘large-scale’ motions also are important, which was suggested by the simulations of Schaeffer et al. (2017). It also may be necessary to average the dynamics in radius to completely remove small-scale motions in that direction. An investigation of the asymptotic behavior of the terms in the fluctuating momentum equation currently is underway and will yield additional insight into the coupling of small-scale and large-scale dynamics.

It often is hypothesized that the interior dynamics of the Earth and other planets are independent of viscosity. Attempts are often made to derive scaling laws for various important quantities such as magnetic field strength that do not depend on viscosity. While such a view is certainly possible, an alternative view, and one that is supported by the present analysis, is that planetary interior dynamics depend on viscosity in an asymptotic manner, rather than being completely independent. This latter view is well known for explaining the linear dynamics of rotating spherical convection, and our present analysis suggests it also may be used to explain much of the nonlinear dynamics. The fact that the numerical simulations show well-defined perturbative dynamics supports this asymptotic view.

## Chapter 4

### Large-Scale Magnetic Field Generation: Saturation and Scaling Behavior

#### 4.1 Introduction

The majority of Solar System planets possess global, or large-scale, magnetic fields that presumably are sustained by a convection-driven dynamo operating deep within their interiors (e.g., Jones, 2011). While all of these fields are thought to arise from the dynamo mechanism, observations show variations in both their structure and magnitudes, possibly hinting at dynamical differences between them. Whereas Jupiter’s magnetic field exhibits an equatorial field strength of  $\sim 4$  G, Mercury’s field is  $\sim 3 \times 10^{-3}$  G (also measured at the equator) (Connerney, 2015). In addition, most of the planets have predominantly dipolar magnetic fields that tend to be aligned with their rotation axis. However, the magnetic fields of both Uranus and Neptune are dominated by their nondipolar components (e.g., Stanley and Bloxham, 2004). The Earth’s magnetic field is strongly dipolar during stable periods, yet becomes dominated by nondipolar components during field reversal events which tend to last several thousand years (Reshetnyak and Pavlov, 2016). These observations have raised questions regarding the physical processes and parameters that control planetary magnetic field strength and structure. In the present work we use data from numerical simulations and asymptotic analysis to examine these questions in more detail.

Due to computational constraints, numerical dynamo models cannot use the same nondimensional parameters that characterize natural dynamos. This limitation is well-known, and implies some caution is warranted when applying model results to planets. Scaling laws provide one approach for extrapolating model results to planetary-like parameter regimes (e.g., Christensen,

2010). Implicit in this extrapolation is that numerical models are dynamically similar (in a qualitative sense) to planets. Dynamic similarity between model and planet typically requires that an asymptotic regime has been reached in the model. Two nondimensional parameters that are useful for characterizing asymptotic behavior are the Ekman number  $\text{Ek}$  and the Rayleigh number  $\text{Ra}$ . Large values of  $\text{Ra}$  imply that the buoyancy force is large relative to diffusive (thermal and viscous) effects and tends to lead to turbulent convection. The Ekman number specifies the strength of viscous effects compared to the Coriolis force. Planets are characterized by  $\text{Ek} \ll 1$  and  $\text{Ra} \gg 1$  (e.g., Connerney, 2015), indicating that they are highly turbulent and rapidly rotating. Asymptotic scaling laws require that  $\text{Ek} \ll 1$ . Observing asymptotic scaling behavior in numerical models is necessary for developing confidence in applying model results to planets.

Dynamos commonly are distinguished by comparing the typical length scales that characterize the magnetic and velocity fields. Large-scale dynamos have magnetic field length scales that are large relative to the velocity length scales. In contrast, small-scale dynamos possess magnetic field scales that are comparable to, and smaller than the velocity length scales. There is no sharp delineating boundary between these two types of dynamos. Rather, the distinction is an asymptotic one. For large-scale dynamos we say that  $\ell_B \gg \ell_u$ , where  $\ell_B$  and  $\ell_u$  denote length scales for the magnetic and velocity fields, respectively. Because planets possess global-scale magnetic fields, it is typically assumed that their dynamos are of large-scale type.

Certain physical ingredients are thought to be necessary for large-scale dynamos. Both rotation (through the Coriolis force) and large-scale shear in the velocity field (through mean flow formation) are thought to be important contributors to large-scale magnetic field generation. The Coriolis force is known to be effective in promoting the generation of large-scale magnetic fields by leading to correlations in the small-scale magnetic and velocity fields (Parker, 1955; Steenbeck et al., 1966). Ultimately, large-scale dynamos require some degree of scale separation in the velocity field. For the case of rotating convection, it is well known that fluid motions tend to align with the rotation axis, thereby forming global-scale motions, in addition to the asymptotically small length scales that characterize fluid motions in the direction perpendicular to the rotation axis (Soward,

1977).

The alignment of the dipole axis with the rotation axis for many planets provides some indirect evidence that rotation is playing a role in these systems (Schubert and Soderlund, 2011). Nevertheless, the fact that at least one planet undergoes polarity reversals, during which time there is no well-defined dipolar component, complicates this simplified picture. By interpreting the results of numerical models, previous studies suggest that the Earth may be in a transition regime in terms of the relative influence of the Coriolis force (e.g., Kutzner and Christensen, 2002; Christensen and Aubert, 2006; Christensen, 2010; Aurnou and King, 2017). However, no model has been simulated that shows, for the same fixed set of nondimensional control parameters, both a strong large-scale magnetic field during certain time intervals, and a reversing field for other time intervals. Models that show polarity reversals always are characterized by a dipolar component that is significantly smaller than the nondipolar components of the magnetic field (Kutzner and Christensen, 2002).

Several ideas have been put forward to describe how the magnetic field might saturate and are described in the review by Christensen (2010). The arguments range from the system satisfying a particular force balance (e.g., Stevenson, 1979), to depending only on the available energy input (Christensen and Aubert, 2006). The arguments of Stevenson (1979) imply that the dynamo reaches an optimum state in which the Lorentz force rises to the same magnitude as the Coriolis force. Under this argument the nondimensional Elsasser number, characterizing the ratio of the Lorentz force to the Coriolis force, reaches an order unity value. Such a mechanism has been found to operate in rotating dynamos that lack significant large-scale mean flows (Childress and Soward, 1972; Calkins et al., 2015; Calkins, 2018). In contrast, the energy argument of Christensen and Aubert (2006) relies on the reasonable assumption that the work done by the buoyancy force must balance the dissipative losses, mainly through ohmic dissipation. These two mechanisms need not be mutually exclusive, and may occur simultaneously.

The spatial-scale separation between small-scale convective flows and large-scale mean flows is a crucial component of mean field dynamo models that help explain the generation of magnetic field in terms of correlations of small-scale helical flow (i.e., the  $\alpha$ -effect) and through shearing on

large-scales (the  $\Omega$ -effect) (Steenbeck et al., 1966). Such large-scale flows play a role in the model of Malkus and Proctor (1975), who showed that a large-scale magnetic field can saturate when a correspondingly large-scale velocity field develops (the so-called Malkus-Proctor scenario).

With the exception of Malkus and Proctor (1975), previous work on dynamo saturation largely has not considered the distinction between large- and small-scale magnetic field. Since distinct force balances can exist on disparate spatial scales, it is possible that contributions to the saturation mechanism differ between the large- and the small-scale components of the field. For example, one might expect different scaling behavior of the magnetic field with increasing buoyancy forcing, which would tend to lead to an increase in small-scale convective and magnetic power. Such an effect seems to have been found in the dynamo models of Kutzner and Christensen (2002). Through those models, they found that the dipolar component of the magnetic field can reach a finite magnitude and saturate with increasing Rayleigh number until the influence of inertia becomes so large that the dynamo reverts to a small-scale dynamo, in which the large-scale magnetic field becomes weak. This behavior may be due to the different saturation processes between the large- and small-scale fields.

In the present work we show that the saturation of the dipolar component of the large-scale magnetic field is robust across varying Ekman numbers. Furthermore, we show that the large-scale magnetic field, which includes the dipolar component as well as all higher degrees, shows a similar saturation that is robust across the Ekman numbers studied here. Our results suggest that this phenomenon likely is related to the force balance in the mean zonal momentum equation, and the relative sizes of the large- and small-scale field components. In this sense, the Elsasser number argument is observed to hold for the large-scale magnetic field since it is observed to become nearly independent of the buoyancy forcing beyond a certain threshold. We show further that the established large-scale force balance gives rise to a large-scale energy balance between the buoyancy work and the Lorentz work.

#### 4.1.1 Methods

The simulations of this chapter are the same ones that were discussed in Chapter 3, but a different analysis is performed here. We recall that these simulations are solved in a rotating Boussinesq MHD system. The equations are reproduced here for convenience, see Section 3.2 for a more complete discussion. The equations are

$$\frac{\partial \mathbf{u}}{\partial t} + \mathbf{u} \cdot \nabla \mathbf{u} = -\frac{1}{\text{Ek}} \nabla P + \frac{\text{Ra}}{\text{Pr}} T \frac{\mathbf{r}}{r_o} + \nabla^2 \mathbf{u} + \frac{1}{\text{PmEk}} \mathbf{J} \times \mathbf{B} + \frac{2}{\text{Ek}} \mathbf{u} \times \hat{\mathbf{z}}, \quad (4.1)$$

$$\frac{\partial T}{\partial t} + \mathbf{u} \cdot \nabla T = \frac{1}{\text{Pr}} \nabla^2 T, \quad (4.2)$$

$$\frac{\partial \mathbf{B}}{\partial t} = \nabla \times (\mathbf{u} \times \mathbf{B}) + \frac{1}{\text{Pm}} \nabla^2 \mathbf{B}, \quad (4.3)$$

$$\nabla \cdot \mathbf{u} = 0, \quad (4.4)$$

$$\nabla \cdot \mathbf{B} = 0, \quad (4.5)$$

and are solved numerically using the ideas of Section 1.3.

These simulations fix the aspect ratio at  $\chi = 0.35$  and use a Prandtl number of unity. The magnetic Prandtl number, the Ekman number, and the Rayleigh number are all varied. The various input parameters and selected output quantities are shown in Table 3.1.

#### 4.2 Energetics

We begin by examining the relative contributions of mean and fluctuating flows and fields to the energy (density) of each simulation. We define the mean kinetic energy as

$$\overline{E}_k = \frac{1}{V} \int \frac{1}{2} |\overline{\mathbf{u}}(\mathbf{r}, t)|^2 dV \quad (4.6)$$

and the fluctuating kinetic energy as

$$E'_k = \frac{1}{V} \int \frac{1}{2} |\mathbf{u}'(\mathbf{r}, t)|^2 dV, \quad (4.7)$$

where  $V$  is the volume of the spherical shell and the integration is computed over the entire domain.

Similarly, the mean and fluctuating magnetic energies are given by

$$\bar{E}_{\text{mag}} = \frac{1}{V} \int \frac{1}{2PmEk} |\bar{\mathbf{B}}(\mathbf{r}, t)|^2 dV \quad (4.8)$$

and

$$E'_{\text{mag}} = \frac{1}{V} \int \frac{1}{2PmEk} |\mathbf{B}'(\mathbf{r}, t)|^2 dV \quad (4.9)$$

respectively.

Figure 4.1 shows the time- and volume-averaged kinetic and magnetic energy decomposed into mean and fluctuating components. The mean energies are shown in panels (a) and (b), and fluctuating energies are shown in panels (c) and (d). At all values of  $E_k$ , the total magnetic energy (not shown) grows as the Rayleigh number is increased, primarily owing to contributions from  $E'_{\text{mag}}$ . For low values of supercriticality  $\text{Ra}/\text{Ra}_{\text{crit}}$ ,  $\bar{E}_{\text{mag}}$  increases with  $\text{Ra}$  until ultimately transitioning to a regime in which the mean magnetic energy remains approximately constant with  $\text{Ra}$ . We refer to the latter as the saturated mean field regime. The transition to the saturated field state occurs at  $\text{Ra} \approx 10 \text{Ra}_{\text{crit}}$  for all Ekman numbers investigated here. In addition to these first two regimes, the highest Ekman number case of  $E_k = 10^{-4}$  and  $Pm = 2$  shows an abrupt transition to a state that is characterized by a low mean magnetic energy. This behavior has been well-explored previously (Kutzner and Christensen, 2002; Soderlund et al., 2012) and arises due to a transition in magnetic field morphology from predominantly dipolar to predominantly multipolar.

The fluctuating kinetic energy is larger than the mean component by approximately an order of magnitude. While the mean flows do not significantly contribute to the total kinetic energy, as we discuss below, they do appear to be important for the saturation of the mean magnetic field.

The fluctuating magnetic energy is larger than the mean magnetic energy in all cases investigated, though the relative size is discussed more later. The mean magnetic energy shows a robust

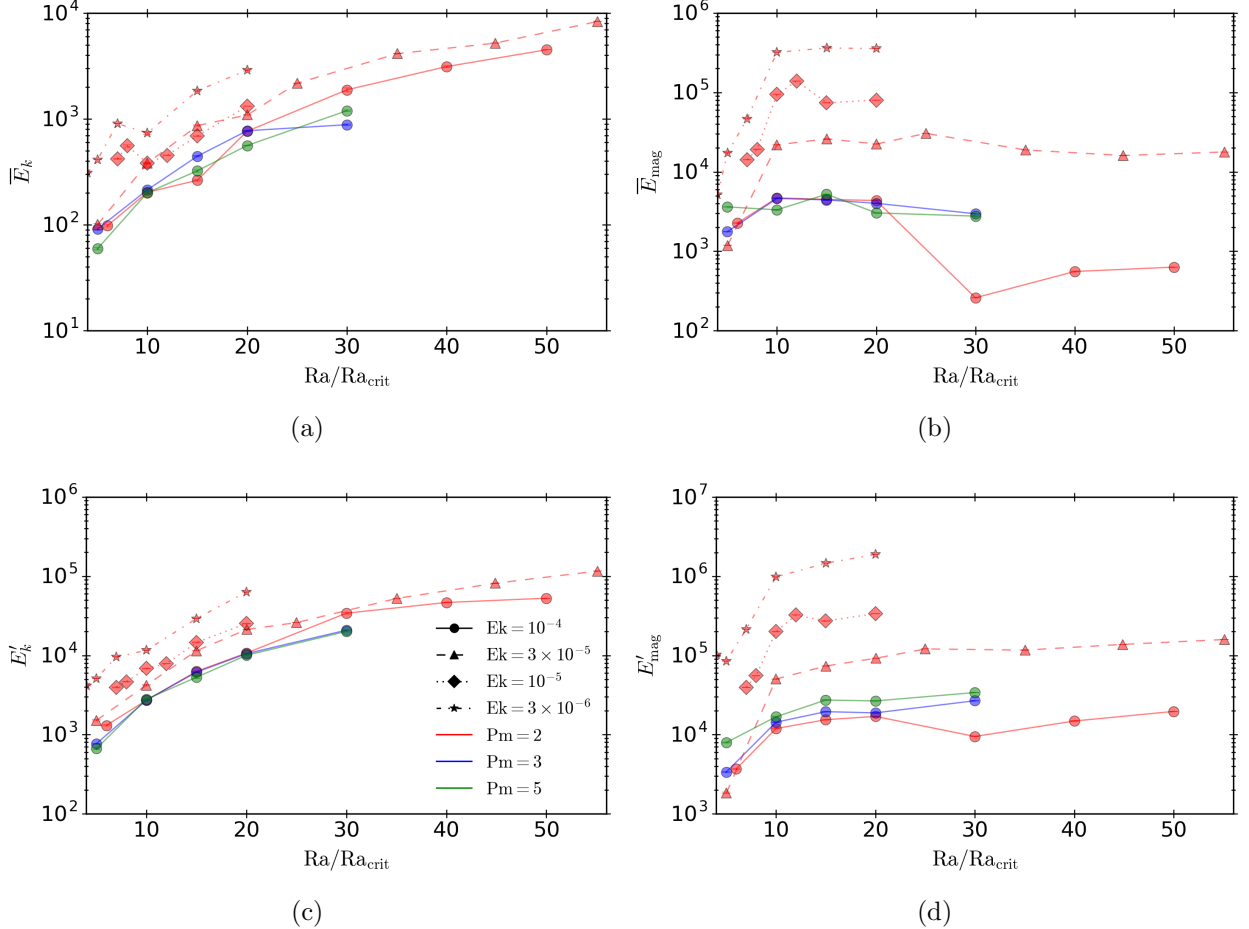


Figure 4.1: Time- and volume-averaged kinetic and magnetic energy for all simulations. (a) Mean kinetic energy; (b) mean magnetic energy; (c) fluctuating kinetic energy; (d) fluctuating magnetic energy. The symbols and line styles correspond to the Ekman numbers, and the colors indicate the magnetic Prandtl number. The mean magnetic energy grows with Ra and saturates at  $\text{Ra} \approx 10 \text{ Ra}_{\text{crit}}$  for all Ekman numbers.

saturation with increasing Rayleigh number and subsequent drop in certain cases. Aside from the sudden drop near the dipolar/multipolar transition, the fluctuating contribution does not saturate, but continues to grow with increasing Rayleigh.

We also can examine how the mean magnetic energy is distributed across spatial scales and how that power varies as a function of Ra and Ek. Figure 4.2 shows the contributions to the mean magnetic energy by the  $\ell = 1$  and  $\ell = 2$  spherical harmonic degrees (integrated over spherical harmonic order  $m$ ) for each of our simulations. The dipolar component shows a clear saturation

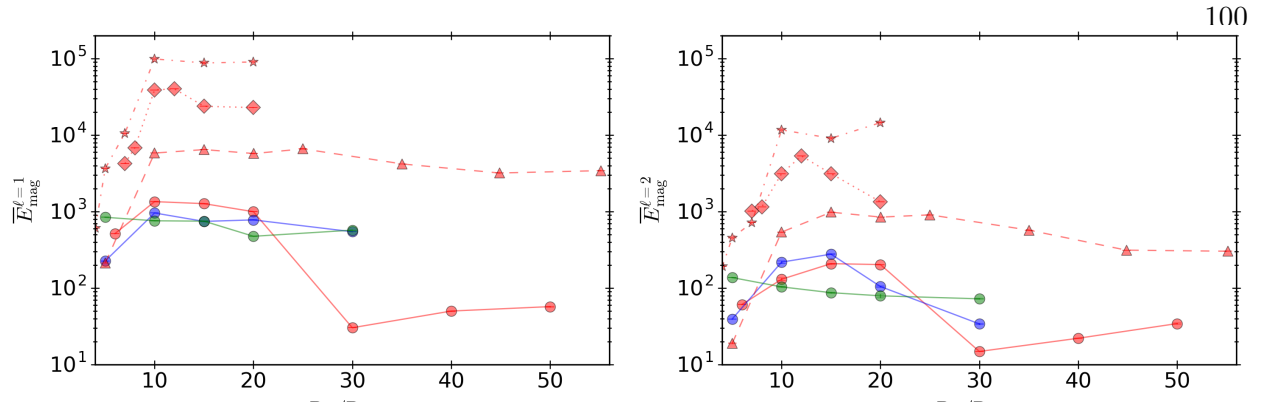


Figure 4.2: Magnetic energy for the first two spherical harmonic ( $\ell$ ) contributions to the mean magnetic energy: (a)  $\ell = 1$ ; (b)  $\ell = 2$ . The colors, symbols and line styles are the same as in Figure 4.1.

starting at  $\text{Ra} \approx 10 \text{Ra}_{\text{crit}}$ . Since this component dominates the magnetic energy, the saturation in the mean magnetic energy is likely indicating that the dipolar component is controlling the saturation of the mean magnetic field. The quadrupolar  $\ell = 2$  component is more complicated if we compare the simulations from different values of  $E_k$  and  $P_m$ , though for most cases it also shows a transition in scaling with  $\text{Ra}$  near  $\text{Ra} \approx 10 \text{Ra}_{\text{crit}}$ .

Velocity and magnetic field power spectra are shown in Figures 4.3 and 4.4 for both the mean and fluctuating quantities for the particular case of  $E_k = 10^{-5}$ . Even spherical harmonic degrees dominate for the mean velocity, showing the preference for equatorially symmetric large-scale flows. For the mean magnetic field spectra we observe that the odd spherical harmonic degrees dominate, showing a preference for equatorially antisymmetric mean fields. The four highest Rayleigh number cases show the saturation in the mean magnetic energy spectra for the lower values of  $\ell$ , though power in high  $\ell$  modes continues to grow. In the saturated regime, only  $\ell \gtrsim 20$  increase with  $\text{Ra}$ , yet because of their relatively small magnitude they have a negligible contribution to the total magnetic energy.

The fluctuating spectra show no parity preference and exhibit relatively broadband behavior. A prominent peak is observed near  $\ell \approx 15$ , corresponding to the critical wavenumber for the

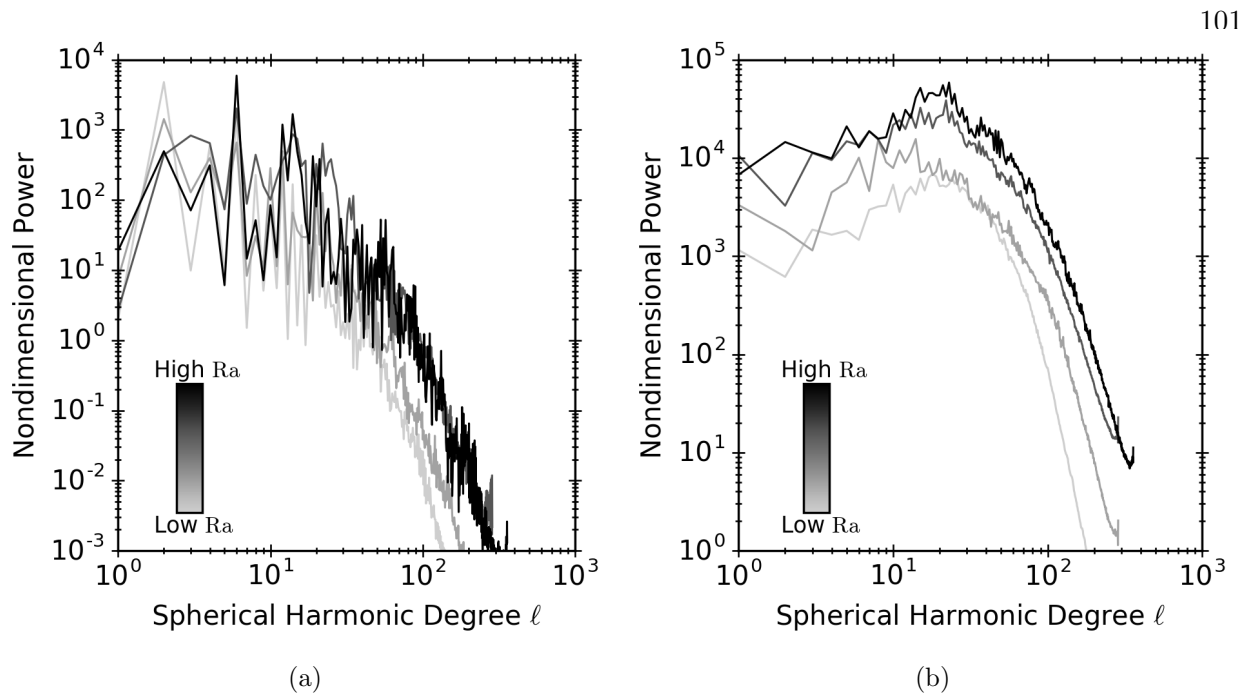


Figure 4.3: Velocity power spectra for the  $\text{Ek} = 10^{-5}$  simulations with the four highest Rayleigh numbers: (a) mean component; (b) fluctuating component.

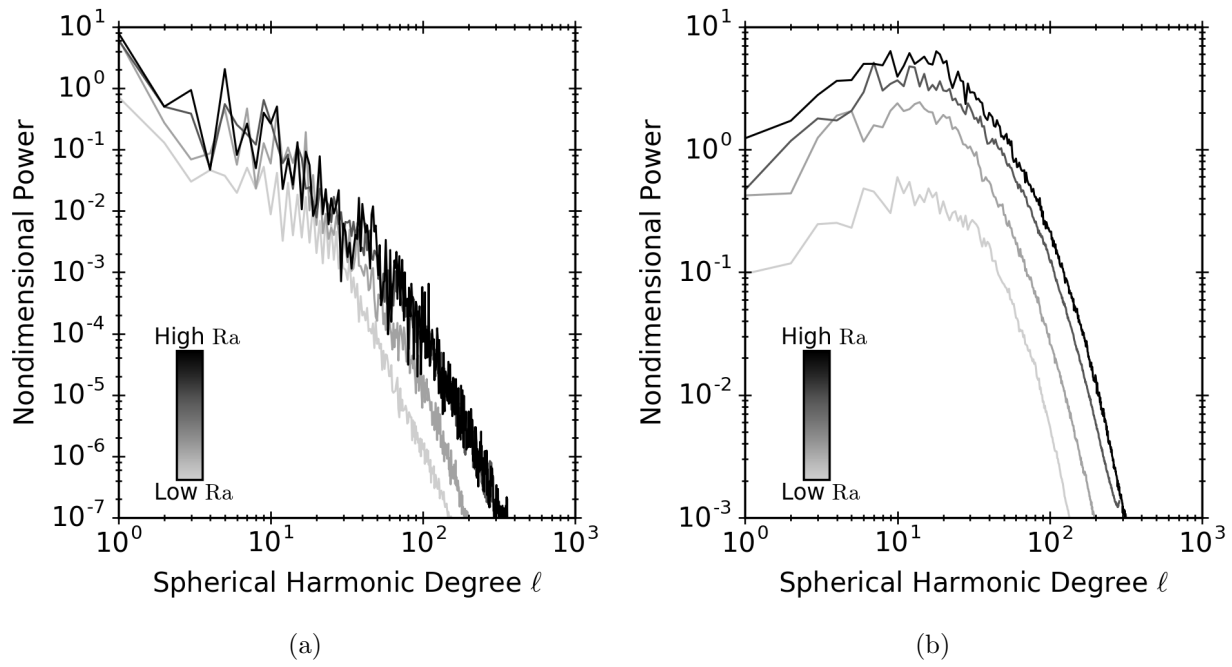


Figure 4.4: Magnetic field power spectra for the  $\text{Ek} = 10^{-5}$  simulations with the four highest Rayleigh numbers: (a) mean component; (b) fluctuating component.

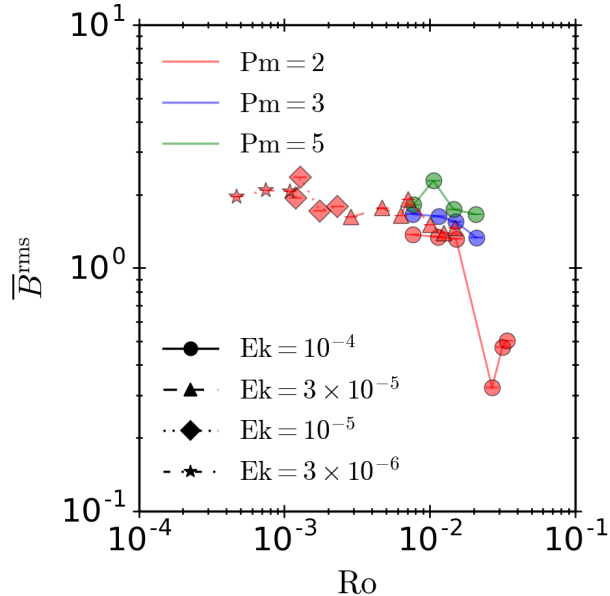


Figure 4.5: The rms of the mean magnetic field for all cases with  $\text{Ra} > 10 \text{Ra}_{\text{crit}}$  as a function of large-scale Rossby number.

onset of convection at this Ekman number. At this Ekman number, we see that the spectra of the fluctuating magnetic field are of very similar shape for the different Rayleigh numbers. For instance the value of the peak of the spectra is approximately five times the  $\ell = 1$  component for all Rayleigh numbers.

Another way to visualize the saturation of the mean magnetic field is to compare it to the global Rossby number of the system. The Rossby number can be described as the ratio of a rotational time scale to a convective turnover time scale. Figure 4.5 shows the rms of the mean magnetic field for all simulations with  $\text{Ra} > 10 \text{Ra}_{\text{crit}}$ , to highlight the more supercritical cases. There is a clear saturation of the mean field as the Rossby number is varied over almost two decades. A similar relationship is seen in observational data of stars across several spectral types ranging from late F to late M (Patten and Simon, 1996; Mohanty and Basri, 2003; Pizzolato et al., 2003; Reiners and Basri, 2007). The observational data shows a clear magnetic activity-rotation relationship, but below a Rossby number threshold the stars show a saturation in the magnetic activity.

Simulations have the luxury of exactly calculating the magnetic field and the Rossby number; in our case these are globally averaged quantities. The observational studies must infer both the magnetic field activity and the Rossby number. Tracers for magnetic activity, e.g., coronal X-ray or chromospheric H $\alpha$  emission, increase with rotational velocity. This was quantified first by Pallavicini et al. (1981) and recently has been studied in more detail (Pizzolato et al., 2003; Wright et al., 2011; Reiners et al., 2014; Wright et al., 2018). The Rossby number is found by using empirical data for the convective time scale that varies as a function of the star's  $V - K$  color in a way that can be calibrated (Wright et al., 2011, 2018). Ultimately, the observational data originates from a small portion of the upper atmosphere and is not a global average. This makes a direct one-to-one comparison of the simulation results and the observational results quite difficult.

The similar saturation behavior found in the observational data and the simulation data presented here is encouraging. It suggests that the low-Rossby number stars could be in a dynamically similar region of parameter space.

### 4.3 Flow Morphology

Figure 4.6 shows meridional views of the velocity field for two different values of Ra. The rows correspond to the two different Rayleigh numbers:  $Ra = 7 Ra_{\text{crit}}$  and  $Ra = 15 Ra_{\text{crit}}$ . The columns show the different components of the flow: radial, co-latitudinal, and zonal. All cases shown used  $Ek = 10^{-5}$  and  $Pm = 2$ . The zonal velocity shows similar behavior in the bulk domain, but inside the tangent cylinder shows more variation in the higher Ra case. The co-latitudinal component of the mean velocity is confined largely to the boundary of the tangent cylinder in lower Ra case. The higher Ra case shows much more variability and smaller scale structure throughout the bulk of the domain. Inside the tangent cylinder shows a significant increase in co-latitudinal flow for the case with the higher Ra. The radial velocity of the lower Ra case is confined predominantly to the boundary of the tangent cylinder, with larger scale structure throughout the bulk of the domain close to the equator. The higher Ra case shows much more convective motions inside the tangent cylinder and an abundance of smaller scale structure near the equatorial region. The larger

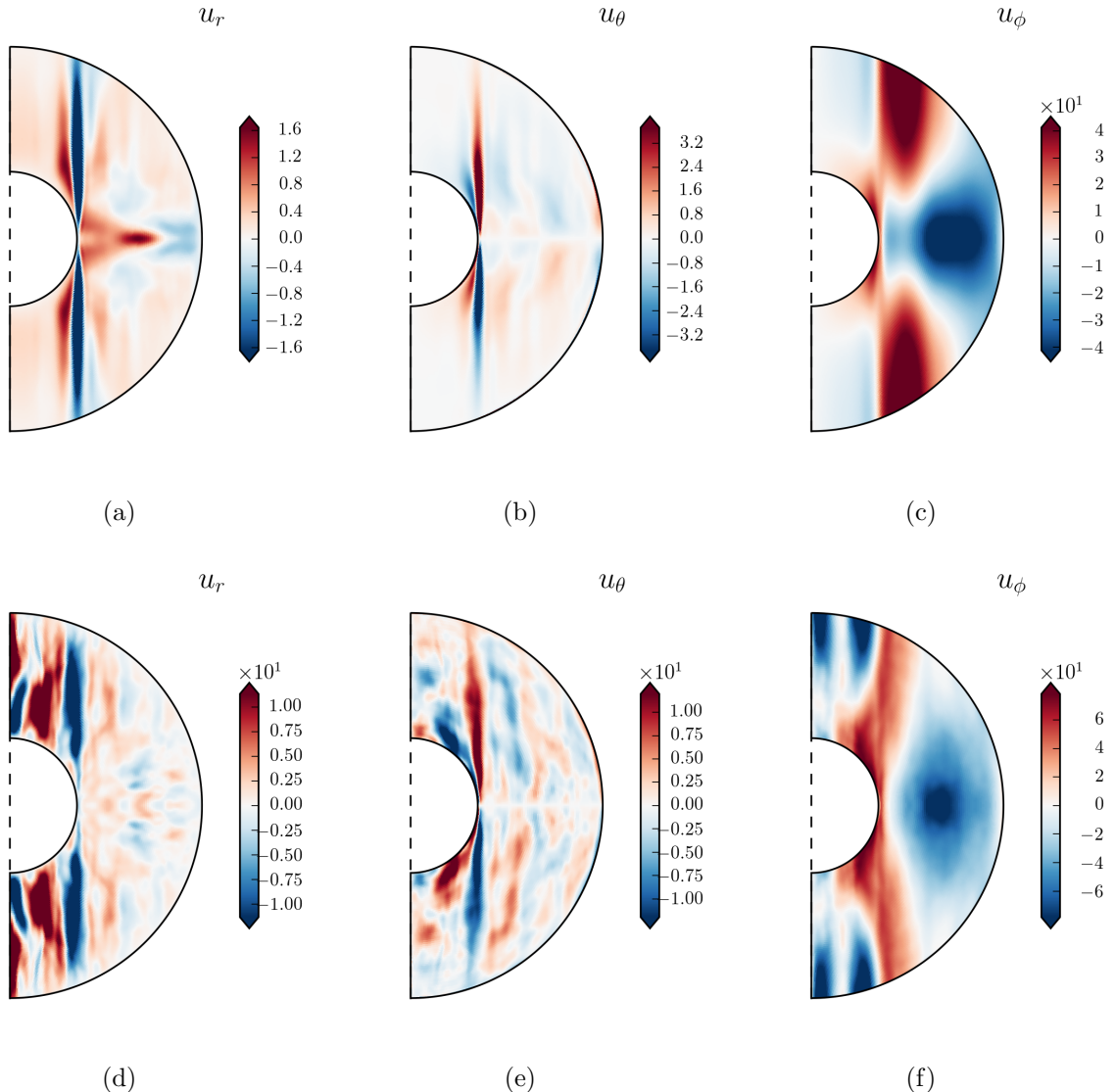


Figure 4.6: Time-averaged meridional views of the mean velocity for two different criticalities. The columns indicate the flow component: radial, co-latitudinal, and zonal. The rows indicate the Rayleigh number:  $\text{Ra} = 7 \text{Ra}_{\text{crit}}$  and  $\text{Ra} = 15 \text{Ra}_{\text{crit}}$ . All cases use  $\text{Ek} = 10^{-5}$  and  $\text{Pm} = 2$ .

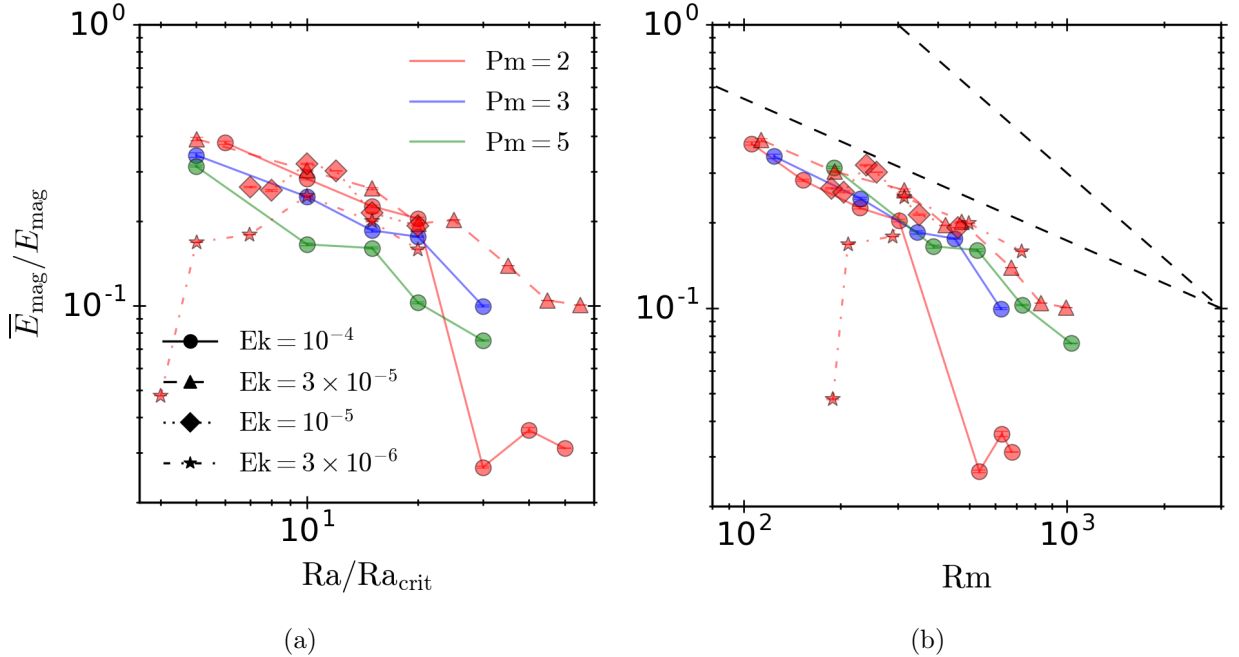


Figure 4.7: The ratio of mean magnetic energy to total magnetic energy for all cases as a function of (a) supercriticality and (b) magnetic Reynolds number. The dashed lines in (b) indicate scalings of  $Rm^{-1}$  and  $Rm^{-1/2}$  and are only shown as references.

Rayleigh number case clearly shows more convective motions inside the tangent cylinder. This is also true for the case with  $\text{Ra} = 10 \text{Ra}_{\text{crit}}$  (not shown), but to a slightly smaller degree. The change in behavior that occurs around  $\text{Ra} = 10 \text{Ra}_{\text{crit}}$  could be tied to a change in the flow morphology, which appears to be driven by the generation of convective motions inside the tangent cylinder.

## 4.4 Influence of R<sub>m</sub>

The ratio of the mean magnetic energy to the total magnetic energy is plotted for all cases in Figure 4.7. The left panel plots the ratio versus the Rayleigh number and the right panel shows the ratio versus the magnetic Reynolds number. An obvious trend with the magnetic Prandtl number is observed: lower values of  $Pm$  yield larger relative mean fields for a fixed value of the Rayleigh number. This behavior is related to the magnetic Reynolds number, where smaller values of  $Rm$  may yield a ‘smoother’ magnetic field morphology. Furthermore, this observation is consistent with

the plane layer theory developed by Calkins et al. (2015a), that showed the predominance of large-scale magnetic field in the limit of rapid rotation and small magnetic Reynolds number. For the current parameter space, the largest ratio observed is  $\bar{E}_{\text{mag}}/E_{\text{mag}} \approx 0.4$ . We recall that planetary interiors typically are characterized by  $Pm \lesssim 10^{-5}$ , suggesting that the ratio  $\bar{E}_{\text{mag}}/E_{\text{mag}}$  can be order unity even for large values of  $\text{Ra}$ .

We find a reasonable collapse of the ratio of mean magnetic energy to total energy when plotted as a function of the magnetic Reynolds number, as shown in Figure 4.7(b). The obvious outliers are the lowest  $\text{Ra}$  cases for  $\text{Ek} = 3 \times 10^{-6}$  and the three multipolar cases for  $\text{Ek} = 10^{-4}$ . If we restrict the data only to those cases that have reached a saturated ( $\text{Ra} \geq 10 \text{ Ra}_{\text{crit}}$ ) dipolar field regime, we can fit a power law of the form

$$\frac{\bar{E}_{\text{mag}}}{E_{\text{mag}}} = CRm^{\alpha} \text{Ek}^{\beta}. \quad (4.10)$$

A least-squares fit produces values of  $\alpha = -0.709 \pm 0.067$ ,  $\beta = -0.102 \pm 0.032$  and  $C \approx 5$ . This fit suggests a very small dependence on the Ekman number, and, as expected a relatively strong dependence on the magnetic Reynolds number. This ratio applies to the field conditions within the interior of the spherical shell domain. Observations cannot currently ascertain the characteristics of the field deep within a natural dynamo, including the Earth and the Sun.

## 4.5 Dipolarity

To further characterize the magnetic field structure, we compute the dipolarity defined as,

$$f_{\text{dip}} = \left( \frac{\int \mathbf{B}_{\ell=1}(r=r_o) \cdot \mathbf{B}_{\ell=1}(r=r_o) dS}{\int \mathbf{B}(r=r_o) \cdot \mathbf{B}(r=r_o) dS} \right)^{1/2}, \quad (4.11)$$

where  $\mathbf{B}(r=r_o)$  is the total magnetic field evaluated at the outer boundary, (see e.g., Christensen and Aubert, 2006; Soderlund et al., 2012). The integration is taken over the entire spherical shell, but only values of  $\ell \leq 13$  are used to provide comparison with previous work. A perfect dipole is characterized by  $f_{\text{dip}} = 1$ ; as with previous work, it is helpful to define dipole-dominant magnetic fields as those in which  $f_{\text{dip}} \geq 0.5$ . We further define the dipolarity for the mean and fluctuating

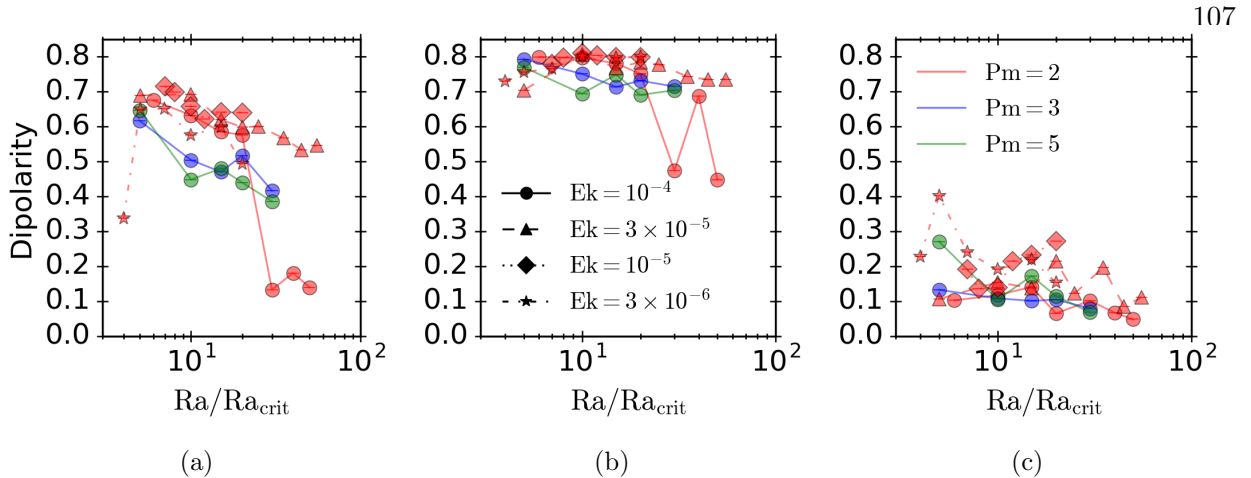


Figure 4.8: Dipolarity as a function of supercriticality: (a) total magnetic field; (b) mean magnetic field; and (c) fluctuating magnetic field. Only spherical harmonic degrees  $\ell \leq 13$  are included.

magnetic fields according to

$$\overline{f}_{\text{dip}} = \left( \frac{\int \overline{B}_{\ell=1}(r=r_o) \cdot \overline{B}_{\ell=1}(r=r_o) dS}{\int \overline{B}(r=r_o) \cdot \overline{B}(r=r_o) dS} \right)^{1/2}, \quad (4.12)$$

$$f'_{\text{dip}} = \left( \frac{\int \mathbf{B}'_{\ell=1}(r=r_o) \cdot \mathbf{B}'_{\ell=1}(r=r_o) dS}{\int \mathbf{B}'(r=r_o) \cdot \mathbf{B}'(r=r_o) dS} \right)^{1/2}. \quad (4.13)$$

Decomposing the dipolarity into mean and fluctuating contributions helps to isolate which component of the field is contributing to changes in the total dipolarity. The dipolarity results for all cases are plotted as a function of the supercriticality in Figure 4.8. The dipolarity using the full magnetic field is shown in Figure 4.8(a). Most cases show a relatively large total dipolarity ( $f_{\text{dip}} \gtrsim 0.5$ ), indicating a dipole-dominated magnetic field structure. A few cases show a rather low total dipolarity, indicating a multipolar field; these are the runs that have exhibited a significant drop in the dipolar magnetic energy. The breakdown of the dipolarity into the mean and fluctuating components is shown in Figures 4.8(b) and 4.8(c), respectively. Both the mean and fluctuating components show only a weak dependence on the Rayleigh number, indicating the dipolar components of these fields remain of comparable relative magnitude over a large range in Ra. The data suggests that the high- $\ell$  components of the fluctuating magnetic field cause the decrease of the

total  $f_{\text{dip}}$  with increasing Ra, since the mean field morphology stays relatively constant over the investigated range of Ra.

#### 4.6 Scaling of the Mean Lorentz Force

One possibility for the observed saturation in the mean magnetic field is due to the force balance that occurs in rapidly rotating spherical dynamos. The leading order mean force balance in the meridional plane is described by the  $\hat{\mathbf{r}}$  and  $\hat{\theta}$  components of the thermal wind equation (e.g., Aubert, 2005),

$$\frac{2}{Ek} \hat{\mathbf{z}} \times \bar{\mathbf{u}} \approx -\frac{1}{Ek} \nabla \bar{P} + \frac{Ra}{Pr} \bar{T} \frac{\mathbf{r}}{r_o}. \quad (4.14)$$

The zonal direction is a balance between the Coriolis force and the Lorentz force,

$$\frac{2}{Ek} \bar{u}_s \approx \frac{1}{Ek Pm} (\bar{\mathbf{J}} \times \bar{\mathbf{B}}) \cdot \hat{\phi}, \quad (4.15)$$

where the cylindrical radial component of the mean velocity is  $\bar{u}_s \equiv \bar{u}_r \sin \theta + \bar{u}_\theta \cos \theta$ . We refer to the force balance expressed by Equations 4.14 and 4.15 as semi-magnetostrophic (MS), since the mean Lorentz force enters only one component of the momentum equation at leading order. Moreover, the mean Lorentz force in Equation 4.15 is asymptotically smaller than the forces in the meridional components of the mean momentum Equation 4.14 so a fully magnetostrophic large-scale force balance is not present. The semi-MS force balance holds so long as the Rossby number is small, and it places several constraints on the large-scale dynamics. Here we focus on the implications that the semi-MS force balance has for the large-scale magnetic field. We note that Equation 4.15 shows that these dynamos saturate via the Malkus-Proctor scenario in which the large-scale field grows to the same amplitude as the large-scale (mean) flow. It is important to note that this mean flow in Equation 4.15 is meridional circulation and is weaker than the mean zonal flow  $\bar{u}_\phi$ .

The mean Lorentz force consists of two separate terms given by

$$\bar{\mathbf{J}} \times \bar{\mathbf{B}} = \bar{\mathbf{J}} \times \bar{\mathbf{B}} + \bar{\mathbf{J}}' \times \bar{\mathbf{B}}'. \quad (4.16)$$

We refer to the first term on the right-hand side as the ‘mean-mean’ term, and the second term as the ‘eddy-eddy’ term; these terms are responsible for the saturation of the mean magnetic field,

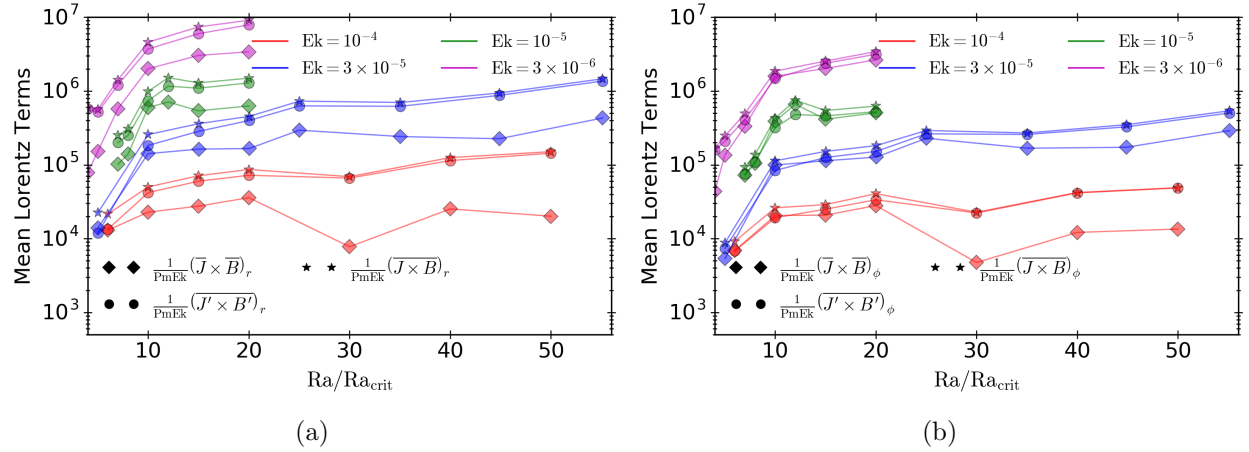


Figure 4.9: Components of the mean Lorentz force as a function of supercriticality, decomposed into mean-mean and eddy-eddy terms for all cases with  $Pm = 2$ : (a) rms of the radial component; and (b) rms of the zonal component.

and the collective action of small-scale fluctuating magnetic field on the meridional circulation, respectively. The relative size of these two terms depends on the magnetic Reynolds number; one might expect that the eddy-eddy term will become increasingly dominant as the magnetic Reynolds number is increased. Figure 4.9 shows the rms of these two contributions to the mean Lorentz force for both the radial and zonal components. We find that there is generally a change in scaling behavior around 10 times supercritical, consistent with the location of the saturation of the mean magnetic field. The radial component behaves similarly to the co-latitudinal component and is therefore not shown. The mean-mean term is almost always smaller than the eddy-eddy term in the radial direction. In the zonal direction, we find that both terms are comparable in magnitude for the majority of the cases. There are cases in which the eddy-eddy term is definitively larger than the mean-mean term for the zonal component; these include the multipolar cases with  $Ek = 10^{-4}$  and the three largest values of  $Ra$  for  $Ek = 3 \times 10^{-5}$ .

Figure 4.10 shows meridional views of the radial and zonal components of the mean Lorentz force for the case with  $Ra = 10 Ra_{\text{crit}}$  and  $Ek = 10^{-5}$ . The top row shows the radial component for the mean-mean and eddy-eddy contributions, as well as the total Lorentz force. The bottom row shows the corresponding terms for the zonal component. The mean-mean term tends to be largest in

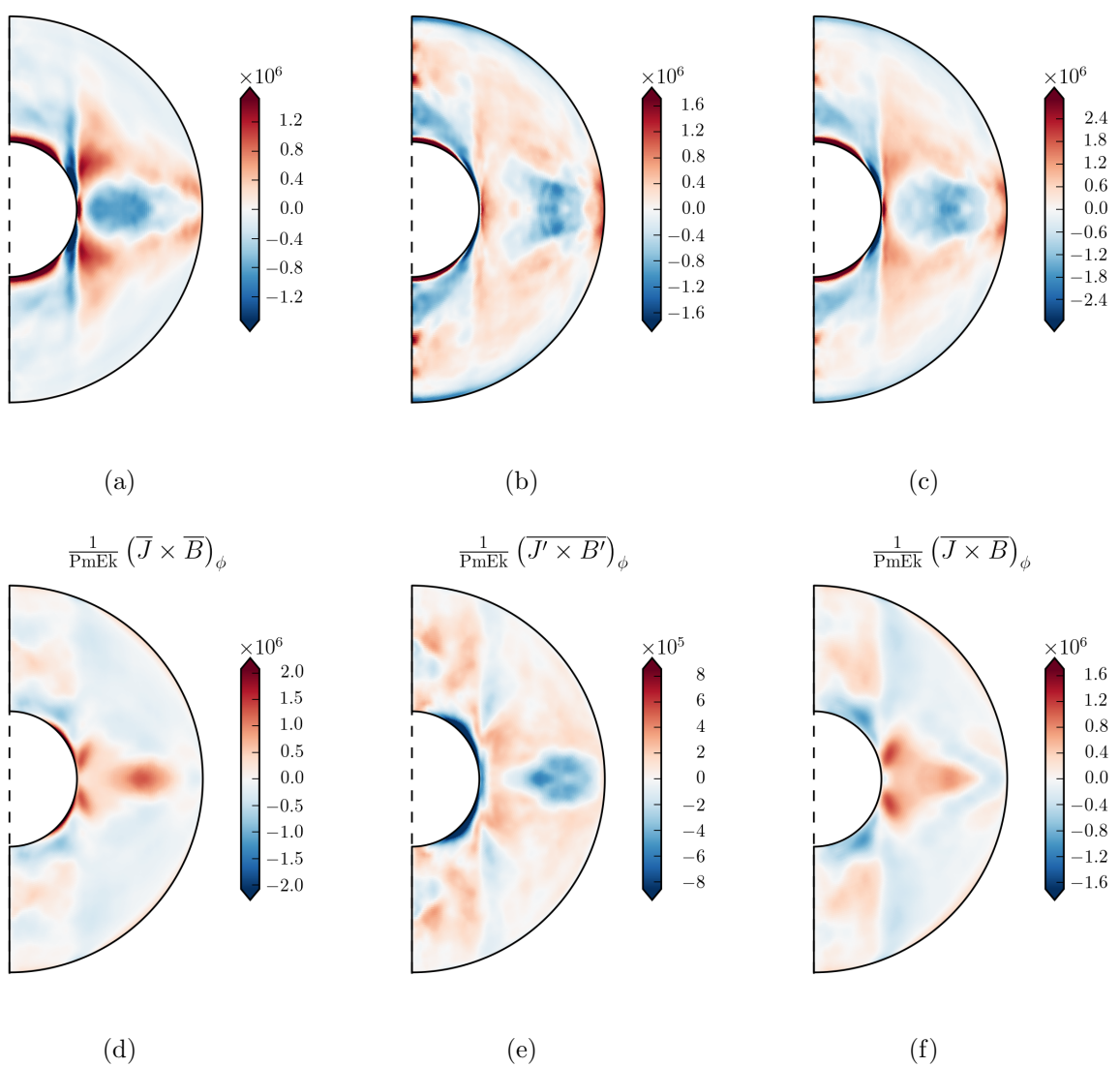


Figure 4.10: Time-averaged meridional views of the mean Lorentz force for the case using  $E_k = 10^{-5}$  and  $Ra = 10 Ra_{crit}$ . The top row shows the radial component of the (a) mean-mean, (b) eddy-eddy, and (c) total Lorentz force. The bottom row shows the zonal component of the (d) mean-mean, (e) eddy-eddy, and (f) total Lorentz force.

magnitude near the equator for the zonal component, whereas the radial component encompasses more of the bulk domain outside the tangent cylinder, but is still dominant at lower latitudes. Interestingly, the largest values of the radial component occur near the inner boundary. The eddy-eddy contribution does not seem to be localized to any particular region since it shows structure

that covers the whole domain for both the radial and zonal components. The zonal component of the mean-mean term is generally positive near the equator and negative at mid latitudes, whereas the zonal component of the eddy-eddy term shows the opposite behavior.

#### 4.7 Energy Source Terms

The evolution equation governing the mean magnetic energy density is derived by multiplying Equation 1.33 by the appropriately normalized mean magnetic field. The resulting equation is

$$\frac{\partial \bar{E}_{\text{mag}}}{\partial t} = -\frac{1}{\text{PmEk}} \nabla \cdot \bar{\mathbf{S}} - \frac{1}{\text{Pm}^2 \text{Ek}} \bar{\mathbf{J}}^2 + \frac{1}{\text{PmEk}} [\bar{\mathbf{J}} \cdot \bar{\mathcal{E}} - \bar{\mathbf{u}} \cdot \bar{\mathbf{J}} \times \bar{\mathbf{B}}], \quad (4.17)$$

where the mean Poynting flux,  $\bar{\mathbf{S}}$ , is

$$\bar{\mathbf{S}} = \left[ -\bar{\mathbf{u}} \times \bar{\mathbf{B}} - \bar{\mathcal{E}} + \frac{1}{\text{Pm}} \bar{\mathbf{J}} \right] \times \bar{\mathbf{B}}. \quad (4.18)$$

Volume averaging the mean energy equation leads to

$$\frac{\partial \langle \bar{E}_{\text{mag}} \rangle}{\partial t} = -\frac{1}{\text{PmEk}} \langle \bar{\mathbf{u}} \cdot \bar{\mathbf{J}} \times \bar{\mathbf{B}} \rangle + \frac{1}{\text{PmEk}} \langle \bar{\mathbf{J}} \cdot \bar{\mathcal{E}} \rangle - \frac{1}{\text{Pm}^2 \text{Ek}} \langle \bar{\mathbf{J}}^2 \rangle. \quad (4.19)$$

The equation for the evolution of the fluctuating magnetic energy density is found in a similar manner and is given by

$$\frac{\partial E'_{\text{mag}}}{\partial t} = \frac{1}{\text{PmEk}} \left[ -\nabla \cdot \mathbf{S}' - \frac{1}{\text{Pm}} \mathbf{J}'^2 - \mathbf{u}' \cdot \mathbf{J}' \times \mathbf{B}' - \mathbf{J}' \cdot \bar{\mathcal{E}} - \mathbf{u}' \cdot \mathbf{J}' \times \bar{\mathbf{B}} - \bar{\mathbf{u}} \cdot \mathbf{J}' \times \mathbf{B}' \right], \quad (4.20)$$

where the fluctuating Poynting flux,  $\mathbf{S}'$ , is

$$\mathbf{S}' = \left[ -\mathbf{u}' \times \bar{\mathbf{B}} - \bar{\mathbf{u}} \times \mathbf{B}' - \mathbf{u}' \times \mathbf{B}' + \bar{\mathcal{E}} + \frac{1}{\text{Pm}} \mathbf{J}' \right] \times \mathbf{B}'. \quad (4.21)$$

Figure 4.11 shows the various time-averaged source terms in both the mean and the fluctuating magnetic energy evolution equations. For clarity, only simulations that have  $\text{Pm} = 2$  are plotted and only two Ekman numbers are shown; the other simulations exhibit qualitatively similar behavior.

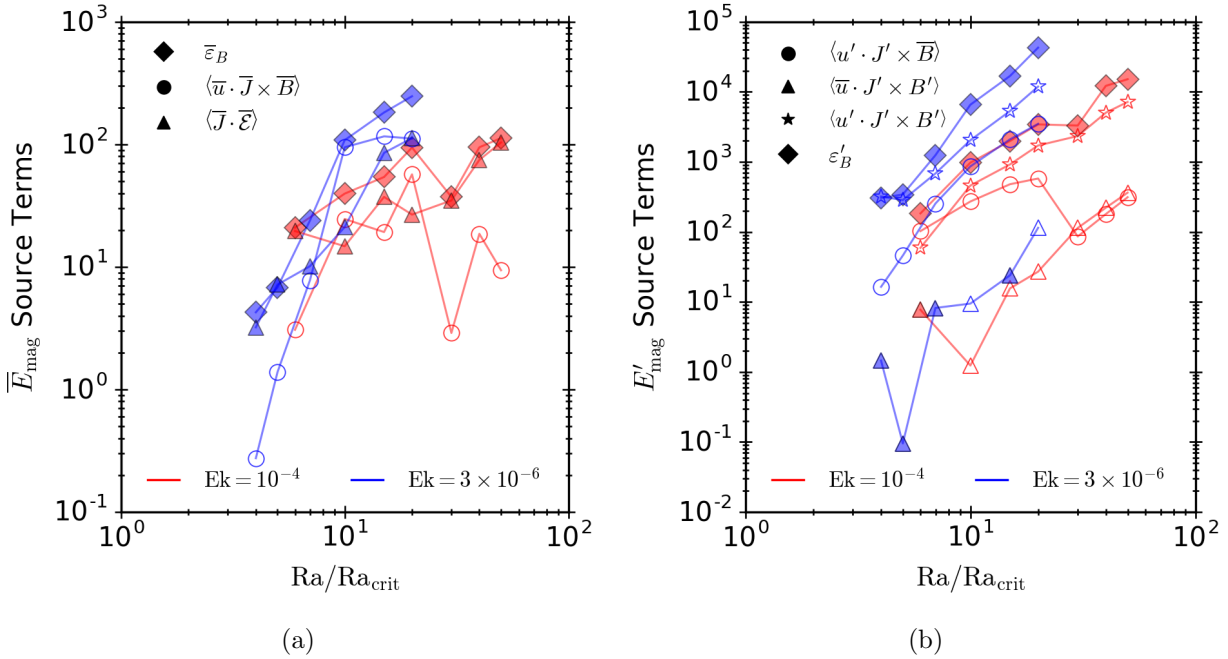


Figure 4.11: Volume and time averaged source terms from the evolution equations: (a) mean terms; (b) fluctuating terms. Empty symbols indicate a negative value. The magnetic Prandtl number is fixed to  $Pm = 2$  for all cases shown. For clarity only simulations with the largest and smallest Ekman numbers are shown.

Time averaging Equation 4.19 yields the balance relation

$$\bar{\varepsilon}_B = -\langle \bar{u} \cdot \bar{J} \times \bar{B} \rangle + \langle \bar{J} \cdot \bar{\mathcal{E}} \rangle \quad (4.22)$$

where the mean ohmic dissipation appears as

$$\bar{\varepsilon}_B = \frac{1}{Pm} \langle \bar{J}^2 \rangle. \quad (4.23)$$

For the mean energetics there are two energy transfer mechanisms: (1) the transfer of mean magnetic energy to mean kinetic energy,  $\langle \bar{u} \cdot \bar{J} \times \bar{B} \rangle$ ; and (2) the emf generation term,  $\langle \bar{J} \cdot \bar{\mathcal{E}} \rangle$ , which effectively represents a transfer of small-scale (magnetic and kinetic) energy to large-scale magnetic energy. The data for the mean magnetic energy balance shown in Figure 4.11(a) shows that  $\langle \bar{u} \cdot \bar{J} \times \bar{B} \rangle$  is negative for all cases investigated, implying that there is a net transfer of mean kinetic energy to mean magnetic energy. We find that the mean magnetic to mean kinetic (mean-mean) energy transfer term  $\langle \bar{u} \cdot \bar{J} \times \bar{B} \rangle$  is smaller (in magnitude) than the emf transfer term

$\langle \bar{\mathbf{J}} \cdot \bar{\mathcal{E}} \rangle$  for small Rayleigh numbers. However, both terms become comparable near  $\text{Ra} \approx 10 \text{ Ra}_{\text{crit}}$ , and both act to generate a large-scale magnetic field. For  $\text{Ek} = 3 \times 10^{-6}$  there is a saturation in the mean-mean term, and both the mean-mean transfer term and the emf transfer term are comparable in magnitude at the largest value of  $\text{Ra}$ .

For the multipolar  $\text{Ek} = 10^{-4}$  cases (the three largest Rayleigh number cases), the mean-mean generation term eventually becomes weak again where it is nearly an order of magnitude smaller than the corresponding emf transfer. The mean ohmic dissipation is generally an increasing function of  $\text{Ra}$  outside of this transition to multipolar dynamos.

Since the zonal component of the mean velocity is larger than the corresponding meridional components, we should expect that the mean magnetic to mean kinetic energy transfer term is dominated by the zonal contribution. The data show that the zonal component of the mean-mean transfer term is about an order of magnitude larger than the meridional component. The mean zonal velocity is also about an order of magnitude larger than the meridional components indicating that the different directions of the Lorentz force are of similar magnitude. All three contributions to the mean-mean transfer term have the same sign and act to generate mean magnetic energy.

For comparison with the large-scale energetics, it is helpful also to examine the small-scale energetics. Time and volume averaging Equation 4.20 yields the balance relation

$$\varepsilon'_B = -\langle \mathbf{u}' \cdot \mathbf{J}' \times \bar{\mathbf{B}} \rangle - \langle \bar{\mathbf{u}} \cdot \mathbf{J}' \times \mathbf{B}' \rangle - \langle \mathbf{u}' \cdot \mathbf{J}' \times \mathbf{B}' \rangle, \quad (4.24)$$

where the fluctuating ohmic dissipation appears as

$$\varepsilon'_B = \frac{1}{\text{Pm}} \langle \mathbf{J}'^2 \rangle. \quad (4.25)$$

The three terms on the right hand side of the balance relation correspond to: (1) the transfer of small-scale kinetic energy to small-scale magnetic energy by the large-scale magnetic field,  $\langle \mathbf{u}' \cdot \mathbf{J}' \times \bar{\mathbf{B}} \rangle$ ; (2) the transfer of large-scale kinetic energy to small-scale magnetic energy,  $\langle \bar{\mathbf{u}} \cdot \mathbf{J}' \times \mathbf{B}' \rangle$ ; and (3) the transfer of small-scale kinetic energy to small-scale magnetic energy by the small-scale magnetic field,  $\langle \mathbf{u}' \cdot \mathbf{J}' \times \mathbf{B}' \rangle$ . Figure 4.11(b) shows each of these terms. We find

that the fluctuating ohmic dissipation  $\varepsilon'_B$  is up to two orders of magnitude larger than the mean ohmic dissipation  $\bar{\varepsilon}_B$ . This is consistent with the observation that the fluctuating magnetic energy is larger than the mean magnetic energy. The transfer of large-scale kinetic energy to small-scale magnetic energy,  $\langle \bar{\mathbf{u}} \cdot \mathbf{J}' \times \mathbf{B}' \rangle$ , is generally negligible in comparison with the two other small-scale magnetic energy source terms. The transfer of small-scale kinetic energy to small-scale magnetic energy,  $\langle \mathbf{u}' \cdot \mathbf{J}' \times \mathbf{B}' \rangle$ , is the largest small-scale source term. The large-scale magnetic field transfer term,  $\langle \mathbf{u}' \cdot \mathbf{J}' \times \bar{\mathbf{B}} \rangle$ , is nonnegligible in the overall balance. For multipolar dynamo cases, all terms involving a large-scale magnetic field become negligible.

#### 4.8 Heat Transfer Induced by the Mean Field

Although the force balances occurring in the mean meridional and zonal components of the mean momentum equation are of different asymptotic size, there are some interesting consequences in terms of the large-scale energetics. The balance equation governing the large-scale energetics is found by computing the inner product of the semi-MS balance equations with the mean velocity (see Appendix B for a full derivation) and reads

$$0 \approx -\frac{1}{\text{Ek}} \nabla \cdot (\bar{\mathbf{u}} \bar{\mathbf{P}}) + \frac{\text{Ra}}{\text{Pr}} \frac{r}{r_o} \bar{u}_r \bar{T} + \frac{1}{\text{EkPm}} \bar{u}_\phi (\bar{\mathbf{J}} \times \bar{\mathbf{B}})_\phi. \quad (4.26)$$

Integrating the above balance over the domain yields

$$-\left\langle \frac{1}{\text{EkPm}} \bar{u}_\phi (\bar{\mathbf{J}} \times \bar{\mathbf{B}})_\phi \right\rangle \approx \left\langle \frac{\text{Ra}}{\text{Pr}} \frac{r}{r_o} \bar{u}_r \bar{T} \right\rangle. \quad (4.27)$$

Figure 4.12 shows these two terms for all cases with  $\text{Pm} = 2$ . The terms are well-balanced in the lowest Ekman cases, with only a factor of 2 to 3 difference in the largest Ekman simulations. This balance shows that, to leading order, the mean buoyancy force does net work only in the presence of mean ohmic dissipation. Thus, a large-scale axisymmetric overturning convective motion is present in rotating dynamos, providing one possible mechanism that allows for enhanced heat transport in dynamos relative to nonmagnetic convection. The consequences of this effect are analyzed below.

The mean convective heat flux can be written as,

$$\bar{u}_r \bar{T} = \bar{u}_r \bar{T} + \bar{u}'_r \bar{T}', \quad (4.28)$$

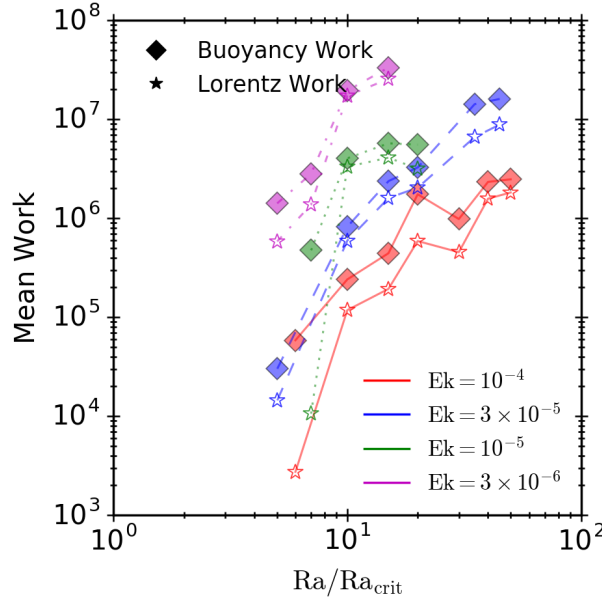


Figure 4.12: Time and volume averaged mean buoyancy work and the zonal contribution of the mean Lorentz work as a function of Rayleigh number. These are the two terms that appear in Equation 4.27. There is good agreement in the values for lower Ekman numbers and only a factor of 2-3 difference for the largest Ekman.

which shows that both the meridional circulation and the small-scale convection will contribute to heat transfer. An important question is whether these different terms scale with  $\text{Ek}$ . We find that  $\bar{u}_r = \mathcal{O}(\text{Ek}^{-1/6})$  and  $\bar{T} = \mathcal{O}(1)$ , such that  $\bar{u}_r \bar{T} = \mathcal{O}(\text{Ek}^{-1/6})$ . The linear theory for the onset of convection in spherical geometry (and for the cylindrical annulus; see Busse, 1970; Calkins et al., 2013) assumes  $u'_r = \mathcal{O}(\text{Ek}^{-1/3})$  and  $T' = \mathcal{O}(1)$ . However, in the plane layer geometry, the small-scale convective speeds scale as  $\mathcal{O}(\text{Ek}^{-1/3})$ , whereas the fluctuating temperature scales as  $\mathcal{O}(\text{Ek}^{1/3})$ . Therefore, using the existing linear spherical theory suggests that  $\overline{u'_r T'} = \mathcal{O}(\text{Ek}^{-1/3})$ , whereas the plane layer scaling should give  $\mathcal{O}(1)$ .

To test the scaling behavior of the heat transfer we volume average the convective heat flux

$$\langle \overline{u_r T} \rangle = \langle \bar{u}_r \bar{T} \rangle + \langle \overline{u'_r T'} \rangle, \quad (4.29)$$

and compute the ratio

$$f_c \equiv \frac{\langle \bar{u}_r \bar{T} \rangle}{\langle u_r T \rangle}, \quad (4.30)$$

which we refer to as the mean convective heat flux ratio. We would, for instance, expect values of  $f_c \rightarrow 0$  in nonrotating convection. Figure 4.13(a) shows this ratio as a function of Rayleigh number. There is no clear systematic dependence on  $\text{Ek}$ , indicating that both contributions to the mean heat flux may scale with  $\text{Ek}$  in the same way, i.e.,  $\bar{u}_r \bar{T} \sim \bar{u}'_r \bar{T}' = \mathcal{O}(\text{Ek}^{-1/6})$ , which lies between the predictions from plane layer theory and linear spherical theory. Figure 4.13(b) shows the eddy-eddy contribution of the mean heat flux rescaled by  $\text{Ek}^{1/6}$ . There is good collapse of the data indicating the heat flux has a scaling exponent of  $-1/6$ .

Using the linear theory predictions of  $u'_r = \mathcal{O}(\text{Ek}^{-1/3})$ , these scalings for the heat flux suggest that the fluctuating temperature has a dependence on the Ekman number that scales as  $T' = \mathcal{O}(\text{Ek}^{1/6})$ . However, the observed scaling for the fluctuating temperature is  $\mathcal{O}(1)$ . This discrepancy was also discussed in Section 3.4.1. The reasoning for this discrepancy is not yet known and still under investigation.

One of the primary reasons the mean-mean heat transfer term is small is due to the relatively small contribution of the mean magnetic energy to the total magnetic energy, i.e., the ratio  $\bar{E}_{\text{mag}}/E_{\text{mag}}$  is less than 0.4 in all of our simulations. We expect that if more realistic (i.e., planetary-like) values of  $Pm$  are employed, heat transport by meridional circulation should increase since mean ohmic dissipation likely also will increase. Thus, this effect may become more important in future simulations carried out with more extreme parameters.

## 4.9 Induction Equation Balances

To understand further the large-scale magnetic field behavior with varying  $\text{Ek}$  and  $\text{Ra}$ , an analysis of the mean induction equation is completed in this section. One of the primary goals is to understand the asymptotic scalings of the terms in the induction equation, if such scalings exist. We first investigate the scaling behavior of the various terms in the mean induction equation for a fixed Ekman number as the Rayleigh number is varied. We then explore the Ekman number dependence for a fixed supercriticality.

The relative sizes of the different terms present in the mean induction equation were computed

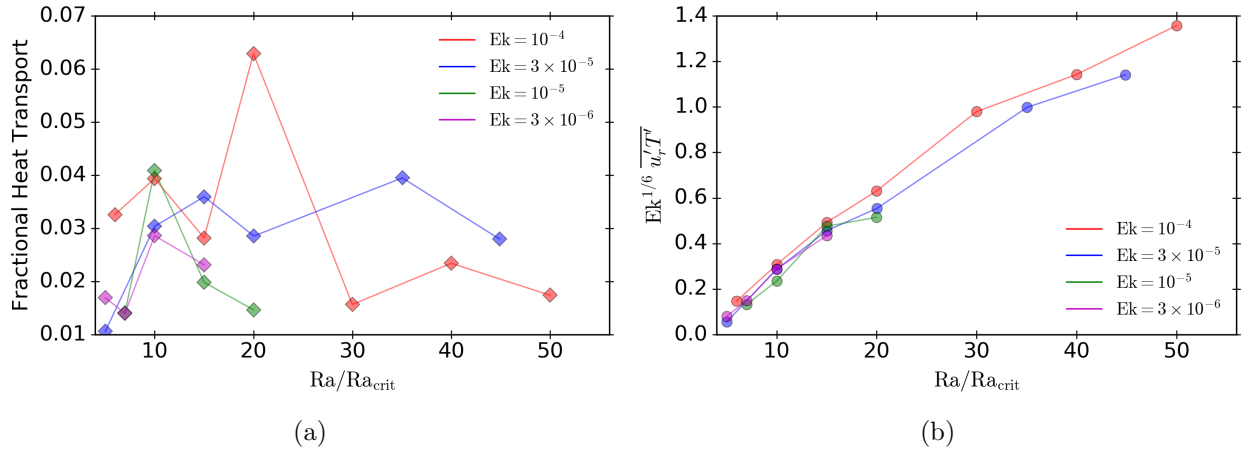


Figure 4.13: (a) Fractional mean heat flux for all simulations with  $Pm = 2$ . (b) Volume averaged heat transport for the eddy-eddy contribution for all cases with  $Pm = 2$  and rescaled by  $Ek^{1/6}$ .

for all cases. We compute a root-mean square average that does not include the Ekman layer on either the inner or outer boundary, then apply a time-average. For clarity, only results for a single Ekman number are shown in Figure 4.14; all other cases exhibit qualitatively similar behavior. We plot results from both the radial and zonal components of the mean induction equation. The behavior of the terms appearing in the  $\theta$  component is similar to the radial component. For both the radial and zonal components, we find that both the time-derivative and the curl of the emf are approximately equal in magnitude. This result is expected when the small-scale magnetic Reynolds number is order unity, i.e.,  $RmEk^{1/3} = \mathcal{O}(1)$ , which is certainly satisfied here (Calkins et al., 2015). By comparison, the stretching of mean magnetic field by the mean velocity field,  $\bar{\mathbf{B}} \cdot \nabla \bar{\mathbf{u}}$ , is smaller in magnitude, though still significant. Indeed, the energy analysis of the previous section showed that this term makes a nonnegligible contribution to the mean ohmic dissipation. We also note that these results suggest that the radial stretching term is comparable to the zonal stretching term in magnitude. The zonal component is systematically larger than the radial component, but only by a factor of about 2. The reason for such similar magnitudes is not yet understood. Diffusion of mean magnetic field plays a similar role to the stretching term; both of these terms show similar scaling behavior with Ra. For most of the simulations we find that advection of the mean magnetic

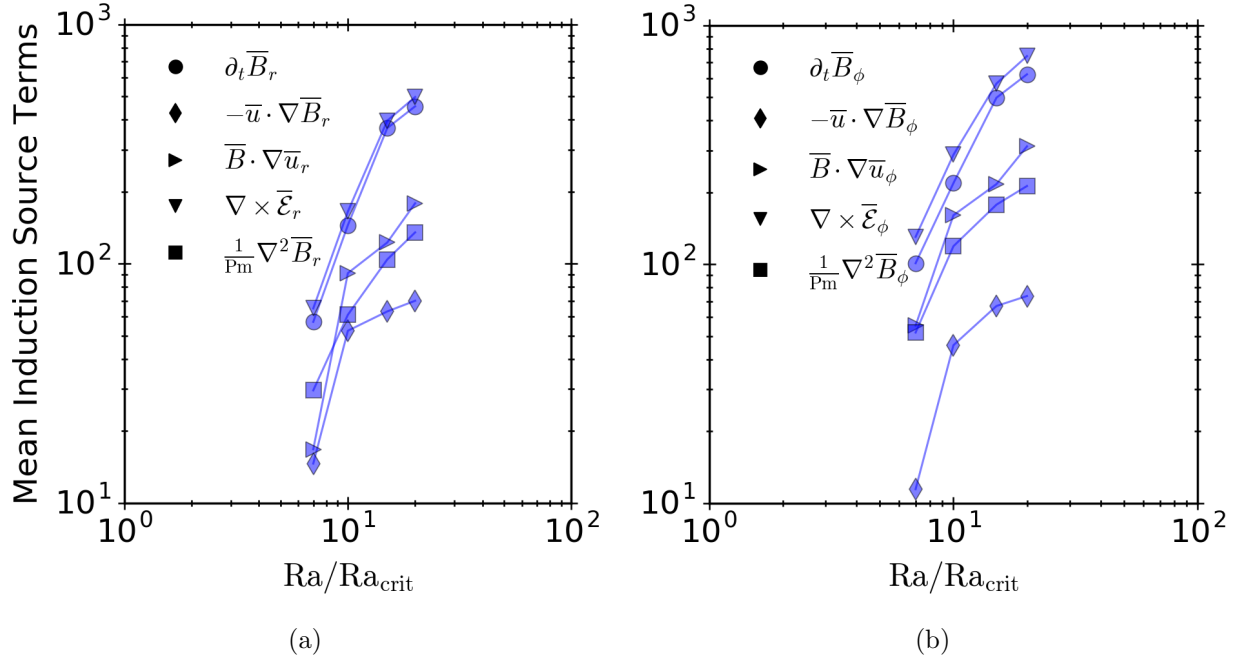


Figure 4.14: Time-averaged rms values of the terms in components of the mean induction equation: (a) radial components; (b) zonal components. For clarity, only simulations with  $Pm = 2$  and  $Ek = 10^{-5}$  are shown; simulations with other parameters show qualitatively similar behavior.

field,  $\bar{u} \cdot \nabla \bar{B}$ , is relatively small, with the exception of cases close to the onset of dynamo action.

We now examine the magnitudes of the terms appearing in the mean induction equation for varying Ekman number. For clarity of presentation, we only show results for a fixed supercriticality of  $Ra = 15 Ra_{crit}$ . The terms all are computed with the same method discussed previously. The results are shown in Figure 4.15. The dashed lines indicate scalings of  $Ek^{-1/3}$  and  $Ek^{-1/2}$ , serving as a useful reference. Clearly, the magnitude of any one term depends on both  $Ra$  and  $Ek$ . As expected from the results shown in Figure 4.14, the ordering of the terms remains the same for all Ekman numbers investigated. It is clear that all of the terms increase in magnitude with decreasing Ekman number, suggesting that the quantities within these terms scale with the Ekman number. It appears that, for fixed  $Ra = 15 Ra_{crit}$ , the terms roughly follow a  $\mathcal{O}(Ek^{-1/3})$  scaling. In addition, both the radial and zonal components of the mean induction equation show grossly similar behavior with varying Ekman number.

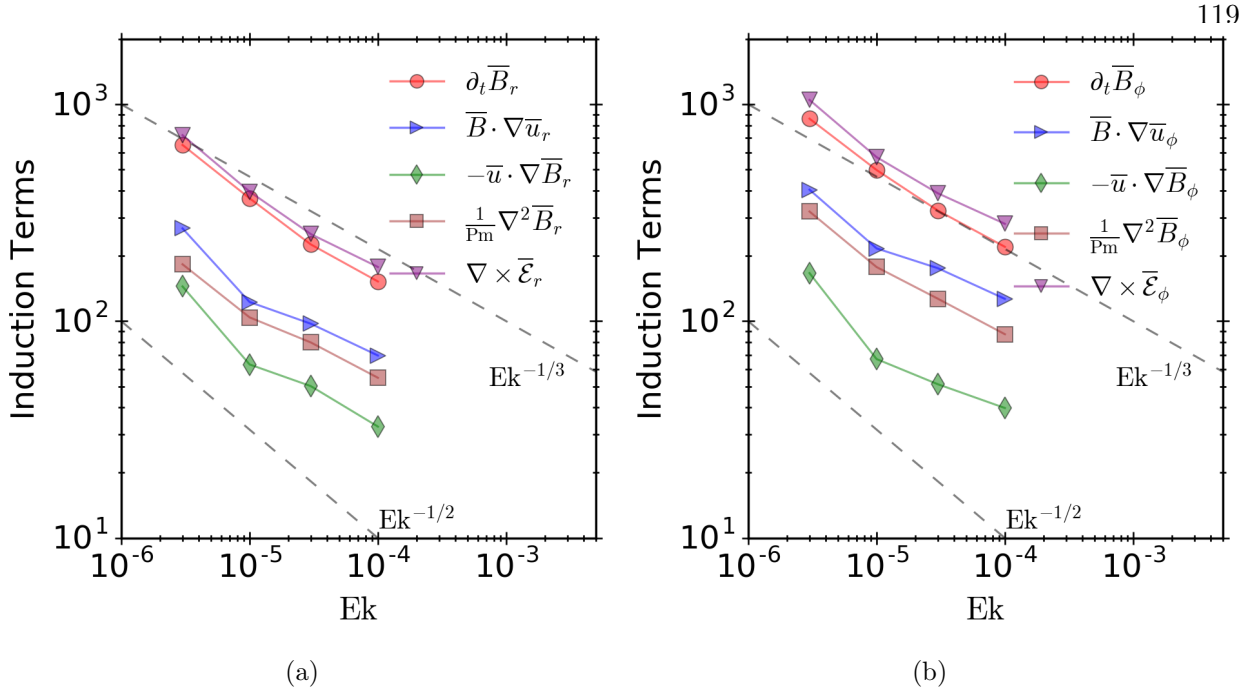


Figure 4.15: Time-averaged rms values of the terms in the mean induction equation as a function of Ekman number for cases with  $\text{Ra} = 15 \text{Ra}_{\text{crit}}$ , (a) the radial components and (b) the zonal components.

The radial component of the shear, shown in Figure 4.15(a), exhibits a slightly flatter slope compared to the emf term. This indicates it could scale weaker than  $\mathcal{O}(\text{Ek}^{-1/3})$ . The zonal component of the shear, shown in Figure 4.15(b), shows the same slope as the emf term, indicating a similar  $\mathcal{O}(\text{Ek}^{-1/3})$  behavior. The advective term in both components shows a slightly weaker scaling, indicating it will not be as important as the other terms when the Ekman number is reduced to smaller values. Some of these scalings are not perfect. This simply means more data with lower Ekman numbers are required to definitively say what the true scalings might be.

In the limit of rapid rotation, to preserve semi-MS balance on the large-scale and geostrophic balance on the small-scale we expect the following asymptotic scalings<sup>1</sup> for the fluctuating and mean velocity,

$$u' = \mathcal{O}(\text{Ek}^{-1/3}), \quad \bar{u}_s = \mathcal{O}(\text{Ek}^{-1/6}), \quad \bar{u}_\phi = \mathcal{O}(\text{Ek}^{-1/3}). \quad (4.31)$$

<sup>1</sup> The origin of these scalings is explored in detail in Chapter 3

Similarly the asymptotic size of the mean and fluctuating magnetic field is expected to be

$$\bar{B} = B' = \mathcal{O}\left(\text{Ek}^{-1/12}\bar{\ell}_B^{1/2}\right), \quad (4.32)$$

where  $\bar{\ell}_B$  is some characteristic length scale for the mean magnetic field. The above scalings can be used to estimate the relative sizes of the terms present in the induction equation. We assume that the del operator scales as  $\nabla = \mathcal{O}\left(\bar{\ell}_B^{-1}\right)$ , regardless whether it acts on the magnetic field, the velocity, or the emf. One possible length scale for the mean magnetic field is the ‘convective envelope’ scale that varies as  $\text{Ek}^{1/6}$  (Jones et al., 2000). We find a posteriori that this scale is consistent with the diffusive length scale for the mean magnetic field. Under this assumption both magnetic fields become  $\mathcal{O}(1)$ . This estimate is approximately true over our investigated range of Ekman number.

Applying these scalings to the meridional components of the induction equation leads to

$$\bar{B} \cdot \nabla \bar{u}_s \sim \frac{\bar{B} \bar{u}_s}{\bar{\ell}_B} = \mathcal{O}\left(\text{Ek}^{-1/3}\right), \quad (4.33)$$

$$\bar{u} \cdot \nabla \bar{B}_s \sim \frac{\bar{u}_s \bar{B}}{\bar{\ell}_B} = \mathcal{O}\left(\text{Ek}^{-1/3}\right), \quad (4.34)$$

$$|\nabla \times \bar{\mathcal{E}}| \sim \frac{u' B'}{\bar{\ell}_B} = \mathcal{O}\left(\text{Ek}^{-1/2}\right), \quad (4.35)$$

$$\frac{1}{\text{Pm}} \nabla^2 \bar{B}_s \sim \frac{\bar{B}}{\bar{\ell}_B^2} = \mathcal{O}\left(\text{Ek}^{-1/3}\right). \quad (4.36)$$

When the zonal component of the induction equation is analyzed in the same way, all terms have the same scaling as the meridional components except for the shear term, which appears as

$$\bar{B} \cdot \nabla \bar{u}_\phi \sim \frac{\bar{B} \bar{u}_\phi}{\bar{\ell}_B} = \mathcal{O}\left(\text{Ek}^{-1/2}\right). \quad (4.37)$$

The data indicates that the time derivative term is comparable in magnitude to the emf term and scales in a similar manner with both Ra and Ek. For this balance to take place, the time scale on

which the mean magnetic field evolves must scale as

$$\partial_t \bar{B} = \frac{\bar{B}}{\tau} = \mathcal{O}(\text{Ek}^{-1/2}). \quad (4.38)$$

This is satisfied if the time scale is  $\tau = \mathcal{O}(\text{Ek}^{1/2})$ . A slope of  $\text{Ek}^{-1/2}$  is indicated in Figure 4.15. Both the radial and zonal components of the time derivative exhibit good agreement with this estimate for lower Ekman numbers. The highest Ekman number shows a departure from this scaling that is closer to  $\text{Ek}^{-1/3}$ .

For the radial components, these scalings indicate that the emf term is the strongest with the shear, advection, and diffusion terms slightly weaker with a flatter slope. This is consistent with Figure 4.15(a), where the emf shows a slightly steeper slope compared to the other terms. The zonal component scalings indicate the emf is expected to have the same slope as the shear term, with the advection and diffusion terms showing a flatter slope. Figure 4.15(b) shows the emf and shear terms have similar slopes. It is less obvious how the advection and diffusion terms behave.

The data suggests that a scaling exponent of  $-1/3$  is appropriate, whereas the scaling arguments from above indicate that some quantities should scale more steeply with a  $-1/2$  slope. The scaling argument invoked some simplifying assumptions, such as the same spatial scale for the shear, advection, and emf terms. Relaxing this assumption would require knowledge of the mean velocity length scale, the mean magnetic length scale, and some estimate of the emf length scale. With the limited number of Ekman numbers included in this study, it is hard to say definitively what the scaling exponents are. Lower Ekman cases will be needed in future work.

## 4.10 Conclusions

The numerical results of 39 dynamo models in a rapidly rotating spherical shell were analyzed to understand large-scale magnetic field generation. The previous work of Kutzner and Christensen (2002) showed a saturation of the dipolar magnetic energy as Ra was increased, but used a single value of Ek and Pm. We extend these results by testing lower values of the Ekman number and more values of the magnetic Prandtl number. As the Rayleigh number was increased, all values of

the Ekman number used in this study showed an initial increase of the mean dipolar magnetic field, followed by a subsequent saturation of the field that was sustained over a finite range in Rayleigh number. Furthermore, we observe a similar saturation behavior in the mean magnetic field, which includes the dipolar component and all higher degrees. We find that the saturation of the mean magnetic field is a robust feature over the range of parameter values investigated here.

All of the simulations in this study have magnetic Prandtl numbers that are orders of magnitude larger compared to geophysical and astrophysical systems. Although the accessible values of  $P_m$  are limited in this study, the data suggests that the relative strength of the the mean magnetic field is controlled by the magnetic Reynolds number: lower values of  $R_m$  lead to larger relative mean fields for a fixed value of the Rayleigh number. As the Ekman number and magnetic Reynolds numbers are decreased even further, we expect the relative mean magnetic field to increase, leading to a predominantly large-scale field morphology, consistent with observations of other Solar System bodies (Jones, 2011).

Upon reaching the saturated mean field regime, the system reaches a semi-magnetostrophic force balance, where the mean Lorentz force only enters the zonal component of the mean momentum equation at leading-order. As a result, the Lorentz force is asymptotically smaller than the forces present in the meridional components of the mean momentum equation. This means the large-scale force balance is not fully magnetostrophic. The fact that the meridional circulation balances the mean zonal Lorentz force in the zonal direction indicates that these dynamos saturate via the Malkus-Proctor scheme in which the large-scale field grows to the same amplitude as the large-scale flow.

Analyzing the mean induction equation terms indicates that the meridional direction is largely governed by the terms involving the emf, giving evidence of an  $\alpha$ -effect. The zonal direction shows a strong stretching term, responsible for shearing the poloidal field into a toroidal field, i.e., the  $\Omega$ -effect. As a result, these dynamos would be considered  $\alpha^2\Omega$  dynamos using the terminology from mean field theory. The scaling argument produces reasonable estimates for the scaling behavior of the various terms. The scaling behaviors were not perfect, indicating that a more complex model

could be in order. Our model only included a single length scale and managed to reproduce most of the scaling behavior. Future work could incorporate multiple length scales. Furthermore, the fluctuating induction equation was not analyzed in this work, but estimates for the scaling of the fluctuating magnetic field were invoked. Future analysis of the fluctuating induction equation could produce a more accurate scaling estimate.

Lastly, our results indicate that these numerical dynamo simulations exhibit an encouraging similarity to stellar observations of magnetic activity as a function of Rossby number (Patten and Simon, 1996; Mohanty and Basri, 2003; Pizzolato et al., 2003; Reiners and Basri, 2007). The observations indicate that a saturation in magnetic activity occurs for rapidly rotating systems below a certain value of Ro. This occurs for multiple types of stars indicating that it is a robust feature of natural dynamo systems. The numerical results discussed here show a similar saturation of magnetic activity for rapidly rotating simulations. This indicates that these simulations could be dynamically similar (in the qualitative sense) to the natural systems.

## Chapter 5

### Final Thoughts

This thesis examined convection and convection-driven dynamos in spherical shells through the use of numerical simulations and millions of computational hours on supercomputers. A consistent theme was the use of parameter studies to provide scaling laws for extrapolating the model results to planetary- and stellar-like parameter regimes.

#### 5.1 Simplified Stellar Models

In Chapter 2 we studied fundamental convection in a solar-like system under the anelastic approximation. Rotation and magnetic fields were excluded. After a parameter sweep over different Prandtl numbers and Rayleigh numbers, we learned that achieving a system where diffusion does not play an appreciable role in the leading-order force balance can be accomplished with moderate values of the diffusivities. We also found a scaling relation for the boundary layer thickness. If the goal of a global simulation with no radiative transfer is to capture accurately the physical extent of the boundary layer, our scaling relation suggests that the Prandtl number should be decreased as the Rayleigh number is increased. The effects of rotation were addressed in the work of Featherstone and Hindman (2016b) and Hindman et al. (2020), although both studies used a Prandtl number of unity. Using a small Prandtl number in the anelastic equations that are rapidly rotating can lead to spurious behavior (Calkins et al., 2015c) that does not exist in nonrotating anelastic convection (Calkins et al., 2015b). Addressing these discrepancies must take place before the Prandtl number sweep described in these results can be extended to the rotating simulations.

## 5.2 Force Balances in Rapidly Rotating Planetary Systems

The results in Chapter 3 focused on the established force balances in these rapidly rotating dynamos and included the first application of asymptotic theory to the large-scale force balance and associated quantities. An important finding from this chapter was the force balance that the large-scale dynamics build and the attempted explanation of this balance using asymptotic theory. The balance is semi-magnetostrophic, where the Lorentz force only enters the zonal component of the mean momentum equation at leading order. Such a balance leaves only the meridional circulation to balance the magnetic field. This indicates that these dynamos saturate via the Malkus-Proctor scenario where the large-scale field grows to the same amplitude as the large-scale flow. This large-scale flow, and thus the Lorentz force, are asymptotically smaller than the forces present in the meridional components of the mean momentum equation. The asymptotic difference is modest, with a separation between the different components of only  $\mathcal{O}(\text{Ek}^{1/6})$ . This separation identifies an upper bound on the level to which Taylor's constraint is satisfied, both in simulations and natural systems. The asymptotic ordering of the forces indicate further that Taylor's constraint can be satisfied (in an approximate sense) even in the absence of a leading-order magnetostrophic balance.

The asymptotic scaling of the fluctuating temperature presents an interesting result in that it scales as  $\mathcal{O}(1)$ . Such scaling behavior is in contrast to the predictions of the asymptotic scaling model as well as predictions from linear theory. It is unclear why this occurs and if it is a hydrodynamical effect or a MHD effect. Future studies could run a hydrodynamical version of the simulations discussed here to see if the fluctuating temperature still shows  $\mathcal{O}(1)$  behavior.

In addition to the fluctuating temperature, estimates of the fluctuating magnetic field also were obtained. The predicted scaling of the fluctuating magnetic field did not depend on the Ekman number, but the data suggested a very clear scaling with  $\text{Ek}$ . This thesis work was focused on the large-scale behavior and therefore the analysis was restricted to the mean evolution equations. Future work could include an analysis of the fluctuating equations to develop improved scaling

arguments. In addition, future studies could look closer at the analytic freedom in writing the equations and how it relates to the analysis. As an example, the mean-mean component of the Lorentz force can be written as  $\bar{\mathbf{B}} \cdot \nabla \bar{\mathbf{B}}$ , where the gradient acts on a single mean quantity. This term can be written equivalently as the divergence of a rank 2 tensor, which is in essence the square of the mean magnetic field. In the first form, the gradient acts on a single mean quantity. The second form has the gradient operating on the product of two mean quantities. This analytic freedom can lead to different estimates of the length scales that are involved. Future analyses could use Rayleigh to output both forms and investigate any differences that could arise.

Lastly, the analysis relied on a particular choice for the field decomposition. Our definition of the large-scale (mean) fields used a simple azimuthal average. This does a reasonable job of differentiating the mean and fluctuations, but it seems likely that nonaxisymmetric ‘large-scale’ motions also could be important (Schaeffer et al., 2017). A necessary improvement may require an additional average in radius to remove completely small-scale motions in that direction.

### 5.3 Saturation of the Large-scale Magnetic Field in Planetary Systems

The discussion presented in Chapter 4 described a suite of rapidly rotating dynamo simulations with several different Ekman numbers. The main result is that dipolar mean magnetic energy saturates as the Rayleigh number is increased for each Ekman number. Furthermore, the mean magnetic energy, which contains both the dipolar mode and all higher modes, exhibited a saturation for all Ekman numbers in the study. This marks the first evidence that the saturation of the mean field is a robust feature of rapidly rotating dynamos. The saturation in our numerical results shows similar behavior to that found in stellar observations for a range of different spectral types (Patten and Simon, 1996; Mohanty and Basri, 2003; Pizzolato et al., 2003; Reiners and Basri, 2007). The similarity between the numerical simulations and the observations hints that these simulations are indeed dynamically similar (in the qualitative sense) to natural systems.

Another important finding from this work was the scaling behavior of the mean convective heat flux. Our results indicate that the heat flux scales as  $\overline{u'_r T'} = \mathcal{O}(\text{Ek}^{-1/6})$ . This result lies in

contrast to the predicted behavior from linear theory and further confirms the unexpected scaling results for the fluctuating temperature that were obtained in Chapter 3. The observed scaling exponent of  $-1/6$  is quite weak over the Ekman numbers in this study. A better constraint on the exact scalings can be achieved with the addition of more cases with lower Ekman numbers.

Dynamo simulations that generate a large-scale magnetic field nearly always include the large-scale magnetic field in the evolution equations. An interesting future study could look into removing the large-scale magnetic field at every iteration in the time evolution. This process could be used to determine the importance of the large-scale magnetic field in its own generation. Can the large-scale field be generated from a purely small-scale magnetic field? This procedure would require careful consideration of the physics, since an artificial energy sink is applied to the system in order to remove the large-scale field. This could have far-reaching implications for analyzing the energetics of the resulting simulations. A related idea with less severe energy considerations would be to “turn off” only the dipole field. The saturation of the mean dipolar magnetic energy is believed to be the main component behind the saturation of the mean magnetic energy. If the dipole component is removed from the simulation, would the mean magnetic energy still show a saturation? This also would require careful consideration of the physical process associated with removing the dipole field. This would have a much smaller impact on the energy budget compared to removing the entire mean field, but it still could be an important effect.

The simulations all show a distinct change in scaling behavior around  $\text{Ra} = 10 \text{Ra}_{\text{crit}}$  for all Ekman numbers that were included. A key question that is raised by this result is why that value? This is a relatively ‘clean’ result suggesting that it potentially could be derived from an analytic approach. In addition to the analytic analysis, this work might benefit from a more formal application of an asymptotic expansion. This could provide more insight into the predicted scaling laws, especially for the fluctuating quantities.

## 5.4 Concluding Remarks

These studies have provided good insight into naturally occurring complex systems. This work also raises more questions. All of the results discussed in this thesis relied on parameter studies. Extending many of these parameter sweeps to include more extreme parameter ranges, even if only by a factor of two, may lead to some very interesting answers and undoubtedly many more questions.

## Bibliography

- Acuna, M. H., Connerney, J. E. P., Wasilewski, P., Lin, R. P., Anderson, K. A., Carlson, C. W., McFadden, J., Curtis, D. W., Mitchell, D., Reme, H., Mazelle, C., Sauvaud, J. A., D'Uston, C., Cros, A., Medale, J. L., Bauer, S. J., Cloutier, P., Mayhew, M., Winterhalter, D., and Ness, N. F. Magnetic Field and Plasma Observations at Mars: Initial Results of the Mars Global Surveyor Mission. *Science*, 279:1676, March 1998. doi: 10.1126/science.279.5357.1676.
- Amit, H. and Olson, P. Helical core flow from geomagnetic secular variation. *Physics of the Earth and Planetary Interiors*, 147:1–25, 2004.
- Ampère, A.-M. Mémoire sur la théorie mathématique des phénomènes électrodynamiques uniquement déduite de l'expérience. *Mémoires de l'Académie Royale des Sciences*, VI, 1823.
- Aubert, J. Steady zonal flows in spherical shell dynamos. *Journal of Fluid Mechanics*, 542:53–67, October 2005. doi: 10.1017/S0022112005006129.
- Aubert, J., Gastine, T., and Fournier, A. Spherical convective dynamos in the rapidly rotating asymptotic regime. *Journal of Fluid Mechanics*, 813:558–593, February 2017. doi: 10.1017/jfm.2016.789.
- Augustson, K. C., Brun, A. S., Miesch, M., and Toomre, J. Grand Minima and Equatorward Propagation in a Cycling Stellar Convective Dynamo. *IAU General Assembly*, 22:2258283, August 2015.
- Augustson, K. C., Brun, A. S., and Toomre, J. The Magnetic Furnace: Intense Core Dynamos in B Stars. *Astrophys. J.*, 829:92, October 2016. doi: 10.3847/0004-637X/829/2/92.
- Aurnou, J. M. and King, E. M. The cross-over to magnetostrophic convection in planetary dynamo systems. *Proceedings of the Royal Society of London Series A*, 473(2199):20160731, March 2017. doi: 10.1098/rspa.2016.0731.
- Aurnou, J. M., Calkins, M. A., Cheng, J. S., Julien, K., King, E. M., Nieves, D., Soderlund, K. M., and Stellmach, S. Rotating convective turbulence in Earth and planetary cores. *Physics of the Earth and Planetary Interiors*, 246:52–71, September 2015. doi: 10.1016/j.pepi.2015.07.001.
- Backus, G. A class of self-sustaining dissipative spherical dynamos. *Annals of Physics*, 4(4):372–447, August 1958. doi: 10.1016/0003-4916(58)90054-X.
- Bercovici, D. The generation of plate tectonics from mantle convection. *Earth and Planetary Science Letters*, 205(3):107 – 121, 2003. ISSN 0012-821X. doi: [https://doi.org/10.1016/S0012-821X\(02\)01009-9](https://doi.org/10.1016/S0012-821X(02)01009-9). URL <http://www.sciencedirect.com/science/article/pii/S0012821X02010099>.

- Biot, J.-B. and Savart, F. Von einer Abhandlung über den Magnetismus der Voltaischen Säule. *Annalen der Physik*, 66(12):392–394, January 1820. doi: 10.1002/andp.18200661203.
- Borrero, J. M. and Ichimoto, K. Magnetic Structure of Sunspots. *Living Reviews in Solar Physics*, 8(1):4, September 2011. doi: 10.12942/lrsp-2011-4.
- Boussinesq, J. Théorie analytique de la chaleur. *Gauthier-Villars*, 1903.
- Braginsky, S. I. On the nearly axially-symmetrical model of the hydromagnetic dynamo of the earth. *Physics of the Earth and Planetary Interiors*, 11(3):191–199, January 1976. doi: 10.1016/0031-9201(76)90063-7.
- Braginsky, S. I. and Roberts, P. H. Equations governing convection in earth's core and the geodynamo. *Geophysical and Astrophysical Fluid Dynamics*, 79:1–97, 1995. doi: 10.1080/03091929508228992.
- Brandenburg, A., Moss, D., and Soward, A. M. New results for the Herzenberg dynamo: steady and oscillatory solutions. *Proceedings of the Royal Society of London Series A*, 454(1973):1283, May 1998. doi: 10.1098/rspa.1998.0207.
- Bray, R. J., Loughhead, R. E., and Durrant, C. J. *The solar granulation*. Cambridge University Press, 2nd edition, 1984.
- Brown, B. P., Miesch, M. S., Browning, M. K., Brun, A. S., and Toomre, J. Magnetic Cycles in a Convective Dynamo Simulation of a Young Solar-type Star. *Astrophys. J.*, 731:69, April 2011. doi: 10.1088/0004-637X/731/1/69.
- Brown, B. P., Vasil, G. M., and Zweibel, E. G. Energy Conservation and Gravity Waves in Soundproof Treatments of Stellar Interiors. Part I. Anelastic Approximations. *Astrophys. J.*, 756(2):109, September 2012. doi: 10.1088/0004-637X/756/2/109.
- Brueckner, G. E., Howard, R. A., Koomen, M. J., Korendyke, C. M., Michels, D. J., Moses, J. D., Socker, D. G., Dere, K. P., Lamy, P. L., Llebaria, A., Bout, M. V., Schwenn, R., Simnett, G. M., Bedford, D. K., and Eyles, C. J. *The Large Angle Spectroscopic Coronagraph (LASCO)*, pages 357–402. Springer Netherlands, Dordrecht, 1995. ISBN 978-94-009-0191-9. doi: 10.1007/978-94-009-0191-9\_10. URL [https://doi.org/10.1007/978-94-009-0191-9\\_10](https://doi.org/10.1007/978-94-009-0191-9_10).
- Brun, A. S., Strugarek, A., Varela, J., Matt, S. P., Augustson, K. C., Emeriau, C., DoCao, O. L., Brown, B., and Toomre, J. On Differential Rotation and Overshooting in Solar-like Stars. *Astrophys. J.*, 836:192, February 2017. doi: 10.3847/1538-4357/aa5c40.
- Brunhes, B. Recherches sur la direction d'aimantation des roches volcaniques. *J. Phys.*, 5:705–724, 1906.
- Brunhes, B. and David, P. Sur la direction d'aimantation dans des couches d'argile transformées en brique par les coulées. *C. R. Hebd. Séances Acad. Sci.*, 131:155–157, 1901.
- Brush, S. G. Discovery of the earths core. *American Journal of Physics*, 48(9):705–724, 1980. doi: 10.1119/1.12026. URL <https://doi.org/10.1119/1.12026>.
- Bullard, E. and Gellman, H. Homogeneous Dynamos and Terrestrial Magnetism. *Philosophical Transactions of the Royal Society of London Series A*, 247(928):213–278, November 1954. doi: 10.1098/rsta.1954.0018.

- Burke, B. F. and Franklin, K. L. Observations of a Variable Radio Source Associated with the Planet Jupiter. *J. Geophys. Res.*, 60(2):213–217, June 1955. doi: 10.1029/JZ060i002p00213.
- Busse, F. H. Thermal instabilities in rapidly rotating systems. *Journal of Fluid Mechanics*, 44: 441–460, January 1970. doi: 10.1017/S0022112070001921.
- Calkins, M. A., Julien, K., and Marti, P. Three-dimensional quasi-geostrophic convection in the rotating cylindrical annulus with steeply sloping endwalls. *Journal of Fluid Mechanics*, 732:214–244, 2013.
- Calkins, M. A., Hale, K., Julien, K., Nieves, D., Driggs, D., and Marti, P. The asymptotic equivalence of fixed heat flux and fixed temperature thermal boundary conditions for rapidly rotating convection. *Journal of Fluid Mechanics*, 784(R2), 2015a.
- Calkins, M. A. Quasi-geostrophic dynamo theory. *Physics of the Earth and Planetary Interiors*, 276:182–189, 2018.
- Calkins, M. A., Julien, K., and Marti, P. Onset of rotating and non-rotating convection in compressible and anelastic ideal gases. *Geophysical & Astrophysical Fluid Dynamics*, 109(4):422–449, 2015b. doi: 10.1080/03091929.2014.987670. URL <http://dx.doi.org/10.1080/03091929.2014.987670>.
- Calkins, M. A., Julien, K., and Marti, P. The breakdown of the anelastic approximation in rotating compressible convection: implications for astrophysical systems. *Proceedings of the Royal Society of London A: Mathematical, Physical and Engineering Sciences*, 471(2175), 2015c. ISSN 1364-5021. doi: 10.1098/rspa.2014.0689. URL <http://rspa.royalsocietypublishing.org/content/471/2175/20140689>.
- Calkins, M. A., Julien, K., Tobias, S. M., and Aurnou, J. M. A multiscale dynamo model driven by quasi-geostrophic convection. *Journal of Fluid Mechanics*, 780:143–166, October 2015. doi: 10.1017/jfm.2015.464.
- Cameron, R. H., Dikpati, M., and Brandenburg, A. The Global Solar Dynamo. *Space Sci. Rev.*, 210(1-4):367–395, September 2017. doi: 10.1007/s11214-015-0230-3.
- Cande, S. C. and Kent, D. V. Revised calibration of the geomagnetic polarity timescale for the Late Cretaceous and Cenozoic. *J. Geophys. Res.*, 100:6093–6095, April 1995. doi: 10.1029/94JB03098.
- Chandrasekhar, S. *Hydrodynamic and hydromagnetic stability*. Dover, 1961.
- Cheng, J. S., Stellmach, S., Ribeiro, A., Grannan, A., King, E. M., and Aurnou, J. M. Laboratory-numerical models of rapidly rotating convection in planetary cores. *Geophysical Journal International*, 201:1–17, April 2015. doi: 10.1093/gji/ggu480.
- Childress, S. and Soward, A. M. Convection-Driven Hydromagnetic Dynamo. *Phys. Rev. Lett.*, 29 (13):837–839, September 1972. doi: 10.1103/PhysRevLett.29.837.
- Christensen, U. Dynamo scaling laws and applications to the planets. *Space Sci. Rev.*, 152:565–590, 2010.
- Christensen, U. R. Geodynamo models: Tools for understanding properties of Earth’s magnetic field. *Physics of the Earth and Planetary Interiors*, 187:157–169, August 2011. doi: 10.1016/j.pepi.2011.03.012.

- Christensen, U. R. and Aubert, J. Scaling properties of convection-driven dynamos in rotating spherical shells and application to planetary magnetic fields. *Geophysical Journal International*, 166:97–114, July 2006. doi: 10.1111/j.1365-246X.2006.03009.x.
- Civet, F., Thébault, E., Verhoeven, O., Langlais, B., and Saturnino, D. Electrical conductivity of the Earth’s mantle from the first Swarm magnetic field measurements. *Geophys. Res. Lett.*, 42(9):3338–3346, May 2015. doi: 10.1002/2015GL063397.
- Connerney, J. 10.06 - planetary magnetism. In Schubert, G., editor, *Treatise on Geophysics (Second Edition)*, pages 195 – 237. Elsevier, Oxford, second edition edition, 2015. ISBN 978-0-444-53803-1. doi: <https://doi.org/10.1016/B978-0-444-53802-4.00171-8>.
- Courtillot, V. and Le Mouel, J. L. Time Variations of the Earth’s Magnetic Field: From Daily to Secular. *Annual Review of Earth and Planetary Sciences*, 16:389, January 1988. doi: 10.1146/annurev.ea.16.050188.002133.
- Cowling, T. G. The magnetic field of sunspots. *Monthly Notices of the Royal Astron. Society*, 94:39–48, November 1933. doi: 10.1093/mnras/94.1.39.
- Davies, C., Pozzo, M., Gubbins, D., and Alfè, D. Constraints from material properties on the dynamics and evolution of Earth’s core. *Nature Geoscience*, 8(9):678–685, September 2015. doi: 10.1038/ngeo2492.
- Delesse, A. Sur le magnétisme polaire dans les minéraux et dans les roches. *Ann. Chimie Phys.*, 25:194–209, 1849.
- Dolginov, S. S., Eroshenko, E. G., and Lewis, L. Nature of the Magnetic Field in the Neighborhood of Venus. *Cosmic Research*, 7:675, September 1969.
- Dormy, E., Soward, A. M., Jones, C. A., Jault, D., and Cardin, P. The onset of thermal convection in rotating spherical shells. *Journal of Fluid Mechanics*, 501:43–70, February 2004. doi: 10.1017/S0022112003007316.
- Dormy, E. Strong-field spherical dynamos. *Journal of Fluid Mechanics*, 789:500–513, February 2016. doi: 10.1017/jfm.2015.747.
- Dormy, E., Oruba, L., and Petitdemange, L. Three branches of dynamo action. *Fluid Dynamics Research*, 50(1):011415, February 2018. doi: 10.1088/1873-7005/aa769c.
- du Trémolet de Lacheisserie, E., Gignoux, D., and Schlenker, M., editors. *Magnetism*. Springer-Verlag New York, 2005. ISBN 9780387229676.
- Duarte, L. D. V., Wicht, J., Browning, M. K., and Gastine, T. Helicity inversion in spherical convection as a means for equatorward dynamo wave propagation. *Monthly Notices of the Royal Astron. Society*, 456(2):1708–1722, 2016. doi: 10.1093/mnras/stv2726. URL <http://dx.doi.org/10.1093/mnras/stv2726>.
- Dziewonski, A. M. and Anderson, D. L. Preliminary reference Earth model. *Physics of the Earth and Planetary Interiors*, 25(4):297–356, Jun 1981. doi: 10.1016/0031-9201(81)90046-7.
- Elphic, R. C. and Russell, C. T. Magnetic flux ropes in the Venus ionosphere: Observations and models. *J. Geophys. Res.*, 88(A1):58–72, January 1983. doi: 10.1029/JA088iA01p00058.

- Elsasser, W. M. On the Origin of the Earth's Magnetic Field. *Physical Review*, 55(5):489–498, March 1939. doi: 10.1103/PhysRev.55.489.
- Elsasser, W. M. Induction Effects in Terrestrial Magnetism Part I. Theory. *Physical Review*, 69 (3-4):106–116, February 1946. doi: 10.1103/PhysRev.69.106.
- Elsasser, W. M. Induction Effects in Terrestrial Magnetism. Part III. Electric Modes. *Physical Review*, 72(9):821–833, November 1947. doi: 10.1103/PhysRev.72.821.
- Faraday, M. V. experimental researches in electricity. *Philosophical Transactions of the Royal Society of London*, 122:125–162, 1832. doi: 10.1098/rstl.1832.0006. URL <https://royalsocietypublishing.org/doi/abs/10.1098/rstl.1832.0006>.
- Featherstone, N. A. and Hindman, B. W. The Spectral Amplitude of Stellar Convection and Its Scaling in the High-Rayleigh-number Regime. *Astrophys. J.*, 818:32, February 2016a. doi: 10.3847/0004-637X/818/1/32.
- Featherstone, N. A. and Hindman, B. W. The Emergence of Solar Supergranulation as a Natural Consequence of Rotationally Constrained Interior Convection. *Astrophys. J. Lett.*, 830:L15, October 2016b. doi: 10.3847/2041-8205/830/1/L15.
- Folgheraiter, G. Sur les variations séculaires de l'inclinaison magnétique dans l'antiquité. *J. Phys.*, 8:5–16, 1899.
- Gaidos, E., Conrad, C. P., Manga, M., and Hernlund, J. Thermodynamic Limits on Magnetodynamics in Rocky Exoplanets. *Astrophys. J.*, 718:596–609, August 2010. doi: 10.1088/0004-637X/718/2/596.
- Gailitis, A. On the Theory of Herzenberg's Dynamo. *Magnitnaia Gidrodinamika*, 4, 1973.
- Gastine, T., Wicht, J., and Aurnou, J. M. Turbulent Rayleigh-Bénard convection in spherical shells. *Journal of Fluid Mechanics*, 778:721–764, September 2015. doi: 10.1017/jfm.2015.401.
- Gastine, T., Wicht, J., and Aubert, J. Scaling regimes in spherical shell rotating convection. *Journal of Fluid Mechanics*, 808:690–732, December 2016. doi: 10.1017/jfm.2016.659.
- Gillet, N., Jault, D., and Finlay, C. C. Planetary gyre, time-dependent eddies, torsional waves, and equatorial jets at the Earth's core surface. *J. Geophys. Res.*, 120:3991–4013, 2015.
- Gillet, N., Jault, D., Canet, E., and Fournier, A. Fast torsional waves and strong magnetic field within the Earth's core. *Nature*, 465(7294):74–77, May 2010. doi: 10.1038/nature09010.
- Gilman, P. A. Nonlinear Dynamics of Boussinesq Convection in a Deep Rotating Spherical Shell. I. *Geophysical and Astrophysical Fluid Dynamics*, 8:93–135, January 1977. doi: 10.1080/03091927708240373.
- Gilman, P. A. and Glatzmaier, G. A. Compressible convection in a rotating spherical shell. I - Anelastic equations. II - A linear anelastic model. III - Analytic model for compressible vorticity waves. *Astrophys. J. Supp.*, 45:335–388, February 1981. doi: 10.1086/190714.
- Gilman, P. A. Linear Simulations of Boussinesq Convection in a Deep Rotating Spherical Shell. *Journal of Atmospheric Sciences*, 32(7):1331–1352, July 1975. doi: 10.1175/1520-0469(1975)032<1331:LSOBCI>2.0.CO;2.

- Glatzmaier, G. A. and Roberts, P. H. A three-dimensional convective dynamo solution with rotating and finitely conducting inner core and mantle. *Physics of the Earth and Planetary Interiors*, 91(1):63–75, January 1995a. doi: 10.1016/0031-9201(95)03049-3.
- Glatzmaier, G. A. and Roberts, P. H. A three-dimensional self-consistent computer simulation of a geomagnetic field reversal. *Nature*, 377(6546):203–209, September 1995b. doi: 10.1038/377203a0.
- Goudard, L. and Dormy, E. Relations between the dynamo region geometry and the magnetic behavior of stars and planets. *EPL (Europhysics Letters)*, 83:59001, September 2008. doi: 10.1209/0295-5075/83/59001.
- Gough, D. O. The Anelastic Approximation for Thermal Convection. *Journal of Atmospheric Sciences*, 26:448–456, May 1969. doi: 10.1175/1520-0469(1969)026<0448:TAAFTC>2.0.CO;2.
- Greer, B. J., Hindman, B. W., Featherstone, N. A., and Toomre, J. Helioseismic Imaging of Fast Convective Flows throughout the Near-surface Shear Layer. *Astrophys. J. Lett.*, 803:L17, April 2015. doi: 10.1088/2041-8205/803/2/L17.
- Griffiths, D. J. *Introduction to Electrodynamics*. Prentice Hall, 3rd edition, 1999. ISBN 9780138053260.
- Guervilly, C., Cardin, P., and Schaeffer, N. Turbulent convective length scale in planetary cores. *Nature*, 570(7761):368–371, June 2019. doi: 10.1038/s41586-019-1301-5.
- Hale, G. E. On the Probable Existence of a Magnetic Field in Sun-Spots. *Astrophys. J.*, 28:315, November 1908. doi: 10.1086/141602.
- Hale, G. E., Ellerman, F., Nicholson, S. B., and Joy, A. H. The Magnetic Polarity of Sun-Spots. *Astrophys. J.*, 49:153, April 1919. doi: 10.1086/142452.
- Halley, E. The Theory of the Variation of the Magnetical Compass. *Philosophical Transactions of the Royal Society of London Series I*, 13:208–221, January 1683.
- Hanasoge, S. M., Duvall, T. L., and Sreenivasan, K. R. Anomalously weak solar convection. *Proceedings of the National Academy of Science*, 109:11928–11932, July 2012. doi: 10.1073/pnas.1206570109.
- Hanasoge, S., Gizon, L., and Sreenivasan, K. R. Seismic Sounding of Convection in the Sun. *Annual Review of Fluid Mechanics*, 48(1):191–217, January 2016. doi: 10.1146/annurev-fluid-122414-034534.
- Hardy, C. M., Livermore, P. W., Niesen, J., Luo, J., and Li, K. Determination of the instantaneous geostrophic flow within the three-dimensional magnetostrophic regime. *Proceedings of the Royal Society of London Series A*, 474(2218):20180412, 2018.
- Hart, A. B. Motions in the Sun at the photospheric level. IV. The equatorial rotation and possible velocity fields in the photosphere. *Monthly Notices of the Royal Astron. Society*, 114:17, 1954. doi: 10.1093/mnras/114.1.17.
- Hathaway, D. H., Beck, J. G., Bogart, R. S., Bachmann, K. T., Khatri, G., Petitto, J. M., Han, S., and Raymond, J. The Photospheric Convection Spectrum. *Solar Physics*, 193:299–312, April 2000. doi: 10.1023/A:1005200809766.

- Hathaway, D. H., Teit, T., Norton, A. A., and Kitiashvili, I. The Sun's Photospheric Convection Spectrum. *Astrophys. J.*, 811:105, October 2015. doi: 10.1088/0004-637X/811/2/105.
- Heaviside, O. *Electrical Papers*, volume 1. Macmillan and Co., 1892.
- Held, L. E. and Latter, H. N. Hydrodynamic convection in accretion discs. *Monthly Notices of the Royal Astron. Society*, 480(4):4797–4816, 08 2018. ISSN 0035-8711. doi: 10.1093/mnras/sty2097. URL <https://doi.org/10.1093/mnras/sty2097>.
- Herzenberg, A. Geomagnetic Dynamos. *Philosophical Transactions of the Royal Society of London Series A*, 250(986):543–583, August 1958. doi: 10.1098/rsta.1958.0007.
- Hindman, B. W., Haber, D. A., and Toomre, J. Subsurface Circulations within Active Regions. *Astrophys. J.*, 698(2):1749–1760, June 2009. doi: 10.1088/0004-637X/698/2/1749.
- Hindman, B. W., Featherstone, N. A., and Julien, K. Morphological Classification of the Convective Regimes in Rotating Stars. *Astrophys. J.*, 898(2):120, August 2020. doi: 10.3847/1538-4357/ab9ec2.
- Hood, L. L. and Hartdegen, K. A crustal magnetization model for the magnetic field of Mars: A preliminary study of the Tharsis Region. *Geophys. Res. Lett.*, 24(6):727–730, January 1997. doi: 10.1029/97GL00497.
- Hough, S. S. and Darwin, G. H. IX. on the application of harmonic analysis to the dynamical theory of the tides. part i. on laplace's "oscillations of the first species" and the dynamics of ocean currents. *Philosophical Transactions of the Royal Society of London. Series A, Containing Papers of a Mathematical or Physical Character*, 189:201–257, 1897. doi: 10.1098/rsta.1897.0009. URL <https://royalsocietypublishing.org/doi/abs/10.1098/rsta.1897.0009>.
- Howard, R., Gilman, P. I., and Gilman, P. A. Rotation of the sun measured from Mount Wilson white-light images. *Astrophys. J.*, 283:373–384, August 1984. doi: 10.1086/162315.
- Howard, R. F., Sivaraman, K. R., Gupta, S. S., and Gilman, P. I. Sunspot Motions from a Study of Kodaikanal and Mount Wilson Observations. In Priest, E. R. and Krishan, V., editors, *Basic Plasma Processes on the Sun*, volume 142 of *IAU Symposium*, page 107, January 1990.
- Hulot, G., Eymin, C., Langlais, B., Mandea, M., and Olsen, N. Small-scale structure of the geodynamo inferred from Oersted and Magsat satellite data. *Nature*, 416:620–623, 2002.
- Jault, D. Axial invariance of rapidly varying diffusionless motions in the Earth's core interior. *Physics of the Earth and Planetary Interiors*, 166(1-2):67–76, January 2008. doi: 10.1016/j.pepi.2007.11.001.
- Jault, D. Illuminating the electrical conductivity of the lowermost mantle from below. *Geophysical Journal International*, 202(1):482–496, July 2015. doi: 10.1093/gji/ggv152.
- Jeffreys, H. The Rigidity of the Earth's Central Core. *Geophysical Journal*, 1:371–383, June 1926. doi: 10.1111/j.1365-246X.1926.tb05385.x.
- Jones, C. A. Planetary Magnetic Fields and Fluid Dynamos. *Annual Review of Fluid Mechanics*, 43:583–614, January 2011. doi: 10.1146/annurev-fluid-122109-160727.

- Jones, C. A. A dynamo model of Jupiter's magnetic field. *Icarus*, 241:148–159, October 2014. doi: 10.1016/j.icarus.2014.06.020.
- Jones, C. A., Boronski, P., Brun, A. S., Glatzmaier, G. A., Gastine, T., Miesch, M. S., and Wicht, J. Anelastic convection-driven dynamo benchmarks. *Icarus*, 216:120–135, November 2011. doi: 10.1016/j.icarus.2011.08.014.
- Jones, C. A., Soward, A. M., and Mussa, A. I. The onset of thermal convection in a rapidly rotating sphere. *Journal of Fluid Mechanics*, 405(1):157–179, February 2000. doi: 10.1017/S0022112099007235.
- Julien, K., Aurnou, J. M., Calkins, M. A., Knobloch, E., Marti, P., Stellmach, S., and Vasil, G. M. A nonlinear model for rotationally constrained convection with Ekman pumping. *Journal of Fluid Mechanics*, 798:50–87, July 2016. doi: 10.1017/jfm.2016.225.
- Julien, K., Knobloch, E., and Werne, J. A New Class of Equations for Rotationally Constrained Flows. *Theoretical and Computational Fluid Dynamics*, 11:251–261, January 1998. doi: 10.1007/s001620050092.
- Kageyama, A., Sato, T., and Complexity Simulation Group. Computer simulation of a magnetohydrodynamic dynamo. II. *Physics of Plasmas*, 2(5):1421–1431, May 1995. doi: 10.1063/1.871485.
- Käpylä, P. J., Mantere, M. J., and Brandenburg, A. Oscillatory large-scale dynamos from Cartesian convection simulations. *Geophysical and Astrophysical Fluid Dynamics*, 107:244–257, February 2013. doi: 10.1080/03091929.2012.715158.
- King, E. M., Soderlund, K. M., Christensen, U. R., Wicht, J., and Aurnou, J. M. Convective heat transfer in planetary dynamo models. *Geochemistry, Geophysics, Geosystems*, 11:Q06016, June 2010. doi: 10.1029/2010GC003053.
- Kuang, W. and Bloxham, J. An Earth-like numerical dynamo model. *Nature*, 389:371–374, September 1997. doi: 10.1038/38712.
- Kuang, W. and Bloxham, J. Numerical Modeling of Magnetohydrodynamic Convection in a Rapidly Rotating Spherical Shell: Weak and Strong Field Dynamo Action. *Journal of Computational Physics*, 153:51–81, July 1999. doi: 10.1006/jcph.1999.6274.
- Kutzner, C. and Christensen, U. R. From stable dipolar towards reversing numerical dynamos. *Physics of the Earth and Planetary Interiors*, 131:29–45, June 2002. doi: 10.1016/S0031-9201(02)00016-X.
- Langel, R. A. The magnetic Earth as seen from MAGSAT, initial results. *Geophys. Res. Lett.*, 9 (4):239–242, April 1982. doi: 10.1029/GL009i004p00239.
- Lantz, S. R. *Dynamical Behavior of Magnetic Fields in a Stratified, Convecting Fluid Layer*. PhD thesis, CORNELL UNIVERSITY., January 1992.
- Larmor, J. How could a rotating body such as the sun become a magnet? *Reports of the British Association*, 87:159–160, 1919.
- Layer, P. W., Kröner, A., and McWilliams, M. An archean geomagnetic reversal in the kaap valley pluton, south africa. *Science*, 273(5277):943–946, 1996. ISSN 0036-8075. doi: 10.1126/science.273.5277.943.

- Lehmann, I. P'. *Publications du Bureau Central Séismologique International*, 14:87–115, 1936.
- Leighton, R. B., Noyes, R. W., and Simon, G. W. Velocity Fields in the Solar Atmosphere. I. Preliminary Report. *Astrophys. J.*, 135:474, March 1962. doi: 10.1086/147285.
- Li, K., Jackson, A., and Livermore, P. W. Taylor state dynamos found by optimal control: axisymmetric examples. *Journal of Fluid Mechanics*, 853:647–697, 2018.
- Livermore, P. W., Hollerbach, R., and Finlay, C. C. An accelerating high-latitude jet in Earth's core. *Nature Geo.*, 10:62–68, 2017.
- Livermore, P. W., Bailey, L. M., and Hollerbach, R. A comparison of no-slip, stress-free and inviscid models of rapidly rotating fluid in a spherical shell. *Sci. Rep.*, 6:22812, 2016.
- Lord, J. W., Cameron, R. H., Rast, M. P., Rempel, M., and Roudier, T. The Role of Subsurface Flows in Solar Surface Convection: Modeling the Spectrum of Supergranular and Larger Scale Flows. *Astrophys. J.*, 793:24, September 2014. doi: 10.1088/0004-637X/793/1/24.
- Luhmann, J. G., Tatrallyay, M., Russell, C. T., and Winterhalter, D. Magnetic field fluctuations in the Venus magnetosheath. *Geophys. Res. Lett.*, 10(8):655–658, August 1983. doi: 10.1029/GL010i008p00655.
- Malkus, W. V. R. and Proctor, M. R. E. The macrodynamics of  $\alpha$ -effect dynamos in rotating fluids. *Journal of Fluid Mechanics*, 67:417–443, 1975.
- Matsui, H., Heien, E., Aubert, J., Aurnou, J. M., Avery, M., Brown, B., Buffet, B. A., Busse, F., Christensen, U. R., Davies, C. J., Featherstone, N., Gastine, T., Glatzmaier, G. A., Gubbins, D., Guermond, J.-L., Hayashi, Y.-Y., Hollerbach, R., Hwang, L. J., Jackson, A., Jones, C. A., Jiang, W., Kellogg, L. H., Kuang, W., Landeau, M., Marti, P., Olson, P., Ribeiro, A., Sasaki, Y., Schaeffer, N., Simitev, R. D., Sheyko, A., Silva, L., Stanley, S., Takahashi, F., Takehiro, S.-i., Wicht, J., and Willis, A. P. Performance benchmarks for a next generation numerical dynamo model. *Geochemistry, Geophysics, Geosystems*, 17:1586–1607, May 2016. doi: 10.1002/2015GC006159.
- Maxwell, J. C. On physical lines of force. *Philosophical Magazine*, 90:11–23, 1861. doi: 10.1080/14786431003659180. URL <https://doi.org/10.1080/14786431003659180>.
- Maxwell, J. C. Viii. a dynamical theory of the electromagnetic field. *Philosophical Transactions of the Royal Society of London*, 155:459–512, 1865. doi: 10.1098/rstl.1865.0008. URL <https://royalsocietypublishing.org/doi/abs/10.1098/rstl.1865.0008>.
- Melloni, M. Sur l'aimantation des roches volcaniques. *C. R. Hebd. Séances Acad Sci.*, 37:229–231, 1853.
- Mercanton, P. Inversion de l'inclinaison magnétique terrestre aux âges géologiques. *J. Geophys. Res.*, 31:187–190, 1926.
- Merrill, R. T., McElhinny, M., and McFadden, P. *The Magnetic Field of the Earth: Paleomagnetism, the Core, and the Deep Mantle*. International geophysics series. Academic Press, 1998. ISBN 9780124912465. URL <https://books.google.com/books?id=96AP14nK91IC>.

- Miesch, M. S., Brun, A. S., DeRosa, M. L., and Toomre, J. Structure and Evolution of Giant Cells in Global Models of Solar Convection. *Astrophys. J.*, 673:557–575, January 2008. doi: 10.1086/523838.
- Miesch, M. S., Featherstone, N. A., Rempel, M., and Trampedach, R. On the Amplitude of Convective Velocities in the Deep Solar Interior. *Astrophys. J.*, 757:128, October 2012. doi: 10.1088/0004-637X/757/2/128.
- Moffatt, H. K. *Magnetic Field Generation in Electrically Conducting Fluids*. Cambridge Univ. Press, Cambridge, 1978.
- Mohanty, S. and Basri, G. Rotation and Activity in Mid-M to L Field Dwarfs. *Astrophys. J.*, 583 (1):451–472, January 2003. doi: 10.1086/345097.
- Nelson, N. J., Brown, B. P., Sacha Brun, A., Miesch, M. S., and Toomre, J. Buoyant Magnetic Loops Generated by Global Convective Dynamo Action. *Solar Physics*, 289:441–458, February 2014. doi: 10.1007/s11207-012-0221-4.
- Ness, N. F., Behannon, K. W., Lepping, R. P., and Whang, Y. C. Magnetic field of Mercury confirmed. *Nature*, 255(5505):204–205, May 1975a. doi: 10.1038/255204a0.
- Ness, N. F., Behannon, K. W., Lepping, R. P., and Whang, Y. C. The magnetic field of Mercury, I. *J. Geophys. Res.*, 80(19):2708, July 1975b. doi: 10.1029/JA080i019p02708.
- Ness, N. F., Acuna, M. H., Behannon, K. W., Burlaga, L. F., Connerney, J. E. P., Lepping, R. P., and Neubauer, F. M. Magnetic Fields at Uranus. *Science*, 233(4759):85–89, July 1986. doi: 10.1126/science.233.4759.85.
- Ness, N. F. Intrinsic Magnetic Fields of the Planets: Mercury to Neptune. *Philosophical Transactions of the Royal Society of London Series A*, 349(1690):249–260, November 1994. doi: 10.1098/rsta.1994.0129.
- Oberbeck, A. Ueber die Wärmeleitung der Flüssigkeiten bei Berücksichtigung der Strömungen infolge von Temperaturdifferenzen. *Annalen der Physik*, 243:271–292, 1879. doi: 10.1002/andp.18792430606.
- Oersted, J. C. Experiments on the effect of a current of electricity on the magnetic needle. *Annals of Philosophy*, 16:273–276, 1820.
- Oldham, R. D. On the Propagation of Earthquake Motion to Great Distances. *Philosophical Transactions of the Royal Society of London Series A*, 194:135–174, January 1900. doi: 10.1098/rsta.1900.0015.
- O'Mara, B., Miesch, M. S., Featherstone, N. A., and Augustson, K. C. Velocity amplitudes in global convection simulations: The role of the Prandtl number and near-surface driving. *Advances in Space Research*, 58:1475–1489, October 2016. doi: 10.1016/j.asr.2016.03.038.
- Orvedahl, R. J., Calkins, M. A., Featherstone, N. A., and Hindman, B. W. Prandtl-number Effects in High-Rayleigh-number Spherical Convection. *Astrophys. J.*, 856(1):13, March 2018. doi: 10.3847/1538-4357/aaaeb5.

- Ossendrijver, M. The solar dynamo. *Astron. Astrophys. Rev.*, 11:287–367, 2003. doi: 10.1007/s00159-003-0019-3.
- Pallavicini, R., Golub, L., Rosner, R., Vaiana, G. S., Ayres, T., and Linsky, J. L. Relations among stellar X-ray emission observed from Einstein, stellar rotation and bolometric luminosity. *Astrophys. J.*, 248:279–290, August 1981. doi: 10.1086/159152.
- Parker, E. N. Hydromagnetic Dynamo Models. *Astrophys. J.*, 122:293, September 1955. doi: 10.1086/146087.
- Pasachoff, J. M., Lockwood, C., Meadors, E., Yu, R., Perez, C., Peñaloza-Murillo, M. A., Seaton, D. B., Voulgaris, A., Dantowitz, R., Rušin, V., and Economou, T. Images and Spectra of the 2017 Total Solar Eclipse Corona from our Oregon Site. *Frontiers in Astronomy and Space Sciences*, 5:37, October 2018. doi: 10.3389/fspas.2018.00037.
- Patten, B. M. and Simon, T. The Evolution of Rotation and Activity in Young Open Clusters: IC 2391. *Astrophys. J. Supp.*, 106:489, October 1996. doi: 10.1086/192346.
- Pavlov, V. and Gallet, Y. Variations in geomagnetic reversal frequency during the Earth’s middle age. *Geochemistry, Geophysics, Geosystems*, 11:Q01Z10, January 2010. doi: 10.1029/2009GC002583.
- Pizzolato, N., Maggio, A., Micela, G., Sciortino, S., and Ventura, P. The stellar activity-rotation relationship revisited: Dependence of saturated and non-saturated X-ray emission regimes on stellar mass for late-type dwarfs. *Astron. Astrophys.*, 397:147–157, January 2003. doi: 10.1051/0004-6361:20021560.
- Plumley, M., Julien, K., Marti, P., and Stellmach, S. The effects of Ekman pumping on quasi-geostrophic Rayleigh-Bénard convection. *Journal of Fluid Mechanics*, 803:51–71, September 2016. doi: 10.1017/jfm.2016.452.
- Pozzo, M., Davies, C., Gubbins, D., and Alfé, D. Thermal and electrical conductivity of iron at Earth’s core conditions. *Nature*, 485(7398):355–358, May 2012. doi: 10.1038/nature11031.
- Proudman, J. and Lamb, H. On the motion of solids in a liquid possessing vorticity. *Proceedings of the Royal Society of London. Series A, Containing Papers of a Mathematical and Physical Character*, 92(642):408–424, 1916. doi: 10.1098/rspa.1916.0026. URL <https://royalsocietypublishing.org/doi/abs/10.1098/rspa.1916.0026>.
- Reiners, A. and Basri, G. The First Direct Measurements of Surface Magnetic Fields on Very Low Mass Stars. *Astrophys. J.*, 656(2):1121–1135, February 2007. doi: 10.1086/510304.
- Reiners, A., Schüssler, M., and Passegger, V. M. Generalized Investigation of the Rotation-Activity Relation: Favoring Rotation Period instead of Rossby Number. *Astrophys. J.*, 794(2):144, October 2014. doi: 10.1088/0004-637X/794/2/144.
- Reshetnyak, M. Y. and Pavlov, V. E. Evolution of the dipole geomagnetic field. Observations and models. *Geomagnetism and Aeronomy*, 56(1):110–124, January 2016. doi: 10.1134/S0016793215060122.

- Roberts, P. H. On the Thermal Instability of a Rotating-Fluid Sphere Containing Heat Sources. *Philosophical Transactions of the Royal Society of London Series A*, 263(1136):93–117, May 1968. doi: 10.1098/rsta.1968.0007.
- Roberts, P. H. and Aurnou, J. M. On the theory of core-mantle coupling. *Geophysical and Astrophysical Fluid Dynamics*, 106(2):157–230, April 2012. doi: 10.1080/03091929.2011.589028.
- Roberts, P. H. and King, E. M. On the genesis of the Earth’s magnetism. *Reports on Progress in Physics*, 76(9):096801, September 2013. doi: 10.1088/0034-4885/76/9/096801.
- Roberts, P. H. and Wu, C.-C. On the modified Taylor constraint. *Geophysical and Astrophysical Fluid Dynamics*, 108(6):696–715, November 2014. doi: 10.1080/03091929.2014.942955.
- Roberts, P. 8.03 - theory of the geodynamo. In Schubert, G., editor, *Treatise on Geophysics*, pages 67 – 105. Elsevier, Amsterdam, 2007. ISBN 978-0-444-52748-6. doi: <https://doi.org/10.1016/B978-044452748-6.00133-4>. URL <http://www.sciencedirect.com/science/article/pii/B9780444527486001334>.
- Schaeffer, N., Jault, D., Nataf, H.-C., and Fournier, A. Turbulent geodynamo simulations: a leap towards Earth’s core. *Geophysical Journal International*, 211:1–29, October 2017. doi: 10.1093/gji/ggx265.
- Scherrer, P. H., Bogart, R. S., Bush, R. I., Hoeksema, J. T., Kosovichev, A. G., Schou, J., Rosenberg, W., Springer, L., Tarbell, T. D., Title, A., Wolfson, C. J., Zayer, I., and MDI Engineering Team. The Solar Oscillations Investigation - Michelson Doppler Imager. *Solar Physics*, 162(1-2): 129–188, December 1995. doi: 10.1007/BF00733429.
- Scherrer, P. H., Schou, J., Bush, R. I., Kosovichev, A. G., Bogart, R. S., Hoeksema, J. T., Liu, Y., Duvall, T. L., Zhao, J., Title, A. M., Schrijver, C. J., Tarbell, T. D., and Tomczyk, S. The Helioseismic and Magnetic Imager (HMI) Investigation for the Solar Dynamics Observatory (SDO). *Solar Physics*, 275(1-2):207–227, January 2012. doi: 10.1007/s11207-011-9834-2.
- Schou, J., Antia, H. M., Basu, S., Bogart, R. S., Bush, R. I., Chitre, S. M., Christensen-Dalsgaard, J., Di Mauro, M. P., Dziembowski, W. A., Eff-Darwich, A., Gough, D. O., Haber, D. A., Hoeksema, J. T., Howe, R., Korzennik, S. G., Kosovichev, A. G., Larsen, R. M., Pijpers, F. P., Scherrer, P. H., Sekii, T., Tarbell, T. D., Title, A. M., Thompson, M. J., and Toomre, J. Helioseismic Studies of Differential Rotation in the Solar Envelope by the Solar Oscillations Investigation Using the Michelson Doppler Imager. *Astrophys. J.*, 505(1):390–417, September 1998. doi: 10.1086/306146.
- Schrinner, M., Petitdemange, L., and Dormy, E. Dipole collapse and dynamo waves in global direct numerical simulations. *Astrophys. J.*, 752:121, June 2012. doi: 10.1088/0004-637X/752/2/121.
- Schubert, G. and Soderlund, K. Planetary magnetic fields: observations and models. *Physics of the Earth and Planetary Interiors*, 187:92–108, 2011.
- Schubert, G., Turcotte, D. L., and Olson, P. *Mantle Convection in the Earth and Planets*. Cambridge University Press, 2001. doi: 10.1017/CBO9780511612879.
- Schwabe, M. Sonnen-und Saturn-Beobachtungen im Jahre 1848, von Herrn Hofrat Schwabe in Dessau. *Astronomische Nachrichten*, 28:302, April 1849.

- Seaton, D. B. and Darnel, J. M. Observations of an eruptive solar flare in the extended EUV solar corona. *The Astrophysical Journal*, 852(1):L9, jan 2018. doi: 10.3847/2041-8213/aaa28e. URL <https://doi.org/10.3847%2F2041-8213%2Faaa28e>.
- Sheyko, A., Finlay, C., Favre, J., and Jackson, A. Scale separated low viscosity dynamos and dissipation within the Earths core. *Sci. Rep.*, 8(1):12566, 2018.
- Smith, E. J., Davis, J., L., and Jones, D. E. Jupiter's magnetic field and magnetosphere. In Gehrels, T. and Matthews, S., editors, *IAU Colloq. 30: Jupiter: Studies of the Interior, Atmosphere, Magnetosphere and Satellites*, pages 788–829, January 1976.
- Smith, E. J., Davis, L., Jones, D. E., Coleman, P. J., Colburn, D. S., Dyal, P., and Sonett, C. P. Saturn's Magnetic Field and Magnetosphere. *Science*, 207(4429):407–410, January 1980a. doi: 10.1126/science.207.4429.407.
- Smith, E. J., Davis, L., Jones, D. E., Coleman, P. J., Colburn, D. S., Dyal, P., and Sonett, C. P. Saturn's Magnetosphere and Its Interaction With the Solar Wind. *J. Geophys. Res.*, 85(A11): 5655–5674, November 1980b. doi: 10.1029/JA085iA11p05655.
- Soderlund, K. M., King, E. M., and Aurnou, J. M. The influence of magnetic fields in planetary dynamo models. *Earth and Planetary Science Letters*, 333:9–20, June 2012. doi: 10.1016/j.epsl.2012.03.038.
- Soderlund, K. M., Sheyko, A., King, E. M., and Aurnou, J. M. The competition between Lorentz and Coriolis forces in planetary dynamos. *Progress in Earth and Planetary Science*, 2:24, December 2015. doi: 10.1186/s40645-015-0054-5.
- Soward, A. M. A Convection-Driven Dynamo: I. The Weak Field Case. *Philosophical Transactions of the Royal Society of London Series A*, 275(1256):611–646, April 1974. doi: 10.1098/rsta.1974.0003.
- Soward, A. M. On the Finite amplitude thermal instability of a rapidly rotating fluid sphere. *Geophysical and Astrophysical Fluid Dynamics*, 9(1):19–74, January 1977. doi: 10.1080/03091927708242315.
- Spiegel, E. A. Thermal Turbulence at Very Small Prandtl Number. *J. Geophys. Res.*, 67:3063, July 1962. doi: 10.1029/JZ067i008p03063.
- Stanley, S. and Bloxham, J. Convective-region geometry as the cause of Uranus' and Neptune's unusual magnetic fields. *Nature*, 428(6979):151–153, March 2004. doi: 10.1038/nature02376.
- Steenbeck, M., Krause, F., and Rädler, K.-H. A calculation of the mean electromotive force in an electrically conducting fluid in turbulent motion, under the influence of coriolis forces. *Z. Naturforsch.*, 21a:369–376, 1966.
- Stein, R. F. and Nordlund, A. Topology of Convection beneath the Solar Surface. *Astrophys. J. Lett.*, 342:L95, July 1989. doi: 10.1086/185493.
- Stein, R. F., Georgobiani, D., Schafenberger, W., Nordlund, Å., and Benson, D. Supergranulation Scale Convection Simulations. In Stempels, E., editor, *15th Cambridge Workshop on Cool Stars, Stellar Systems, and the Sun*, volume 1094 of *American Institute of Physics Conference Series*, pages 764–767, February 2009. doi: 10.1063/1.3099227.

- Stellmach, S., Lischper, M., Julien, K., Vasil, G., Cheng, J. S., Ribeiro, A., King, E. M., and Aurnou, J. M. Approaching the Asymptotic Regime of Rapidly Rotating Convection: Boundary Layers versus Interior Dynamics. *Phys. Rev. Lett.*, 113(25):254501, December 2014. doi: 10.1103/PhysRevLett.113.254501.
- Stevenson, D. J. Dynamo generation in Mercury. *Nature*, 256(5519):634, August 1975. doi: 10.1038/256634a0.
- Stevenson, D. J. Turbulent thermal convection in the presence of rotation and a magnetic field: a heuristic theory. *Geophysical & Astrophysical Fluid Dynamics*, 12(1):139–169, 1979.
- Stevenson, D. J. Planetary magnetic fields. *Earth and Planetary Science Letters*, 208(1):1 – 11, 2003. ISSN 0012-821X. doi: [https://doi.org/10.1016/S0012-821X\(02\)01126-3](https://doi.org/10.1016/S0012-821X(02)01126-3). URL <http://www.sciencedirect.com/science/article/pii/S0012821X02011263>.
- Strik, G., Blake, T. S., Zegers, T. E., White, S. H., and Langereis, C. G. Palaeomagnetism of flood basalts in the Pilbara Craton, Western Australia: Late Archaean continental drift and the oldest known reversal of the geomagnetic field. *J. Geophys. Res. (Solid Earth)*, 108:2551, December 2003. doi: 10.1029/2003JB002475.
- Tarduno, J. A., Cottrell, R. D., Watkeys, M. K., Hofmann, A., Doubrovine, P. V., Mamajek, E. E., Liu, D., Sibeck, D. G., Neukirch, L. P., and Usui, Y. Geodynamo, Solar Wind, and Magnetopause 3.4 to 3.45 Billion Years Ago. *Science*, 327(5970):1238, March 2010. doi: 10.1126/science.1183445.
- Tarduno, J. A., Cottrell, R. D., Davis, W. J., Nimmo, F., and Bono, R. K. A Hadean to Paleoproterozoic geodynamo recorded by single zircon crystals. *Science*, 349(6247):521–524, July 2015. doi: 10.1126/science.aaa9114.
- Taylor, G. I. Experiments on the Motion of Solid Bodies in Rotating Fluids. *Proceedings of the Royal Society of London Series A*, 104(725):213–218, September 1923. doi: 10.1098/rspa.1923.0103.
- Taylor, G. I. and Lamb, H. Motion of solids in fluids when the flow is not irrotational. *Proceedings of the Royal Society of London. Series A, Containing Papers of a Mathematical and Physical Character*, 93(648):99–113, 1917. doi: 10.1098/rspa.1917.0007. URL <https://royalsocietypublishing.org/doi/abs/10.1098/rspa.1917.0007>.
- Taylor, J. B. The Magneto-Hydrodynamics of a Rotating Fluid and the Earth's Dynamo Problem. *Proceedings of the Royal Society of London Series A*, 274(1357):274–283, July 1963. doi: 10.1098/rspa.1963.0130.
- Thomsen, M. F., Roussos, E., Andriopoulou, M., Kollmann, P., Arridge, C. S., Paranicas, C. P., Gurnett, D. A., Powell, R. L., Tokar, R. L., and Young, D. T. Saturn's inner magnetospheric convection pattern: Further evidence. *J. Geophys. Res. Space Physics*, 117(A9), 2012. doi: 10.1029/2011JA017482. URL <https://agupubs.onlinelibrary.wiley.com/doi/abs/10.1029/2011JA017482>.
- Thual, O. Zero-Prandtl-number convection. *Journal of Fluid Mechanics*, 240:229–258, 1992. doi: 10.1017/S0022112092000089.
- Todoeschuck, J. P., Crossley, D. J., and Rochester, M. G. Saturn's magnetic field and dynamo theory. *Geophys. Res. Lett.*, 8(5):505–508, May 1981. doi: 10.1029/GL008i005p00505.

- Ustyugov, S. D. Realistic magnetohydrodynamical simulation of solar local supergranulation. *Physica Scripta Volume T*, 142(1):014031, December 2010. doi: 10.1088/0031-8949/2010/T142/014031.
- Vasil, G. M., Lecoanet, D., Brown, B. P., Wood, T. S., and Zweibel, E. G. Energy Conservation and Gravity Waves in Sound-proof Treatments of Stellar Interiors. II. Lagrangian Constrained Analysis. *Astrophys. J.*, 773(2):169, August 2013. doi: 10.1088/0004-637X/773/2/169.
- Vine, F. J. Spreading of the Ocean Floor: New Evidence. *Science*, 154(3755):1405–1415, December 1966. doi: 10.1126/science.154.3755.1405.
- Vine, F. J. and Matthews, D. H. Magnetic Anomalies Over Oceanic Ridges. *Nature*, 199(4897):947–949, September 1963. doi: 10.1038/199947a0.
- Volta, A. On the Electricity Excited by the Mere Contact of Conducting Substances of Different Kinds. *Proceedings of the Royal Society of London Series I*, 1:27–29, January 1800.
- Warwick, J. W., Evans, D. R., Peltzer, G. R., Peltzer, R. G., Romig, J. H., Sawyer, C. B., Riddle, A. C., Schweitzer, A. E., Desch, M. D., Kaiser, M. L., Farrell, W. M., Carr, T. D., de Pater, I., Staelin, D. H., Gulkis, S., Poynter, R. L., Boischot, A., Genova, F., Leblanc, Y., Lecacheux, A., Pedersen, B. M., and Zarka, P. Voyager Planetary Radio Astronomy at Neptune. *Science*, 246(4936):1498–1501, December 1989. doi: 10.1126/science.246.4936.1498.
- Wicht, J. and Meduri, D. G. A gaussian model for simulated geomagnetic field reversals. *Physics of the Earth and Planetary Interiors*, 259:45–60, October 2016. doi: 10.1016/j.pepi.2016.07.007.
- Wicht, J. Inner-core conductivity in numerical dynamo simulations. *Physics of the Earth and Planetary Interiors*, 132(4):281–302, October 2002. doi: 10.1016/S0031-9201(02)00078-X.
- Wicht, J. and Christensen, U. R. Torsional oscillations in dynamo simulations. *Geophysical Journal International*, 181(3):1367–1380, June 2010. doi: 10.1111/j.1365-246X.2010.04581.x.
- Wiechert, E. About the mass distribution in the interior of the earth. *News from the Society of Sciences to Göttingen, Mathematical-Physical Class*, 1897(3):221–243, 1897.
- Wright, N. J., Drake, J. J., Mamajek, E. E., and Henry, G. W. The Stellar-activity-Rotation Relationship and the Evolution of Stellar Dynamos. *Astrophys. J.*, 743(1):48, December 2011. doi: 10.1088/0004-637X/743/1/48.
- Wright, N. J., Newton, E. R., Williams, P. K. G., Drake, J. J., and Yadav, R. K. The stellar rotation-activity relationship in fully convective M dwarfs. *Monthly Notices of the Royal Astron. Society*, 479(2):2351–2360, September 2018. doi: 10.1093/mnras/sty1670.
- Wu, C.-C. and Roberts, P. H. On magnetostrophic mean-field solutions of the geodynamo equations. *Geophysical and Astrophysical Fluid Dynamics*, 109(1):84–110, 2015.
- Yadav, R. K., Gastine, T., Christensen, U. R., Wolk, S. J., and Poppenhaeger, K. Approaching a realistic force balance in geodynamo simulations. *Proceedings of the National Academy of Science*, 113(43):12065–12070, October 2016. doi: 10.1073/pnas.1608998113.
- Yano, J.-I. Basic convective element: bubble or plume? a historical review. *Atmospheric Chemistry and Physics*, 14(13):7019–7030, 2014. doi: 10.5194/acp-14-7019-2014. URL <https://acp.copernicus.org/articles/14/7019/2014/>.

## Appendix A

### Selected Output Parameters

We make repeated use of the root mean square (rms); in particular, the rms of the radial magnetic field would be computed as

$$B_r^{\text{rms}} = \left\{ \sqrt{\frac{1}{V} \int B_r^2 dV} \right\}, \quad (\text{A.1})$$

where  $V$  is the volume of the spherical shell and the curly brackets indicate an average over time.

The flow velocity may be characterized using the Reynolds number  $\text{Re} = \sqrt{2E_k}$ . A related quantity is the magnetic Reynolds number  $\text{Rm} \equiv u^{\text{rms}} D / \eta = \text{RePm}$ , which measures the ratio of induction to magnetic diffusion. The relative importance of inertia compared to the Coriolis force is measured using the Rossby number defined as  $\text{Ro} \equiv u^{\text{rms}} / \Omega D = \text{ReEk}$ . We also use a local Rossby number,  $\text{Ro}_\ell \equiv \text{Ro} \bar{\ell}_p / \pi$ , based on the mean harmonic degree,  $\bar{\ell}_p$ , of the poloidal velocity field given by

$$\bar{\ell}_p = \sum_\ell \ell \frac{[(\mathbf{u}_p)_\ell \cdot (\mathbf{u}_p)_\ell]}{[\mathbf{u}_p \cdot \mathbf{u}_p]}, \quad (\text{A.2})$$

where the  $[\cdot]$  brackets indicate an average over radius and time. We use the poloidal velocity,  $\mathbf{u}_p \equiv u_r \hat{\mathbf{r}} + u_\theta \hat{\boldsymbol{\theta}}$ , following Schrinner et al. (2012), not the full velocity as used by Christensen and Aubert (2006). We do not see an appreciable difference in the Rossby numbers between the two definitions.

The Taylor microscale is used for the mean and fluctuating vector fields. For example, the Taylor microscale for the mean velocity is given by

$$\bar{\ell}_u = \left\{ \sqrt{\frac{\int |\bar{\mathbf{u}}|^2 dV'}{\int |\nabla \times \bar{\mathbf{u}}|^2 dV'}} \right\} \quad (\text{A.3})$$

and the Taylor microscale for the fluctuating magnetic field appears similarly as

$$\ell'_B = \left\{ \sqrt{\frac{\int |\mathbf{B}'|^2 dV'}{\int |\nabla \times \mathbf{B}'|^2 dV'}} \right\}. \quad (\text{A.4})$$

The curly braces indicate a time average as before. The radial integral involved in the volume integration does not include the Ekman layer on either boundary, i.e., the radial limits of integration are  $[r_i + Ek^{1/2}, r_o - Ek^{1/2}]$ .

## Appendix B

### Semi-Magnetostrophic Energetics

The semi-MS equations involve thermal wind in the meridional plane, described by the  $\hat{\mathbf{r}}$  and  $\hat{\theta}$  components of

$$\frac{2}{Ek} \hat{\mathbf{z}} \times \bar{\mathbf{u}} \approx -\frac{1}{Ek} \nabla \bar{P} + \frac{Ra}{Pr} \bar{T} \frac{\mathbf{r}}{r_o}, \quad (B.1)$$

as well as a Coriolis-Lorentz balance in the zonal direction given by

$$\frac{2}{Ek} \bar{u}_s \approx \frac{1}{Ek Pm} (\bar{\mathbf{J}} \times \bar{\mathbf{B}}) \cdot \hat{\phi}. \quad (B.2)$$

The cylindrical radial component of the mean velocity is  $\bar{u}_s \equiv (\hat{\mathbf{z}} \times \bar{\mathbf{u}}) \cdot \hat{\phi} = \bar{u}_r \sin \theta + \bar{u}_\theta \cos \theta$ . The three components of the semi-MS balance equations are explicitly

$$\hat{\mathbf{r}} : \quad \frac{2}{Ek} \hat{\mathbf{r}} \cdot (\hat{\mathbf{z}} \times \bar{\mathbf{u}}) = -\frac{2}{Ek} \bar{u}_\phi \sin \theta \approx -\frac{1}{Ek} \hat{\mathbf{r}} \cdot \nabla \bar{P} + \frac{Ra}{Pr} \bar{T} \frac{r}{r_o} \quad (B.3)$$

$$\hat{\theta} : \quad \frac{2}{Ek} \hat{\theta} \cdot (\hat{\mathbf{z}} \times \bar{\mathbf{u}}) = -\frac{2}{Ek} \bar{u}_\phi \cos \theta \approx -\frac{1}{Ek} \hat{\theta} \cdot \nabla \bar{P} \quad (B.4)$$

$$\hat{\phi} : \quad \frac{2}{Ek} \hat{\phi} \cdot (\hat{\mathbf{z}} \times \bar{\mathbf{u}}) = \frac{2}{Ek} \bar{u}_s \approx \frac{1}{Ek Pm} (\bar{\mathbf{J}} \times \bar{\mathbf{B}}) \cdot \hat{\phi}. \quad (B.5)$$

To derive the large-scale energetics in the semi-MS force balance, we take the inner product of the semi-MS balance equations with the mean velocity. This results in a single equation

$$0 \approx -\frac{1}{Ek} \bar{\mathbf{u}} \cdot \nabla \bar{P} + \frac{Ra}{Pr} \bar{u}_r \bar{T} \frac{r}{r_o} + \frac{1}{Ek Pm} \bar{u}_\phi (\bar{\mathbf{J}} \times \bar{\mathbf{B}})_\phi. \quad (B.6)$$

This can be rewritten in a slightly more useful form by exploiting the solenoidal constraint on the velocity to rearrange the pressure term. The final equation becomes

$$0 \approx -\nabla \cdot \left( \frac{1}{Ek} \bar{\mathbf{u}} \bar{P} \right) + \frac{Ra}{Pr} \bar{u}_r \bar{T} \frac{r}{r_o} + \frac{1}{Ek Pm} \bar{u}_\phi (\bar{\mathbf{J}} \times \bar{\mathbf{B}})_\phi. \quad (B.7)$$

## Appendix C

### Additional Scaling Relations

Many scaling relations were discussed in Chapter 3, specifically Section 3.4. A summary of all the scalings can be found in Table 3.3. Here we highlight other scaling relations that were computed, but not directly addressed during the discussions in the previous sections.

The scaling arguments that were presented in Chapter 3 started with the assumption that the mean temperature should not depend on Ekman number. The rms of the mean temperature is shown in Figure C.1(a). There is very little scatter indicating that the mean temperature does not depend strongly on the Ekman number. The highest Ekman number cases do exhibit a small deviation from the rest: they are slightly lower by about 5%. However, the lower Ekman number cases show a strong clustering with no observable trends as the Ekman number is changed, further indicating the absence of any Ekman number scaling. The mean temperature gradient length scale is shown in Figure C.1(b). It also shows good collapse of the different Ekman number cases without any rescaling. This indicates that the length scale does not depend strongly on Ekman number.

Throughout the discussion concerning the mean meridional circulation, the individual components were never mentioned. It could be possible that the meridional circulation is dominated by a single component. This is tested by computing the rms of the individual components of the mean meridional circulation. The radial component of the mean velocity is shown in Figure C.2(a) and the co-latitudinal component is shown in Figure C.2(b). Both components have been rescaled by  $\text{Ek}^{1/6}$  and show good collapse. This indicates that both components are  $\mathcal{O}\left(\text{Ek}^{-1/6}\right)$ , consistent with the previously obtained scaling for the full meridional circulation.

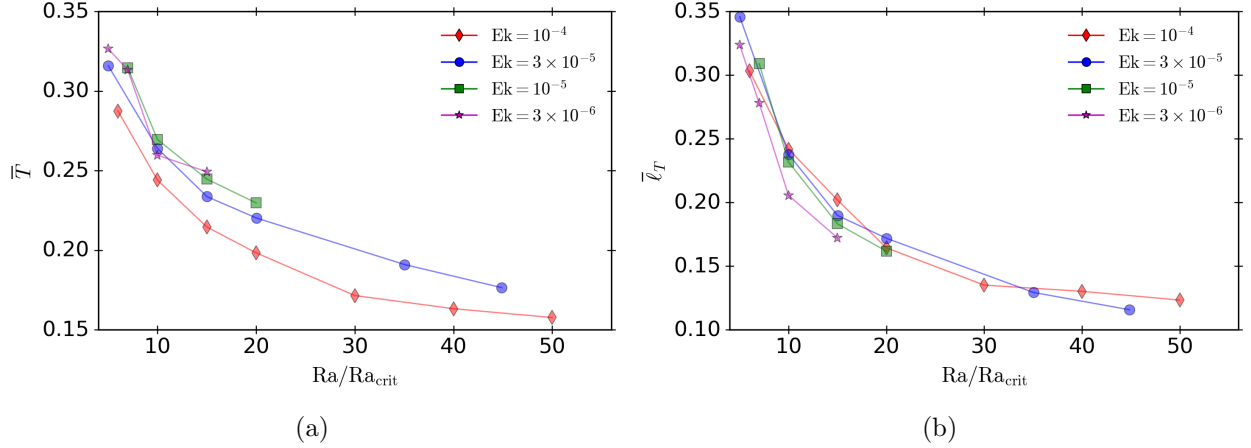


Figure C.1: (a) Rms of the mean temperature and (b) mean temperature gradient length scale. Both exhibit order unity behavior.

The scaling argument that was used to estimate the mean magnetic field scaling originated from the zonal component of the Lorentz force. The Lorentz force was assumed to scale as the magnitude of the full mean magnetic field squared as opposed to a particular component of the mean magnetic field. We test this assumption here by examining the individual components of the mean magnetic field. Figure C.2(c) shows the rms of the radial component of the mean magnetic field and Figure C.2(d) shows the zonal component. Both components have been rescaled by  $\text{Ek}^{1/9}$ , resulting in a good collapse of the data; there is very little difference between the lowest and highest Ekman numbers. We also note that the magnitude of the mean magnetic field has saturated for all components. This is related to the saturation of the mean magnetic field discussed in Chapter 4 and indicates the saturation takes place throughout all components of the magnetic field. We also note that the co-latitudinal component (not shown in the figure) exhibits similar behavior. Since all components show the same scaling, the full mean magnetic field also displays the  $\mathcal{O}(\text{Ek}^{-1/9})$  behavior.

The discussion surrounding the estimate of the fluctuating magnetic field scaling assumed that the eddy-eddy Lorentz force made use of the same length scale as the mean-mean contribution. As an estimate of the length scale appropriate for the fluctuating magnetic field, we compute the

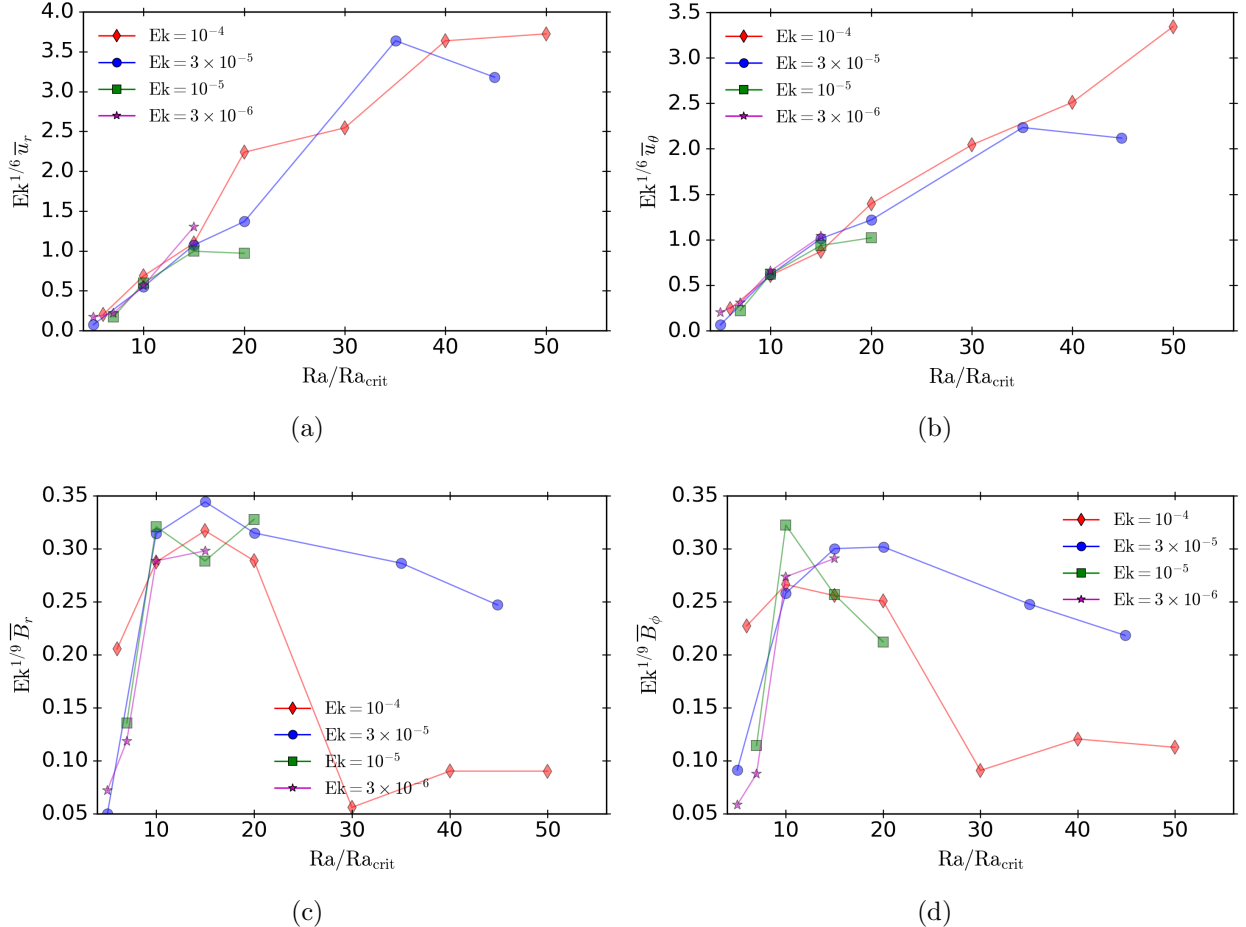


Figure C.2: Rms of the (a) radial and (b) co-latitudinal components of the mean velocity. Both components of the velocity have been rescaled by  $Ek^{1/6}$ . Rms of the (c) radial and zonal (d) components of the mean magnetic field. Both components of the magnetic field have been rescaled by  $Ek^{1/9}$ .

Taylor microscale. Figure C.3(a) shows the Taylor microscale for the fluctuating magnetic field and it is rescaled by  $Ek^{-1/9}$  in Figure C.3(b). There appears to be a trend where the length scale becomes smaller as the Ekman number is lowered. The collapse of the data under the rescaling factor suggests that the Taylor microscale for the fluctuating magnetic field scales as  $\mathcal{O}(Ek^{1/9})$ . This is different than the  $\mathcal{O}(1)$  scaling that was obtained for the mean magnetic field Taylor microscale. This indicates that the mean magnetic field varies on different spatial scales compared to the fluctuating magnetic field as the Ekman number changes.

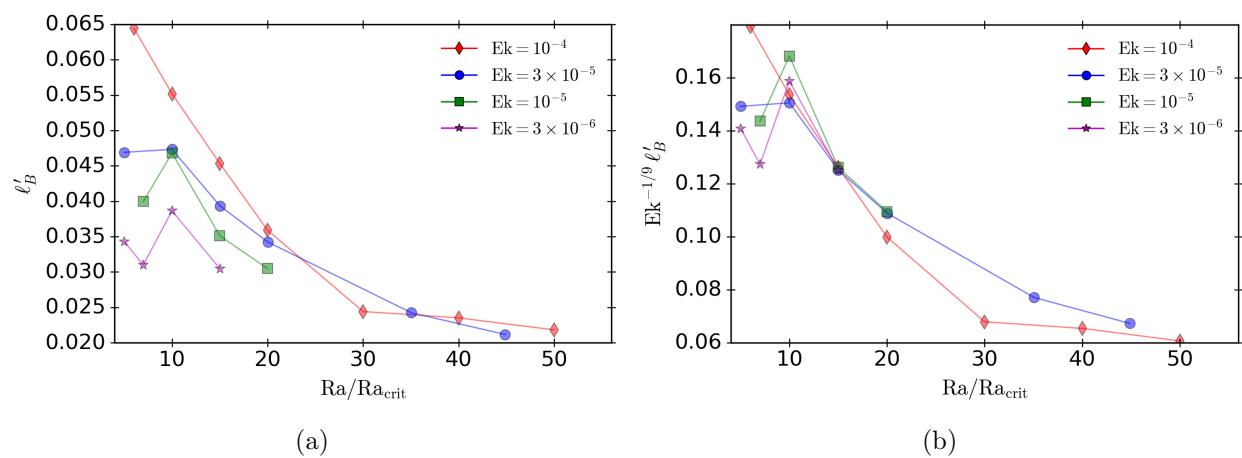


Figure C.3: Taylor microscale for the (a) fluctuating magnetic field, (b) rescaled by  $Ek^{-1/9}$ .

ProQuest Number: 28262583

INFORMATION TO ALL USERS

The quality and completeness of this reproduction is dependent on the quality  
and completeness of the copy made available to ProQuest.



Distributed by ProQuest LLC (2021).

Copyright of the Dissertation is held by the Author unless otherwise noted.

This work may be used in accordance with the terms of the Creative Commons license  
or other rights statement, as indicated in the copyright statement or in the metadata  
associated with this work. Unless otherwise specified in the copyright statement  
or the metadata, all rights are reserved by the copyright holder.

This work is protected against unauthorized copying under Title 17,  
United States Code and other applicable copyright laws.

Microform Edition where available © ProQuest LLC. No reproduction or digitization  
of the Microform Edition is authorized without permission of ProQuest LLC.

ProQuest LLC  
789 East Eisenhower Parkway  
P.O. Box 1346  
Ann Arbor, MI 48106 - 1346 USA